A stochastic, particle based model for testing the impact of correlated representation error on data assimilation

Florian Semrau

München 2024

A stochastic, particle based model for testing the impact of correlated representation error on data assimilation

Florian Semrau

Dissertation
der Fakultät für Physik
der Ludwig-Maximilians-Universität
München

vorgelegt von
Florian Semrau
aus Starnberg

München, den 17.09.2024

Erstgutachter: Prof. Dr. Tijana Janjić
Zweitgutachter: Prof. Dr. George Craig
Tag der mündlichen Prüfung: 15.11.2024

Contents

Zusammenfassung **xiii**

Abstract **xv**

1 Introduction **1**

2 Background **5**
2.1 Data assimilation 5
2.1.1 Equations for data assimilation 6
2.1.1.1 Kalman filter 6
2.1.1.2 Ensemble Kalman filter 9
2.1.2 Importance of covariances 11
2.2 Reference model and two moment scheme 15

3 Model (Toy model) **19**
3.1 Motivation 19
3.2 Stochastic particle model (SPM) 22
3.2.1 Particle definition of L and N 23
3.2.2 Advection and stochastic initial conditions 25
3.2.3 Cylindrical hydrometeors 27
3.3 Summary 28

4 Expectation values and error covariances **29**
4.1 Expectation values and error covariances for the SPM 29
4.2 Expectation values and error covariances for the reference model 31
4.3 Numerically calculated values 35
4.3.1 Profiles 36
4.3.2 Covariances and correlations 38
4.3.2.1 Covariance matrix for large spherical hydrometeors 38
4.3.2.2 Influence of particle geometry and orientation on correlations 39
4.3.2.3 Time dependence of variances for large spherical hydrometeors 40
4.3.3 Comparison of velocity models 41

4.4 Summary . . . 43

5 Data assimilation with SPM 45
5.1 Experimental design . . . 45
5.2 Numerical details . . . 47
5.3 Results . . . 52
5.3.1 Dynamic observation error covariance . . . 52
5.3.2 Time averaged observation error covariance . . . 62
5.3.3 Initial and final observation error covariance . . . 65
5.3.4 Modified observation operator . . . 69
5.4 Summary . . . 71

6 Influence of correlated observation errors on non-negativity of analysis 73
6.1 Preservation of non-negativity . . . 73
6.2 Illustration of the effect of non-diagonal observation error covariances on non-negativity . . . 76
6.3 Numerical experiments and distribution of analysis . . . 79
6.3.1 Effect of background correlations . . . 80
6.3.2 Effect of background variances . . . 87
6.3.3 Effect of unobserved grid points . . . 93
6.4 Analytical examples and use as counterexamples . . . 96
6.4.1 Examples illustrating the effect of observation error covariances on non-negativity preservation . . . 96
6.4.2 Consequences for generalisation of proposition 6.1.1 . . . 98
6.5 Summary . . . 100

7 Future work 101
7.1 Extensions to the SPM . . . 101
7.1.1 Observation operators . . . 101
7.1.1.1 General setup and constraints . . . 101
7.1.1.2 Kernel based observation operators . . . 103
7.1.2 Generalization to variable particle number . . . 106
7.1.3 Interaction models . . . 108
7.2 Possible applications of the SPM . . . 109
7.3 Neural network . . . 109

8 Conclusion 113

A Relation between the definitions of SPM and WSRM 117

B Geometric considerations for cylindrical hydrometeors 119
B.1 General description and case distinction . . . 119
B.2 Intersection areas . . . 122
B.2.1 The large angle case (full ellipse) . . . 123

B.2.2 The small angle case (ellipse section) . . . 126
B.2.3 Complete formula . . . 128

C Proofs for Chapter 4 **131**
C.1 Proof of Proposition 4.1.1 . . . 131
C.2 Proof of Proposition 4.1.2 . . . 132

D Simplification of auxiliary quantities from Chapter 4 **139**

E Velocity models **145**

F Upwind scheme **147**
F.1 Diagonalization . . . 147
F.2 System of equations . . . 148

G Additional plots for Chapter 6 **157**

H Additional calculations, proofs and examples for Chapter 6 **161**
H.1 Calculations for Example 6.4.1 . . . 161
H.2 Analytical example for non-negativity violation without influence from measurements at other grid points . . . 162
H.3 Analytical examples involving multiple grid points . . . 163
H.4 Proof of Proposition 6.4.3 . . . 164

Acknowledgments **170**

List of Figures

3.1 Model modifications ensuring well defined covariances 20
3.2 Relation between full and resolved state for the SPM 21
3.3 Information contained in model states 22
3.4 Schematic depiction of hydrometeor 24

4.1 Expectation values of N and L compared to reference model 36
4.2 Expectation values of N and L for cylindrical hydrometeors 38
4.3 Correlation matrix 39
4.4 Covariance profiles for various hydrometeor geometries 40
4.5 Variances and profiles of L and N for spherical hydrometeors 41
4.6 Variances of L and N for different hydrometeor size distributions 42
4.7 Centered covariance profiles obtained from different velocity models 43

5.1 Average observation error standard deviations 52
5.2 RMSE-values for N from using dynamic R 53
5.3 RMSE-values for L from using dynamic R 54
5.4 Ensemble spread for N from using dynamic R 55
5.5 Ensemble spread for L from using dynamic R 55
5.6 Spread ratio for N from using dynamic R 56
5.7 Spread ratio for L from using dynamic R 56
5.8 Snapshots N 58
5.9 Snapshots L 58
5.10 Snapshots N 59
5.11 Snapshots L 59
5.12 DA results for N, using full $\mathbf{R}$ and multiplicative inflation by a factor of 1.2 60
5.13 DA results for L, using full $\mathbf{R}$ and multiplicative inflation by a factor of 1.2 61
5.14 RMSE-values from using time averaged R 63
5.15 Ensemble spread from using time averaged R 63
5.16 Spread ratio from using time averaged R 64
5.17 RMSE-values for N from using initial and final $\mathbf{R}$ 65
5.18 RMSE-values for L from using initial and final $\mathbf{R}$ 66
5.19 Ensemble spread for N from using initial and final $\mathbf{R}$ 67
5.20 Ensemble spread for L from using initial and final $\mathbf{R}$ 67

5.21 Spread ratio for N from using initial and final $\mathbf{R}$ . . . 68
5.22 Spread ratio for L from using initial and final $\mathbf{R}$ . . . 68
5.23 RMSE-values from using dynamic $\mathbf{R}$, observing every second grid point . 70
5.24 Ensemble spread from using dynamic $\mathbf{R}$, observing every second grid point 70
5.25 Spread ratios from using dynamic $\mathbf{R}$, observing every second grid point . . 71

6.1 Background mean and covariance constructed from triangular ensemble . . 77
6.2 Triangular example for amplitude and positional error . . . 78
6.3 Triangular example for combined amplitude and positional error . . . 78
6.4 Analysis covariances for triangular example . . . 79
6.5 Negative analysis prevalence (positive background correlations) . . . 81
6.6 Histograms of analysis for positive background correlations . . . 82
6.7 Negative analysis prevalence (zero background correlations) . . . 83
6.8 Histograms of analysis for zero background correlations . . . 83
6.9 Negative analysis prevalence (negative background correlations) . . . 84
6.10 Histograms of analysis for negative background correlations . . . 85
6.11 Negative analysis prevalence as function of background correlation . . . 86
6.12 Negative analysis prevalence as function of $\frac{c_o}{c_f}$ . . . 88
6.13 Negative w_1^a and w_2^a prevalence as function of $\frac{c_o}{c_f}$ . . . 89
6.14 Histograms for $\mathbf{w}^a$ (overview) . . . 90
6.15 Histograms for w_1^a and w_2^a (overview) in the reference experiment . . . 91
6.16 Histograms for $\mathbf{w}^a$, w_1^a and w_2^a (overview) . . . 92
6.17 Negative w_2^a and w_3^a prevalence as function of $\frac{c_o}{c_f}$ (positive background correlations) . . . 94
6.18 Negative w_2^a and w_3^a prevalence as function of $\frac{c_o}{c_f}$ (zero background correlations) 94
6.19 Negative w_2^a and w_3^a prevalence as function of $\frac{c_o}{c_f}$ (negative background correlations) . . . 95

7.1 Illustration of possible constructions of observation operators . . . 102
7.2 Simple interaction model . . . 108
7.3 Neural network architecture . . . 111
7.4 Neural network architecture detail . . . 112

B.1 Basic case distinction . . . 119
B.2 Illustration of calculation of d_{max} . . . 120
B.3 Illustration of calculation of d_{inner} . . . 121
B.4 Intersection between cylinder of infinite length and (x, y)-plane . . . 122
B.5 Intersection between cylinder of length h and (x, y)-plane (large angle case) 123
B.6 Intersection between cylinder of length h and (x, y)-plane (small angle case) 127

E.1 Terminal fall velocities for different hydrometeor geometries . . . 146

G.1 Moments of w_2^a-distribution as function of background correlation for $\frac{c_o}{c_f} < 1$ 158

G.2 Moments of w_2^a-distribution as function of background correlation for $\frac{c_o}{c_f} > 1$ 159

List of Tables

6.1 Impact of non-diagonal $\mathbf{R}$ on non-negativity 86

Zusammenfassung

Ein in vielen Fachgebieten verbreitetes Problem ist die optimale Abschätzung eines Systemzustandes aus der Kombination einer Vorhersage mit Messdaten. Diese Aufgabe ist die zentrale Fragestellung auf dem Gebiet der Datenassimilation (DA). In diesem Zusammenhang sind die Unsicherheiten und Korrelationen einzelner Messungen in Form der Beobachtungsfehlerkovarianzmatrix gegeben. Die analogen Größen für die Vorhersage sind entsprechend in der Vorhersagefehlerkovarianzmatrix enthalten. Der Beobachtungsfehler beinhaltet üblicherweise mehrere Komponenten. Diese rühren aus dem Messprozess, der Abbildung des Zustandsraums, in dem das System modelliert wurde, auf den der Messungen, sowie aus dem sogenannten Repräsentationsfehler her. Letzterer wird durch den Unterschied zwischen dem Modell, das zur Beschreibung des Systems verwendet wird, und der physikalischen Realität verursacht und wird das Kernthema dieser Arbeit sein. Trotz der entscheidenden Rolle der Beobachtungsfehlerkovarianzmatrix in der DA ist die Bedeutung ihrer räumlichen Struktur und zeitlichen Entwicklung immer noch schlecht verstanden. Darüber hinaus ist ihre genaue Bestimmung in den meisten praktischen Anwendungen extrem schwierig. Deswegen werden häufig diagonale Beobachtungsfehlerkovarianzmatrizen verwendet, wodurch unkorrelierte Daten benötigt werden. Dies führt oftmals dazu, dass ein großer Anteil der verfügbaren Daten verworfen werden muss.

Zur systematischen Untersuchung der Rolle der Beobachtungsfehlerkovarianzmatrix in der DA konstruieren wir in dieser Arbeit das Stochastische Partikelmodell (SPM), ein einfaches partikelbasiertes Spielzeugmodell für Wassergehalt und Anzahlkonzentration, das über wohldefinierte Kovarianzen verfügt. Nach der Konstruktion des SPM berechnen wir die zugehörigen Kovarianzmatrizen numerisch und erklären ihre Eigenschaften durch gravitational sorting und Partikelgeometrie. Anschließend nutzen wir die aus dem SPM gewonnenen Kovarianzmatrizen in einer Reihe von DA-Experimenten, in denen wir die mit statischen und dynamischen, sowie mit kompletten, diagonalen und blockdiagonalen Beobachtungsfehlerkovarianzmatrizen erlangten Ergebnisse vergleichen. In diesen Experimenten sehen wir, dass eine korrekte Beschreibung der zeitlichen Entwicklung der Beobachtungsfehlerkovarianzmatrix erheblich wichtiger als die Berücksichtigung ihrer räumlichen Struktur ist.

Ein weiterer wichtiger Aspekt bei der Wahl zwischen diagonalen und nichtdiagonalen Beobachtungsfehlerkovarianzmatrizen bei der DA ist die Nichtnegativitätserhaltung. Deswe-

gen betrachten wir stark vereinfachte Beispiele, um zu zeigen, dass ein nichtnegatives Ergebnis des Kalmanfilters (ein verbreiteter DA Algorithmus), bei der Verwendung von nichtdiagonalen Vorhersage- und Beobachtungsfehlerkovarianzmatrizen, nicht garantiert werden kann. Darüber hinaus führen wir eine Reihe numerischer Experimente durch, um zu untersuchen, wie sich die Verwendung von nichtdiagonalen Beobachtungsfehlerkovarianzmatrizen auf die Häufigkeit von Nichtnegativitätsverletzungen auswirkt.

Abstract

In many disciplines, a common problem is to estimate the state of a system by combining a forecast or prediction with observations. Addressing this issue is the central goal of Data Assimilation (DA). In this context, the uncertainties and error correlations of individual observations are encoded in the observation error covariance matrix, and those of the forecast are encoded in the background error covariance matrix. The observation error usually consists of multiple components, originating from the measurement process, the mapping of the state space used to model the system to the observations and the so-called representation error. The latter one originates from the difference between the model used to describe the system and physical reality and will be the focus of this thesis. Despite the fact that the observation error covariance matrix plays a crucial role in DA, the role of its spatial structure and temporal development is still poorly understood and estimating it is extremely difficult for most practical applications. Thus in many cases a diagonal observation error covariance matrix is employed, requiring an uncorrelated data set and often leading to a large percentage of the available data being discarded.

To be able to systematically study the role of the observation error covariance matrix in DA, in this thesis we construct the Stochastic Particle Model (SPM), a simple particle based toy model for liquid water content and number density with well-defined covariances. After constructing the SPM, we numerically calculate the according covariance matrices and relate their features to gravitational sorting and particle geometry. Subsequently, we use the covariance matrices obtained from the SPM in a series of DA experiments, in which we compare the results obtained when using dynamic and static, as well as full, diagonal and block diagonal observation error covariance matrices. In these experiments, we find that correctly specifying the temporal evolution of the observation error covariance matrix is far more important than accounting for its spatial structure.

A further important aspect relevant for the choice between using diagonal or non-diagonal observation error covariance matrices in DA is non-negativity preservation. Thus we consider several strongly simplified examples to show that with non-diagonal background and observation error covariances, we can not ensure that the analysis of the Kalman filter (a common DA algorithm) is non-negative. Furthermore, we carry out a series of numerical experiments to investigate, how using non-diagonal observation error covariance matrices affects the frequency of non-negativity violations.

Chapter 1

Introduction

A common problem in many fields ranging from numerical weather prediction and finance over oceanography to navigation is estimating the state of a system by combining an uncertain forecast (background) with uncertain observations. The discipline dealing with this fundamental question is data assimilation (DA). In this context, the state space that we would like to estimate consists of the values of one or more fields evaluated on a grid. Information about the uncertainty of the forecasts at a certain grid point, as well as the correlation between forecast errors at different grid points, is provided by the *background error covariance matrix* $\mathbf{P^b}$. The *observation error covariance matrix* $\mathbf{R}$ contains analogue information about the observation error. The state estimate is called *analysis* and information about its uncertainty is usually provided by the DA algorithm in form of the *analysis error covariance matrix* $\mathbf{P^a}$. Combining this procedure with a mathematical/numerical model describing the temporal evolution of the dynamical system allows to iteratively incorporate observations carried out at different times into the model. Furthermore, applying the model to the most recent estimate of the system state allows the prediction of future system states. Commonly used DA algorithms on which this thesis will focus are the Kalman filter and the Ensemble Kalman filter (EnKF), a version of the Kalman filter representing uncertainty by an ensemble of states distributed around the estimated value.

The observation error covariance matrix $\mathbf{R}$ plays an important role in DA and its off-diagonal elements can contain crucial information. Though the use of full $\mathbf{R}$ matrix can significantly improve the results of DA (Weston et al., 2014), in practice the off-diagonal elements of $\mathbf{R}$ are difficult to estimate and thus diagonal matrices are often used instead. In this case, thinning, i.e. discarding observations to obtain an uncorrelated data set, is often necessary to ensure that the observation errors are uncorrelated (Janjić et al., 2018). This results in a large percentage of the available observations not being used during DA. The $\mathbf{R}$ matrix can also depend on the time or the state of the system (Janjić et al., 2018). Nevertheless, the influence of temporal and spatial variations in $\mathbf{R}$ on DA is still poorly understood.

In this thesis, we will concentrate on numerical weather prediction, which is an impor-

tant application for DA. In particular, we will research the assimilation of observations of quantities describing hydrometeors, i.e. "product[s] of condensation or deposition of atmospheric water vapour", such as rain, hail, graupel and ice crystals (AMS, 2022). A possible approach to modelling the evolution of hydrometeors is shown in Wacker and Seifert (2001). The authors construct their reference model describing the evolution of the liquid water content L and number density N of spherical hydrometeors in the case of pure sedimentation, i.e. in the absence of interactions between hydrometeors and of processes that can create or destroy hydrometeors. Furthermore, Wacker and Seifert (2001) approximate their reference model by a two-moment scheme, i.e. a model describing the state of the system and its evolution by two different moments (here liquid water content and number density) of the so called size *distribution function* of the hydrometeors (Wacker and Seifert, 2001). Two- (or more) moment schemes are recommended to be used in numerical simulations (e.g. Igel et al., 2015). Also Wacker and Seifert (2001) found a one-moment scheme to produce solutions strongly differing from their reference model.

Among the possible reasons for non-diagonal $\mathbf{R}$ matrices is the representation error, i.e. the part of the observation error originating from the model differing from the physical reality (Janjić et al., 2018). In order to study the representation error, performing DA experiments with analytically calculated covariances of a sufficiently simple physical model is desirable. The covariances of the error originating from the stochastic initial conditions of the Wacker and Seifert (2001) reference model are seemingly suitable for this task. However, we will see that the covariances of the Wacker and Seifert (2001) reference model depend on a free parameter without physical analogue, which is undesirable. Furthermore, as the models provided by Wacker and Seifert (2001) are limited to spherical hydrometeors, an extension to other geometries, such as cylindrical hydrometeors which are better suitable for modelling ice crystals, is of great interest. This is especially of interest for investigating the assimilation of measurements from polarimetric radars, which are influenced strongly by the axis ratio of hydrometeors. Furthermore, as the Wacker and Seifert (2001) reference model is designed for the parametrization of physical processes at length scales far larger than the typical hydrometeor diameter, it is not realistic on very small length scales and does not distinguish explicitly between stochastic and deterministic quantities. The latter makes the calculation of covariances difficult and limits the model to applications with a large amount of hydrometeors present. Though there exist models with available covariance matrices, like those summarized in Onof et al. (2000), they rely on *a priori* assuming a probability distribution for relatively complex large scale phenomena, such as the duration of storms.

Also work regarding the impact of accounting for observation error correlations in DA usually focusses on larger length scales or uses abstract models. E.g. Weston et al. (2014) found that accounting for observation error correlations by employing a Desroziers method (see Section 2.1.2 for description) in combination with *reconditioning*, i.e. decreasing the condition number of the observation error covariance matrix, results in the assimilation of infrared sounder data yielding a more accurate forecast (with respect to the standard

forecast verification method of the Met Office). However, the observations and simulations employed in their work had resolutions of several kilometres. Also Rainwater et al. (2015) found improved prediction of small scale features, when using suitable non-diagonal observation error covariance matrices. Their experiments belonged to the so called observation system simulation experiments (OSSEs), in which a more detailed simulation (refered to as the nature run) is used to create "observations" (so called pseudo-observations), and employed a modified Bishop and Hodyss (2009) model drawing pseudo-observations from an idealized distribution. Also in other OSSEs usually either pseudo-observations drawn from strongly idealized probability distributions (such as e.g. in Bishop, 2016) or generated by simulations of comparatively large scale phenomena (such as e.g. in Simon and Bertino, 2009) are employed. To our knowledge, there is no work focusing on length scales of less than $1m$ (which can be relevant e.g. for processes related to radar measurements) and employing observation errors directly derived from a physical model. Of special interest in this context is the work of Janjić and Cohn (2006b), which studied the advection of a tracer on a sphere (i.e. under conditions typical for a global scale model), as they focused on the impact of the *error due to unresolved scales* on DA. Similarly, in this thesis we will study the *error due to unresolved scales and processes* (see Section 2.1.2 for details and references).

Especially difficult is the estimation of quantities, that cannot become negative like the liquid water content and number density. Their necessarily non-Gaussian distribution violates a key assumption of many DA algorithms. When conducting an OSSE, it is unclear to what extent issues encountered during the assimilation of non-negative quantities can be attributed to the non-Gaussianity of the observation or other peculiarities such as a need for enforcing the positivity of the analysis before applying the model for time evolution. A further topic of interest is the effect of correlated observation errors on non-negativity preservation, i.e. the ability to guarantee non-negativity of the analysis when background and observations are guaranteed to be non-negative. However, there is little systematic research on this topic besides the work of Cohn (1997) and a generally known proposition guaranteeing non-negative analysis for the Kalman filter, in case of diagonal background and observation error covariance matrices.

To overcome the limitations of the Wacker and Seifert (2001) reference model, we construct the Stochastic Particle Model (SPM), which is based on the underlying particle model of the Wacker and Seifert (2001) reference model. The SPM features well-defined, physically meaningful error covariances. Furthermore, it is also capable of describing cylindrical hydrometeors. In contrast to the more top-down oriented approach of the previous work, the SPM allows to directly derive the covariances from the stochastic initial conditions of a modern microphysics scheme. As it focuses on very small scales, it can link features in the spatial structure of $\mathbf{R}$ to the geometry of hydrometeors and processes like gravitational sorting.

Furthermore, the availability of detailed information about the according covariances makes

the SPM suitable for studying the effect of ignoring the spatial and temporal structure of $\mathbf{R}$ in DA using an observation error derived from a smaller scale model. To address this question, we carry out a series of OSSEs employing pseudo-observations retrieved from a nature run created by the SPM. In addition, we repeat these experiments with pseudo-observations created by the Wacker and Seifert (2001) reference model with additive Gaussian noise. The variance of the noise is set to the observation error variance assumed by the DA algorithm and thus fits that of the SPM. For our experiments, we are going to use an EnKF without further modifications, as it is simple to implement, stable and does not need to be provided with an explicit background error covariance matrix. The ensemble is evolved in all experiments by the Wacker and Seifert (2001) two-moment scheme (also introduced in Wacker and Seifert (2001)), to keep the model error as small as possible. To evaluate the performance of our DA experiments, we employ the root mean square error (RMSE) despite the existence of more sophisticated diagnostics like the forecasts skill score (FSS), which avoids multiply accounting for positional errors (Roberts and Lean, 2008). Furthermore, we calculate the ensemble spread and the spread ratio to assess whether our DA implementation correctly estimates the uncertainty of the analysis.

Furthermore, to study the estimation of quantities that for physical reasons should not become negative, we consider a strongly simplified setup and try to identify scenarios in which non-negativity violations occur in analysis. Subsequently, we use them as counterexamples to show that non-negative analysis for the Kalman filter can not be guaranteed in case of non-diagonal background and observation error covariance matrices, without further constraints (Janjić et al., 2014). Furthermore, we are going to discuss the influence of using non-diagonal $\mathbf{R}$ on non-negativity preservation.

The remainder of this thesis will be structured as follows: We start by giving a summary of the relevant background for the thesis in Chapter 2, starting with the equations for the Kalman filter and the EnKF, and the role of covariances in DA. In Chapter 2 we will also introduce the Wacker and Seifert (2001) reference model and two-moment scheme. Subsequently, we construct the SPM in Chapter 3 by modifying the definitions of L and N of the Wacker and Seifert (2001) reference model to a particle based formulation. In Chapter 4, we obtain the covariance matrices of the error resulting from the stochastic initial conditions for the SPM and the Wacker and Seifert (2001) reference model. These matrices will then be used as observation error covariances in our DA experiments in Chapter 5. In Chapter 5, we study the effect of spatial and temporal variations in $\mathbf{R}$ on the performance of DA. These will consist of two parallel twin experiments, using pseudo-observations obtained from the SPM and pseudo-observations obtained from the Wacker and Seifert (2001) reference model. In Chapter 6 we investigate the effect of employing non-diagonal observation error covariances for the assimilation of non-negative variables with a Kalman filter. Finally, we provide an outlook on promising further research topics, including possible applications and extensions of the SPM in Chapter 7 and summarize the thesis in Chapter 8.

Chapter 2

Background

In this chapter, we introduce the methods and models later used in this thesis. Furthermore, we repeat some results from the literature, that allow to better motivate or interpret our research and provide background information for later chapters.

A general introduction to DA is given in Section 2.1, starting with the equations of the Kalman filter, which we will later investigate with respect to non-negativity preservation in Chapter 6, and ensemble Kalman filter, which we will employ in our DA experiments in Chapter 5. This is followed by the role of covariance matrices in DA in Section 2.1.2, motivating our research and providing background information, allowing us later to contextualize our results. Finally, in Section 2.2 we introduce the Wacker and Seifert (2001) reference model, which will be the basis for the construction of the SPM in Chapter 3 and an important reference for our DA experiments in Chapter 5, as well as the Wacker and Seifert (2001) two-moment scheme, which will be later used to evolve the ensemble in our DA experiments in Chapter 5.

2.1 Data assimilation

In this section, we are going to give a short introduction to data assimilation (DA), focusing on the following problem: Given a physical system modelled by (a system of) partial differential equations (e.g. Cohn (1997)) or an ordinary differential equation (e.g. Hunt et al. (2007)), a common problem is estimating the trajectory $\{\mathbf{x}(t)\}$ of the system from observations. The set of observations can (e.g. Hunt et al. (2007)) be assumed to be given by $\left\{\left(t_j, \mathbf{y}_j^o, H_j, \mathbf{R}_j\right) : j = 1, \cdots, n\right\}$, with t_j the *time* of the j-th observation, $\mathbf{y}_j^o$ the *values* of the observation at time t_j, $\mathbf{R}_j$ the according *observation error covariance matrix* and H_j the according *observation operator*, i.e. a map fulfilling

$$\mathbf{y}_j^o = H_j\left(\mathbf{x}\left(t_j\right)\right) + \epsilon_j, \text{ with } \epsilon_j \sim \mathcal{N}\left(\mathbf{0}, \mathbf{R}_j\right). \tag{2.1}$$

Furthermore, one defines $M_{t,t'}$ to be an operator evolving the solution of the underlying

model from time t to t' (e.g. Hunt et al. (2007)). Here $M_{t,t'}$ can either be assumed to be perfect or afflicted with an error, resulting from differences between the model and the dynamics of the actual physical system. Usually (e.g. Burgers et al. (1998)), this is modelled as

$$\mathbf{x}(t_j) = M_{t,t'}(\mathbf{x}(t)) + \hat{\epsilon}_{t,t'}, \text{ with } \hat{\epsilon}_{t,t'} \sim \mathcal{N}(\mathbf{0}, \mathbf{Q}_{t,t'}), \tag{2.2}$$

with $\mathbf{Q}_{t,t'}$ the according *model error covariance matrix*.

Now, assuming perfect model and employing a maximum likelihood approach to estimate the state of the system at time t, using the observations only, yields the cost function

$$J_t^o(\mathbf{x}) = \sum_{j=1}^{n} \left(\mathbf{y}_j^o - H_j\left(M_{t,t_j}(\mathbf{x})\right)\right)^T \mathbf{R}_j^{-1} \left(\mathbf{y}_j^o - H_j\left(M_{t,t_j}(\mathbf{x})\right)\right), \tag{2.3}$$

for the system being in the state $\mathbf{x}$ at time t (e.g. Hunt et al. (2007)).

In this chapter, we are going to give a short summary of some common approaches to this problem in Section 2.1.1 and then discuss the importance of covariances in Section 2.1.2.

2.1.1 Equations for data assimilation

We are now going to give a short summary of two commonly used data assimilation methods, that will also be employed in this thesis. We start with the equations for the Kalman filter in Section 2.1.1.1 and then move to the Ensemble Kalman filter (EnKF) in Section 2.1.1.2.

2.1.1.1 Kalman filter

We now give a short derivation of the Kalman filter, which can be employed to solve the problem described above, if the model and the observation operator are linear (Kalman et al., 1960). A more detailed derivation from the estimation point of view can be found e.g. in Cohn (1997). However our summary will be based on the description in Hunt et al. (2007), due to their more compact approach.

Assuming perfect model, (like Kalman et al. (1960)) Hunt et al. (2007) start by noticing that, if they are linear, one can rewrite the model and the observation operator as

$$M_{t,t'}(\mathbf{x}) = \mathbf{M}_{t,t'}\mathbf{x} \tag{2.4}$$

$$H_j(\mathbf{x}) = \mathbf{H}_j\mathbf{x}, \tag{2.5}$$

in terms of matrices $\mathbf{M}_{t,t'}$ and $\mathbf{H}_j$.

Now, they iteratively construct the Kalman filter by assuming that at time t_{n-1} the analysis (i.e. the part of the Kalman filter updating the estimate with new observations) has resulted in a Gaussian distribution with mean $\bar{\mathbf{x}}^a_{n-1}$ and covariance matrix $\mathbf{P}^a_{n-1}$. Thus, they can use M_{t_{n-1},t_n} to evolve the distribution obtained in the analysis step to time t_n, resulting (as linear models map Gaussian distributions to Gaussian distributions) in a Gaussian distribution with mean $\bar{\mathbf{x}}^b_n$ (*background mean*) and covariance matrix $\mathbf{P}^b_n$ (*background covariance*) given by

$$\bar{\mathbf{x}}^b_n = \mathbf{M}_{t_{n-1},t_n}\bar{\mathbf{x}}^a_{n-1} \tag{2.6}$$

$$\mathbf{P}^b_n = \mathbf{M}_{t_{n-1},t_n}\mathbf{P}^a_{n-1}\mathbf{M}^T_{t_{n-1},t_n}. \tag{2.7}$$

Now (still following the description in Hunt et al. (2007)), using (2.4), (2.5) and $M_{t,t} = \mathrm{Id}$ allows to rewrite the cost function given in (2.3) for the time step t_n as

$$\begin{aligned} J^o_{t_n}(\mathbf{x}) &= \sum_{j=1}^{n} \left(\mathbf{y}^o_j - \mathbf{H}_j\mathbf{M}_{t_n,t_j}\mathbf{x}\right)^T \mathbf{R}_j^{-1} \left(\mathbf{y}^o_j - \mathbf{H}_j\mathbf{M}_{t_n,t_j}\mathbf{x}\right) \\ &= \sum_{j=1}^{n-1} \left(\mathbf{y}^o_j - \mathbf{H}_j\mathbf{M}_{t_n,t_j}\mathbf{x}\right)^T \mathbf{R}_j^{-1} \left(\mathbf{y}^o_j - \mathbf{H}_j\mathbf{M}_{t_n,t_j}\mathbf{x}\right) \\ &\quad + \left(\mathbf{y}^o_n - \mathbf{H}_n\mathbf{x}\right)^T \mathbf{R}_n^{-1} \left(\mathbf{y}^o_n - \mathbf{H}_n\mathbf{x}\right). \end{aligned} \tag{2.8}$$

Now, (following, but slightly shortening the argumentation in Hunt et al. (2007)), observing that the first term is the cost function at time t_{n-1}, allows to rewrite this in terms of the analysis at t_{n-1} as

$$\begin{aligned} J^o_{t_n}(\mathbf{x}) &= \left(\mathbf{M}_{t_n,t_{n-1}}\mathbf{x} - \bar{\mathbf{x}}^a_{n-1}\right)^T \left(\mathbf{P}^a_{n-1}\right)^{-1} \left(\mathbf{M}_{t_n,t_{n-1}}\mathbf{x} - \bar{\mathbf{x}}^a_{n-1}\right) \\ &\quad + \left(\mathbf{y}^o_n - \mathbf{H}_n\mathbf{x}\right)^T \mathbf{R}_n^{-1} \left(\mathbf{y}^o_n - \mathbf{H}_n\mathbf{x}\right) + c \\ &= \left(\mathbf{M}^{-1}_{t_{n-1},t_n}\mathbf{x} - \mathbf{M}^{-1}_{t_{n-1},t_n}\mathbf{M}_{t_{n-1},t_n}\bar{\mathbf{x}}^a_{n-1}\right)^T \left(\mathbf{P}^a_{n-1}\right)^{-1} \left(\mathbf{M}^{-1}_{t_{n-1},t_n}\mathbf{x} - \mathbf{M}^{-1}_{t_{n-1},t_n}\mathbf{M}_{t_{n-1},t_n}\bar{\mathbf{x}}^a_{n-1}\right) \\ &\quad + \left(\mathbf{y}^o_n - \mathbf{H}_n\mathbf{x}\right)^T \mathbf{R}_n^{-1} \left(\mathbf{y}^o_n - \mathbf{H}_n\mathbf{x}\right) + c \\ &= \left(\mathbf{x} - \mathbf{M}_{t_{n-1},t_n}\bar{\mathbf{x}}^a_{n-1}\right)^T \left(\mathbf{M}^{-1}_{t_{n-1},t_n}\right)^T \left(\mathbf{P}^a_{n-1}\right)^{-1} \mathbf{M}^{-1}_{t_{n-1},t_n} \left(\mathbf{x} - \mathbf{M}_{t_{n-1},t_n}\bar{\mathbf{x}}^a_{n-1}\right) \\ &\quad + \left(\mathbf{y}^o_n - \mathbf{H}_n\mathbf{x}\right)^T \mathbf{R}_n^{-1} \left(\mathbf{y}^o_n - \mathbf{H}_n\mathbf{x}\right) + c \\ &= \left(\mathbf{x} - \bar{\mathbf{x}}^b_n\right)^T \left(\mathbf{P}^b_n\right)^{-1} \left(\mathbf{x} - \bar{\mathbf{x}}^b_n\right) + \left(\mathbf{y}^o_n - \mathbf{H}_n\mathbf{x}\right)^T \mathbf{R}_n^{-1} \left(\mathbf{y}^o_n - \mathbf{H}_n\mathbf{x}\right) + c, \end{aligned} \tag{2.9}$$

with c constant. Now (again following Hunt et al. (2007)), noticing that (if at time t_n the analysis again results in a Gaussian distribution with $\bar{\mathbf{x}}^a_n$ and covariance matrix $\mathbf{P}^a_n$) the cost function could also be written as

$$J^o_{t_n}(\mathbf{x}) = (\mathbf{x} - \bar{\mathbf{x}}^a_n)^T (\mathbf{P}^a_n)^{-1} (\mathbf{x} - \bar{\mathbf{x}}^a_n) + c', \tag{2.10}$$

with c' constant, equating (2.9) and (2.10) results in

$$\mathbf{P}^a_n = \left(\left(\mathbf{P}^b_n\right)^{-1} + \mathbf{H}^T_n \mathbf{R}^{-1}_n \mathbf{H}_n \right)^{-1} \tag{2.11}$$

from the terms of order $\mathbf{x}^2$ and

$$\bar{\mathbf{x}}^a_n = \mathbf{P}^a_n \left(\left(\mathbf{P}^b_n\right)^{-1} \bar{\mathbf{x}}^b_n + \mathbf{H}^T_n \mathbf{R}^{-1}_n \mathbf{y}^o_n \right) \tag{2.12}$$

from the terms of order $\mathbf{x}$. Finally (still following Hunt et al. (2007)), (2.11) and (2.12) can be written in the form

$$\bar{\mathbf{x}}^a_n = \bar{\mathbf{x}}^b_n + \mathbf{P}^a_n \mathbf{H}^T_n \mathbf{R}^{-1}_n \left(\mathbf{y}^o_n - \mathbf{H}_n \bar{\mathbf{x}}^b_n \right) \tag{2.13}$$

$$\mathbf{P}^a_n = \left(\mathrm{Id} + \mathbf{P}^b_n \mathbf{H}^T_n \mathbf{R}^{-1}_n \mathbf{H}_n \right)^{-1} \mathbf{P}^b_n. \tag{2.14}$$

We finally show, that this is equivalent to the more commonly used form (e.g. Cohn (1997)) of the Kalman filter equations

$$\bar{\mathbf{x}}^a_n = \bar{\mathbf{x}}^b_n + \mathbf{K} \left(\mathbf{y}^o_n - \mathbf{H}_n \bar{\mathbf{x}}^b_n \right) \tag{2.15}$$

$$\mathbf{K}_n = \mathbf{P}^b_n \mathbf{H}^T_n \left(\mathbf{H}_n \mathbf{P}^b_n \mathbf{H}^T_n + \mathbf{R}_n \right)^{-1} \tag{2.16}$$

$$\mathbf{P}^a_n = (\mathrm{Id} - \mathbf{K}\mathbf{H})\, \mathbf{P}^b_n. \tag{2.17}$$

The equivalence of (2.17) with (2.14) follows could be shown by proving that $(\mathrm{Id} - \mathbf{K}\mathbf{H})$ is the inverse of $\left(\mathrm{Id} + \mathbf{P}^b_n \mathbf{H}^T_n \mathbf{R}^{-1}_n \mathbf{H}_n \right)$, that is[1]

$$\begin{aligned}
&(\mathrm{Id} - \mathbf{K}_n \mathbf{H}_n) \left(\mathrm{Id} + \mathbf{P}^b_n \mathbf{H}^T_n \mathbf{R}^{-1}_n \mathbf{H}_n \right) = \qquad (2.18)\\
&= \mathrm{Id} - \mathbf{K}_n \mathbf{H}_n + \mathbf{P}^b_n \mathbf{H}^T_n \mathbf{R}^{-1}_n \mathbf{H}_n - \mathbf{K}_n \mathbf{H}_n \mathbf{P}^b_n \mathbf{H}^T_n \mathbf{R}^{-1}_n \mathbf{H}_n \\
&= \mathrm{Id} - \left[\mathbf{K}_n - \mathbf{P}^b_n \mathbf{H}^T_n \mathbf{R}^{-1}_n + \mathbf{K}_n \mathbf{H}_n \mathbf{P}^b_n \mathbf{H}^T_n \mathbf{R}^{-1}_n \right] \mathbf{H}_n \\
&= \mathrm{Id} - \left[\mathbf{P}^b_n \mathbf{H}^T_n \left(\mathbf{H}_n \mathbf{P}^b_n \mathbf{H}^T_n + \mathbf{R}_n \right)^{-1} - \mathbf{P}^b_n \mathbf{H}^T_n \mathbf{R}^{-1}_n + \mathbf{P}^b_n \mathbf{H}^T_n \left(\mathbf{H}_n \mathbf{P}^b_n \mathbf{H}^T_n + \mathbf{R}_n \right)^{-1} \mathbf{H}_n \mathbf{P}^b_n \mathbf{H}^T_n \mathbf{R}^{-1}_n \right] \mathbf{H}_n \\
&= \mathrm{Id} - \mathbf{P}^b_n \mathbf{H}^T_n \left(\mathbf{H}_n \mathbf{P}^b_n \mathbf{H}^T_n + \mathbf{R}_n \right)^{-1} \left[\mathrm{Id} - \left(\mathbf{H}_n \mathbf{P}^b_n \mathbf{H}^T_n + \mathbf{R}_n \right) \mathbf{R}^{-1}_n + \mathbf{H}_n \mathbf{P}^b_n \mathbf{H}^T_n \mathbf{R}^{-1}_n \right] \mathbf{H}_n \\
&= \mathrm{Id} - \mathbf{P}^b_n \mathbf{H}^T_n \left(\mathbf{H}_n \mathbf{P}^b_n \mathbf{H}^T_n + \mathbf{R}_n \right)^{-1} \underbrace{\left[\mathrm{Id} - \mathbf{H}_n \mathbf{P}^b_n \mathbf{H}^T_n \mathbf{R}^{-1}_n - \mathrm{Id} + \mathbf{H}_n \mathbf{P}^b_n \mathbf{H}^T_n \mathbf{R}^{-1}_n \right]}_{=0} \mathbf{H}_n \\
&= \mathrm{Id}\,.
\end{aligned}$$

[1] We only show that it is a right inverse and forego the analogue calculation showing that it is also a left inverse for simplicity.

Now using (2.17), the equivalence of (2.15) and (2.16) with (2.13) follows from

$$
\begin{aligned}
\mathbf{P}_n^a \mathbf{H}_n^T \mathbf{R}_n^{-1} &= (\mathrm{Id} - \mathbf{K}\mathbf{H})\, \mathbf{P}_n^b \mathbf{H}_n^T \mathbf{R}_n^{-1} \\
&= \mathbf{P}_n^b \mathbf{H}_n^T \mathbf{R}_n^{-1} - \mathbf{K}\mathbf{H}\mathbf{P}_n^b \mathbf{H}_n^T \mathbf{R}_n^{-1} \\
&= \mathbf{P}_n^b \mathbf{H}_n^T \mathbf{R}_n^{-1} - \mathbf{P}_n^b \mathbf{H}_n^T \left(\mathbf{H}_n \mathbf{P}_n^b \mathbf{H}_n^T + \mathbf{R}_n\right)^{-1} \mathbf{H}\mathbf{P}_n^b \mathbf{H}_n^T \mathbf{R}_n^{-1} \\
&= \mathbf{P}_n^b \mathbf{H}_n^T \left[\mathrm{Id} - \left(\mathbf{H}_n \mathbf{P}_n^b \mathbf{H}_n^T + \mathbf{R}_n\right)^{-1} \mathbf{H}\mathbf{P}_n^b \mathbf{H}_n^T\right] \mathbf{R}_n^{-1} \\
&= \mathbf{P}_n^b \mathbf{H}_n^T \left[\mathrm{Id} - \left(\mathbf{H}_n \mathbf{P}_n^b \mathbf{H}_n^T + \mathbf{R}_n\right)^{-1} \mathbf{H}\mathbf{P}_n^b \mathbf{H}_n^T - \left(\mathbf{H}_n \mathbf{P}_n^b \mathbf{H}_n^T + \mathbf{R}_n\right)^{-1} \mathbf{R}_n + \right. \\
&\quad \left. + \left(\mathbf{H}_n \mathbf{P}_n^b \mathbf{H}_n^T + \mathbf{R}_n\right)^{-1} \mathbf{R}_n\right] \mathbf{R}_n^{-1} \\
&= \mathbf{P}_n^b \mathbf{H}_n^T \left[\mathrm{Id} - \left(\mathbf{H}_n \mathbf{P}_n^b \mathbf{H}_n^T + \mathbf{R}_n\right)^{-1} \left(\mathbf{H}_n \mathbf{P}_n^b \mathbf{H}_n^T + \mathbf{R}_n\right) + \left(\mathbf{H}_n \mathbf{P}_n^b \mathbf{H}_n^T + \mathbf{R}_n\right)^{-1} \mathbf{R}_n\right] \mathbf{R}_n^{-1} \\
&= \mathbf{P}_n^b \mathbf{H}_n^T \left(\mathbf{H}_n \mathbf{P}_n^b \mathbf{H}_n^T + \mathbf{R}_n\right)^{-1} \mathbf{R}_n \mathbf{R}_n^{-1} \\
&= \mathbf{P}_n^b \mathbf{H}_n^T \left(\mathbf{H}_n \mathbf{P}_n^b \mathbf{H}_n^T + \mathbf{R}_n\right)^{-1} \\
&= \mathbf{K}_n.
\end{aligned}
\tag{2.19}
$$

2.1.1.2 Ensemble Kalman filter

As the Kalman filter relies on the linearity of the model (Kalman et al., 1960), its applicability is limited and there have been constructed many generalizations of the Kalman filter, that do not require this assumption, such as the *ensemble transform Kalman filter* (ETKF) (Bishop et al., 2001), the *local ensemble transform Kalman filter* (LETKF) (Hunt et al., 2007) and the *ensemble Kalman filter* (EnKF) (Burgers et al., 1998; Evensen, 1994). Due to its easy implementation and stability, we will use the EnKF for the data assimilation experiments in this thesis. Thus, we give here a short derivation of the ensemble Kalman filter based on the description in Burgers et al. (1998), who developed it in the currently used form. Their notation will be changed to the current standard notation described in Ide et al. (1997), which is used throughout this thesis.

The EnKF uses two ensembles, one to describe the state estimate (i.e. background and analysis) and one to describe the observations at time t, where the spread of the ensemble corresponds to the uncertainty of the according quantity (Burgers et al., 1998). This has the advantage, that the members of the ensemble representing the state estimate can be propagated individually also by a non-linear model and the ensemble representation of the observations prevents (for large enough ensembles) the underestimation of the analysis error covariance and problems arising from spurious correlations (Burgers et al., 1998).

Burgers et al. (1998) start their derivation with an ensemble $\mathbf{X}^b$ of N members, representing the state estimate at time t_n prior to analysis, i.e. with

$$\mathbf{P}_n^b \approx \mathbf{P}_{n,e}^b \coloneqq \overline{\left(\mathbf{X}^b - \overline{\mathbf{X}^b}\right)\left(\mathbf{X}^b - \overline{\mathbf{X}^b}\right)^T} \tag{2.20}$$

$$\bar{\mathbf{x}}_n^b \approx \overline{\mathbf{X}^b} \tag{2.21}$$

and create an ensemble $\mathbf{Y}^o$ of N members, representing the observations at time t_n , by setting

$$\mathbf{y}_n^{o(i)} = \mathbf{y}_n^o + \epsilon_i, \text{ with } \epsilon_i \sim \mathcal{N}(\mathbf{0}, \mathbf{R}_n), \tag{2.22}$$

for $i \in \{1, \cdots, N\}$. Then they uptate every member $\mathbf{X}_i^b$ of $\mathbf{X}^b$ individually with the according $\mathbf{y}_n^{o(i)}$ analogue to the Kalman Filter, yielding

$$\mathbf{X}_i^a = \mathbf{X}_i^b + \mathbf{K}_e\left(\mathbf{y}_n^{o(i)} - \mathbf{H}_n\mathbf{X}_i^b\right), \tag{2.23}$$

with (note that this is equivalent to (2.15))

$$\mathbf{K}_e = \mathbf{P}_{n,e}^b\mathbf{H}_n^T\left(\mathbf{H}_n\mathbf{P}_{n,e}^b\mathbf{H}_n^T + \mathbf{R}_n\right)^{-1}, \tag{2.24}$$

and finally

$$\overline{\mathbf{X}^a} = \overline{\mathbf{X}^b} + \mathbf{K}_e\left(\overline{\mathbf{Y}^o} - \mathbf{H}_n\overline{\mathbf{X}^b}\right). \tag{2.25}$$

For the covariance, they obtain

$$\begin{aligned}\mathbf{P}_{n,e}^a &= \overline{\left(\mathbf{X}^a - \overline{\mathbf{X}^a}\right)\left(\mathbf{X}^a - \overline{\mathbf{X}^a}\right)^T} \qquad (2.26)\\ &= \overline{\left[(\mathrm{Id} - \mathbf{K}_e\mathbf{H})\left(\mathbf{X}^b - \overline{\mathbf{X}^b}\right) + \mathbf{K}_e\left(\mathbf{Y}^o - \overline{\mathbf{Y}^o}\right)\right]\left[(\mathrm{Id} - \mathbf{K}_e\mathbf{H})\left(\mathbf{X}^b - \overline{\mathbf{X}^b}\right) + \mathbf{K}_e\left(\mathbf{Y}^o - \overline{\mathbf{Y}^o}\right)\right]^T},\end{aligned}$$

using (2.23) and (2.25), which they simplify to

$$\begin{aligned}\mathbf{P}_{n,e}^a &= (\mathrm{Id} - \mathbf{K}_e\mathbf{H})\underbrace{\overline{\left(\mathbf{X}^b - \overline{\mathbf{X}^b}\right)\left(\mathbf{X}^b - \overline{\mathbf{X}^b}\right)^T}}_{=\mathbf{P}_{n,e}^b}(\mathrm{Id} - \mathbf{K}_e\mathbf{H})^T + \qquad (2.27)\\ &\quad + \mathbf{K}_e\underbrace{\overline{\left(\mathbf{Y}^o - \overline{\mathbf{Y}^o}\right)\left(\mathbf{Y}^o - \overline{\mathbf{Y}^o}\right)^T}}_{=\mathbf{R}_n + \mathcal{O}\left(N^{-\frac{1}{2}}\right)}\mathbf{K}_e^T + (\mathrm{Id} - \mathbf{K}_e\mathbf{H})\underbrace{\overline{\left(\mathbf{X}^b - \overline{\mathbf{X}^b}\right)\left(\mathbf{Y}^o - \overline{\mathbf{Y}^o}\right)^T}}_{\mathcal{O}\left(N^{-\frac{1}{2}}\right)}\mathbf{K}_e^T + \\ &\quad + \mathbf{K}_e\underbrace{\overline{\left(\mathbf{Y}^o - \overline{\mathbf{Y}^o}\right)\left(\mathbf{X}^b - \overline{\mathbf{X}^b}\right)^T}}_{\mathcal{O}\left(N^{-\frac{1}{2}}\right)}(\mathrm{Id} - \mathbf{K}_e\mathbf{H})^T \\ &= (\mathrm{Id} - \mathbf{K}_e\mathbf{H})\,\mathbf{P}_{n,e}^b\,(\mathrm{Id} - \mathbf{K}_e\mathbf{H})^T + \mathbf{K}_e\mathbf{R}_n\mathbf{K}_e^T + \mathcal{O}\left(N^{-\frac{1}{2}}\right) \\ &= (\mathrm{Id} - \mathbf{K}_e\mathbf{H})\,\mathbf{P}_{n,e}^b + \mathcal{O}\left(N^{-\frac{1}{2}}\right).\end{aligned}$$

Note that, (2.27) is equivalent to (2.17). Thus (as also mentioned by Burgers et al. (1998)) ensemble mean and (up to $\mathcal{O}\left(N^{-\frac{1}{2}}\right)$) covariances update as in the Kalman filter. Finally, Burgers et al. (1998) use $M_{t_n,t_{n+1}}$ to individually evolve the members of the analysis ensemble $\mathbf{X}^a$ to the next time step, yielding the background ensemble for t_{n+1} and allowing to repeat the procedure described above with the observations available at t_{n+1}.

The limitations of the EnKF are according to Burgers et al. (1998) the assumption of approximately Gaussian errors, potential uncertainties in the determination of $\mathbf{R}_n$ and (if the model is not assumed to be perfect) $\mathbf{Q}$ as well as underestimation of the analysis error covariances, when using a small ensemble.

2.1.2 Importance of covariances

Covariances play an important role in DA: While the background error covariance matrix allows observations to impact the analysis at unobserved grid points, the observation error covariance matrix can account for limited representativeness of observations in case of a mismatch between the scales relevant for the observations and for the model (Janjić et al., 2017). Thus, in this section we are going to discuss the covariance matrices relevant for DA, as well as their composition, which we are going to shortly summarize in this section. As the main focus of this thesis will lie on the calculation of the observation error covariance matrix $\mathbf{R}$ and its use in DA, we start with a discussion of $\mathbf{R}$ and its components, closely following the description in Janjić et al. (2018). According to Janjić et al. (2018), the observation error consists of the following contributions:

- *Measurement error:* Error originating from the measurement process. Also denoted *instrument error* or *instrument noise*. For satellite based observations, the distribution of the *instrument noise* can be accurately determined using *calibration targets* (Weston et al., 2014).

- *Representation error:* Error originating from the model differing from the physical reality. Its contribution can be significant (Janjić et al., 2018). According to Janjić et al. (2018) it is consisting of:

  - *Error due to unresolved scales and processes:* Error originating from processes in physical reality occurring at scales (in space and/or time), which the model is unable to resolve. This can e.g. be caused by the model only depending on a averaged quantity or missing processes.

  - *Observation operator error:* Error originating from the observation operator. This can e.g. be caused by a lack of knowledge about the according physics or the exact behaviour of the employed instruments, as well as by simplifying approximations for the calculation of model equivalents for the observations (see (2.1)).

– *Pre processing error/ Quality control error:* Error originating from preprocessing and quality control, such as *retrievals* or procedures to sort out unsuitable observations, e.g. observations influenced by clouds, when employing a "clear-sky radiative transfer model" (Janjić et al., 2018). Preprocessing and quality control procedures (and thus the according error) differ between different DA schemes, models and implementations.

Of special interest for the further course of this thesis will be the representation error, as the source of the error in the SPM will essentially fall into this category. Thus we will take a closer look at it. Distinguishing between the components of the representation error is often not easy (Janjić et al. (2018), see also Zeng et al. (2021)) and we will encounter this issue also in the SPM. Furthermore, the contribution to the representation error of its individual components can be influenced by the choice of the control variables, model and observation operator. Also, the magnitude of the different components can depend on the exact situation, e.g. if clouds are present for *satellite radiances* (Janjić et al., 2018) and we will also encounter this state dependence in the SPM. Moreover, the representation error plays a larger role "for coarse grids and point observations, as well as for finer scale fields like [atmospheric water]" (Bannister et al., 2020). The former can also be seen in the SPM, when changing the grid spacing and size distribution of the hydrometeors. Representation error can lead to observation error covariance matrices becoming non-diagonal or changing with time (Janjić et al., 2018). This will also be the case for the $\mathbf{R}$ matrices obtained later for the SPM. Also, several examples of practical applications from different fields affected by this phenomenon can be found in Janjić et al. (2018). This also motivates our DA experiments that systematically research the impact of accounting for spatial and temporal variations in $\mathbf{R}$, using the SPM.

To better understand the problems encountered when separating the components of the representation error for the SPM, we will now have a closer look at the according definitions and their underlying assumptions. Janjić et al. (2018) assume, that the (space and time dependent) state in physical reality and in the model can be described by the *full state* $\mathbf{w}$ and the *resolved state* $\mathbf{w}^r$ and that $\mathbf{w}$ and $\mathbf{w}^r$ are elements of the same space. Furthermore, they define the *continuum observation operator* $\mathbf{h}^c$, such that the *observation* $\mathbf{y}$ is given by

$$\mathbf{y} = \mathbf{h}^c(\mathbf{w}) + \epsilon^m + \epsilon''', \tag{2.28}$$

with ϵ^m being the measurement error and ϵ''' being the preprocessing error, as well as the *discrete observation operator* $\mathbf{h}$, designed to act on $\mathbf{w}^r$ such that

$$\mathbf{y} = \mathbf{h}(\mathbf{w}^r) + \epsilon^0, \tag{2.29}$$

with ϵ^o being the observation error. This (together with the assumption of $\mathbf{w}^r$ also lying in the domain of $\mathbf{h}$), allows them to define the error due to unresolved scales and processes ϵ' as

$$\epsilon' = \mathbf{h}^c(\mathbf{w}) - \mathbf{h}^c(\mathbf{w}^r) \tag{2.30}$$

and the observation operator error ϵ'' as

$$\epsilon'' = \mathbf{h}^c\left(\mathbf{w}^r\right) - \mathbf{h}\left(\mathbf{w}^r\right). \tag{2.31}$$

We now conclude this topic by a short discussion of common approaches to obtain $\mathbf{R}$ matrices, when analytical calculations are not possible. According to Janjić et al. (2018), common methods to quantify the representation error include among many others:

- Comparison of observation equivalent from numerical models with different resolutions. This method has e.g. been employed by Zeng et al. (2021).
- Comparison of observations of same quantity with different resolutions.
- The *Hollingsworth-Lönnberg method*, that estimates the observation error covariance matrix from samples of $\mathbf{y} - \mathbf{h}\left(\mathbf{w}^b\right)$ using

$$E\left[\left(\mathbf{y} - \mathbf{h}\left(\mathbf{w}^b\right)\right) \cdot \left(\mathbf{y} - \mathbf{h}\left(\mathbf{w}^b\right)\right)^T\right] \approx \mathbf{H}\mathbf{P}^b\mathbf{H}^T + \mathbf{R}, \tag{2.32}$$

  with $\mathbf{w}^b$ being the according background mean and $\mathbf{H}$ the linearization of $\mathbf{h}$.

- The *Desroziers method*, that uses the Kalman Filter equations to derive

$$E\left[\left(\mathbf{y} - \mathbf{h}\left(\mathbf{w}^b\right) - \mathbf{H}\tilde{\mathbf{P}}^b\mathbf{H}^T\left(\mathbf{H}\tilde{\mathbf{P}}^b\mathbf{H}^T + \tilde{\mathbf{R}}\right)^{-1}\left(\mathbf{y} - \mathbf{h}\left(\mathbf{w}^b\right)\right)\right) \cdot \left(\mathbf{y} - \mathbf{h}\left(\mathbf{w}^b\right)\right)^T\right] \approx \mathbf{R}, \tag{2.33}$$

  with $\tilde{\mathbf{P}}^b$ and $\tilde{\mathbf{R}}$ being an initial guess for the background error covariance matrix and the observation error covariance matrix. The method is iteratively applied to estimate the observation error covariance matrix from samples. It has e.g. been employed by Zeng et al. (2021) for estimating the observation error covariances of *radar reflectivity* and *radial wind* and by Lange and Janjić (2016) for Mode-S data. The (horizontal) representation error can be estimated e.g. by comparing the results of the Desroziers method for DA experiments employing models with different spatial resolutions (Weston et al., 2014). A drawback of the Desroziers method is its need for a large amount of observations to compute the expectation value, often only allowing for the calculation of a time averaged observation error covariances (Degelia and Wang, 2022).

Here, the Hollingsworth-Lönnberg method and the Desroziers method rely on the assumption that observations and background are unbiased and that there is no correlation between the observation error and the background error (Janjić et al., 2018). The Desroziers method can yield negative observation error variances, as well as asymmetric or non positive definite observation error covariance matrices, if these assumptions are not fulfilled (Weston et al., 2014). Due to numerical error, we will encounter a similar problem when calculating the $\mathbf{R}$ matrices for the SPM.

We now turn to the role of observation error covariances in DA. In DA, employing correlated observation error covariance matrices on average decreases the impact of observations, but can also have the opposite effect in some cases (Weston et al., 2014). Furthermore, under the commonly employed assumption of diagonal observation error covariances, thinning the observations is necessary, to ensure this assumption being valid, thus leading to the loss of a large percentage of the observations (Gustafsson et al., 2018; Janjić et al., 2018; Terasaki and Miyoshi, 2023). Therefore being able to use also non-diagonal observation error covariances effectively during DA is highly desirable (Gustafsson et al., 2018; Janjić et al., 2018). Weston et al. (2014) e.g. was able to achieve a "significant improvement in forecast accuracy" by employing correlated observation error covariance matrices for the assimilation of IASI data. This further motivates our experiments studying the impact of using non-diagonal $\mathbf{R}$ matrices in DA using the SPM.

The decision whether diagonal or correlated observation error covariance matrices are used in DA, is accompanied by a trade-off between possibly achieving significantly better results and computational efficiency (Janjić et al., 2018). A compromise often employed is ignoring possible correlations between measurements from different measurement devices (and potentially also correlations in space), yielding a *block-diagonal* observation error covariance matrix. We will also test this approach in our DA experiments with the SPM.

In the context of 4D-Var, the increased computational cost of using correlated observation errors in DA is (for satellite data) predominately caused by a slower convergence of the algorithm, while the increased cost for inverting $\mathbf{R}$ is insignificant (Weston et al., 2014), though stability can become an issue (Terasaki and Miyoshi, 2023). The former is likely caused by a large increase in the condition number of the correlated $\mathbf{R}$ compared to the diagonal version, leading to the condition number of $\mathbf{R}$ becoming an important consideration for DA (Weston et al., 2014). Using ill conditioned $\mathbf{R}$ matrices can even lead to divergence of the DA algorithm (Terasaki and Miyoshi, 2023). There exist different methods for decreasing the condition number of a matrix (*reconditioning*) and depending on the method used, reconditioning of $\mathbf{R}$ can (by increasing variances) strongly decrease correlations (Weston et al., 2014). In our DA experiments with the SPM, we will see similar results, also obtaining slower convergence, when using correlated $\mathbf{R}$ matrices.

In many cases, inflation of the *instrument error* is used to account for the representation error (Courtier et al., 1998). In the experiments of Degelia and Wang (2022), when assimilating data from *atmospheric emitted radiance interferometers* using an EnSRF, adaptive inflation and the Desroziers method exhibited roughly the same performance, while static inflation produced worse results. Nevertheless, in our experiments, we only test (static) multiplicative inflation without seeing a significant impact.

Of particular interest are the results of Bishop (2019), who obtained better results, when choosing $\mathbf{R}$ as "the ensemble mean of the observation error variances associated with each member of an ensemble forecast", than when choosing it as "the true observation error

variance associated with the (unknown) true state", which they attributed to the requirements for the EnKF yielding the *best linear unbiased estimator*. Thus repeating our DA experiments with the according $\mathbf{R}$ matrices might be interesting for further work.

Finally, we shortly discuss background error covariance matrices, which will only be of importance for our investigation of non-negativity preservation in Chapter 6, where we show that non-negativity of analysis can not be guaranteed for non-diagonal background error covariance matrices. Here, we will focus especially on the potential of background error covariance matrices to cause problems in DA, to be later able to better understand the issues observed in our simplified setup.

Background error covariance matrices only need to be modelled for variational (and some hybrid) DA methods. They can also be *flow-dependent* and e.g. depend on the presence (and strength) of an *inversion* (Bannister et al., 2020). This flow-dependence (especially of the off-diagonal elements) can lead to the following problem: When assimilating e.g. the *specific humidity* q, large off-diagonal elements in the background error covariance matrix can lead to observations at locations with large values of q strongly increasing the analysis at locations with small values of q (*flooding*) (Bannister et al., 2020). Also, errors in the correlation between temperature and humidity in the background error covariance matrix can lead to an underestimation of the temperature and consequently an overestimation of precipitation (*spin down*) due to *anomalous condensation* (Bannister et al., 2020).

According to Destouches et al. (2023), obtaining background error covariance matrices for quantities describing hydrometeors is particularly difficult, due to their high spatial and temporal variability and non-linear dynamics. A special problem for these quantities is that when derived from ensembles, the according background error covariance matrices can have a high percentage of their diagonal elements equalling zero, causing the DA to be unable to change the quantity at the affected grid points.

2.2 Reference model and two moment scheme

Here, we are going to review the models presented in Wacker and Seifert (2001), which will be modified and extended to smaller length scales when defining the SPM in Chapter 3. Further, these models will be used as reference and for the time evolution of the ensemble in our DA experiments.

The central quantity on which the derivation in Wacker and Seifert (2001) is based is the *size distribution function* $f(D, x, y, z, t)$, where $f(D, x, y, z, t)\, dD$ represents "the number of drops per unit volume in the diameter interval $(D, D + dD)$", with x, y and z being spacial coordinates, t time and D the particle diameter. We note that Wacker and Seifert (2001) do not explicitly state, if $f(D, x, y, z, t)$ is to be interpreted as stochastic or deterministic quantity, which is (due to the large number of hydrometeors and resulting

convergence of stochastic quantities to their expectation value) not necessary on the length scales $\sim 5km$ considered by their paper (as long as covariances do not need to be obtained).

We now introduce the assumptions made in their work:

- Hydrometeors are assumed to be spherical and moving with terminal fall velocity which is assumed to be given by $v_T(D) = \alpha \left(\frac{D}{D_v}\right)^{\beta}$, with α, β and D_v free parameters.
- The distribution of the hydrometeors is assumed to be constant in space and time and to be given by $n_0 e^{-\lambda D}$, with λ and n_0 free parameters.
- Homogeneity in x- and y-direction is assumed and hydrometeors are assumed to be initially contained in the interval $[z_l, z_u]$.
- Hydrometeors are assumed not to be interacting with each other, they are not created or destroyed and their diameter is constant.

The quantities described by the models of Wacker and Seifert (2001) are the *liquid water content* $L(z,t)$ and the *number concentration* $N(z,t)$, which they define as

$$L(z,t) = \int \frac{\pi}{6} \rho_w D^3 f(D,z,t)\, dD \tag{2.34}$$

$$N(z,t) = \int f(D,z,t)\, dD, \tag{2.35}$$

with ρ_w being the density of water.

We are going to review two of the models presented in Wacker and Seifert (2001), the *reference model*, which is the most realistic model presented in their paper and thus will be used as alternative truth run in our DA experiments, and the *two-moment scheme*, which only requires knowledge of the L and N profiles at a given time to approximate their time evolution and will thus be used to evolve our ensemble in the DA experiments.

The reference model is obtained by Wacker and Seifert (2001) by solving the "spectral budget equation for the distribution function"

$$\frac{\partial f(D,z,t)}{\partial t} - \frac{\partial \left(v_T(D) f(D,z,t)\right)}{\partial z} = 0, \tag{2.36}$$

under the assumptions summarized above, yielding

$$L(z,t) = \frac{\pi \rho_w n_0}{\lambda^4} \left[e^{-\lambda D_l} \left(1 + \lambda D_l + \frac{1}{2}\lambda^2 D_l^2 + \frac{1}{6}\lambda^3 D_l^3\right) - \right. \tag{2.37}$$

$$\left. - e^{-\lambda D_u} \left(1 + \lambda D_u + \frac{1}{2}\lambda^2 D_u^2 + \frac{1}{6}\lambda^3 D_u^3\right) \right] \tag{2.38}$$

with

$$D_l = \begin{cases} \left(\frac{1}{\alpha}\frac{z_l - z}{t}\right)^{\frac{1}{\beta}} D_v & \text{, if } z \leq z_l \\ 0 & \text{, if } z > z_l \end{cases} \tag{2.39}$$

$$D_u = \begin{cases} \left(\frac{1}{\alpha}\frac{z_u - z}{t}\right)^{\frac{1}{\beta}} D_v & \text{, if } z \leq z_u \\ 0 & \text{, if } z > z_u \end{cases}. \tag{2.40}$$

This also allows for an analogue calculation of $N(z,t)$ (Seifert, 2022).

The two-moment scheme is obtained by Wacker and Seifert (2001) by integrating the spectral budget equation, yielding

$$\frac{\partial}{\partial t}\begin{pmatrix} N(z,t) \\ L(z,t) \end{pmatrix} - \frac{\partial}{\partial z}\begin{pmatrix} F_N(z,t) \\ F_L(z,t) \end{pmatrix} = 0, \tag{2.41}$$

with

$$F_N(z,t) = \int v_T(D)\, f(D,z,t)\, dD \tag{2.42}$$

$$F_L(z,t) = \int v_T(D)\, \frac{\pi}{6}\rho_w D^3 f(D,z,t)\, dD, \tag{2.43}$$

which they approximate by

$$F_N = \chi_N \bar{x}^\gamma N \tag{2.44}$$

$$F_L = \chi_L \bar{x}^\gamma L, \tag{2.45}$$

with

$$\bar{x} = \frac{L}{\rho_w D_v^3 N} \tag{2.46}$$

$$\chi_N = \frac{\alpha \pi^{\frac{1}{3}}}{2} \tag{2.47}$$

$$\chi_L = \frac{35}{16}\chi_N \tag{2.48}$$

$$\gamma = \frac{\beta}{3}, \tag{2.49}$$

allowing them to rewrite (2.41) as

$$\frac{\partial}{\partial t}\begin{pmatrix} N(z,t) \\ L(z,t) \end{pmatrix} - A(\bar{x})\frac{\partial}{\partial z}\begin{pmatrix} N(z,t) \\ L(z,t) \end{pmatrix} = 0, \tag{2.50}$$

with

$$A(\bar{x}) = \begin{pmatrix} \chi_N(1-\gamma)\bar{x}^{\gamma} & \chi_N \bar{x}^{\gamma-1}\rho_w^{-1}D_v^{-3} \\ -\chi_L \bar{x}^{\gamma+1}\rho_w D_v^3 & \chi_L(1+\gamma)\bar{x}^{\gamma} \end{pmatrix}. \tag{2.51}$$

Chapter 3

Model (Toy model)

In this chapter, we introduce the stochastic particle model (SPM), which later will be the foundation of our DA experiments in Chapter 5. Furthermore its covariances will be studied in detail in Chapter 4. Before we construct the model in Section 3.2, we give a short motivation in Section 3.1. The actual construction of the model consists of the extension of the definitions of L and N to small length scales in Section 3.2.1, the introduction of advection and stochastic initial conditions in Section 3.2.2 and the extension to cylindrical hydrometeors in Section 3.2.3.

3.1 Motivation

As seen in Section 2.1.2, observation error covariance matrices are of great importance for DA and can have complicated spatial structures and time dependences. However, in practice the actual observation error covariances are often unknown and constant diagonal matrices are used instead (e.g. Degelia and Wang (2022), Weston et al. (2014) or Janjić et al. (2018)). This necessitates further research on the temporal and spatial structure of observation error covariance matrices (Degelia and Wang, 2022).

One approach to investigate the importance of correctly specifying the spatial and temporal structure of the observation error covariances is to analytically derive them for a sufficiently simple model, that can then be used as truth in DA experiments (Janjić and Cohn, 2006a). A relatively simple model seemingly suitable for this task is the reference model constructed by Wacker and Seifert (2001), as summarized in Section 2.2, which is designed for length scales far larger than the diameter of a typical hydrometeor and large particle numbers. In this model, we will interpret the errors resulting from the stochastic initial conditions as part of the representation error (and thus of the observation error), as the stochastic initial conditions account for the lack of knowledge about the exact initial positions and diameters of the hydrometeors. Thus the stochastic initial conditions would make the model a suitable test case for experiments investigating the role of observation error resulting from unresolved sub-grid scale processes.

However, this model defines the liquid water content L as the mass of liquid water per volume and the number density N as the number of hydrometeors per volume. To this end, hydrometeors are assumed to be points and a free parameter ϵ describing the size of the volume under consideration needs to be introduced (see upper panel of Figure 3.1). As seen in Section 4.2, this free parameter can explicitly appear in the according covariance matrices, which is problematic, as ϵ has no physical analogue.

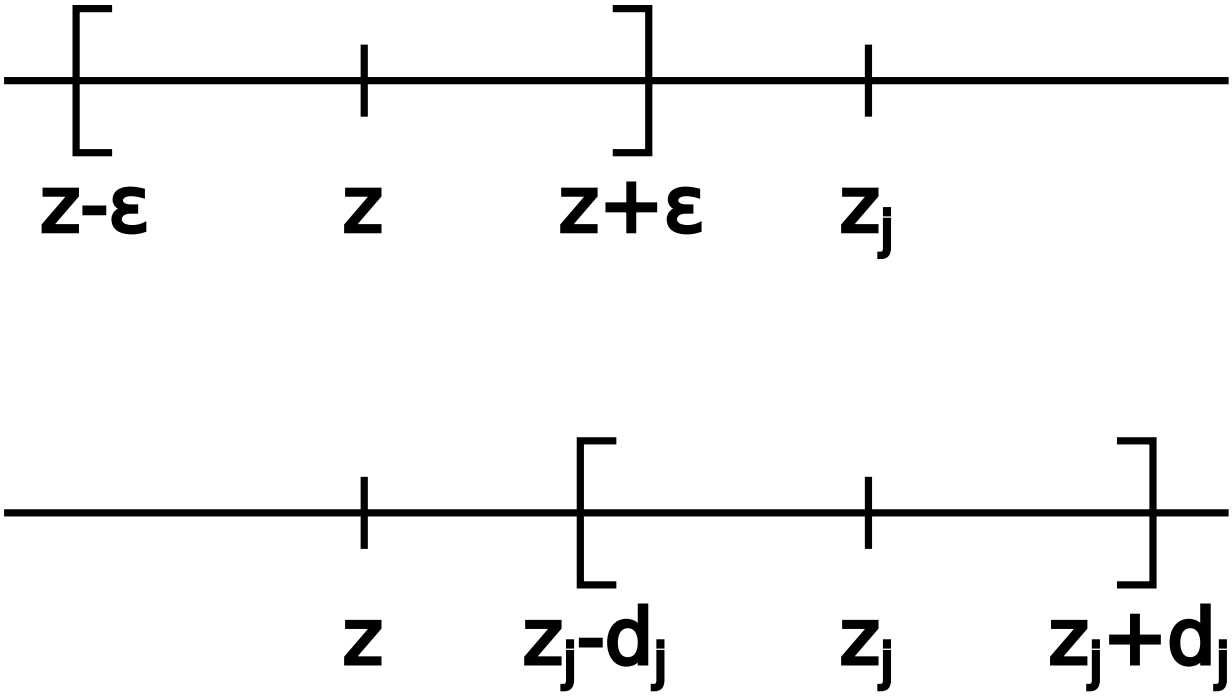

Figure 3.1: Interval of points at which a hydrometeor can impact L or N at location z for the model of Wacker and Seifert (2001) (upper panel) and interval of locations at which L or N can be influenced by a hydrometeor of diameter d_j centred at z_j for the SPM (lower panel).

However, we can construct a toy model, from here on denoted as stochastic particle model (SPM), with well defined covariances by modifying the Wacker and Seifert (2001) model: Instead of introducing a volume of arbitrary size, we drop the assumption of hydrometeors being points and represent them by a sum over Dirac measures instead, as similarly employed e.g. in Semrau (2020) for a problem from theoretical ecology. This yields a situation mathematically similar to Wacker and Seifert (2001) (see lower panel of Figure 3.1), without the need for an additional free parameter, though the size of the interval considered now depends on the diameter of the hydrometeor, which may vary in a realistic setup, yielding much more complicated calculations.

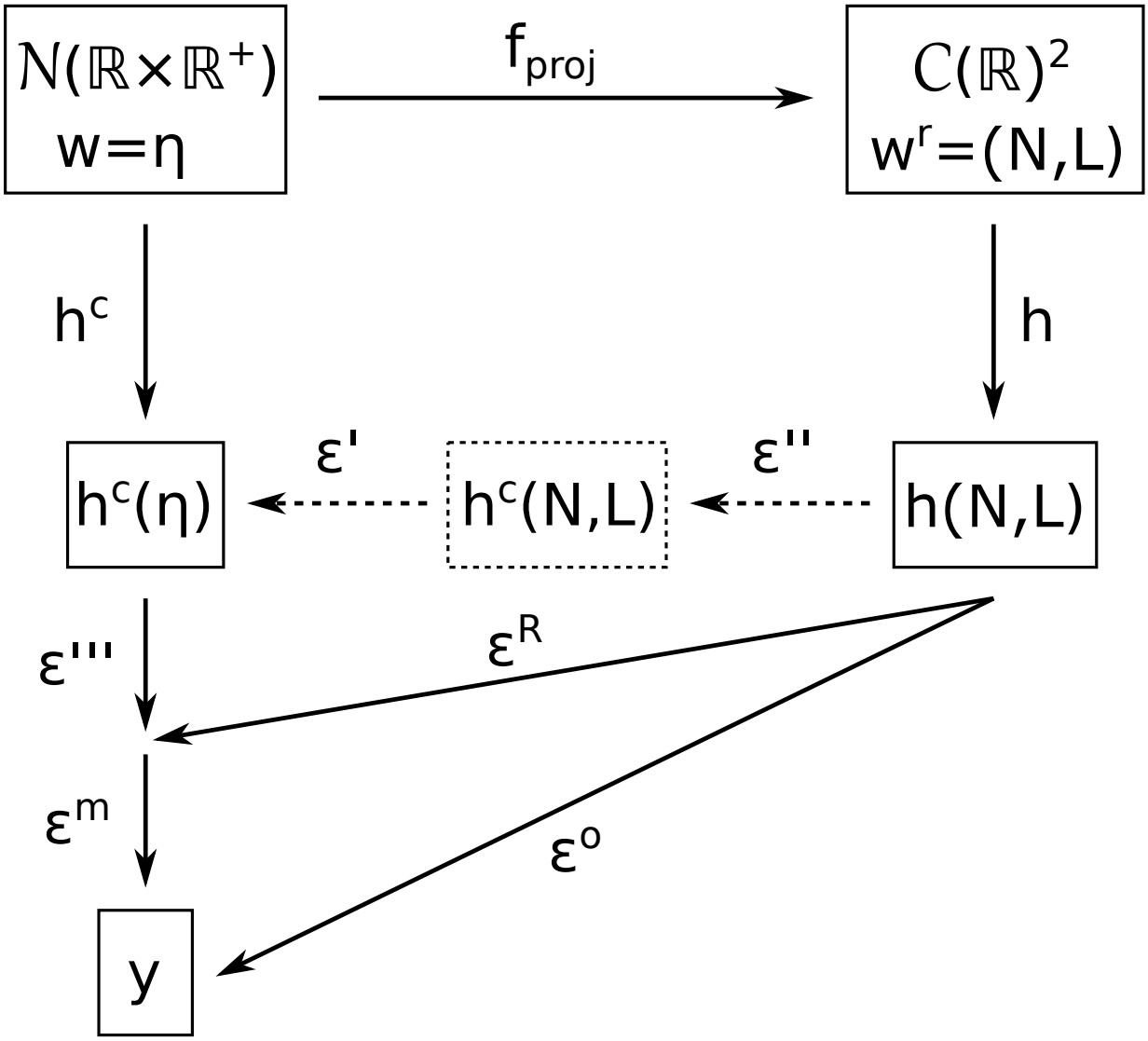

Figure 3.2: Relation between full and resolved state for the SPM analogue to Figure 1 of Janjić et al. (2018). The quantities indicated by dashed boxes or arrows are not well defined for the SPM.

This modification however changes the state space from[1] $\mathcal{C}(\mathbb{R})^2$ to the space $\mathcal{N}(\mathbb{R}\times\mathbb{R}^+)$ of (locally) finite counting measures on $\mathbb{R}\times\mathbb{R}^+$. When using the SPM as truth and the two moment scheme of Wacker and Seifert (2001) (which lives on the state space $\mathcal{C}(\mathbb{R})^2$, or $\mathbb{R}^{2k}$ when discretized to a grid with k points) to evolve the ensemble during DA, separation of the error due to unresolved scales and processes and the observation operator error in the way shown in Janjić et al. (2018) becomes impossible: If the true and the resolved

[1]Technically, the state space would be a Sobolev space, as the model accepts discontinuous initial conditions and (at least the two moment scheme) requires differentiability. However, in our DA experiments we are going to have long enough spin-up times for all profiles being continuous, so we ignore this detail.

state belong to disjoint spaces, taking $\mathbf{h}^c(\mathbf{w}^r)$ is not possible anymore[2]. Thus, also the definition of the error due to unresolved scales and processes and the observation operator error in (2.30) and (2.31) are not applicable here (see Figure 3.2). As this separation is not possible in practical applications anyhow and only the total representation error is relevant for common DA algorithms, this issue has no consequences for DA.

Note also, that the state space of the SPM contains more information than that of the Wacker and Seifert (2001) reference model. The L- and N-profiles can easily be calculated from the hydrometeor positions and diameters, however the converse is not true, as different hydrometeor configurations can yield identical profiles (see Figure 3.3 for example). This further supports interpreting the resulting fluctuations as representation error.

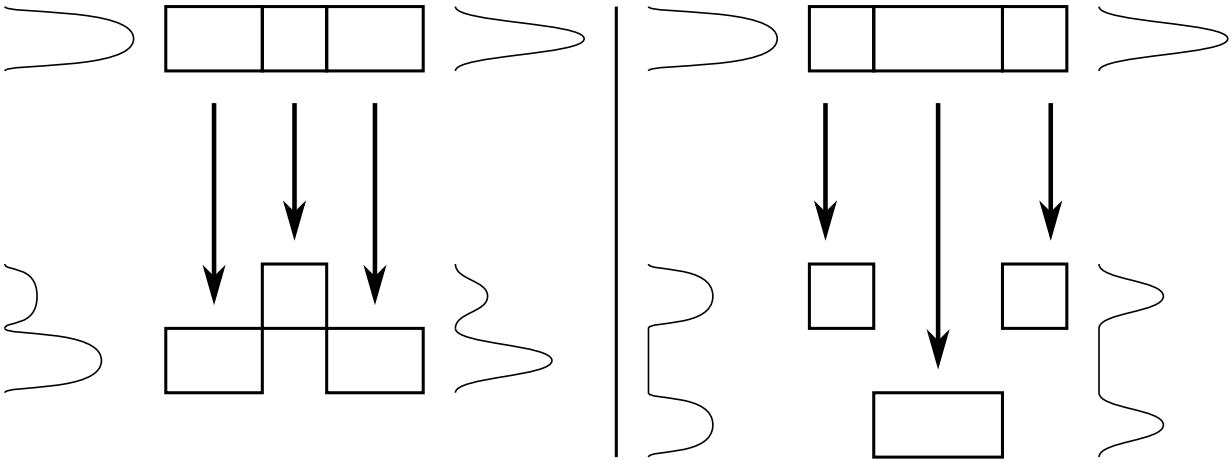

Figure 3.3: Symbolic depiction of two different cases of horizontally oriented cylindric hydrometeors, with initially identical L- and N-profiles and the according time evolution.

Due to its simplicity and as its covariances are well defined and can be obtained at least numerically, the SPM allows to attribute individual features of covariance matrices to physical processes such as gravitational sorting or the geometry of hydrometeors. This results can also function as baseline for more complicated models encompassing (stochastic or deterministic) particle interactions.

3.2 Stochastic particle model (SPM)

We now start with the construction of the stochastic particle model (SPM). To this end, we will modify the Wacker and Seifert (2001) reference model, effectively extracting the underlying particle model, and formulate the results in terms of stochastic geometry. An

[2]As we are working with a particle based model, also the labelling "continuum observation operator" is slightly unsuitable here. For consistency however, we keep the according notation here.

introduction to stochastic geometry can be found e.g. in Jansen (2018) and the references therein. Throughout the thesis, we will use the same notation as Jansen (2018) with regards to concepts from stochastic geometry. Although the employed concepts are relatively common in the field of stochastic geometry, when employing them we will reference Jansen (2018).

3.2.1 Particle definition of L and N

We will focus here on the liquid water content L and number density N in the case of pure sedimentation, as discussed in Wacker and Seifert (2001). Assuming the considered volume to be much larger than the diameter of the hydrometeors and containing a sufficiently large amount of hydrometeors, usually the *liquid water content* L is defined as the mass of liquid water per unit volume[3] and the *number concentration* N as the number of hydrometeors per unit volume. These definitions break down at length scales equal to or smaller than the typical particle size, which still might be relevant for the definition of observation operators. Furthermore, when calculating covariances, using theses definitions introduces a free parameter describing the size of the unit volume, which strongly complicates calculations and might cause further problems.

However, it is possible to extend these definitions to smaller length scales, if we replace the distribution function used by Wacker and Seifert (2001) to express the state of a system by a locally finite counting measure (i.e. sum over Dirac measures) (see Jansen (2018)), effectively reconstructing the underlying particle model and extending it to represent particles of finite diameter by modifying the definitions of L and N accordingly.

Definition 3.2.1. The *state* η of a system consisting of n spherical hydrometeors with diameters $D_1, \cdots, D_n \in \mathbb{R}^n_+$ and positions $(x_1, y_1, z_1), \cdots, (x_n, y_n, z_n) \in \mathbb{R}^{3n}$ is defined as

$$\eta = \sum_{j=1}^{n} \delta_{(x_j, y_j, z_j, D_j)}. \tag{3.1}$$

Remark 3.2.1. As long as we assume n to be constant (which is the case in this thesis) and if dynamics and state dependent functions (e.g. to experimentally accessible quantities or variables of coarser models) are invariant under permutations (which should likely be fulfilled in physically meaningful models), the state defined in Definition 3.2.1 is up to permutations equivalent to $(x_1, \cdots, x_n, y_1, \cdots, y_n, z_1, \cdots, z_n, D_1, \cdots, D_n) \in \mathbb{R}^{3n} \times \mathbb{R}^n_+$. However, as soon as processes that destroy or create hydrometeors are involved resulting in n varying over time, the use of (3.1) becomes necessary.

The notation introduced in Definition 3.2.1 is standard in the field of stochastic geometry and point processes, which provides extensive theory allowing also to model the destruction or creation of hydrometeors. This provides a framework for easy generalization of the

[3]Note that identifying this volume with the grid box of a numerical model can become problematic when measurements are involved, as these should be independent of the model.

SPM (see e.g. Jansen (2018) for introduction and further references): States of the form (3.1) belong to the *(locally) finite counting measures* $\mathcal{N}$ and random variables on $\mathcal{N}$ (*point processes*) can be used to model uncertainty, e.g. from stochastic initial conditions. Furthermore, *marked point processes* can be used to include multiple species of hydrometeors and *birth death and movement processes* or *Feller processes* on $\mathcal{N}$ can be used to model stochastic dynamics. Also, there is extensive research concerning the behaviour of these quantities in the infinite particle limit.

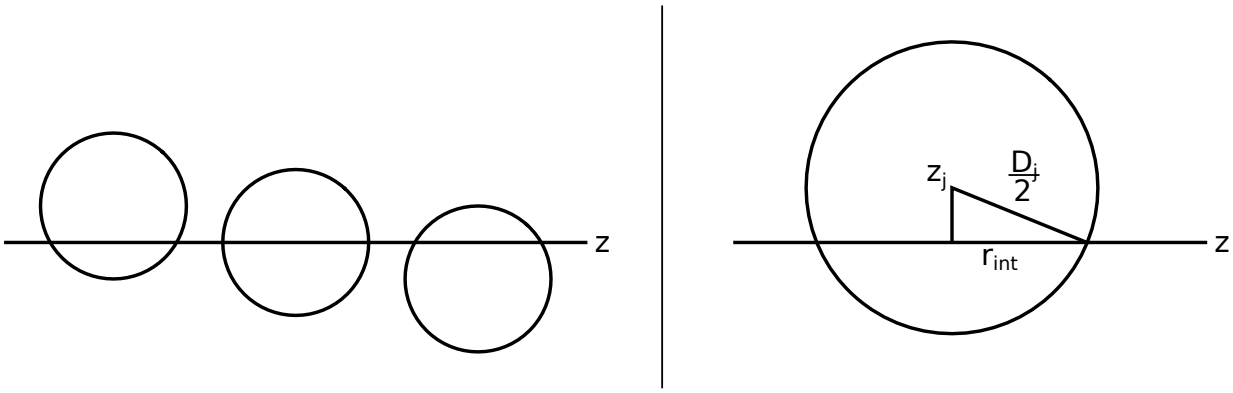

Figure 3.4: Schematic depiction of hydrometeors with different relative positions with respect to z, to illustrate the changing size of the intersection area with the (x, y)-plane (left panel) and of the quantities employed in Definition 3.2.2 (right panel).

Now, assuming analogue to Wacker and Seifert (2001) homogeneity in the x- and y-direction, we define:

Definition 3.2.2. Given a state η of a system consisting of n spherical hydrometeors and assuming that all hydrometeors have the density $\rho_H \in \mathbb{R}_+$, let $l_\eta : \mathbb{R} \to \mathbb{R}_+$, $z \mapsto l_\eta(z)$ with

$$\begin{aligned} l_\eta(z) &= \rho_H \sum_{j=1}^{n} \left| P_{x,y}(z) \cap B_{\frac{D_j}{2}}(x_j, y_j, z_j) \right|_A \\ &= \rho_H \pi \sum_{j=1}^{n} \mathbf{1}_{\left[z_j - \frac{D_j}{2}, z_j + \frac{D_j}{2}\right]}(z) \left[\frac{D_j^2}{4} - (z_j - z)^2 \right] \end{aligned} \tag{3.2}$$

be the *liquid water content* and $n_\eta : \mathbb{R} \to \mathbb{R}_+$, $z \mapsto n_\eta(z)$ with

$$\begin{aligned} n_\eta(z) &= \sum_{j=1}^{n} \left| P_{x,y}(z) \cap \frac{1}{\left| B_{\frac{D_j}{2}}(x_j, y_j, z_j) \right|_V} B_{\frac{D_j}{2}}(x_j, y_j, z_j) \right|_A \\ &= 6 \sum_{j=1}^{n} \mathbf{1}_{\left[z_j - \frac{D_j}{2}, z_j + \frac{D_j}{2}\right]}(z) \frac{1}{D_j^3} \left[\frac{D_j^2}{4} - (z_j - z)^2 \right] \end{aligned} \tag{3.3}$$

be the *number density*. Here $\mathbf{1}$ denotes the indicator function, $P_{x,y}(z)$ the (x,y)-plane at level z, $|S|_V$ volume and $|S|_A$ area of a set S.

Note, that as seen in Figure 3.4, $r_{int}^2 = \frac{D_j^2}{4} - (z_j - z)^2$. Thus the area of intersection of the j-th hydrometeor with the (x,y)-plane at level z is $\pi\left[\frac{D_j^2}{4} - (z_j - z)^2\right]$. The indicator functions ensure, that only hydrometeors actually intersecting the (x,y)-plane at level z are counted. Furthermore, the remaining prefactors are chosen such that integrating $n_\eta(z)$ over the whole domain yields the particle number, while integrating $l_\eta(z)$ yields the total mass of all hydrometeors. Moreover, the implicit average over the (x,y)-plane in Definition 3.2.2 ensures continuity, though n_η and l_η are still not (strongly) differentiable. It also facilitates re-expressing the problem in terms of measures and linking it to existing theory from stochastic geometry, useful for further generalization.

A discussion of the relation between Definition 3.2.2 and the standard definitions of N and L can be found in Appendix A. Furthermore, in Section 7.1.2, we will show the first steps of constructing measures representing liquid water content and number density and show how these relate to the standard definitions.

3.2.2 Advection and stochastic initial conditions

We now can formulate the dynamics for the case of the hydrometeors moving with their terminal fall velocity. We assume here also for simplicity the hydrometeors being spherical (however, we will extend the SPM to cylindrical hydrometeors in the next section) and drag and gravity being the only involved forces.

Definition 3.2.3. Given a system of spherical hydrometeors in the initial state η_0 at time $t_0 = 0$, with

$$\eta_0 = \sum_{j=1}^{n} \delta_{\left(x_j^0, y_j^0, z_j^0, D_j\right)} \tag{3.4}$$

and let D_j, x_j and y_j be constant for all $j \in \{1, \cdots, n\}$, as well as

$$z_j(t) = z_j^0 + v_T(D_j)\, t \tag{3.5}$$

$$v_T(D_j) = \alpha\sqrt{D_j}, \tag{3.6}$$

with[4] $\alpha < 0$. We define the *time dependent state*

$$\eta_t = \sum_{j=1}^{n} \delta_{\left(x_j^0, y_j^0, z_j(t), D_j\right)}. \tag{3.7}$$

[4]In all DA experiments, as well as in the simplified setup mentioned in Appendix E, we employ a value obtained from equating gravitational force and drag for α. This is always $\alpha = \sqrt{\frac{4\rho_H g}{3\rho_A c_W}}$, where g is the gravitational constant, ρ_A is the density of air and c_W is the drag coefficient of a sphere.

In further notation the variables x_j^0 and y_j^0 will be dropped and z_j^0 will be referred to as z_j from now on to improve readability.

As n_η and l_η are entirely defined by η, the initial state η_0 and the dynamics given by Definition 3.2.3 suffice to determine them for all times $t \geq 0$. This allows introducing the following notation.

Notation 3.2.1. Given the assumptions of Definition 3.2.3, let

$$n_{\eta_0}(z,t) = n_{\eta_t}(z) \tag{3.8}$$
$$l_{\eta_0}(z,t) = l_{\eta_t}(z). \tag{3.9}$$

Extending Definition 3.2.3 and Notation 3.2.1 to more complicated dynamics is easily possible, but necessitate modifying Definition 3.2.1 to include additional variables (e.g. velocity) in the definition of η.

To further simplify calculations we introduce a notation, having in mind Definition 3.2.2 and Notation 3.2.1:

Definition 3.2.4. Given the assumptions of Definition 3.2.3, let

$$f(D_j, z_j, t, z) = \left[\frac{D_j^2}{4} - (z_j(t) - z)^2\right] \tag{3.10}$$
$$= \left[\frac{D_j^2}{4} - \left(z_j + \alpha\sqrt{D_j}t - z\right)^2\right] \tag{3.11}$$
$$g_L(D_j) = \pi\rho_H \tag{3.12}$$
$$g_N(D_j) = \frac{6}{D_j^3} \tag{3.13}$$

and let

$$Z_{z,t} = \sum_{j=1}^{n} \mathbf{1}_{\left[z-\frac{D_j}{2}, z+\frac{D_j}{2}\right]}(z_j(t))\, g_Z(D_j)\, f(D_j, z_j, t, z), \tag{3.14}$$

for $g_Z \in \{g_N, g_L\}$ and $Z \in \{N, L\}$.

We note that (3.14) generalizes (3.8) and (3.9). Furthermore, we have dropped the initial state in the notation to increase readability. Analogue to (Wacker and Seifert, 2001), we now assume the following stochastic initial conditions:

Assumption 3.2.1. Let the particles be initially uniformly distributed in the interval $[z_{min}, z_{max}]$ and their diameters exponentially distributed, as well as all quantities independent, yielding the according probability densities being given by[5]

[5]The parameter n_0 occurring in the analogue definitions of Wacker and Seifert (2001) differs from our n, as it models a density rather than a particle number.

$$\varrho_{z_j}(z_j) = \frac{1}{z_{max} - z_{min}} \mathbf{1}_{[z_{min}, z_{max}]}(z_j) \tag{3.15}$$

$$\varrho_{D_j}(D_j) = \lambda e^{-\lambda D_j}. \tag{3.16}$$

This defines a probability measure $\mathbb{P}_j$ on $\mathbb{R}^3 \times \mathbb{R}_+$ (equipped with the Borel σ-algebra $\mathcal{B}$) for every hydrometeor and the according product measure $\mathbb{P}$ models the distribution of the initial state of the system.

Remark 3.2.2. Now, according to Corollary 2.6 of Jansen (2018), equipping $\mathcal{N}$ with a suitable σ-algebra $\mathfrak{N}$, $\Phi : \left(\mathbb{R}^{3n} \times \mathbb{R}_+^n, \mathcal{B}^n\right) \to (\mathcal{N}, \mathfrak{N})$, $(z_1, \cdots, z_n, D_1, \cdots, D_n) \mapsto \sum_{j=1}^n \delta_{(z_j, D_j)}$ is measurable allowing $\mathbb{P}$ to define a point process.

This[6] allows us later to calculate the expectation value of $Z_{z,t}$ and the according covariance matrices. Interpreting the stochastic initial conditions as a lack of knowledge about the initial positions and diameters of the hydrometeors, allows later to use these covariance matrices as observation error covariance matrices in our DA experiments.

3.2.3 Cylindrical hydrometeors

We will now repeat the previous considerations for cylindrical hydrometeors[7], in which case Definition 3.2.1 will be replaced by

Definition 3.2.5. The *state* η of a system consisting of n cylindrical hydrometeors with heights $h_1, \cdots, h_n \in \mathbb{R}_+^n$, radii $r_1, \cdots, r_n \in \mathbb{R}_+^n$, inclination angles $\varphi_1, \cdots, \varphi_n \in [0, 2\pi]$ and positions $(x_1, y_1, z_1), \cdots, (x_n, y_n, z_n) \in \mathbb{R}^{3n}$ is defined as

$$\eta = \sum_{j=1}^{n} \delta_{(x_j, y_j, z_j, h_j, r_j, \varphi_j)} \tag{3.17}$$

We will use the power laws given in Auer and Veal (1970) to link h and r for the according hydrometeor type, effectively eliminating one degree of freedom and allowing the geometry of the hydrometeor to be completely determined by its volume. Thus we can convert the size distribution given in Assumption 3.2.1 to cylindrical hydrometeors, allowing for easy comparison.

As the drag coefficients of an inclined cylinder are relatively complicated and not well understood, instead of directly calculating simplified terminal fall velocities, we use those given in Brdar and Seifert, 2018, also providing a more realistic velocity model. Now after replacing the ball in Definition 3.2.2 by the according cylinder, expectation values and

[6] For simplicity, here we included the time evolution directly in the definition. For generalizations, working with a separate time evolution operator might be necessary.

[7] This results in observations not being continuous anymore, which might create new mathematical challenges for generalization.

covariance matrices for liquid water content and number density can be obtained analogue to the calculations in Section 4.1. The according equations are relatively complicated and can be partially found in Appendix B. Furthermore, a discussion of different velocity models for spherical and cylindrical hydrometeors can be found in Appendix E.

3.3 Summary

In this section, we have motivated and defined the SPM. To this end, we extracted the particle model underlying the Wacker and Seifert (2001) reference model and expressed the model state in terms of counting measures, allowing for easier generalization. Furthermore, we modified the definitions of number density and liquid water content to be valid also at length scales smaller than the typical particle diameter. Finally, we extended the model to cylindrical hydrometeors.

Chapter 4

Expectation values and error covariances

In this chapter, we investigate the expectation values and covariances for the SPM and the Wacker and Seifert (2001) reference model. We start by deriving the covariance matrices resulting from the stochastic initial conditions of the SPM in Section 4.1. Interpreting these as a lack of knowledge about the initial positions and diameters of the hydrometeors, allows later to regard them as a form of representation error and to use the according covariance matrices as observation error covariance matrices in our DA experiments in Chapter 5. Subsequently we repeat these calculations for the Wacker and Seifert (2001) reference model in Section 4.2. As the reference model does not distinguish between stochastic and deterministic quantities[1], we again need to turn to its underlying particle model (interpreting the N and L profiles predicted by the Wacker and Seifert (2001) reference model as an implicit expectation value). However, this time we use a definition of N and L as close as possible to that of Wacker and Seifert (2001), also introducing a free parameter ϵ. Finally, in Section 4.3 we conduct a series of numerical experiments to illustrate the covariances for the SPM. These allow us to link features in the covariance matrices to gravitational sorting and the geometry of hydrometeors.

4.1 Expectation values and error covariances for the SPM

Using our previous results, we can now calculate the expectation values and error covariance matrices for the SPM. We start by providing a way to calculate the expectation value of $Z_{z,t}$ in Proposition 4.1.1. To this end, we introduce the auxiliary quantities A, h_2 and I_Z. Here A is a set summarizing the according indicator functions/integral boundaries, h_2 is an interim result encompassing the spatial integral over the z_j-dependent terms, while I_Z

[1]This leaves some ambiguity, so a different interpretation (yielding different covariances) might be possible. However the interpretation used in this thesis is probably the most consistent one, requiring as few changes as possible.

(which is proportional to the contribution from an individual particle to the expectation value) also includes the remaining terms and the integral over the particle diameter.

Proposition 4.1.1. *Given Assumption 3.2.1 and Definition 3.2.4, let*

$$A\left(z,t,D_j,z_{min},z_{max}\right) = \left[z-\alpha\sqrt{D_j}t-\frac{D_j}{2}, z-\alpha\sqrt{D_j}t+\frac{D_j}{2}\right]\cap\left[z_{min},z_{max}\right] \tag{4.1}$$
$$= \left[\max\left(z-\alpha\sqrt{D_j}t-\frac{D_j}{2}, z_{min}\right), \min\left(z-\alpha\sqrt{D_j}t+\frac{D_j}{2}, z_{max}\right)\right],$$

$$h_2\left(z,t,D_j,z_{min},z_{max}\right) = \int_{A(z,t,D_j,z_{min},z_{max})} f\left(D_j,z_j,t,z\right)dz_j, \tag{4.2}$$

$$I_Z\left(z,t,z_{min},z_{max}\right) = \int_0^\infty g_Z\left(D_j\right)\lambda e^{-\lambda D_j} h_2\left(z,t,D_j,z_{min},z_{max}\right)dD_j, \tag{4.3}$$

then

$$\mathbb{E}\left[Z_{z,t}\right] = \frac{n}{z_{max}-z_{min}} I_Z\left(z,t,z_{min},z_{max}\right). \tag{4.4}$$

Proof. See appendix □

An analogue approach yields a way to obtain the error covariances in Proposition 4.1.2. This is facilitated by the introduction of the further auxiliary quantities B, K_2 and J_{XY}, which to some extent are analogue to A, h_2 and I_Z.

Proposition 4.1.2. *Given Assumption 3.2.1, let $X_{x,t}$ and $Y_{y,s}$ be as in Definition 3.2.4, and define*

$$B\left(x,y,t,s,D_j,z_{min},z_{max}\right) = \left[x-\alpha\sqrt{D_j}t-\frac{D_j}{2}, x-\alpha\sqrt{D_j}t+\frac{D_j}{2}\right]\cap \tag{4.5}$$
$$\cap\left[y-\alpha\sqrt{D_j}s-\frac{D_j}{2}, y-\alpha\sqrt{D_j}s+\frac{D_j}{2}\right]\cap\left[z_{min},z_{max}\right]$$
$$= \left[\max\left(\left\{x-\alpha\sqrt{D_j}t-\frac{D_j}{2}, y-\alpha\sqrt{D_j}s-\frac{D_j}{2}, z_{min}\right\}\right),\right.$$
$$\left.,\min\left(\left\{x-\alpha\sqrt{D_j}t+\frac{D_j}{2}, y-\alpha\sqrt{D_j}s+\frac{D_j}{2}, z_{max}\right\}\right)\right],$$

$$k_2\left(x,y,t,s,D_j,z_{min},z_{max}\right) = \int_{B(x,y,t,s,D_j,z_{min},z_{max})} f\left(D_j,z_j,t,x\right)f\left(D_j,z_j,s,y\right)dz_j \tag{4.6}$$

$$J_{XY}\left(x,y,t,s,z_{min},z_{max}\right) = \int_0^\infty g_X\left(D_j\right)g_Y\left(D_j\right)\lambda e^{-\lambda D_j} k_2\left(x,y,t,s,D_j,z_{min},z_{max}\right)dD_j, \tag{4.7}$$

then

$$\mathrm{Cov}\left(X_{x,t},Y_{y,s}\right) = \frac{n}{z_{max}-z_{min}} J_{XY}\left(x,y,t,s,z_{min},z_{max}\right) - \tag{4.8}$$
$$-\frac{n}{\left(z_{max}-z_{min}\right)^2} I_X\left(x,t,z_{min},z_{max}\right) I_Y\left(y,s,z_{min},z_{max}\right).$$

Proof. See appendix □

The calculation of the expectation values and covariances can at least be carried out numerically, obtaining an approximation for the covariances of the error originating from the stochastic initial conditions. These can be regarded as a form of representation error allowing the use of the according matrices as observation error covariance matrices in our DA experiments in Chapter 5.

4.2 Expectation values and error covariances for the reference model

Now, for comparison we also calculate covariances for observables defined more similar to that considered in Wacker and Seifert (2001): We will assume every hydrometeor to fully contribute to the liquid water content and number density at height z, if and only if its centre z_j is located within the interval $[z-\epsilon, z+\epsilon]$, for some fixed ϵ. Thus we define analogue to Definition 3.2.2:

Definition 4.2.1. Given an arbitrary but fixed $\epsilon \in \mathbb{R}_+$ and a state η and assuming that all hydrometeors have the density $\rho_H \in \mathbb{R}_+$, let $L_\eta^\epsilon : \mathbb{R} \to \mathbb{R}_+$, $z \mapsto L_\eta^\epsilon(z)$ with

$$L_\eta^\epsilon(z) = \frac{1}{2\epsilon}\rho_H \sum_{j=1}^{n} \mathbf{1}_{[z-\epsilon,z+\epsilon]}(z_j) \left| B_{\frac{D_j}{2}}(x_j, y_j, z_j) \right|_V \tag{4.9}$$

$$= \frac{1}{2\epsilon}\frac{\rho_H \pi}{6} \sum_{j=1}^{n} \mathbf{1}_{[z-\epsilon,z+\epsilon]}(z_j) D_j^3 \tag{4.10}$$

and $N_\eta^\epsilon : \mathbb{R} \to \mathbb{R}_+$, $z \mapsto N_\eta^\epsilon(z)$ with

$$N_\eta^\epsilon(z) = \frac{1}{2\epsilon} \sum_{j=1}^{n} \mathbf{1}_{[z-\epsilon,z+\epsilon]}(z_j). \tag{4.11}$$

Analogue to the considerations in Section 3.2, we can introduce advection resulting in a time dependence of the state η and generalize Definition 4.2.1 to

Definition 4.2.2. Given the assumptions of Definition 4.2.1 and Notation 3.2.1, let

$$Z_{z,t}^\epsilon = \frac{1}{2\epsilon} \sum_{j=1}^{n} \mathbf{1}_{[z-\epsilon,z+\epsilon]}(z_j(t)) g_Z^\epsilon(D_j), \tag{4.12}$$

with

$$g_L^\epsilon(D_j) = \frac{\rho_H \pi}{6} D_j^3 \tag{4.13}$$

$$g_N^\epsilon(D_j) = 1. \tag{4.14}$$

Similar to Section 3.2, assuming (analogue to Assumption 3.2.1) the probability of the system being in a given state to be described by the product measure $\mathbb{P}$ of the probability measures $\mathbb{P}_j$, $j \in \{1, \cdots, n\}$ defined by the probability densities

$$\varrho^{\epsilon}_{z_j}(z_j) = \frac{1}{z_{max} - z_{min}} \mathbf{1}_{[z_{min}, z_{max}]}(z_j) \tag{4.15}$$

$$\varrho^{\epsilon}_{D_j}(D_j) = \delta_D(D_j), \tag{4.16}$$

for[2] $D \in \mathbb{R}$, we can calculate the expectation value of $Z^{\epsilon}_{z,t}$:

$$\begin{aligned}
\mathbb{E}\left[Z^{\epsilon}_{z,t}\right] &= \frac{1}{2\epsilon}\mathbb{E}\left[\sum_{j=1}^{n} \mathbf{1}_{[z-\epsilon, z+\epsilon]}(z_j(t))\, g^{\epsilon}_Z(D_j)\right] \\
&= \frac{1}{2\epsilon}\sum_{j=1}^{n} \int \mathbf{1}_{[z-\epsilon, z+\epsilon]}(z_j(t))\, g^{\epsilon}_Z(D_j)\, d\mathbb{P}(z_j, D_j) \\
&= \frac{1}{2\epsilon}\sum_{j=1}^{n} \int \mathbf{1}_{[z-\epsilon, z+\epsilon]}(z_j + v_T(D_j)\, t)\, g^{\epsilon}_Z(D_j)\, d\mathbb{P}(z_j, D_j) \\
&= \frac{1}{2\epsilon}\sum_{j=1}^{n} \int \mathbf{1}_{[z-v_T(D_j)t-\epsilon, z-v_T(D_j)t+\epsilon]}(z_j)\, g^{\epsilon}_Z(D_j)\, d\mathbb{P}(z_j, D_j),
\end{aligned} \tag{4.17}$$

which can be further simplified to

$$\begin{aligned}
\mathbb{E}\left[Z^{\epsilon}_{z,t}\right] &= \frac{1}{2\epsilon}\sum_{j=1}^{n} \int_0^{\infty}\int_{-\infty}^{\infty} \mathbf{1}_{[z-v_T(D_j)t-\epsilon, z-v_T(D_j)t+\epsilon]}(z_j)\, g^{\epsilon}_Z(D_j)\, \varrho^{\epsilon}_{z_j}(z_j)\, \varrho^{\epsilon}_{D_j}(D_j)\, dz_j dD_j \\
&= \frac{1}{2\epsilon}\frac{1}{z_{max} - z_{min}}\sum_{j=1}^{n} \int_0^{\infty}\int_{-\infty}^{\infty} \underbrace{\mathbf{1}_{[z-v_T(D_j)t-\epsilon, z-v_T(D_j)t+\epsilon] \cap [z_{min}, z_{max}]}(z_j)}_{=\mathbf{1}_{A^{\epsilon}\left(z,t,D_j,z_{min},z_{max}\right)}(z_j)} \cdot \\
&\quad \cdot g^{\epsilon}_Z(D_j)\, \delta_D(D_j)\, dz_j dD_j \\
&= \frac{1}{2\epsilon}\frac{1}{z_{max} - z_{min}}\sum_{j=1}^{n} \int_{-\infty}^{\infty} \mathbf{1}_{A^{\epsilon}(z,t,D,z_{min},z_{max})}(z_j)\, g^{\epsilon}_Z(D)\, dz_j \\
&= \frac{1}{2\epsilon}\frac{n g^{\epsilon}_Z(D)}{z_{max} - z_{min}} \int_{-\infty}^{\infty} \mathbf{1}_{A^{\epsilon}(z,t,D,z_{min},z_{max})}(z_j)\, dz_j \\
&= \frac{1}{2\epsilon}\frac{n g^{\epsilon}_Z(D)}{z_{max} - z_{min}} \lambda\left(A^{\epsilon}(z, t, D, z_{min}, z_{max})\right),
\end{aligned} \tag{4.18}$$

with λ being the Lebesque measure.

[2] Here δ_D is the Dirac measure centred at D. Note, that other than in Section 3.2 and different from Wacker and Seifert (2001), we now assume the diameter of all hydrometeors being identical, to facilitate computations.

In a similar way, we obtain the covariance of two observables $X^\epsilon_{x,t}$ and $Y^\epsilon_{y,s}$. By definition

$$\mathrm{Cov}\left(X^\epsilon_{x,t}, Y^\epsilon_{y,s}\right) = \mathbb{E}\left[X^\epsilon_{x,t} Y^\epsilon_{y,s}\right] - \mathbb{E}\left[X^\epsilon_{x,t}\right]\mathbb{E}\left[Y^\epsilon_{y,s}\right], \tag{4.19}$$

analogue to the proof of Proposition 4.1.2, becomes

$$\begin{aligned}
\mathrm{Cov}\left(X^\epsilon_{x,t}, Y^\epsilon_{y,s}\right) &= \frac{1}{4\epsilon^2}\sum_{j=1}^{n}\int \mathbf{1}_{[x-v_T(D_j)t-\epsilon, x-v_T(D_j)t+\epsilon]}(z_j)\, g^\epsilon_X(D_j)\cdot \\
&\quad \cdot \mathbf{1}_{[y-v_T(D_j)s-\epsilon, y-v_T(D_j)s+\epsilon]}(z_j)\, g^\epsilon_Y(D_j)\, d\mathbb{P}(z_j, D_j) - \\
&\quad - \frac{1}{4\epsilon^2}\sum_{j=1}^{n}\int \mathbf{1}_{[x-v_T(D_j)t-\epsilon, x-v_T(D_j)t+\epsilon]}(z_j)\, g^\epsilon_X(D_j)\, d\mathbb{P}(z_j, D_j)\cdot \\
&\quad \cdot \int \mathbf{1}_{[y-v_T(D_j)s-\epsilon, y-v_T(D_j)s+\epsilon]}(z_j)\, g^\epsilon_Y(D_j)\, d\mathbb{P}(z_j, D_j). \\
&= \frac{1}{4\epsilon^2}\sum_{j=1}^{n}\int_0^\infty\int_{-\infty}^\infty \mathbf{1}_{[x-v_T(D_j)t-\epsilon, x-v_T(D_j)t+\epsilon]}(z_j)\, g^\epsilon_X(D_j)\cdot \\
&\quad \cdot \mathbf{1}_{[y-v_T(D_j)s-\epsilon, y-v_T(D_j)s+\epsilon]}(z_j)\, g^\epsilon_Y(D_j)\, \varrho^\epsilon_{z_j}(z_j)\, \varrho^\epsilon_{D_j}(D_j)\, dz_j dD_j - \\
&\quad - \frac{1}{4\epsilon^2}\frac{n g^\epsilon_X(D)\, g^\epsilon_Y(D)}{(z_{max}-z_{min})^2}\lambda\left(A^\epsilon(x,t,D,z_{min},z_{max})\right)\lambda\left(A^\epsilon(y,s,D,z_{min},z_{max})\right) \\
&= \frac{1}{4\epsilon^2}\frac{1}{z_{max}-z_{min}}\sum_{j=1}^{n}\int_0^\infty\int_{-\infty}^\infty g^\epsilon_X(D_j)\, g^\epsilon_Y(D_j)\, \delta_D(D_j)\cdot \\
&\quad \cdot \underbrace{\mathbf{1}_{[x-v_T(D_j)t-\epsilon, x-v_T(D_j)t+\epsilon]\cap[y-v_T(D_j)s-\epsilon, y-v_T(D_j)s+\epsilon]\cap[z_{min}, z_{max}]}(z_j)}_{\mathbf{1}_{B^\epsilon\left(x,y,t,s,D_j,z_{min},z_{max}\right)}(z_j)} dz_j dD_j - \\
&\quad - \frac{1}{4\epsilon^2}\frac{n g^\epsilon_X(D)\, g^\epsilon_Y(D)}{(z_{max}-z_{min})^2}\lambda\left(A^\epsilon(x,t,D,z_{min},z_{max})\right)\lambda\left(A^\epsilon(y,s,D,z_{min},z_{max})\right).
\end{aligned} \tag{4.20}$$

This can be simplified to

$$\begin{aligned}
\mathrm{Cov}\left(X^\epsilon_{x,t}, Y^\epsilon_{y,s}\right) &= \frac{1}{4\epsilon^2}\frac{1}{z_{max}-z_{min}}\sum_{j=1}^{n}\int_{-\infty}^\infty g^\epsilon_X(D)\, g^\epsilon_Y(D)\, \mathbf{1}_{B^\epsilon(x,y,t,s,D_j,z_{min},z_{max})}(z_j)\, dz_j - \\
&\quad - \frac{1}{4\epsilon^2}\frac{n g^\epsilon_X(D)\, g^\epsilon_Y(D)}{(z_{max}-z_{min})^2}\lambda\left(A^\epsilon(x,t,D,z_{min},z_{max})\right)\lambda\left(A^\epsilon(y,s,D,z_{min},z_{max})\right) \\
&= \frac{1}{4\epsilon^2}\frac{n g^\epsilon_X(D)\, g^\epsilon_Y(D)}{z_{max}-z_{min}}\lambda\left(B^\epsilon(x,y,t,s,D,z_{min},z_{max})\right) - \\
&\quad - \frac{1}{4\epsilon^2}\frac{n g^\epsilon_X(D)\, g^\epsilon_Y(D)}{(z_{max}-z_{min})^2}\lambda\left(A^\epsilon(x,t,D,z_{min},z_{max})\right)\lambda\left(A^\epsilon(y,s,D,z_{min},z_{max})\right).
\end{aligned} \tag{4.21}$$

If we now assume $x = y$ and $t = s$, we have

$$B^\epsilon\left(x,x,t,t,D,z_{min},z_{max}\right)=A^\epsilon\left(x,t,D,z_{min},z_{max}\right), \tag{4.22}$$

which allows us to simplify (4.21) to

$$\begin{aligned}\mathrm{Cov}\left(X^\epsilon_{x,t},Y^\epsilon_{x,t}\right)&=\frac{1}{4\epsilon^2}\frac{ng^\epsilon_X\left(D\right)g^\epsilon_Y\left(D\right)}{z_{max}-z_{min}}\lambda\left(B^\epsilon\left(x,x,t,t,D,z_{min},z_{max}\right)\right)-\\&\quad-\frac{1}{4\epsilon^2}\frac{ng^\epsilon_X\left(D\right)g^\epsilon_Y\left(D\right)}{\left(z_{max}-z_{min}\right)^2}\lambda\left(A^\epsilon\left(x,t,D,z_{min},z_{max}\right)\right)^2\\&=\frac{1}{4\epsilon^2}\frac{ng^\epsilon_X\left(D\right)g^\epsilon_Y\left(D\right)}{z_{max}-z_{min}}\lambda\left(A^\epsilon\left(x,t,D,z_{min},z_{max}\right)\right)-\\&\quad-\frac{1}{4\epsilon^2}\frac{ng^\epsilon_X\left(D\right)g^\epsilon_Y\left(D\right)}{\left(z_{max}-z_{min}\right)^2}\lambda\left(A^\epsilon\left(x,t,D,z_{min},z_{max}\right)\right)^2\\&=\frac{1}{4\epsilon^2}\frac{ng^\epsilon_X\left(D\right)g^\epsilon_Y\left(D\right)}{z_{max}-z_{min}}\left[\lambda\left(A^\epsilon\left(x,t,D,z_{min},z_{max}\right)\right)-\frac{\lambda\left(A^\epsilon\left(x,t,D,z_{min},z_{max}\right)\right)^2}{z_{max}-z_{min}}\right].\end{aligned} \tag{4.23}$$

If we now additionally assume[3] $[z-\epsilon,z+\epsilon]\subset[z_{min}+v_T\left(D_j\right)t,z_{max}+v_T\left(D_j\right)t]$, we obtain

$$\begin{aligned}\lambda\left(A^\epsilon\left(x,t,D,z_{min},z_{max}\right)\right)&=\lambda\left(\left[z-v_T\left(D_j\right)t-\epsilon,z-v_T\left(D_j\right)t+\epsilon\right]\cap\left[z_{min},z_{max}\right]\right)\\&=\lambda\left(\left[z-v_T\left(D_j\right)t-\epsilon,z-v_T\left(D_j\right)t+\epsilon\right]\right)\\&=\left|z-v_T\left(D_j\right)t+\epsilon-\left(z-v_T\left(D_j\right)t-\epsilon\right)\right|\\&=2\epsilon\end{aligned} \tag{4.24}$$

and can further simplify (4.23) to

$$\begin{aligned}\mathrm{Cov}\left(X^\epsilon_{x,t},Y^\epsilon_{x,t}\right)&=\frac{1}{4\epsilon^2}\frac{ng^\epsilon_X\left(D\right)g^\epsilon_Y\left(D\right)}{z_{max}-z_{min}}\left[2\epsilon-\frac{4\epsilon^2}{z_{max}-z_{min}}\right]\\&=\frac{ng^\epsilon_X\left(D\right)g^\epsilon_Y\left(D\right)}{z_{max}-z_{min}}\left[\frac{1}{2\epsilon}-\frac{1}{z_{max}-z_{min}}\right]\\&=\frac{1}{2\epsilon}\frac{ng^\epsilon_X\left(D\right)g^\epsilon_Y\left(D\right)}{z_{max}-z_{min}}-\frac{ng^\epsilon_X\left(D\right)g^\epsilon_Y\left(D\right)}{\left(z_{max}-z_{min}\right)^2}.\end{aligned} \tag{4.25}$$

$\mathrm{Cov}\left(X^\epsilon_{x,t},Y^\epsilon_{x,t}\right)$ in (4.25) depends explicitly on ϵ and one possible way to get rid of this dependence would be taking the limit $\epsilon\to0$. If we however take the limit, we obtain

[3] We can obtain this e.g. for $t=0$ and $x\in[z_{min}+\epsilon,z_{max}-\epsilon]$.

$$\begin{aligned}\lim_{\epsilon\to 0}\mathrm{Cov}\left(X^{\epsilon}_{x,t},Y^{\epsilon}_{x,t}\right) &= \lim_{\epsilon\to 0}\left(\frac{1}{2\epsilon}\frac{ng^{\epsilon}_X(D)\,g^{\epsilon}_Y(D)}{z_{max}-z_{min}}-\frac{ng^{\epsilon}_X(D)\,g^{\epsilon}_Y(D)}{(z_{max}-z_{min})^2}\right) \\ &= \underbrace{\lim_{\epsilon\to 0}\frac{1}{2\epsilon}\frac{ng^{\epsilon}_X(D)\,g^{\epsilon}_Y(D)}{z_{max}-z_{min}}}_{=\infty}-\frac{ng^{\epsilon}_X(D)\,g^{\epsilon}_Y(D)}{(z_{max}-z_{min})^2} \\ &= \infty,\end{aligned} \tag{4.26}$$

yielding i.a. an infinite variance.

So, as seen in (4.25) using the unmodified definitions of Wacker and Seifert (2001) yields covariance matrices that (at least in the variances of L and N, as well as the covariance between L and N at the same grid point) explicitly depend on the free parameter ϵ for the special case of all hydrometeors having the same diameter. This is problematic, as ϵ is an arbitrary[4] constant, that has no physical analogue and should not appear in any measurable quantity. Especially its appearance in the variances is problematic for DA, as use of these quantities cannot be avoided, e.g. by thinning the observations and using a diagonal observation error covariance matrix.

As seen in (4.26), also taking the limit $\epsilon \to 0$ does not solve that problem, as it results in divergence at least of the variances of L and N, as well as the covariance between L and N at the same grid point. Again especially the variances are problematic, as this would practically mean that no observation would carry any information in this case.

In general, we have seen that as soon as covariances are calculated, a collection of severe problems occurs when using the unmodified definitions. However, none of these issues occurs when using the definitions of Section 3.2. This motivates the changes made to the Wacker and Seifert (2001) reference model when constructing the SPM.

4.3 Numerically calculated values

Now, we numerically calculate the expectation values and covariance matrices for some exemplary cases, using a log-transformation to ensure the tails of distributions being adequately sampled in numerical integration (Berry and Reinhardt, 1974). We perform a series of numerical experiments, comparing the expectation values predicted by the SPM for number concentration and liquid water content to the Wacker and Seifert (2001) reference model. Furthermore, we investigate the effect of particle geometry and velocity model on the expectation values and covariances of number concentration and liquid water content. We employ the axis ratios for cylindrical hydrometeors determined by the according

[4]Note that the asymptotic behaviour of ϵ is different from what we would expect from the size of the grid box of a model. Thus we can also not dispose of ϵ by identifying it with the model resolution.

power laws given in Auer and Veal (1970) and terminal fall velocities calculated using the results of Brdar and Seifert, 2018, as well as (for spherical hydrometeors) from a simplified setup obtained from equating friction and gravitational force. The nomenclature of the cylindrical hydrometeor geometries follows that of Auer and Veal (1970) throughout the entire thesis.

The remainder of this section is structured as follows: In Section 4.3.1 we show profiles obtained from the expectation values of the SPM for the liquid water content and number density and compare them to the predictions of the Wacker and Seifert (2001) reference model. Then in Section 4.3.2 we discuss the covariances obtained for the SPM, before we investigate the impact of different velocity models on profiles and covariances in Section 4.3.3. Furthermore, a summary of the employed velocity models, which might be useful for interpreting the results can be found in Appendix E.

4.3.1 Profiles

We now discuss the liquid water content and number density profiles obtained from the SPM in comparison to that obtained from the Wacker and Seifert (2001) reference model in the same situation. Here we focus on large spherical hydrometeors, as the Wacker and Seifert (2001) reference model is only defined for spherical hydrometeors and the SPM is affected less by noise for larger hydrometeors.

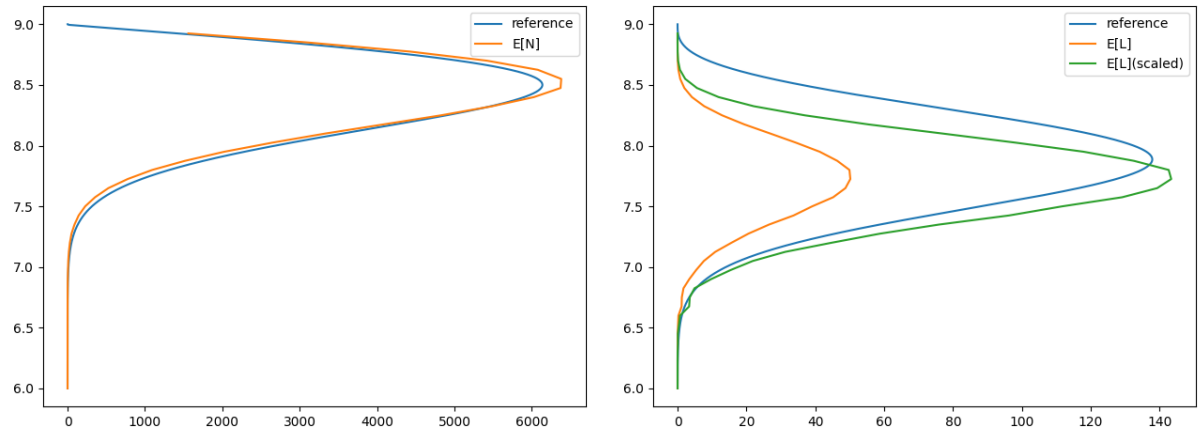

Figure 4.1: Expectation values of number density (left panel) and liquid water content (right panel) compared to the reference model of Wacker and Seifert (2001), for large spherical hydrometeors with diameters following an exponential distribution with $\lambda = 70\frac{1}{m}$ and initial positions given by $z_{init} \sim U([8.99m, 9.00m])$ at $t = 0.039s$. The scaled version of $\mathbb{E}[L]$ is rescaled by a factor of $\frac{1}{z_{max}^{init} - z_{min}^{init}} \frac{\mathbb{E}[V_{sphere}]}{\mathbb{E}[A_{intersect}]}$, to account for differences of the definition of L on smaller length scales.

Note 4.3.1. Number density per hydrometeor exceeding 1 (such as in Figure 4.1) could

be explained by the geometry of the hydrometeors. A hydrometeor intersecting the investigated z-level with a larger portion than its average cross section can cause a number density above 1 at that z-level.

In Figure 4.1, a comparison of the expectation values of number density and liquid water content to the reference model of Wacker and Seifert (2001) is shown for large spherical hydrometeors with diameters following an exponential distribution with $\lambda = 70\frac{1}{m}$ and initial positions given by $z_{init} \sim U([8.99m, 9.00m])$ at $t = 0.039s$. Furthermore, we assume the system consisting of $n = 5000$ hydrometeors with velocities equal to the terminal fall velocity obtained from the simplified setup that equates friction and gravitational force (see also Figure E.1).

The number densities predicted by both models agree relatively well. However, the liquid water content differs in peak position and especially amplitude. This might be explained by a different dependence of the liquid water content on the particle size: Whereas (3.2) defines it using an area of intersection (i.e. in first order $\sim D^2$), Wacker and Seifert (2001) defines it as mass per grid spacing (i.e. $\sim D^3$), which results in a stronger dependence of the peak position on particle size and gravitational sorting, likely explaining the downward shift of the expectation value of (3.2) compared to the model of Wacker and Seifert (2001). Furthermore, approximately correcting the difference in the definitions by multiplying $\mathbb{E}[L]$ by a factor[5] of $\frac{1}{z_{max}^{init} - z_{min}^{init}} \frac{\mathbb{E}\left[V_{sphere}\right]}{\mathbb{E}[A_{intersect}]} = \frac{1}{z_{max}^{init} - z_{min}^{init}} \frac{2}{\lambda}$ leads to the amplitudes of the liquid water content profiles predicted by both models agreeing well. So we can conclude that the difference in amplitude (and likely also that in peak position) of L is caused by the different dependency on the particle size.

We now turn to cylindrical hydrometeors with different aspect ratios. In Figure 4.2, we show a comparison of the expectation values of number density and liquid water content, for a system consisting of $n = 5000$ cylindrical hydrometeors with different axis ratios (corresponding to the 'hexagonal plate' and 'thick plate' type of Auer and Veal, 1970). Particle volumes are assumed to be equal to that of spherical hydrometeors with diameters following an exponential distribution with $\lambda = 500\frac{1}{m}$ and initial positions to be given by $z_{init} \sim U([8.99m, 9.00m])$ at $t = 0.1s$. Particle orientations are assumed to be constant, with $\varphi = 90°$.

The number density and liquid water profiles of the thick plates are both significantly shifted downwards compared to the that of the hexagonal plates, which can likely be explained by the higher fall velocities of the thick plates (see Figure E.1). Furthermore, both profiles are much narrower for the hexagonal plates, which is likely caused by weaker gravitational sorting due to the smaller dependence of the according velocities on particle size. The small increase of the number density at the upper end of the domain is likely caused

[5]Note, that this factor does not explicitly depend on the hydrometeor diameter, as this quantity is integrated out by the expectation value.

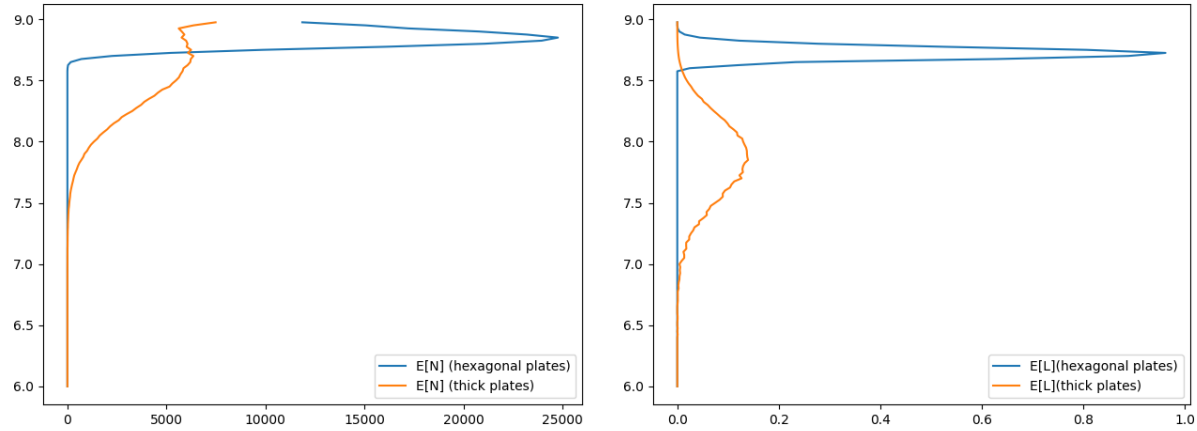

Figure 4.2: Expectation values of number density (left panel) and liquid water content (right panel), for cylindrical hydrometeors with particle volumes equal to that of spherical hydrometeors with diameters following an exponential distribution with $\lambda = 500\frac{1}{m}$ and initial positions given by $z_{init} \sim U([8.99m, 9.00m])$ at $t = 0.1s$.

by very small and slow particles, that have not noticeably moved from their initial position.

So we have seen that the profiles predicted by the SPM (up to a different scaling behaviour) agree relatively well with those obtained from the Wacker and Seifert (2001) reference model. Furthermore, the profiles seem to be physically plausible, with their shape (as well as the differences between different setups) well explainable by gravitational sorting.

4.3.2 Covariances and correlations

Now, we investigate the large (here: lenght scales much larger than typical hydrometeor diameter) and small (here: lenght scales smaller than or equal to typical hydrometeor diameter) scale structures of the covariance matrices obtained from our model. We will also discuss the effects of gravitational sorting, particle geometry and orientation on the covariances.

4.3.2.1 Covariance matrix for large spherical hydrometeors

We now calculate the covariance matrix for large spherical hydrometeors moving with the terminal fall velocity predicted by Brdar and Seifert, 2018. The diameters are assumed to be following an exponential distribution with $\lambda = 70\frac{1}{m}$, which should roughly describe relatively large hail stones. We focus on larger hydrometeors here, because the according covariances are less affected by numerical noise. Furthermore, the effects of gravitational sorting are expected to be better visible for larger hydrometeors, as the covariance matrices for smaller hydrometeors become diagonal, when the resolution is not increased substantially. The initial positions are assumed to be given by $z_{init} \sim U([8.99m, 9.00m])$ and we

consider the case $t = 0.039s$. The z-axis is selected such that both the liquid water content and the number density are large enough to avoid division by zero when calculating the correlations.

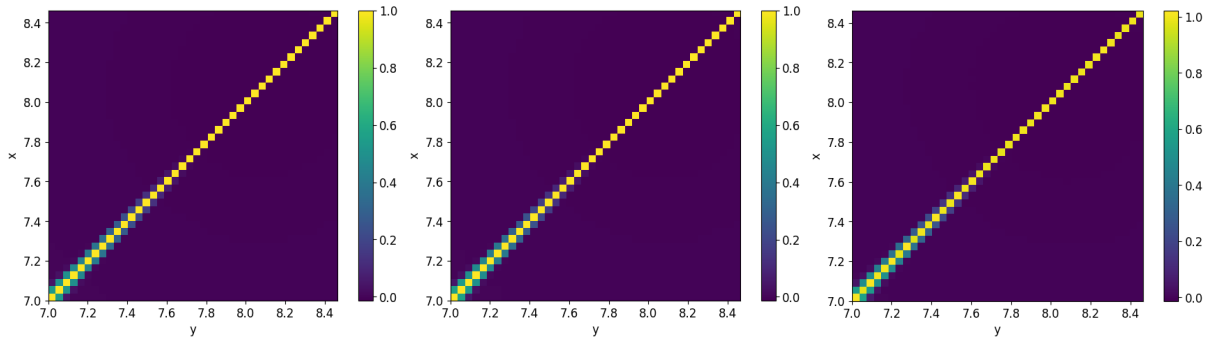

Figure 4.3: (N, N)-part (left panel), (L, L)-part (central panel) and (N, L)-part (right panel) of the correlation matrix for large spherical hydrometeors with diameters following an exponential distribution with $\lambda = 70\frac{1}{m}$ and initial positions given by $z_{init} \sim U([8.99m, 9.00m])$ at $t = 0.039s$. The NN-and LL-part have been symmetrized for numerical improvement.

The results obtained numerically using (4.8) are shown in Figure 4.3. All parts of the correlation matrix exhibit a similar behaviour: The correlation length increases with decreasing z. This is likely caused by gravitational sorting, as larger hydrometeors which are capable of connecting multiple grid points fall faster, resulting in them having moved to lower z-levels than smaller ones already at the considered time step. Slightly negative correlations with extremely low absolute values (not visible in the plot) obtained between distant grid points are likely either a side effect of the fixed particle number, or a numerical artefact.

4.3.2.2 Influence of particle geometry and orientation on correlations

To investigate the influence of particle geometry and orientation on correlations, we consider cylindrical and spherical hydrometeors. To allow for easy comparison of the different hydrometeor types, we assume all particle volumes to be equal to that of spherical hydrometeors with diameters following an exponential distribution with $\lambda = 500\frac{1}{m}$, which should yield particle sizes plausible for all considered geometries. For the cylindrical hydrometeors, we assume the diameter-hight-ratio to be equal to that of the 'hexagonal plate' type of Auer and Veal, 1970 and consider the cases $\phi = 90°$ and $\phi \sim U([0°, 90°])$, to investigate the effect of particle orientation. The initial positions are assumed to be given by $z_{init} \sim U([8.99m, 9.00m])$ and we consider the case $t = 0.1s$. For numerical reasons, we plot sections of the correlations at the position of a hydrometeor of median diameter, initial position and orientation, as we expect a large number of hydrometeors present there. The results are shown in Figure 4.4.

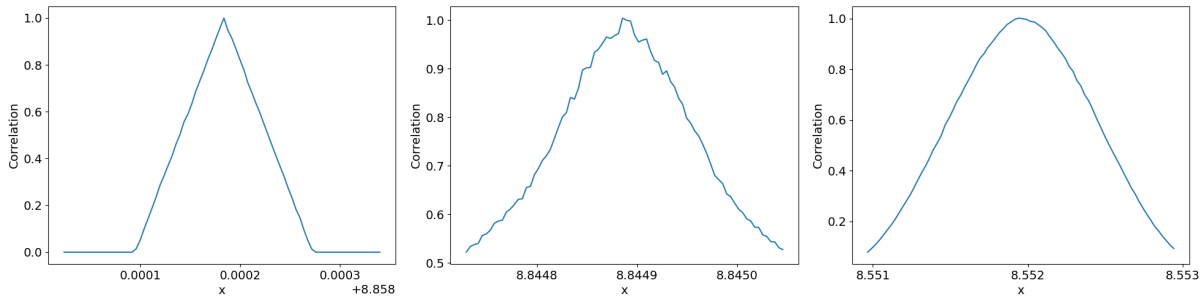

Figure 4.4: Covariance profile centred at the position of a hydrometeor of median diameter, initial position and orientation, for cylindrical hydrometeors (with diameter-hight-ratio corresponding to the 'hexagonal plate' type of Auer and Veal, 1970) and $\phi = 90°$ (left panel), $\phi \sim U([0°, 90°])$ (central panel) and spherical hydrometeors (right panel). Particle volumes are assumed to be equal to that of spherical hydrometeors with diameters following an exponential distribution with $\lambda = 500\frac{1}{m}$.

For the cylindrical hydrometeors with constant orientation, we see a triangular covariance profile, whereas cylindrical hydrometeors with uniformly distributed orientation and spherical hydrometeors show a more bell shaped profile. The finite support of the triangular profile might be explained by gravitational sorting only allowing for hydrometeors up to a certain size to be present close enough to the considered z-level.

4.3.2.3 Time dependence of variances for large spherical hydrometeors

We now discuss the time dependence of variances. To this end, we again (to reduce numerical noise) focus on large spherical hydrometeors and calculate the according variances at several time steps. The diameters are assumed to be following an exponential distribution with $\lambda = 70\frac{1}{m}$. The initial positions are assumed to be given by $z_{init} \sim U([8.99m, 9.00m])$ and we consider the initial time $t = 0.03s$. Variances and profiles are calculated for the initial time step and after additional 5, 10, 15 and 20 time steps of $0.001s$ (see Figure 4.5 for profiles).

The variance of the liquid water content follows a bell shaped curve that broadens over time, while its mean quickly shifts to lower z-values. This might be explained by the variances of the liquid water content (like the liquid water content itself) being predominantly influenced by the larger hydrometeors, which exhibit larger terminal fall velocities. Furthermore, gravitational sorting causes the hydrometeors large enough to have a significant effect on the liquid water content to spread out over a wider domain, leading to a broadening of the profile and the variance curve.

In contrast, the variance of the number density is almost constant over time, with very high values at the top of the domain, roughly exponentially decreasing with z. This might be explained by the variances of the number density being predominantly influenced by

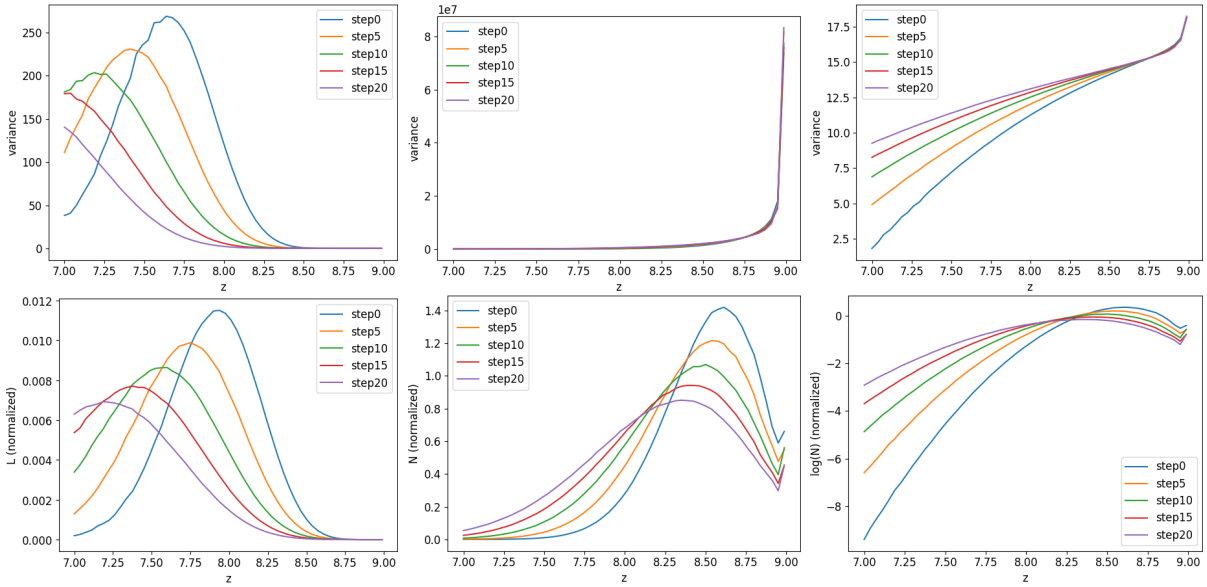

Figure 4.5: Variances (upper panel) and profiles (lower panel) of liquid water content (left panel), number density (central panel) and logarithm of number density (right panel) for spherical hydrometeors with exponentially distributed diameters with $\lambda = 70\frac{1}{m}$ and initial positions given by $z_{init} \sim U([8.99m, 9.00m])$ at $0.03s$ (step 0) and after additional 5, 10, 15 and 20 time steps of $0.001s$. Profiles normalized to total number of hydrometeors.

the smaller hydrometeors, which move very slowly, while the smallest hydrometeors stay in the upper part of the domain for the entire period under consideration. Due to their small size and the high weight assigned by the D_j^{-3}-term in (3.3), even small fluctuations in their position can strongly affect the number density, leading to them dominating its variance. As seen in the logarithmic plot, the variances at lower z-levels increase very slowly, while those at the top of the domain decrease minimally.

When comparing to the according profiles, the variances of the liquid water content follow (despite somewhat shifted) those of the according expectation value to some extent, while that of the number concentration remain relatively independent. However, in the logarithmic plots for the number concentration some correlation can be seen between variances and profiles in the lower part of the domain.

4.3.3 Comparison of velocity models

Finally, we investigate the effect of different velocity models on expectation values and covariances of number density and liquid water content. In Figure 4.6 expectation values of number density and liquid water content, calculated using a simplified velocity model (obtained from equating friction and gravitational force) and the McSnow model of Brdar and Seifert, 2018 are shown for spherical hydrometeors with initial positions given by $z_{init} \sim U([8.99m, 9.00m])$ and diameters following an exponential distribution, for $\lambda = 70\frac{1}{m}$

at $t = 0.039s$ and $\lambda = 500\frac{1}{m}$ at $t = 0.1s$.

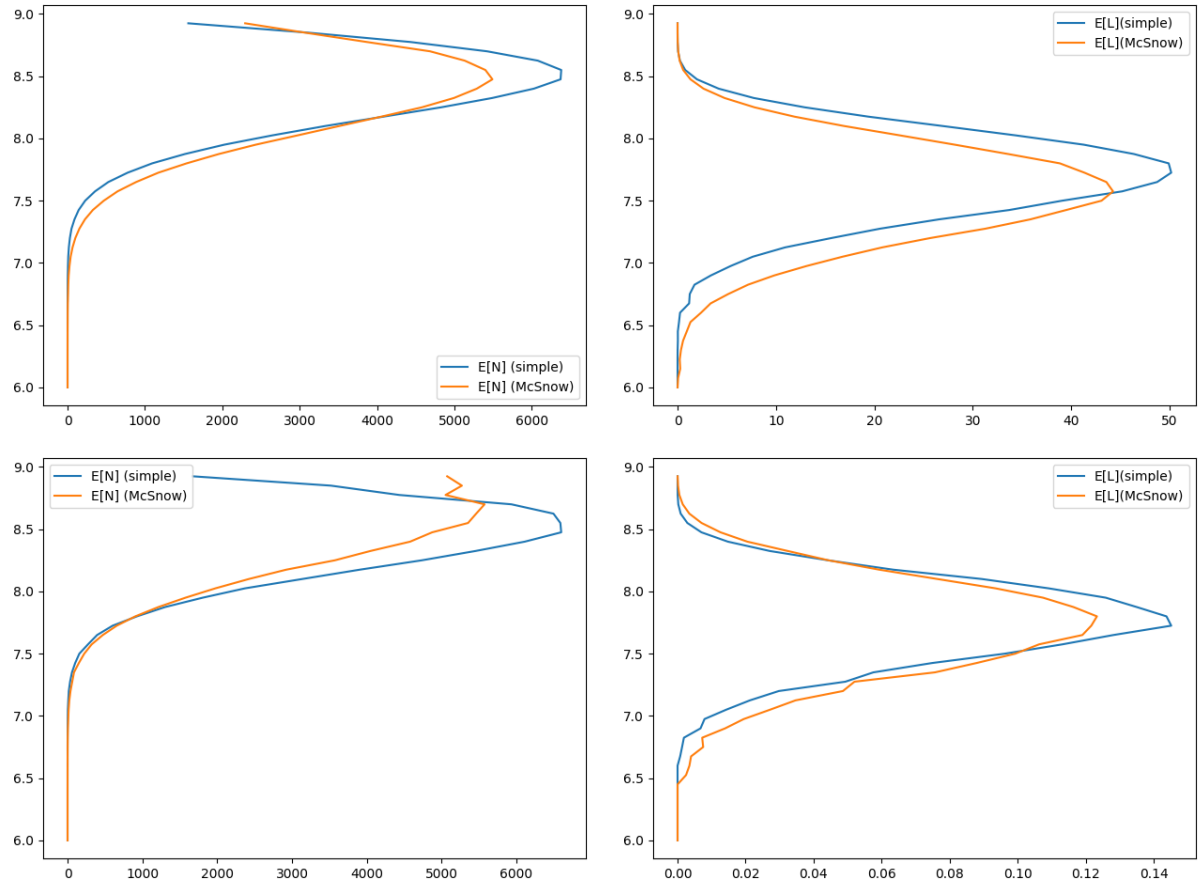

Figure 4.6: Expectation values of number density (left panels) and liquid water content (right panels), calculated using a simplified velocity model and the McSnow model of Brdar and Seifert, 2018, for spherical hydrometeors with initial positions given by $z_{init} \sim U([8.99m, 9.00m])$ and diameters following an exponential distribution, for $\lambda = 70\frac{1}{m}$ at $t = 0.039s$ (upper panels) and $\lambda = 500\frac{1}{m}$ at $t = 0.1s$ (lower panels).

In the case of the larger hydrometeors with $\lambda = 70\frac{1}{m}$, we see the peak of the liquid water content profile calculated using the McSnow model shifted downwards compared to that calculated using the simplified model, whereas the peaks of the number density profiles agree relatively well. This might be explained by the McSnow model producing higher velocities than the simplified model for larger hydrometeors (which predominantly shape the liquid water content profile). On the other hand, in the case of the smaller hydrometeors with $\lambda = 500\frac{1}{m}$, the peaks of the liquid water content profiles agree relatively well, whereas we see the peak of the number density profile calculated using the McSnow model shifted upwards compared to that calculated using the simplified model. This might be explained by the McSnow model producing lower velocities than the simplified model for

smaller hydrometeors (which predominantly shape the number density profile). Furthermore, all profiles calculated using the McSnow model are wider than those calculated using the simplified model, which might be explained by stronger gravitational sorting caused by a (slightly) stronger dependence of the terminal fall velocity on hydrometeor size in the McSnow model.

In Figure 4.7, we show the covariance profiles centred at the position of a hydrometeor of median diameter and initial position, for spherical hydrometeors with initial positions given by $z_{init} \sim U([8.99m, 9.00m])$ and diameters following an exponential distribution with $\lambda = 500\frac{1}{m}$ at $t = 0.1s$, calculated using a simplified velocity model and the McSnow model of Brdar and Seifert (2018).

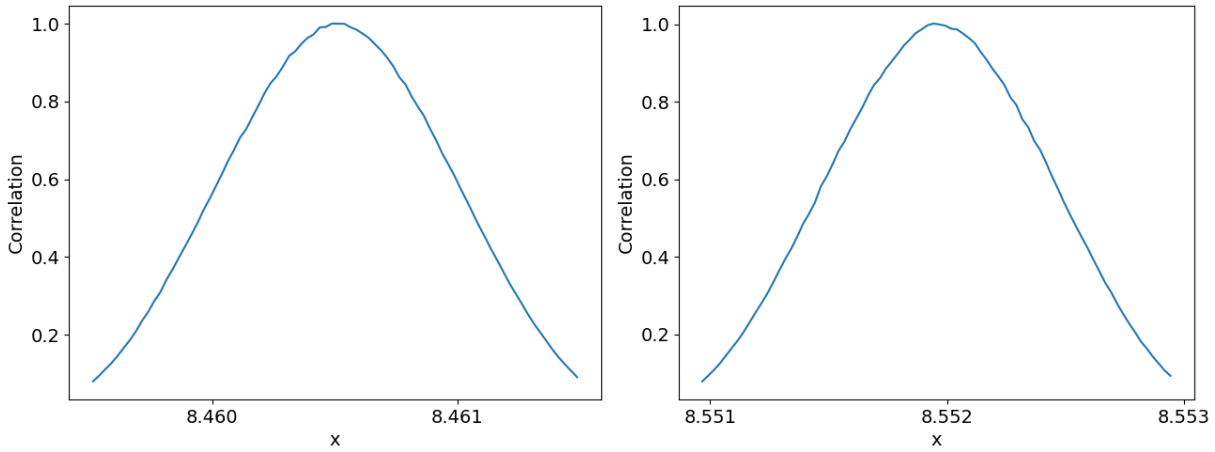

Figure 4.7: Covariance profiles centred at the position of a hydrometeor of median diameter and initial position, for spherical hydrometeors with initial positions given by $z_{init} \sim U([8.99m, 9.00m])$ and diameters following an exponential distribution with $\lambda = 500\frac{1}{m}$ at $t = 0.1s$, calculated using a simplified velocity (left panel) model and the McSnow model of Brdar and Seifert (2018) (right panel).

Despite differences in the z-level considered, the correlations obtained using both models have the same shape and width, so there seems to be no influence of the velocity model on the small scale structures of the correlation matrix.

4.4 Summary

In summary, in this section we have seen that the SPM produces physically plausible expectation values agreeing sufficiently well with those obtained from the Wacker and Seifert (2001) reference model. Remaining differences between both models are likely caused by a different dependence of L on the particle size. Noting that in our setup (positive) correlations are only possible by a single hydrometeor intersecting multiple grid

points, we found that the structure of the covariance matrices predicted by the SPM can be explained (on length scales smaller than the typical particle size) by the geometry of the hydrometeors and (on length scales larger than the typical particle size) by gravitational sorting. As gravitational sorting causes larger hydrometeors to be present at lower grid points, it results in correlation lengths increasing with decreasing height. We also found that employing different velocity models did not visibly impact the covariance matrices at small length scales.

Chapter 5

Data assimilation with SPM

In this chapter we use covariance matrices obtained in Section 4.1 in a series of DA experiments, to research the role of temporal and spatial variations in observation error covariances. We start with a general overview over the experimental design in Section 5.1, before we discuss the details of the numerical implementation in Section 5.2. Finally, we present the results of our DA experiments in Section 5.3.

5.1 Experimental design

We conduct a series of double twin experiments with two nature runs differing in the underlying physics assumptions. One nature run is created employing the stochastic particle model, while the other is obtained using the Wacker and Seifert (2001) reference model. Thus, to improve readability we will label the according DA experiments as SPM and WSRM during the entire section.

Prior to the DA experiments, the analytic observation error covariances for the SPM are obtained by numerically integrating the according equations from Proposition 4.1.2, employing the same parameters as the according DA experiments. To this end, we calculate the (N, N)-, (N, L)- and (L, L)-block of the matrix individually, employing a Monte Carlo integral with $12,000,000$ samples. The blocks are subsequently combined and the resulting matrix is symmetrized by averaging it with its transposed[1]. To obtain positive semidefinite matrices, we use the implementation of Croucher (2014) for the NCM method of Higham (2002). Furthermore, it is possible to optionally apply ridge regression (see Tabeart et al., 2020) to improve the condition number.

During the DA experiments, the data created from both truth runs will be assimilated employing an EnKF and using the same $n_{ens} = 100$ member ensemble and parameters in both experiments. The observed grid points can be specified to be e.g. every grid point or

[1]Note, that this effectively doubles the number of samples used to calculate the non-diagonal elements of the matrix.

every second grid point (in space). For evolving the ensemble members we always employ the two moment scheme of Wacker and Seifert, 2001, using an upwind scheme (see Courant et al., 1952a and Harten et al., 1983), and DA is carried out every 5th time step. Optionally, profiles of ensemble members can be smoothed after every model evolution, using a running average (equally weighting all values within a range of 5 grid points) and negative values are set to a small positive threshold (1 for N and 0.01 for L). The observation error covariance matrix used by the EnKF can be specified to be either the full analytic observation error covariance matrix obtained for the SPM, a block diagonal version of the full analytic observation error covariance matrix obtained by setting the correlations between N and L to zero, or a diagonal matrix extracted from the full analytic observation error covariance matrix.

After a spin-up of 30 model iterations of $0.0002s$, we carry out 20 assimilation cycles with the time interval between assimilation cycles being $0.001s$. The domain is chosen to be $[7m, 9m]$, while the grid spacing is set to $0.0375m$. The number of hydrometeors is set to 10.000 and they are initially distributed uniformly in the interval $[8.99m, 9m]$, while their diameters are assumed to be exponentially distributed with $\lambda = 70\frac{1}{m}$. These choices are made to ensure that the profiles change noticeably over time, while remaining mostly contained in the domain (though the L profile starts to extend beyond the lower boundary of the domain at later time steps). Furthermore, the density of hydrometeors has to be high enough to ensure that the profiles from the particle based simulations roughly resemble those of the analytic model and the number of grid points has to be low enough to ensure that the calculation of the analytical observation error covariances is possible with the available computational resources.

The initial background is obtained by shifting the N and L profiles produced by the SPM downwards by 10 grid points. This induces an initial positional error, avoiding the experiments starting with a perfect estimate and providing a more challenging problem than pure amplitude error.

Finally, we outline the implementation of the algorithm (without details or optional steps):

- Initialize the first nature run (employing the SPM) and create particles
- Evolve first nature run to spin-up time
- Use (3.2) and (3.3) to calculate L and N profiles on all grid points for first nature run
- Create initial ensemble by evolving the profiles from the nature run for 0 to $n_{ens} = 100$ model time steps
- Initialize second nature run (employing the WSRM) with according data (including the ensemble) from the first nature run

- Shift profiles of all ensemble members down by 10 grid points (for both experiments), to obtain a background ensemble at initial time that includes a positional error
- Iterate:
  - Obtain "observations" from both nature runs
  - Carry out DA for both experiments, employing the "observations" of the according nature runs
  - Plot snapshots of the profiles, the ensemble and the background and analysis covariance matrices
  - Calculate and store RMSE for both experiments
  - Evolve both ensembles
- Plot RMSE over time

5.2 Numerical details

We now give an overview over the implementation of an upwind scheme used to evolve the ensemble. Note that we will evolve each ensemble member separately and thus discuss the application of the scheme to an individual ensemble member here.

Our goal is to use the methods from Courant et al. (1952b) to solve the two-moment scheme from Wacker and Seifert (2001), which is given by (2.46), (2.47), (2.48), (2.49), (2.50) and (2.51). We will focus on the case $\gamma = \frac{1}{6}$.

The Courant et al. (1952b) scheme is designed to solve systems of equations of the form

$$\sum_{i=1}^{n} A^{ij}(x, y, \mathbf{u})\, u_x^i + B^{ij}(x, y, \mathbf{u})\, u_y^i = C^j(x, y, \mathbf{u}), \tag{5.1}$$

for $j \in \{1, \cdots, n\}$. Despite the scheme allowing more general[2] initial conditions, we will focus here on the special case

$$\mathbf{u}(x, y_0) = \mathbf{u}_0, \tag{5.2}$$

for $y_0 \in \mathbb{R}$, $\mathbf{u}_0 \in \mathbb{R}^n$ and for all $x \in \mathbb{R}$.

Note that we can rewrite (2.50) in the form (5.1), by setting $n = 2$, $x = z$, $y = t$, $A^{ij} = A_{ji}$, $B^{ij} = \mathrm{Id}_{n\times n}$ and $C^j = 0$. The initial conditions in this case are $u_0^1 = N_0$ and $u_0^2 = L_0$ with

[2]The scheme actually admits an initial curve $y_0(x)$. This can be transformed in the form considered here by choosing $y_0(x) = y_0 = \text{const}$.

N_0 and L_0 being the initial number density and liquid water content.

The first step of the Courant et al. (1952b) scheme is to transform the system of equations given in (5.1) to the form

$$\sum_{i=1}^{n} a^{ij}\left(x, y, \mathbf{u}\right)\left(u_y^i + c^j\left(x, y, \mathbf{u}\right) u_x^i\right) = b^j\left(x, y, \mathbf{u}\right), \tag{5.3}$$

for $j \in \{1, \cdots, n\}$. We will sketch this process for the Wacker and Seifert (2001) two-moment scheme in this chapter, however details of the calculations can be found in Appendix F. In order to rewrite the Wacker and Seifert (2001) two-moment scheme in the form (5.3), we set

$$c\left(x, y, \mathbf{u}\right) = \begin{pmatrix} c^1\left(x, y, \mathbf{u}\right) & \cdots & 0 \\ \vdots & \ddots & \vdots \\ 0 & \cdots & c^n\left(x, y, \mathbf{u}\right) \end{pmatrix}, \tag{5.4}$$

and rewrite (5.3) in vectorial form as

$$\mathbf{a}^T\left(x, y, \mathbf{u}\right)\mathbf{u}_y + c\left(x, y, \mathbf{u}\right)\mathbf{a}^T\mathbf{u}_x = \mathbf{b}\left(x, y, \mathbf{u}\right), \tag{5.5}$$

with $c\left(x, y, \mathbf{u}\right)$ of the form (5.4), $\mathbf{u} \in \mathbb{R}^n$, $\mathbf{a} \in \mathbb{R}^{n \times n}$ and $\mathbf{b}\left(x, y, \mathbf{u}\right) \in \mathbb{R}^n$, for all x, y and $\mathbf{u}$. Now assuming $\left(\mathbf{a}^T\right)$ to be invertible, we can multiply (5.5) from the left by $\left(\mathbf{a}^T\right)^{-1}$, which yields

$$\mathbf{u}_y + \left(\mathbf{a}^T\right)^{-1} c\mathbf{a}^T\mathbf{u}_x = \left(\mathbf{a}^T\right)^{-1}\mathbf{b}, \tag{5.6}$$

where we dropped the arguments of the functions from the notation to improve readability. We now notice that (if A is diagonalizable) we can rewrite (2.50) in this form, by setting

$$x = z \tag{5.7}$$
$$y = t \tag{5.8}$$
$$\left(\mathbf{a}^T\right)^{-1} c\mathbf{a}^T = -A \tag{5.9}$$
$$\mathbf{b} = 0. \tag{5.10}$$

Note also that in this case (5.9) guarantees the existence of $\left(\mathbf{a}^T\right)^{-1}$, which we assumed above. We can now retreive $\mathbf{a}$ and c by diagonalizing A: Employing Wolfram|Alpha (n.d.) and explicitly making use of $\gamma = \frac{\beta}{3} = \frac{1}{6}$, we obtain

$$\lambda_{\pm} = \chi_N \bar{x}^{\frac{1}{6}} \frac{1}{192} \left(325 \mp \sqrt{13785}\right) \tag{5.11}$$

$$\mathbf{v}_{\pm} = \begin{pmatrix} \frac{165 \pm \sqrt{13785}}{420} \frac{N}{L} \\ 1 \end{pmatrix} \tag{5.12}$$

and (see Appendix F.1 for explicit matrices)

$$A\left(\bar{x}\right) = \chi_N \bar{x}^{\frac{1}{6}} \cdot S \cdot J \cdot S^{-1}, \tag{5.13}$$

Now, comparing (5.13) and (5.9) (assigning the minus to c) and using (F.19), we can read off

$$\mathbf{a}^T = S^{-1} \tag{5.14}$$

$$= \begin{pmatrix} 14\sqrt{\frac{15}{919}} \frac{L}{N} & \frac{1}{2}\left(1 - 11\sqrt{\frac{15}{919}}\right) \\ -14\sqrt{\frac{15}{919}} \frac{L}{N} & \frac{1}{2}\left(1 + 11\sqrt{\frac{15}{919}}\right) \end{pmatrix}, \tag{5.15}$$

yielding

$$\mathbf{a} = \begin{pmatrix} 14\sqrt{\frac{15}{919}} \frac{L}{N} & -14\sqrt{\frac{15}{919}} \frac{L}{N} \\ \frac{1}{2}\left(1 - 11\sqrt{\frac{15}{919}}\right) & \frac{1}{2}\left(1 + 11\sqrt{\frac{15}{919}}\right) \end{pmatrix}. \tag{5.16}$$

Analogue, using (F.16) and (2.46) we get

$$\begin{aligned} c &= -\chi_N \bar{x}^{\frac{1}{6}} \cdot J \\ &= -\chi_N \bar{x}^{\frac{1}{6}} \cdot \begin{pmatrix} \frac{1}{192}\left(325 - \sqrt{13785}\right) & 0 \\ 0 & \frac{1}{192}\left(325 + \sqrt{13785}\right) \end{pmatrix} \\ &= \frac{\chi_N \bar{x}^{\frac{1}{6}}}{192} \cdot \begin{pmatrix} \sqrt{13785} - 325 & 0 \\ 0 & -\sqrt{13785} - 325 \end{pmatrix} \\ &= \frac{\chi_N}{192} \left(\frac{1}{\rho_w D_v^3}\right)^{\frac{1}{6}} \left(\frac{L}{N}\right)^{\frac{1}{6}} \cdot \begin{pmatrix} \sqrt{13785} - 325 & 0 \\ 0 & -\sqrt{13785} - 325 \end{pmatrix} \\ &=: \begin{pmatrix} c_+ & 0 \\ 0 & c_- \end{pmatrix}. \end{aligned} \tag{5.17}$$

Now, we can insert our results into the Courant et al. (1952b) scheme, yielding

$$0 = A_{kl}^{1j} \left[\frac{N_{k,l+1} - N_{k,l}}{\Delta t} + C_{kl}^{j} \frac{N_{k+1,l} - N_{k,l}}{\Delta x}\right] + A_{kl}^{2j} \left[\frac{L_{k,l+1} - L_{k,l}}{\Delta t} + C_{kl}^{j} \frac{L_{k+1,l} - L_{k,l}}{\Delta x}\right], \tag{5.18}$$

where $N_{k,l} = N(z_k, t_l)$, $L_{k,l} = L(z_k, t_l)$, $A^{ij}_{kl} = a^{ij}(z_k, t_l, N_{k,l}, L_{k,l})$, $C^j_{kl} = c^j(z_k, t_l, N_{k,l}, L_{k,l})$ and $B^j_{kl} = b^j(z_k, t_l, N_{k,l}, L_{k,l})$.

Note that, as here $C^j_{kl} \leq 0$ always holds, no case distinction is necessarry. We now obtain

$$\begin{aligned} 0 = 14\sqrt{\frac{15}{919}}\frac{L_{k,l}}{N_{k,l}}\left[\frac{N_{k,l+1} - N_{k,l}}{\Delta t} + c_+(k,l)\frac{N_{k+1,l} - N_{k,l}}{\Delta x}\right] + \\ + \frac{1}{2}\left(1 - 11\sqrt{\frac{15}{919}}\right)\left[\frac{L_{k,l+1} - L_{k,l}}{\Delta t} + c_+(k,l)\frac{L_{k+1,l} - L_{k,l}}{\Delta x}\right], \end{aligned} \tag{5.19}$$

for $j = 1$ and

$$\begin{aligned} 0 = -14\sqrt{\frac{15}{919}}\frac{L_{k,l}}{N_{k,l}}\left[\frac{N_{k,l+1} - N_{k,l}}{\Delta t} + c_-(k,l)\frac{N_{k+1,l} - N_{k,l}}{\Delta x}\right] + \\ + \frac{1}{2}\left(1 + 11\sqrt{\frac{15}{919}}\right)\left[\frac{L_{k,l+1} - L_{k,l}}{\Delta t} + c_-(k,l)\frac{L_{k+1,l} - L_{k,l}}{\Delta x}\right], \end{aligned} \tag{5.20}$$

for $j = 2$.
Now, we can solve the according system of equations (for details see Appendix F.2): Adding (5.19) and (5.20), yields after inserting $c_+(k,l)$ and $c_-(k,l)$

$$L_{k,l+1} = L_{k,l}\left[1 - \frac{\Delta t}{\Delta x}\frac{\chi_N}{192}\left(\frac{1}{\rho_w D_v^3}\right)^{\frac{1}{6}}\left(\frac{L_{k,l}}{N_{k,l}}\right)^{\frac{1}{6}}\left(s_1\left(\frac{N_{k+1,l}}{N_{k,l}} - 1\right) + s_2\left(\frac{L_{k+1,l}}{L_{k,l}} - 1\right)\right)\right], \tag{5.21}$$

with

$$s_1 \coloneqq 420 \tag{5.22}$$

$$s_2 \coloneqq -490 \tag{5.23}$$

Analogue, setting

$$F \coloneqq \frac{\left(1 - 11\sqrt{\frac{15}{919}}\right)}{\left(1 + 11\sqrt{\frac{15}{919}}\right)} \tag{5.24}$$

$$s_3 \coloneqq -160 \tag{5.25}$$

$$s_4 \coloneqq -32 \tag{5.26}$$

Subtracting $F\cdot$(5.20) from (5.19) yields after multiplying with $\frac{1}{14}\sqrt{\frac{919}{15}}\frac{N_{k,l}}{L_{k,l}}\frac{1}{(1+F)}$

$$N_{k,l+1} = N_{k,l}\left(1 - \frac{\Delta t}{\Delta x}\frac{\chi_N}{192}\left(\frac{1}{\rho_w D_v^3}\right)^{\frac{1}{6}}\left(\frac{L_{k,l}}{N_{k,l}}\right)^{\frac{1}{6}}\left[s_3\left(\frac{N_{k+1,l}}{N_{k,l}} - 1\right) + s_4\left(\frac{L_{k+1,l}}{L_{k,l}} - 1\right)\right]\right). \tag{5.27}$$

Finally, we can write (5.21) and (5.27) as

$$L_{k,l+1} = L_{k,l}\left[1 - K_1\left(\frac{L_{k,l}}{N_{k,l}}\right)^{\frac{1}{6}}\left(s_1\left(\frac{N_{k+1,l}}{N_{k,l}} - 1\right) + s_2\left(\frac{L_{k+1,l}}{L_{k,l}} - 1\right)\right)\right] \tag{5.28}$$

$$N_{k,l+1} = N_{k,l}\left(1 - K_1\left(\frac{L_{k,l}}{N_{k,l}}\right)^{\frac{1}{6}}\left[s_3\left(\frac{N_{k+1,l}}{N_{k,l}} - 1\right) + s_4\left(\frac{L_{k+1,l}}{L_{k,l}} - 1\right)\right]\right), \tag{5.29}$$

with

$$K_1 = \frac{\Delta t}{\Delta x}\frac{\chi_N}{192}\left(\frac{1}{\rho_w D_v^3}\right)^{\frac{1}{6}}. \tag{5.30}$$

This equations are implemented in the following way:

$$L_{k,l+1} = L_{k,l}\left[1 - K_1 \cdot \mathrm{fac}_{LN} \cdot (s_1 \cdot \mathrm{incr}_N + s_2 \cdot \mathrm{incr}_L)\right] \tag{5.31}$$

and

$$N_{k,l+1} = N_{k,l}\left(1 - K_1 \cdot \mathrm{fac}_{LN} \cdot [s_3 \cdot \mathrm{incr}_N + s_4 \cdot \mathrm{incr}_L]\right), \tag{5.32}$$

with

$$\mathrm{fac}_{LN} = \left(\frac{L_{k,l}}{N_{k,l}}\right)^{\frac{1}{6}} \tag{5.33}$$

$$\mathrm{incr}_N = \left(\frac{N_{k+1,l}}{N_{k,l}} - 1\right) \tag{5.34}$$

$$\mathrm{incr}_L = \left(\frac{L_{k+1,l}}{L_{k,l}} - 1\right) \tag{5.35}$$

5.3 Results

We are now going to present the results of our DA experiments. We start with the experiments employing a diagonal observation error covariance matrix in Section 5.3.1, followed by those using time averaged covariances in Section 5.3.2 and the initial or final covariances in Section 5.3.3. Finally, in Section 5.3.4 we investigate the effect of only observing every second grid point.

The RMSE values are always calculated with respect to the according nature run. Note that this leads for the SPM to truth and observations being identical, which limits the validity of the according RMSE especially in the case of observing every grid point. Furthermore, all quantities are averaged over 50 experiments, to reduce noise.

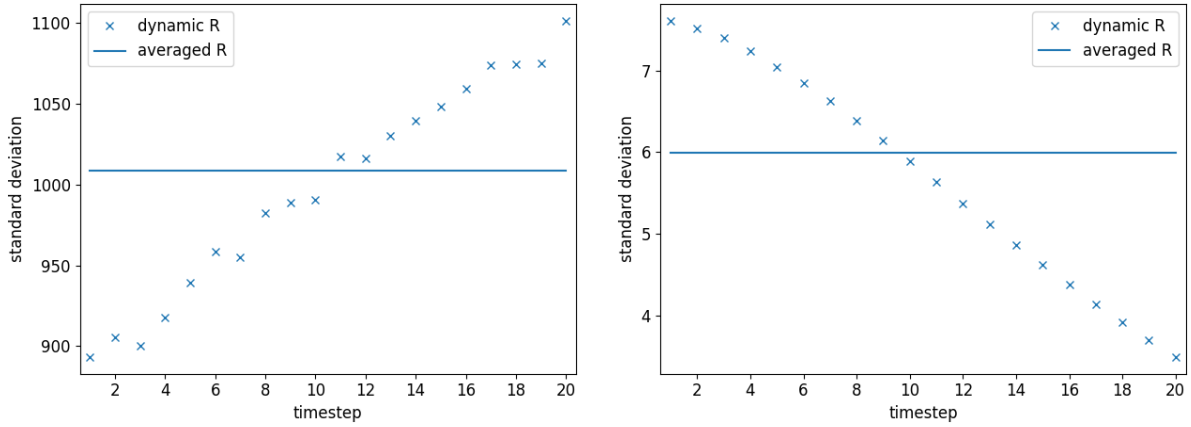

Figure 5.1: Average observation error standard deviations for N (left panel) and L (right panel) for the dynamic $\mathbf{R}$ matrices plotted against time, as well as for the time averaged $\mathbf{R}$ matrix.

To evaluate the performance of our DA algorithms, in Figure 5.1 we show the average observation error standard deviations for N and L for the dynamic $\mathbf{R}$ matrices, as well as for the time averaged $\mathbf{R}$ matrix. While we see a steady decline in the standard deviation for L over time, the standard deviation for N increases over time.

5.3.1 Dynamic observation error covariance

We start with the setup using a dynamic $\mathbf{R}$ matrix, individually calculated for the time at which the according observations are assimilated, using the methods described in Section 4.1. To investigate the effect of the spatial structure of $\mathbf{R}$ on DA, we compare the DA results obtained for the case of using the full $\mathbf{R}$ matrix, a block diagonal version ignoring the correlations between N and L, as well as a diagonal one. Furthermore, we consider either employing an unmodified EnKF, or smoothing the ensemble after evolution with

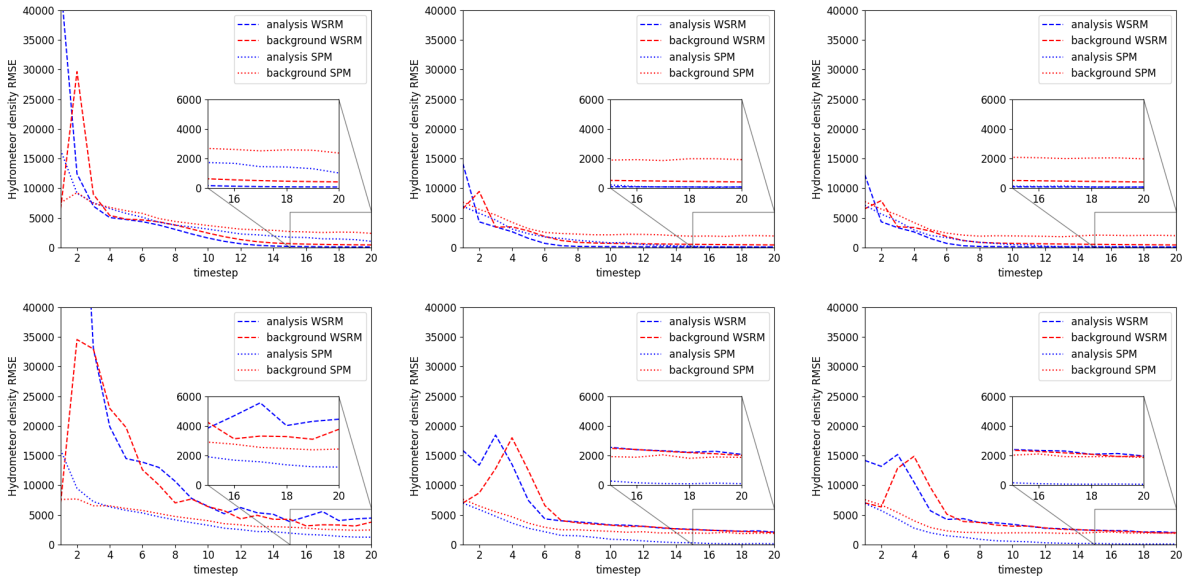

Figure 5.2: RMSE-values (averaged over 50 experiments) for DA of N with a time stepping of $5 \times 0.0002s$. DA is carried out using the full analytic (left panel), block diagonal (middle panel) or diagonal (right panel) time dependent covariance matrix, with (upper panel) and without smoothing of the ensemble (lower panel). The SPM (dotted line) and the WSRM (dashed line) are used as truth.

the Wacker and Seifert (2001) two-moment scheme by applying a running average (equally weighting all values within a range of 5 grid points). The according RMSE values (averaged over 50 experiments) of background and analysis for N and L in the SPM and WSRM scenario[3] are shown in Figure 5.2 and Figure 5.3. The initial RMSE of the analysis for N in the WSRM scenario reaches values of over 40000 when smoothing is applied and over 100000 without smoothing and thus lies outside of the plot range.

First, we note that the filter converges in all experiments. The speed of convergence however differs significantly between the different setups. Smoothing practically does not affect the RMSE in the SPM scenario in all cases for both N and L. In the WSRM scenario, however we see a significantly improved performance for both variables and all possible choices of $\mathbf{R}$, when smoothing is enabled. Furthermore, in the unmodified case, the performance in the WSRM scenario is always worse than that in the SPM scenario. When smoothing is applied however, no clear pattern can be seen. Due to its positive effect in the WSRM scenario, in the subsequent experiments, we are going to employ smoothing after evolution.

When comparing the full, block diagonal and diagonal $\mathbf{R}$ matrices in Figure 5.2 and Fig-

[3]To improve readability of the text, we speak of *scenarios* when comparing the results for the different truth runs, while we speak of *cases* when distinguishing between experiments employing different $\mathbf{R}$ matrices.

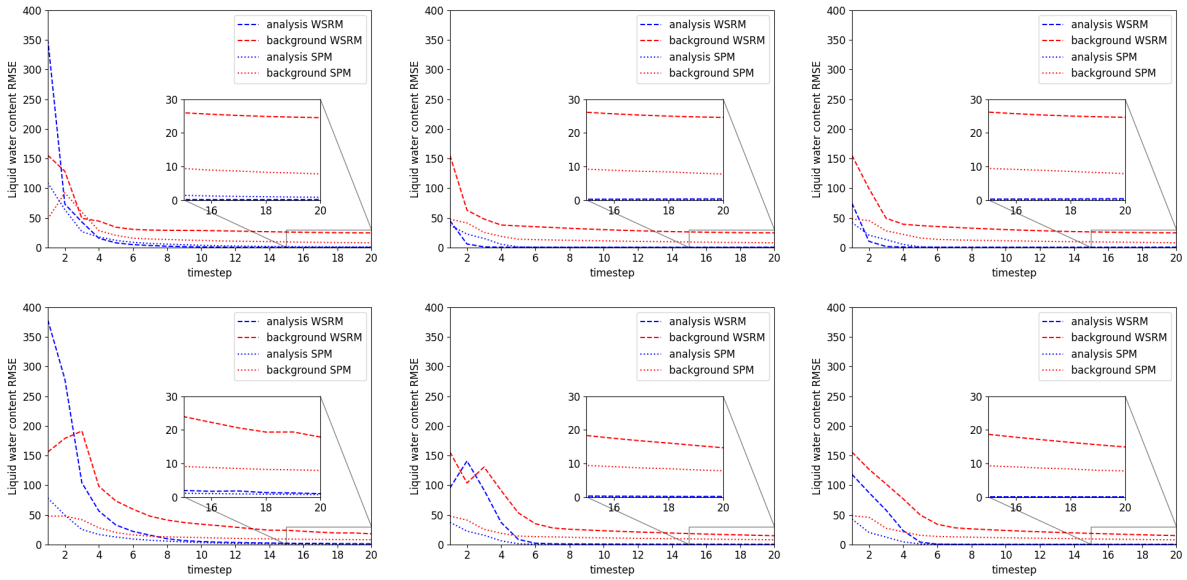

Figure 5.3: RMSE-values (averaged over 50 experiments) for DA of L with a time stepping of $5 \times 0.0002s$. DA is carried out using the full analytic (left panel), block diagonal (middle panel) or diagonal (right panel) time dependent covariance matrix, with (upper panel) and without smoothing of the ensemble (lower panel). The SPM (dotted line) and the WSRM (dashed line) are used as truth.

ure 5.3, the worst performance for N and L is obtained when using the full $\mathbf{R}$ matrix in both the WSRM and SPM scenario, while the diagonal and block diagonal $\mathbf{R}$ perform similarly. When using smoothing, in the final steps for the block diagonal and diagonal case, the RMSE for the analysis of both quantities is significantly below the according average observation error standard deviations. However, the background RMSE remains clearly above the average observation error standard deviations for L in the WSRM scenario and for N in both scenarios.

To evaluate whether the uncertainty of the analysis is estimated correctly in our DA experiments, we are showing the spread of the analysis ensemble in Figure 5.4 for N and in Figure 5.5 for L, as well as the according spread ratio (RMSE-values divided by ensemble spread) in Figure 5.6 for N and in Figure 5.7 for L. The initial spread ratios in the WSRM scenario reaches values of over 2500 for N and over 350 for L when smoothing is applied and over 5000 for N and over 350 for L without smoothing and thus lie outside of the plot range.

In all cases (except for initial peaks in the unmodified EnKF in the WSRM scenario), the spread initially is extremely low, but approaches a constant value over time (for N there remains a slow increase for the unmodified EnKF in the WSRM scenario). This is likely caused by large portions of both profiles becoming negative in the first analysis and being set to a constant value, significantly reducing the ensemble spread. As the EnKF tries

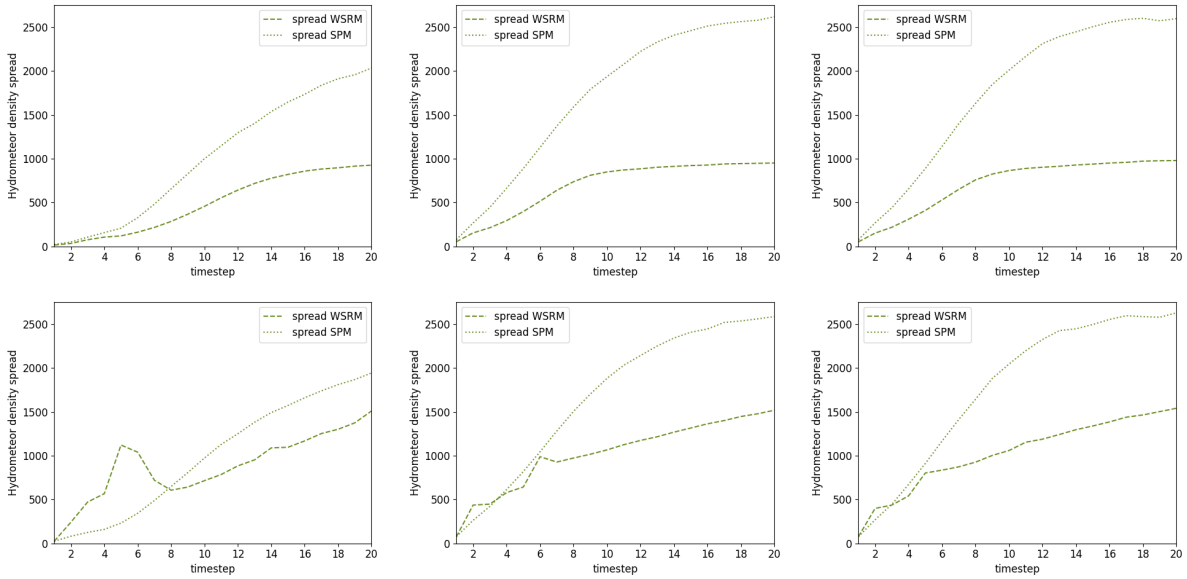

Figure 5.4: Ensemble spread (averaged over 50 experiments) for DA of N with a time stepping of $5 \times 0.0002s$. DA is carried out using the full analytic (left panel), block diagonal (middle panel) or diagonal (right panel) time dependent covariance matrix, with (upper panel) and without smoothing of the ensemble (lower panel). The SPM (dotted line) and the WSRM (dashed line) are used as truth.

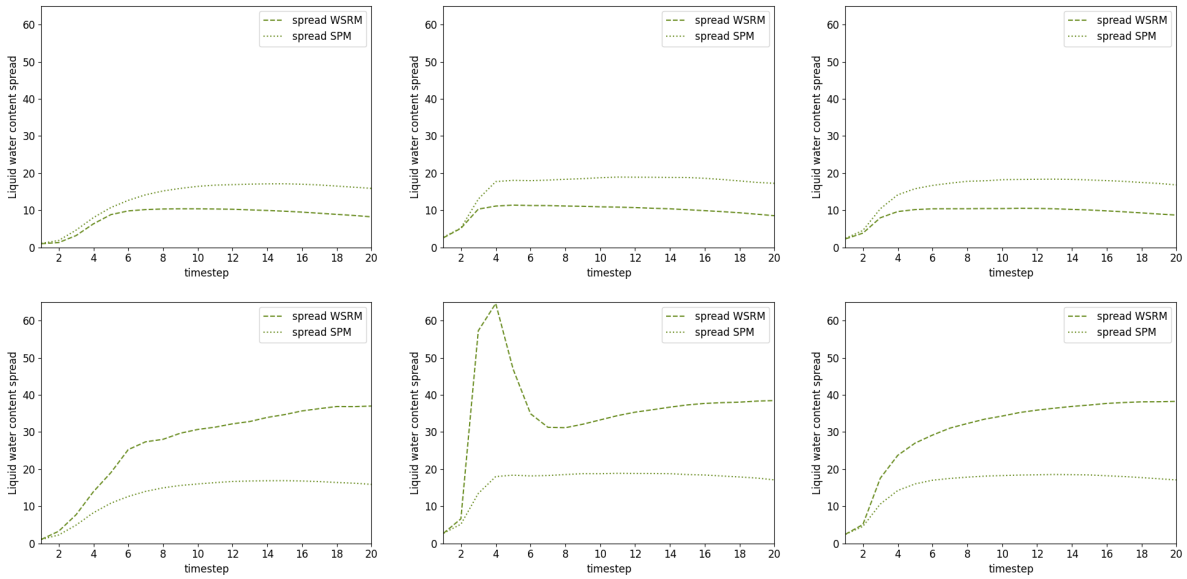

Figure 5.5: Ensemble spread (averaged over 50 experiments) for DA of L with a time stepping of $5 \times 0.0002s$. DA is carried out using the full analytic (left panel), block diagonal (middle panel) or diagonal (right panel) time dependent covariance matrix, with (upper panel) and without smoothing of the ensemble (lower panel). The SPM (dotted line) and the WSRM (dashed line) are used as truth.

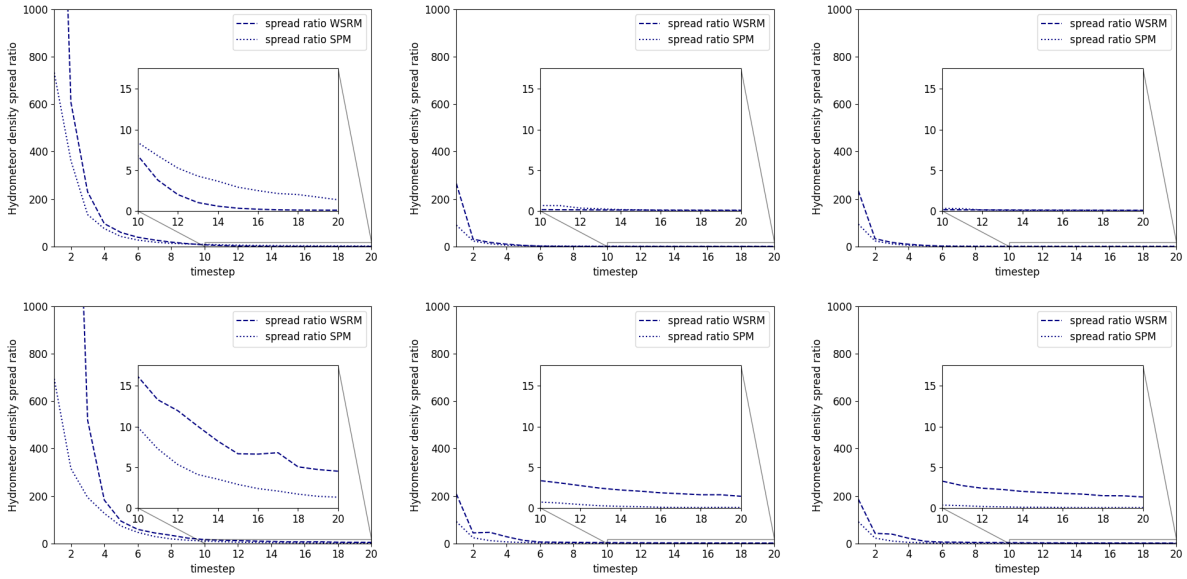

Figure 5.6: Spread ratio (averaged over 50 experiments) for DA of N with a time stepping of $5 \times 0.0002s$. DA is carried out using the full analytic (left panel), block diagonal (middle panel) or diagonal (right panel) time dependent covariance matrix, with (upper panel) and without smoothing of the ensemble (lower panel). The SPM (dotted line) and the WSRM (dashed line) are used as truth.

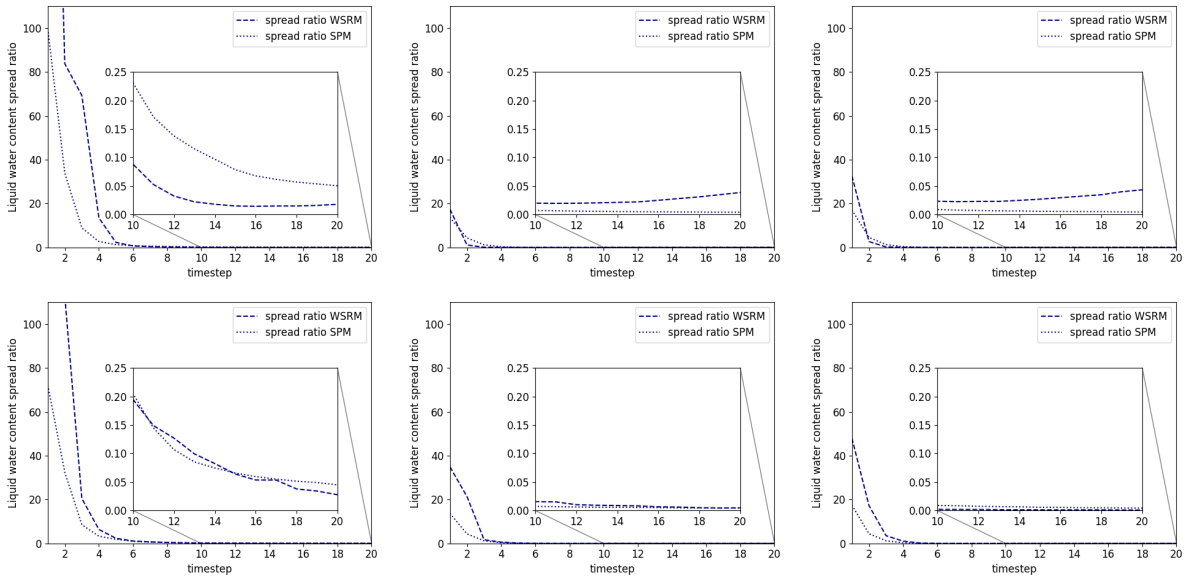

Figure 5.7: Spread ratio (averaged over 50 experiments) for DA of L with a time stepping of $5 \times 0.0002s$. DA is carried out using the full analytic (left panel), block diagonal (middle panel) or diagonal (right panel) time dependent covariance matrix, with (upper panel) and without smoothing of the ensemble (lower panel). The SPM (dotted line) and the WSRM (dashed line) are used as truth.

to compensate this, the spread increases again over time. This is in agreement with the findings of Gleiter et al. (2022) who encountered the same issue in their experiments with their skeleton model of the Madden-Julian oscillation. However, in their case it even led to a divergence of the filter, while it still converges in our experiments.

The spread ratios start with relatively high values and decrease fast in all cases for both scenarios. For N the initial spread ratios are lower for the SPM scenario in all cases, however this changes over time in some cases. For L, no clear picture is seen. The final spread ratios are (except for the full case) very low. Furthermore (again excluding the full case), in the WSRM scenario smoothing improves the spread ratio for N at the cost of deteriorating that of L in a similar magnitude. Also when smoothing is applied, the spread ratio starts to slightly increase again in the later time steps, for all cases in the WSRM scenario.

As for the RMSE, the ensemble spread and the spread ratio are not noticeably affected by smoothing of the ensemble in the SPM scenario. In the WSRM scenario, smoothing of the ensemble removes the initial peaks in the spread and significantly reduces the spread for L. For N, the effect is weaker, however smoothing now leads to the spread clearly approaching a constant. Without smoothing, the spread is always higher in the SPM than in the WSRM scenario. However, smoothing of the ensemble reverses the situation for L. The spread ratios converge to zero for both variables in all scenarios. This might be caused by extremely low RMSEs obtained due to the relatively small error variances and observing every grid point.

To better understand the these results, in Figure 5.8 and Figure 5.9 we show a series of snapshots for the profiles of N and L taken at the time steps 1, 3 and 10 for a run of the DA experiment, using the full $\mathbf{R}$ matrix and employing smoothing of the ensemble. The time steps are selected to depict the initial situation, the time when the filter starts to converge and a later time step, where the filter is relatively stable. In the run investigated, the RMSE values (not shown) of the analysis for N are higher than that of the background till time step 3 in the SPM scenario and at the timesteps 1 and 4 in the WSRM scenario. Furthermore, in the SPM scenario, the RMSE values (not shown) of the analysis for L are higher than that of the background till time step 3.

In the first time step, the analysis takes values below -40000 for N and values below -200 as well as above 300 for L, in the SPM scenario. In the WSRM scenario, the analysis takes values above 150000 for N and above 600 for L. All these values lie outside the plot range. Note also, that the large underestimation of N at the top of the domain is (despite continuous improvements over time) not fully corrected even at time step 20 (not shown). This is likely caused by the filter prioritizing the minimization of the error in L, which results in initial errors in N being corrected only very slowly.

In the first time step, we see the analysis for N becoming (strongly) negative over large

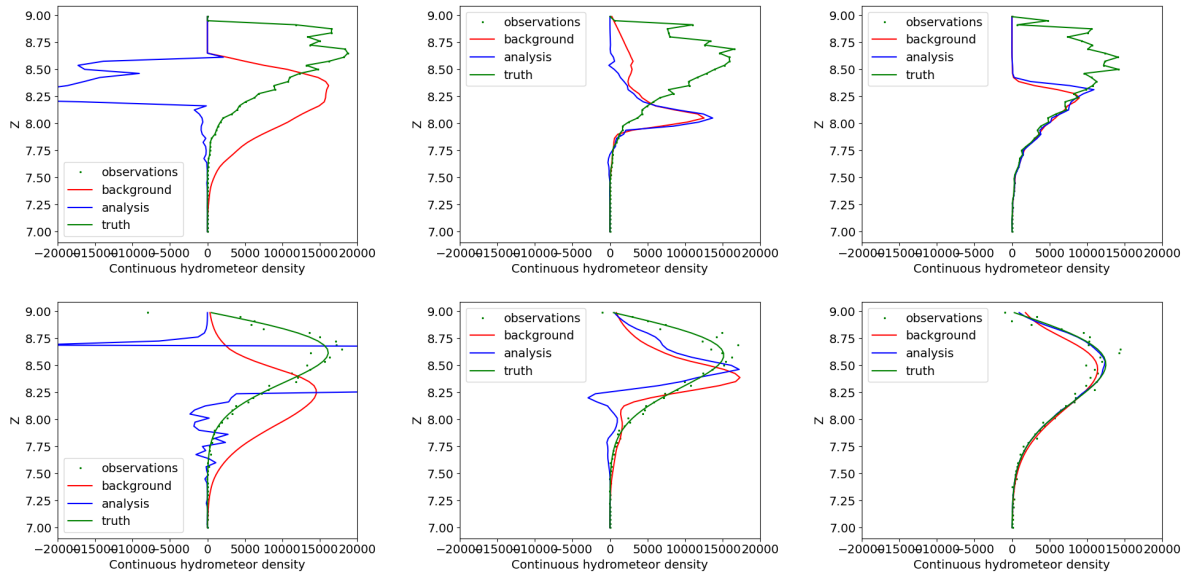

Figure 5.8: Example snapshots of the profiles of N at time steps 1, 3 and 10 for a DA experiment using the setup of Figure 5.2 and Figure 5.3, using the full $\mathbf{R}$ matrix and employing smoothing, with the nature run generated by the SPM (upper panel) and the WSRM (lower panel).

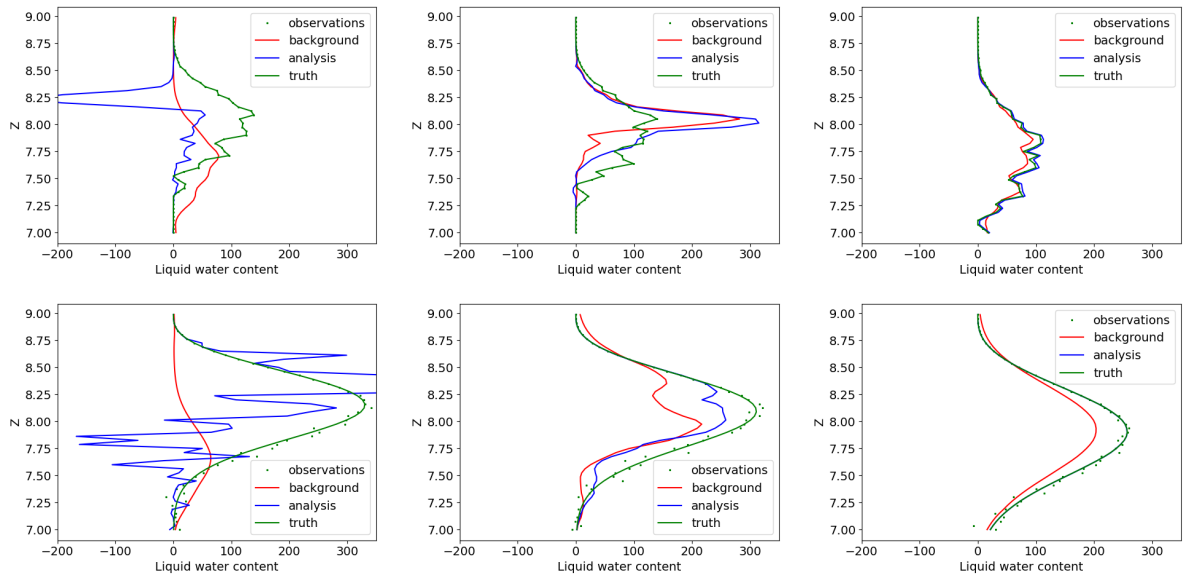

Figure 5.9: Example snapshots of the profiles of L at time steps 1, 3 and 10 for a DA experiment using the setup of Figure 5.2 and Figure 5.3, using the full $\mathbf{R}$ matrix and employing smoothing, with the nature run generated by the SPM (upper panel) and the WSRM (lower panel).

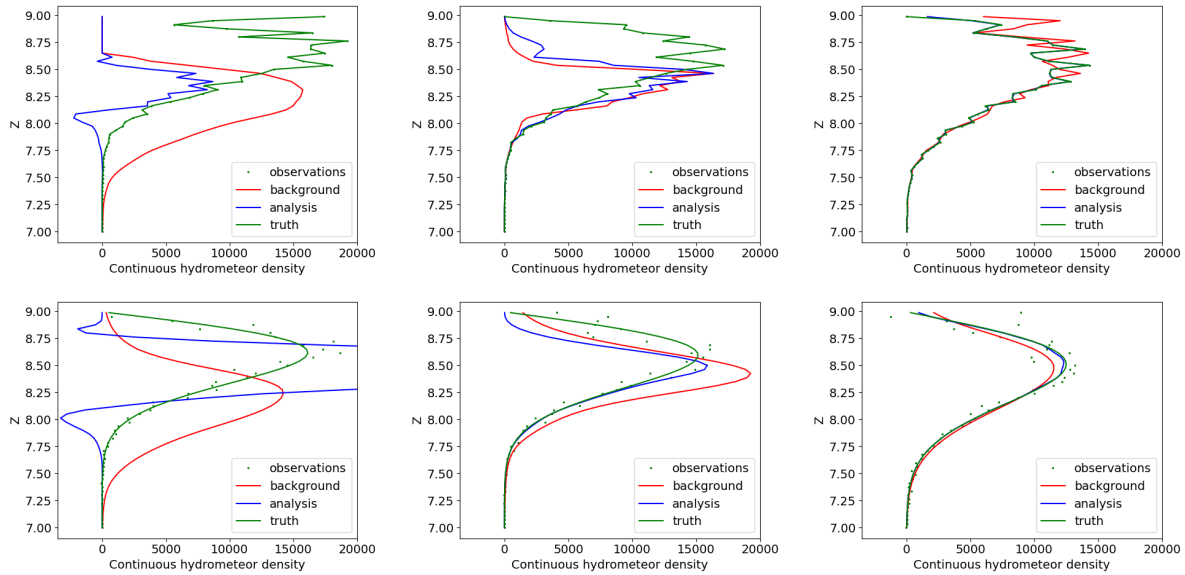

Figure 5.10: Example snapshots of the profiles of N at time steps 1, 3 and 10 for a DA experiment using the setup of Figure 5.2 and Figure 5.3, with the diagonal $\mathbf{R}$ matrix and employing smoothing, with the nature run generated by the SPM (upper panel) and the WSRM (lower panel).

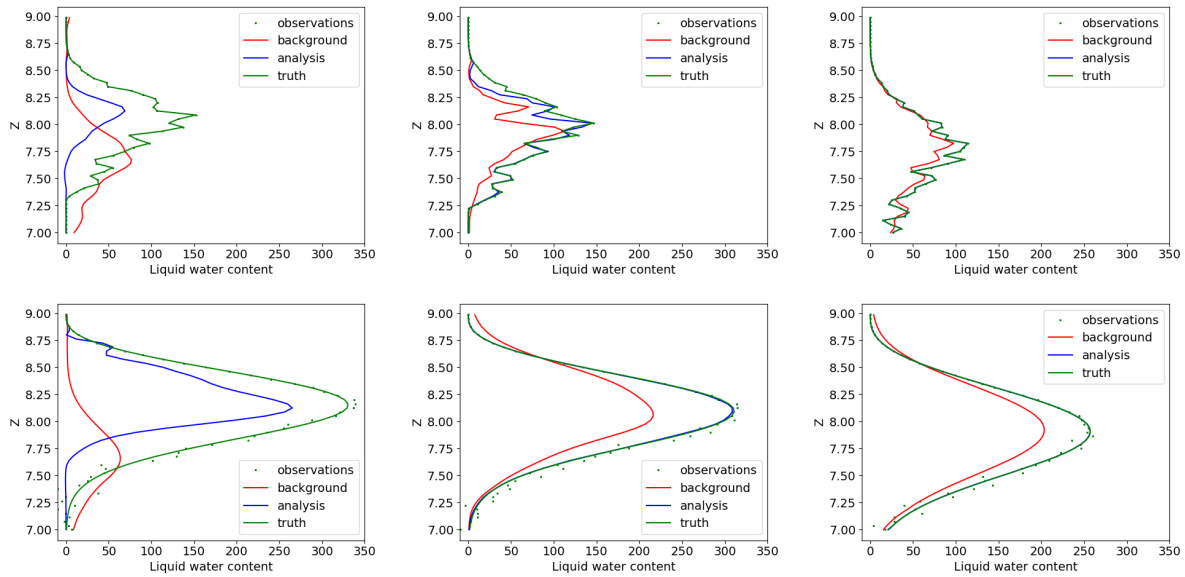

Figure 5.11: Example snapshots of the profiles of L at time steps 1, 3 and 10 for a DA experiment using the setup of Figure 5.2 and Figure 5.3, with the diagonal $\mathbf{R}$ matrix and employing smoothing, with the nature run generated by the SPM (upper panel) and the WSRM (lower panel).

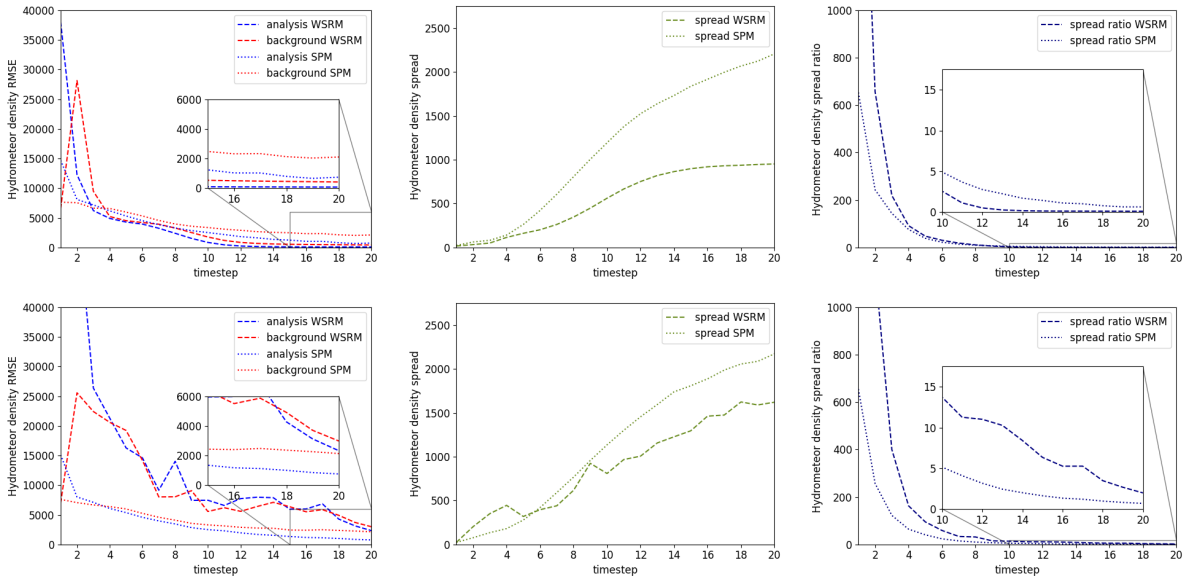

Figure 5.12: RMSE-values (left panel), Ensemble spread (middle panel) and spread ratio (right panel) for DA of N (averaged over 50 experiments) with time stepping of $5 \times 0.0002s$. DA is carried out using the full analytic time dependent covariance matrix, with (upper panel) and without smoothing of the ensemble (lower panel), using multiplicative inflation by a factor of 1.2. The SPM (dotted line) and the WSRM (dashed line) are used as truth.

parts of the profile in the SPM scenario, while in the WSRM scenario we see negative values at a smaller percentage of the grid points and a large peak with extremely large values. For L, we see a similar picture, but in less extreme form and the analysis in the WSRM scenario already shows a slight tendency to approach the truth. This corroborates our previous hypothesis of negative analysis values (like in Gleiter et al. (2022)) being responsible for the initially very small ensemble spread.

As in a similar run employing a diagonal (Figure 5.10 and Figure 5.11) or block diagonal (not shown) $\mathbf{R}$ matrix a negative analysis only occurs at very few grid points, this problem is likely caused by correlations especially those between L and N. This also explains the slightly higher initial ensemble spreads found in the diagonal and block diagonal cases when compared to that employing a full $\mathbf{R}$ matrix. Note however, that there is a degree of randomness in these experiments, somewhat limiting the significance of snapshots from a single run. Note also that in general the L-profiles tend to approach the truth a little faster than the N-profiles. This agrees with the observation that the RMSE values also seem to decrease faster for L than for N.

We also repeat our experiment for the full $\mathbf{R}$ matrix employing multiplicative inflation by a factor of 1.2. However, besides removing the large peak in the ensemble spread of L for the WSRM scenario without smoothing (see Figure 5.12), it has no significant effects

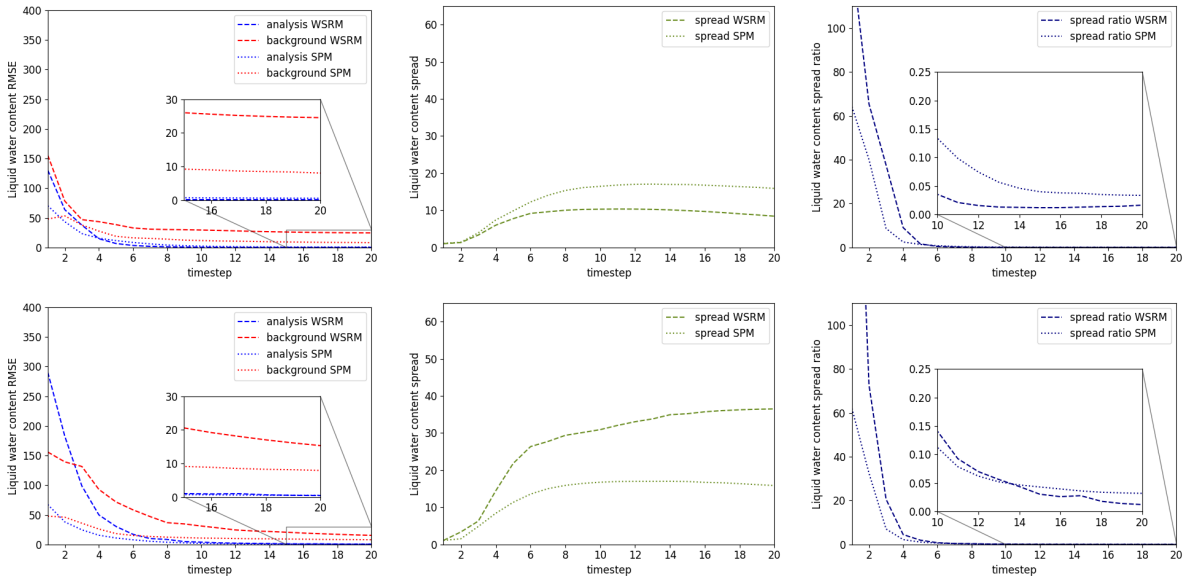

Figure 5.13: RMSE-values (left panel), Ensemble spread (middle panel) and spread ratio (right panel) for DA of L (averaged over 50 experiments) with time stepping of $5 \times 0.0002s$. DA is carried out using the full analytic time dependent covariance matrix, with (upper panel) and without smoothing of the ensemble (lower panel), using multiplicative inflation by a factor of 1.2. The SPM (dotted line) and the WSRM (dashed line) are used as truth.

(see Figure 5.13). Thus we will not use inflation in the further experiments. We also do not implement localization, which is often used to reduce the effect of observations on far away grid points and combat harmful effects of spurious correlations, as sufficient results are obtained without it.

Furthermore, we repeat our experiment applying an absolute value to the (Gaussian distributed) observations in the WSRM scenario (plots not shown). In the diagonal and block-diagonal $\mathbf{R}$ case, there are no differences seen to the unmodified experiments, while in the full $\mathbf{R}$ case higher initial RMSE values are found in the modified experiment, especially for the number density. However, the experiments in the full $\mathbf{R}$ case converge in general relatively slow and the difference between the modified and unmodified WSRM scenario might (due to the relatively small sample size of 50 experiments) be explained by numerical noise. Thus issues encountered during the assimilation of non-negative quantities can likely rather be attributed to the need for enforcing the positivity of the analysis before applying the model for time evolution, than to the non-Gaussianity of the observation errors. Though the modified WSRM scenario is more realistic than the unmodified one, the non-Gaussian distributed pseudo-observation violate an important condition of the EnKF. As the additional truth run employing the WSRM scenario is intended to stay as close as possible to the assumptions of the DA algorithm, we will not employ this modification in the further experiments. We will also forego measures like thresholding or

discarding negative pseudo-observations, which would introduce non-Gaussian distributed pseudo-observations or impede comparability to the SPM scenario by assimilating a different number of pseudo-observations.

In general, the strong difference between the SPM and WSRM scenario with regard to smoothing might indicate that using OSSEs for estimating the usefulness of DA algorithms (or of modifications thereof) in practical applications can be problematic. This is especially the case, if the nature run is not able to completely resolve the according processes (which usually is the case).

5.3.2 Time averaged observation error covariance

We repeat the experiments shown above, using time averaged $\mathbf{R}$ matrices. The according full $\mathbf{R}$ matrix is obtained by averaging the (full) $\mathbf{R}$ matrices used above over all time steps at which observations are assimilated. Subsequently, the block diagonal and diagonal $\mathbf{R}$ matrices are extracted as previously.

In Figure 5.14, the RMSE values (averaged over 50 experiments) of background and analysis for N and L in the SPM and WSRM scenario are shown. The initial RMSE of the analysis in the SPM scenario reaches values of over 2500000 for N and over 800 for L and thus lies outside of the plot range.

In Figure 5.14, we see (with exception of an increase of the analysis RMSE of N in the WSRM scenario with full $\mathbf{R}$ until time step 10) convergence of the filter in all experiments. However (despite the final RMSE values being inconclusive), in comparison to the experiments using a dynamic $\mathbf{R}$, we see significantly higher initial errors, especially when employing full $\mathbf{R}$. Afrer 20 time steps, the errors become more similar to that obtained when using a dynamic $\mathbf{R}$, though they still are is still slightly higher. This indicates that accounting for spatial correlations of $\mathbf{R}$, while ignoring its temporal variations can (especially in the beginning) have a strongly negative effect on DA. The relative good performance in the WSRM scenario is owed to smoothing of the ensemble and repeating the experiment without smoothing results in extremely bad performance (not shown). Again, in the final steps for the block diagonal and diagonal case, the RMSE for the analysis of both quantities is below the according average observation error standard deviations. However, the background RMSE remains clearly above the average observation error standard deviations for L in the WSRM scenario and for N in both scenarios. Furthermore, comparing the final steps to the experiments using a dynamic $\mathbf{R}$ matrix, we find a similar performance for L, while the time averaged $\mathbf{R}$ matrix performs slightly worse for N (except for the background in the SPM scenario).

The ensemble spread shown in Figure 5.15 behaves similar to the previous experiments using a dynamic $\mathbf{R}$. The spread ratios shown in Figure 5.16 are (with exception of N in the diagonal $\mathbf{R}$ case) generally higher than in the dynamic $\mathbf{R}$ case. Especially when using

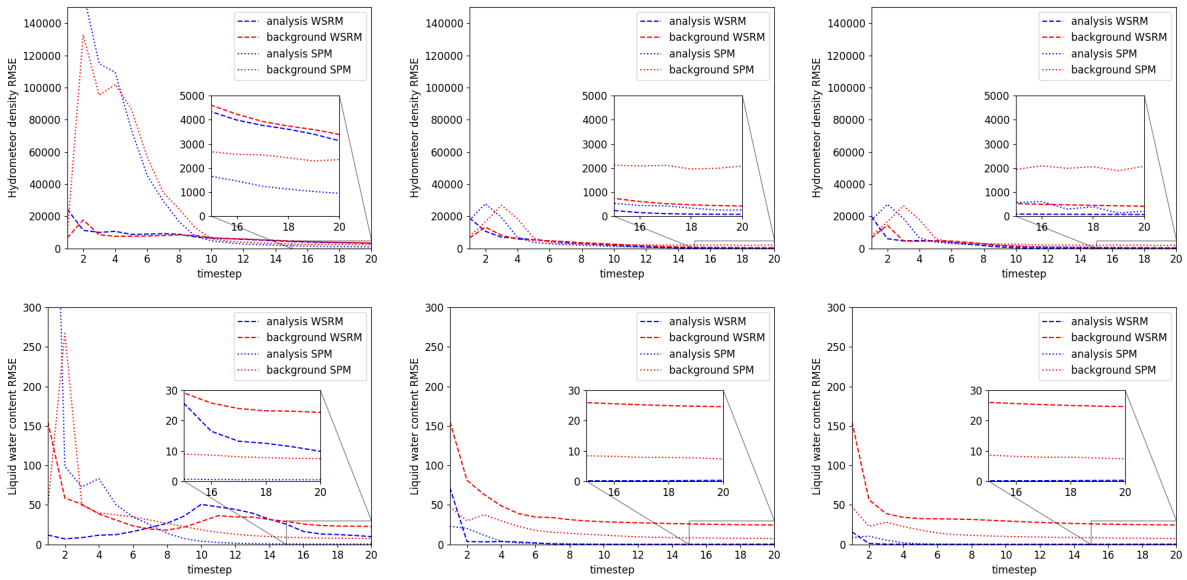

Figure 5.14: RMSE-values (averaged over 50 experiments) for DA of N (upper panel) and L (lower panel) with a time stepping of $5 \times 0.0002s$. DA is carried out using the full analytic (left panel), block diagonal (middle panel) or diagonal (right panel) time averaged covariance matrix. The SPM (dotted line) and the WSRM (dashed line) are used as truth.

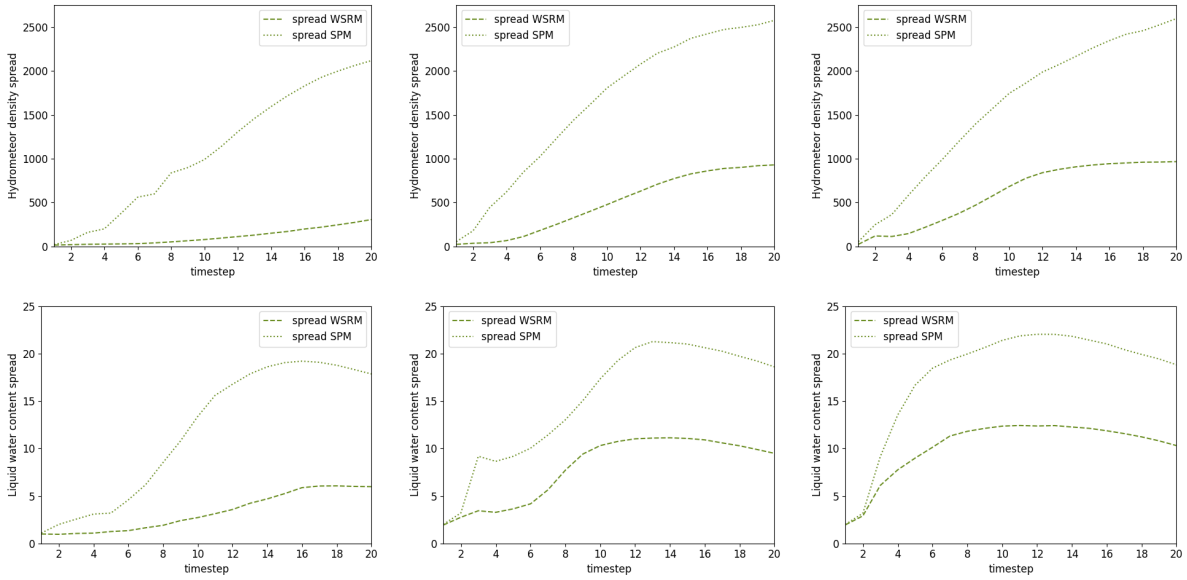

Figure 5.15: Ensemble spread (averaged over 50 experiments) for DA of N (upper panel) and L (lower panel) with a time stepping of $5 \times 0.0002s$. DA is carried out using the full analytic (left panel), block diagonal (middle panel) or diagonal (right panel) time averaged covariance matrix. The SPM (dotted line) and the WSRM (dashed line) are used as truth.

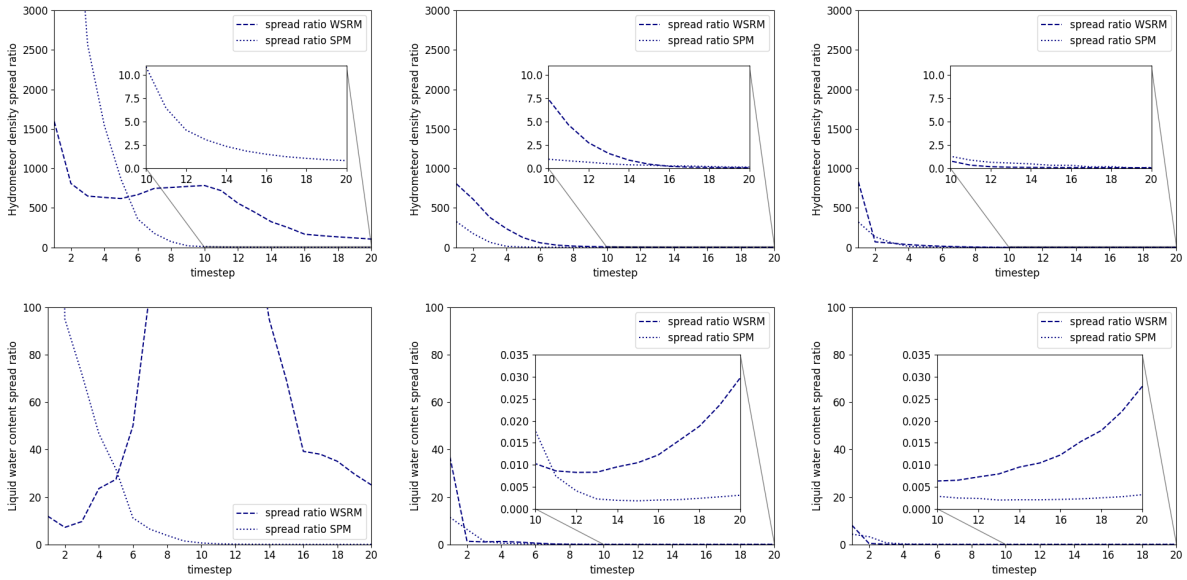

Figure 5.16: Spread ratio (averaged over 50 experiments) for DA of N (upper panel) and L (lower panel) with a time stepping of $5 \times 0.0002s$. DA is carried out using the full analytic (left panel), block diagonal (middle panel) or diagonal (right panel) time averaged covariance matrix. The SPM (dotted line) and the WSRM (dashed line) are used as truth.

full $\mathbf{R}$ in the WSRM scenario, extremely high values are obtained (that for L strongly increase till time step 10), which despite eventually decreasing over time indicate a severe underestimation of uncertainty by the ensemble during the entire timespan. The initial spread ratio in the SPM scenario reaches values of over 12000 for N and over 800 for L and thus lies outside of the plot range. Furthermore, in the SPM scenario, the spread ratio for L rises above 350, leaving the plot range. Also note that in the diagonal and block diagonal case, the spread ratio starts to slightly increase in the later time steps for the WSRM scenario. This behaviour is similar to that observed in the experiments using dynamic $\mathbf{R}$ without smoothing.

When looking at exemplaric snapshots of the profiles (not shown), we see similar problems as in the previous experiments, however to a much larger extent. When using full $\mathbf{R}$, the initial negative values now can attain absolute values many times larger than the peak of the true profile. Furthermore, in this case some profiles show a strong deviation from the truth even in the final time steps. In the diagonal case, these problems are way smaller, however the profiles still approach the truth slower than when using dynamic $\mathbf{R}$. Note again, that snapshots only provide limited informative value due to the large variations between experiments.

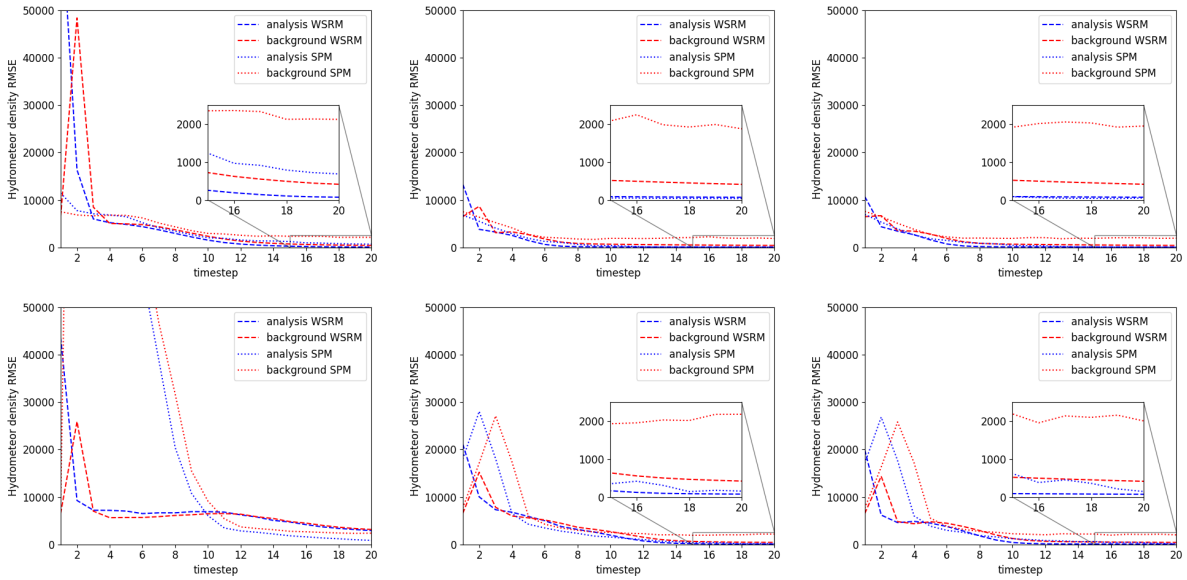

Figure 5.17: RMSE-values (averaged over 50 experiments) for DA of N with a time stepping of $5 \times 0.0002s$. DA is carried out using the full analytic (left panel), block diagonal (middle panel) or diagonal (right panel) covariance matrix calculated for the initial (upper panel) or final (lower panel) time step, with smoothing of the ensemble. The SPM (dotted line) and the WSRM (dashed line) are used as truth.

5.3.3 Initial and final observation error covariance

We repeat the experiments shown previously, using the $\mathbf{R}$ matrix employed above for the initial or final time step. The according block diagonal and diagonal $\mathbf{R}$ matrices are obtained as above. We note that in practical applications compared to time averaging or using dynamic $\mathbf{R}$ matrices, this is computationally much cheaper, as the according $\mathbf{R}$ matrix only needs to be estimated for a single time step.

The according RMSE values are shown in Figure 5.17 for N and in Figure 5.18 for L. In the initial $\mathbf{R}$ setup for the WSRM scenario, the initial RMSE of the analysis reaches values of over 70000 for N and over 800 for L and the RMSE of the background reaches values of almost 1000 for L in the second time step. Furthermore, in the final $\mathbf{R}$ setup for the SPM scenario, the initial RMSE of the analysis reaches values of almost 400000 for N and almost 800 for L and the RMSE of the background reaches values of almost 200000 for N. All these values lie outside of the plot range.

We again see convergence for all setups, cases, scenarios and variables. However, for the final $\mathbf{R}$ setup using full $\mathbf{R}$, convergence is very slow for N in the SPM scenario and for L in the WSRM scenario the analysis RMSE increases again between time step 4 and 10 to slowly drop again. As in the previous experiments, using full $\mathbf{R}$ always yields the worst results, while block diagonal and diagonal $\mathbf{R}$ matrices perform similarly. Furthermore, using

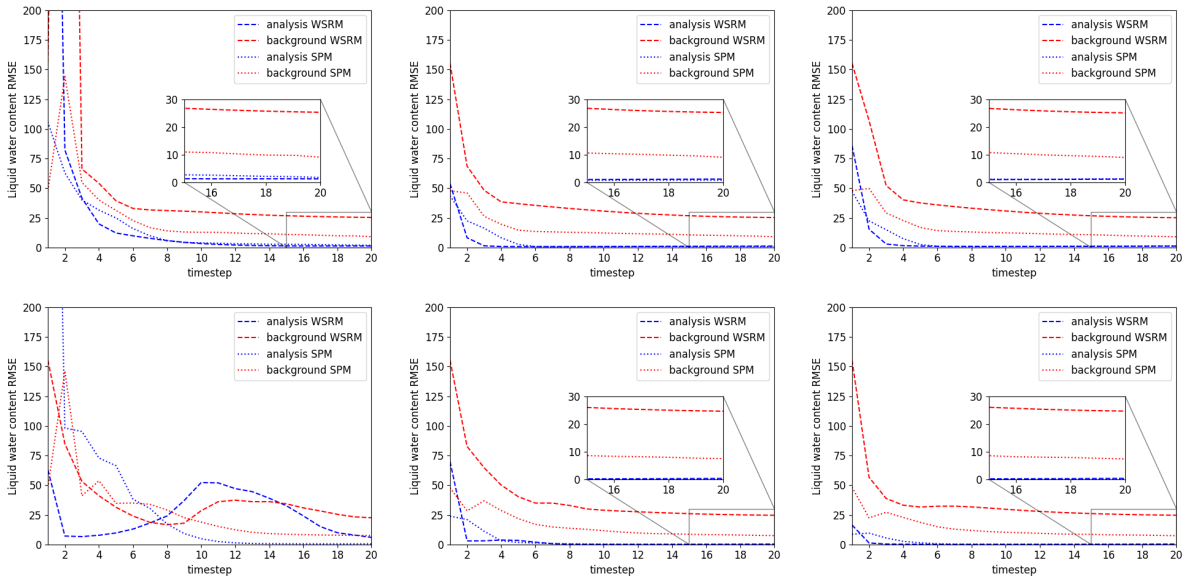

Figure 5.18: RMSE-values (averaged over 50 experiments) for DA of L with a time stepping of $5 \times 0.0002s$. DA is carried out using the full analytic (left panel), block diagonal (middle panel) or diagonal (right panel) covariance matrix calculated for the initial (upper panel) or final (lower panel) time step, with smoothing of the ensemble. The SPM (dotted line) and the WSRM (dashed line) are used as truth.

the initial $\mathbf{R}$ matrix always results in better outcomes than using the final $\mathbf{R}$ matrix. This is especially the case for the initial time steps, while the difference vanishes in the last steps. This might hint to correctly specifying $\mathbf{R}$ being especially important when the background differs strongly from the truth and an almost converged filter being better able to deal with misspecified $\mathbf{R}$. Furthermore, the final RMSE values in general are comparable to that obtained in the setup using a time averaged $\mathbf{R}$ matrix. Thus the additional overhead of this method does not pay off. In general, all tested methods employing a constant $\mathbf{R}$ matrix perform suboptimally and there might not be an optimal choice for a constant $\mathbf{R}$. Thus (if possible) using a dynamic $\mathbf{R}$ is strongly advisable.

The according ensemble spread is shown for N in Figure 5.19 and for L in Figure 5.20. It behaves relatively similar to the previous experiments without any peculiarities.
The according spread ratios are shown for N in Figure 5.21 and for L in Figure 5.22. In the initial $\mathbf{R}$ setup for the WSRM scenario, the initial spread ratio reaches values of over 4000 for N and over 800 for L. In the final $\mathbf{R}$ setup for the WSRM scenario, the spread ratio initial assumes values of over 2500 for N and reaches a peak over 300 for L at time step 10, while in the SPM scenario it initially assumes values of almost 20000 for N and of over 700 for L. All these values lie outside of the plot range.

We see generally higher spread ratios when using full $\mathbf{R}$ matrices, when compared to block

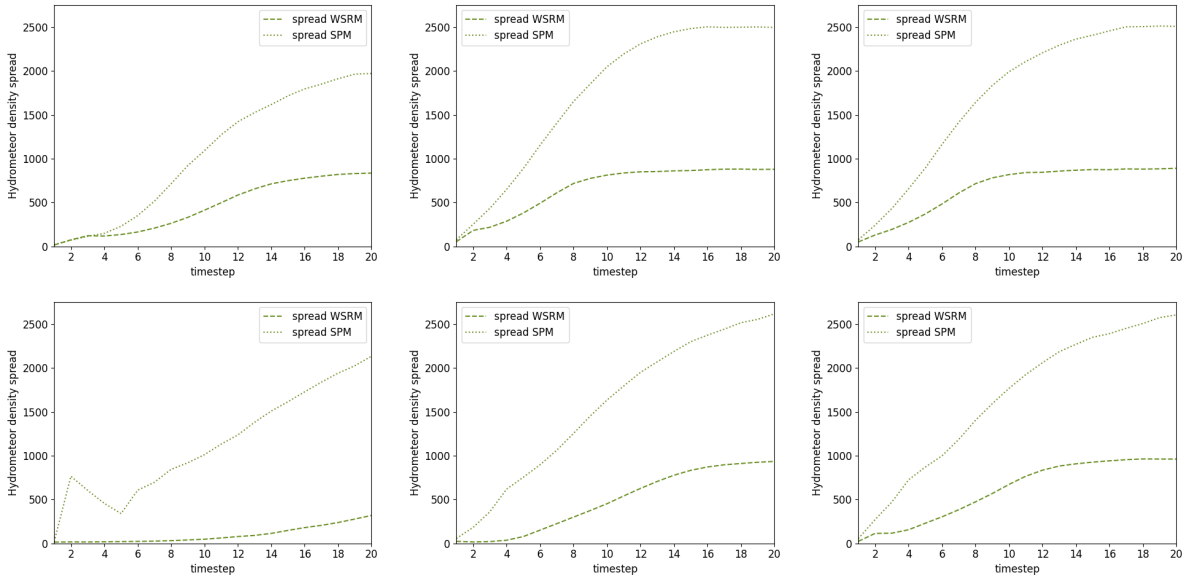

Figure 5.19: Ensemble spread (averaged over 50 experiments) for DA of N with a time stepping of $5 \times 0.0002s$. DA is carried out using the full analytic (left panel), block diagonal (middle panel) or diagonal (right panel) covariance matrix calculated for the initial (upper panel) or final (lower panel) time step, with smoothing of the ensemble. The SPM (dotted line) and the WSRM (dashed line) are used as truth.

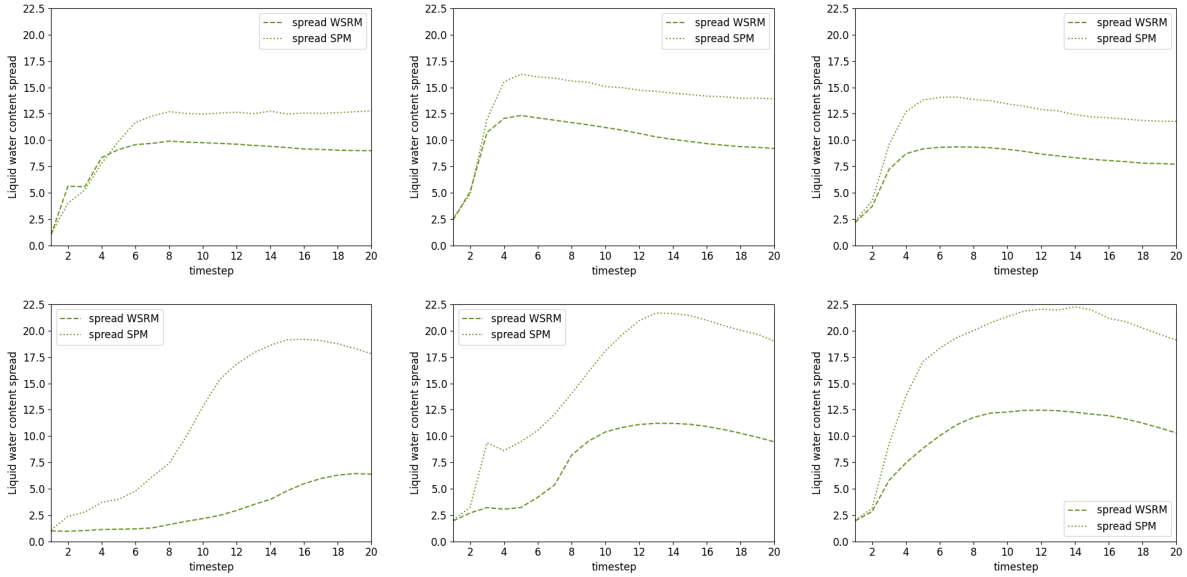

Figure 5.20: Ensemble spread (averaged over 50 experiments) for DA of L with a time stepping of $5 \times 0.0002s$. DA is carried out using the full analytic (left panel), block diagonal (middle panel) or diagonal (right panel) covariance matrix calculated for the initial (upper panel) or final (lower panel) time step, with smoothing of the ensemble. The SPM (dotted line) and the WSRM (dashed line) are used as truth.

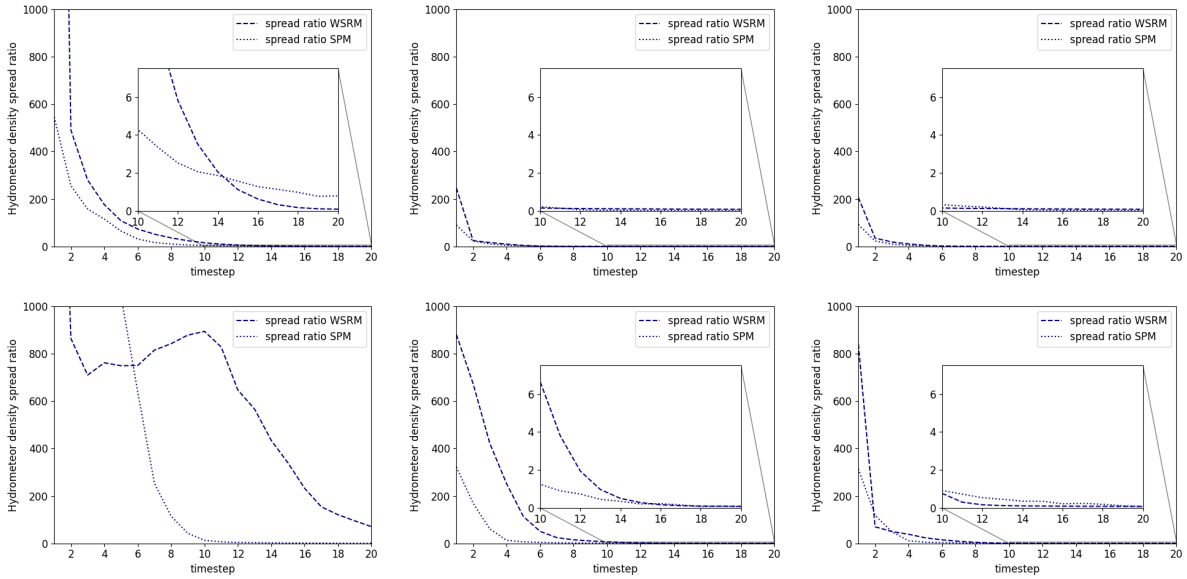

Figure 5.21: Spread ratios (averaged over 50 experiments) for DA of N with a time stepping of $5 \times 0.0002s$. DA is carried out using the full analytic (left panel), block diagonal (middle panel) or diagonal (right panel) covariance matrix calculated for the initial (upper panel) or final (lower panel) time step, with smoothing of the ensemble. The SPM (dotted line) and the WSRM (dashed line) are used as truth.

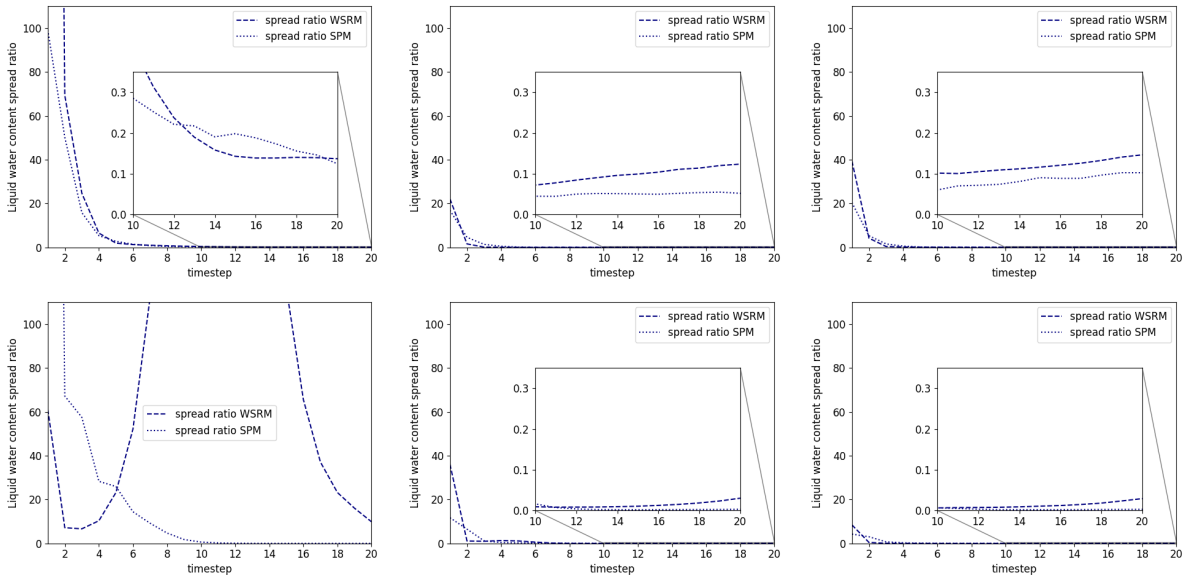

Figure 5.22: Spread ratios (averaged over 50 experiments) for DA of L content with a time stepping of $5 \times 0.0002s$. DA is carried out using the full analytic (left panel), block diagonal (middle panel) or diagonal (right panel) covariance matrix calculated for the initial (upper panel) or final (lower panel) time step, with smoothing of the ensemble. The SPM (dotted line) and the WSRM (dashed line) are used as truth.

diagonal or diagonal **R**, though results for the final time steps are inconclusive. Also, in the block diagonal and diagonal case very low spread ratios are achived in the later steps. However spread ratios for L start to slightly increase towards the later time steps, especially in the WSRM scenario. In the initial **R** setup we generally obtain lower spread ratios, than in the final **R** setup, substantiating the better performance of the initial **R** setup.

With respect to the options considered up to now, the previous results seem to indicate that the EnKF copes relatively well with a single suboptimal choice, while multiple problematic choices strongly deteriorate the results. So foregoing smoothing or time averaging the **R** matrix had the strongest negative impact on the RMSE values, when employing a full **R** matrix.

5.3.4 Modified observation operator

We repeat the experiments shown previously, again using the dynamic **R** matrix. The according block diagonal and diagonal **R** matrices are again obtained as above. However, in this experiment we only observe every second grid point by setting the according entries of the observation operator matrix **H** (which was the identity in all previous experiments) to zero.

The according RMSE values are shown in Figure 5.23. First, we notice that unlike in all previous experiments, there is no noticeable difference in the performance between employing the full, block diagonal and diagonal **R** matrix. Furthermore, we see the RMSE-values of the background and analysis for N converging to roughly 1000 (which is approximately the time and space averageed observation error variance) in the WSRM scenario, while in the SPM scenario, they approach 2000. The RMSE-values of the background and analysis for L however converge properly only in the SPM scenario, where they approach 20 (which is approximately five times as large as the time and space averageed observation error variance), while they show strong oscillations (around approximately 65 for the analysis and around approximately 85 for the background), which only slowly decrease in amplitude, in the WSRM scenario.

The according ensemble spread is shown in Figure 5.24. Here again the usual behaviour is seen without any anomalies for N. For L the initial values are already relatively high and (especially in the WSRM scenario) only a small increase is seen, before they start to slowly decrease again.

The spread ratios are shown in Figure 5.25. For N, the spread ratio quickly decreases in both scenarios, approaching values of about 0.75 in the SPM scenario and 0.5 in the WSRM scenario. For L however, in the SPM scenario the spread ratio quickly drops to 2 and remains at that value, while in the WSRM scenario it strongly oscillates (due to the oscillations in the according RMSE values) and tendencially increases over time, reaching

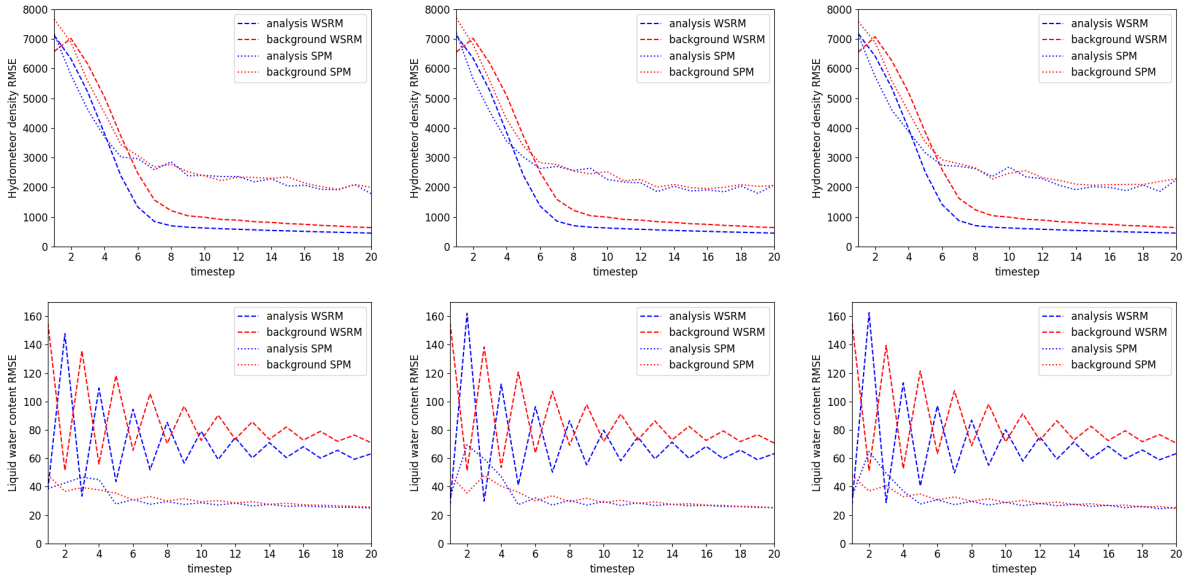

Figure 5.23: RMSE-values (averaged over 50 experiments) for DA of N (upper panel) and L (lower panel) with a time stepping of $5 \times 0.0002s$. DA is carried out using the full analytic (left panel), block diagonal (middle panel) or diagonal (right panel) time dependent covariance matrix, with smoothing of the ensemble, observing only every second grid point. The SPM (dotted line) and the WSRM (dashed line) are used as truth.

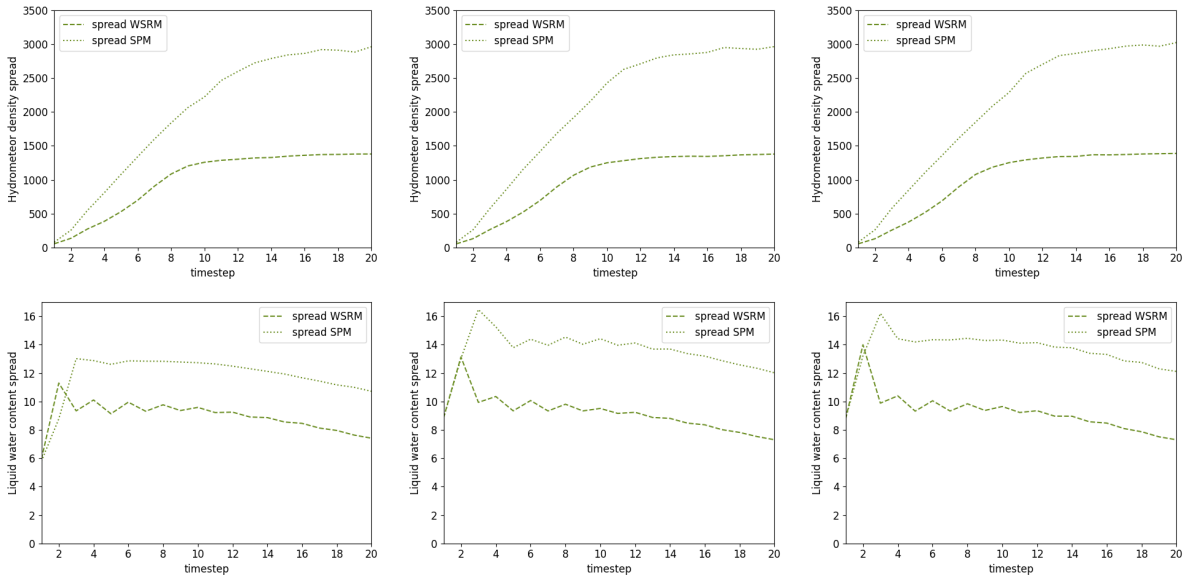

Figure 5.24: Ensemble spread (averaged over 50 experiments) for DA of N (upper panel) and L (lower panel) with a time stepping of $5 \times 0.0002s$. DA is carried out using the full analytic (left panel), block diagonal (middle panel) or diagonal (right panel) time dependent covariance matrix, with smoothing of the ensemble, observing only every second grid point. The SPM (dotted line) and the WSRM (dashed line) are used as truth.

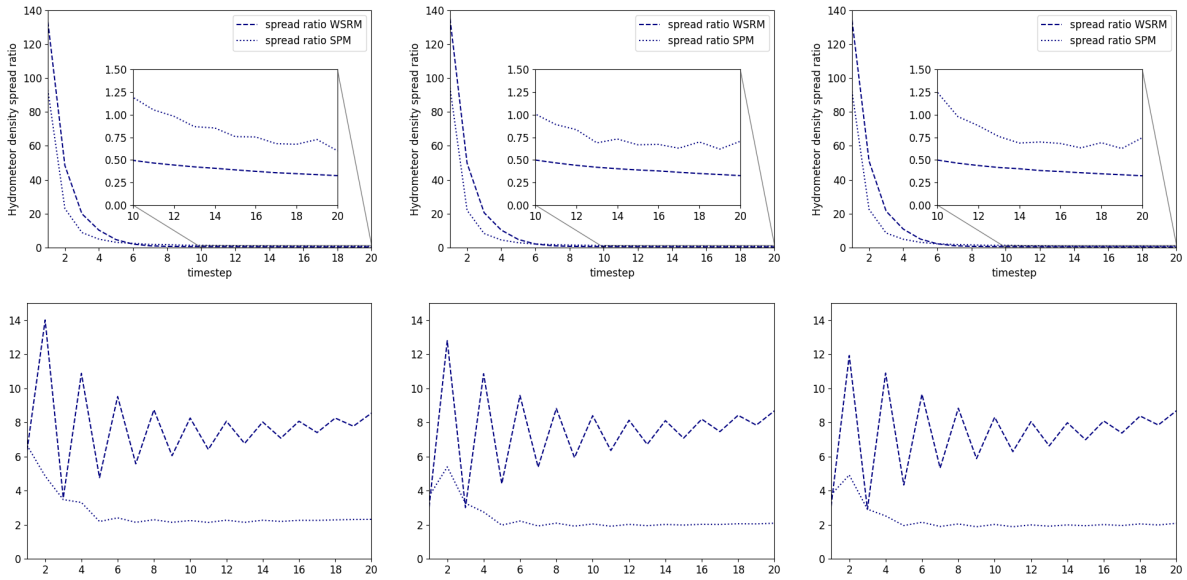

Figure 5.25: Spread ratios (averaged over 50 experiments) for DA of N (upper panel) and L (lower panel) with a time stepping of $5 \times 0.0002s$. DA is carried out using the full analytic (left panel), block diagonal (middle panel) or diagonal (right panel) time dependent covariance matrix, with smoothing of the ensemble, observing only every second grid point. The SPM (dotted line) and the WSRM (dashed line) are used as truth.

a value of over 8 in the last time step. This indicates that the ensemble strongly underestimates the according uncertainty, which can negatively affect DA.

When again looking at snapshots (not shown) both in the diagonal $\mathbf{R}$ case and the full $\mathbf{R}$ case, the main difference to observing every grid point is an amplitude error in L remaining uncorrected throughout all time steps. Note again that the considered snapshots are only examples and might not be representative for all experiments.

5.4 Summary

When comparing the covariances obtained for the SPM to those obtained for a model as closely as possible following the Wacker and Seifert (2001) reference model, we found the latter to explicitly depend on a free parameter without physical analogue, which we were unable to dispose of. Thus in the context of DA, the changes made when introducing the SPM appear to be warranted.

In our numerical experiments with the SPM, we found that correctly specifying the temporal evolution of $\mathbf{R}$ is far more important than accounting for its spatial structure. Employing a non-diagonal $\mathbf{R}$ matrix usually resulted in worse outcomes than a diagonal $\mathbf{R}$ matrix.

Especially accounting for spatial correlations of $\mathbf{R}$, while ignoring its temporal variations can (particularly in the beginning) have a strongly negative effect on DA. Furthermore, similar to Gleiter et al. (2022), we found an extremely small initial ensemble spread, likely caused by negative values set to a constant value, to be common.

Chapter 6

Influence of correlated observation errors on non-negativity of analysis

In this chapter, we look at a series of strongly simplified examples to better understand non-negativity preservation and facilitate interpreting the results of chapter 5. Of special interest is the influence of correlated observation errors. We start with a summary of known theorems regarding preservation of non-negativity for the Kalman Filter in section 6.1. Subsequently, in section 6.2 we illustrate the effect of non-diagonal observation error covariances on non-negativity, employing simple examples. Then we carry out a series of numerical experiments and investigate the obtained distributions for the analysis in section 6.3 and construct a series of counterexamples to disprove several possible generalisations of Proposition 6.1.1 in section 6.4.

Note, that this section (as it was intended to be consistent with the notation of Cohn (1997)) uses a slightly different notation than the rest of the thesis, with $\bar{\mathbf{x}}^a$, $\bar{\mathbf{x}}^b$ and $\mathbf{y}^o$ referred to as $\mathbf{w}^a$, $\mathbf{w}^f$ and $\mathbf{w}^o$ and the subscript n being dropped.

6.1 Preservation of non-negativity

We start by giving a short summary of established results on non-negativity preservation for the Kalman filter. Except for section 6.3.3, where we want to study the effect of the observation operator on non-negativity, we will from now on assume direct observation at each grid point, i.e. $\mathbf{H} = \mathrm{Id}$, which greatly simplifies the according equations and also gives us a best case scenario, in which the state is fully observed.

The following proposition about non-negativity conservation for diagonal error covariance matrices is known:

Proposition 6.1.1. *Let* $\mathbf{H} = \mathrm{Id}$, $\mathbf{P}^f, \mathbf{R} \in M_n$ *diagonal and positive definite and let* $w_i^f, w_i^o \geq 0$, *for all* $i \in \{1, \cdots, n\}$, *then* $w_i^a \geq 0$, *for all* $i \in \{1, \cdots, n\}$.

Proof. Assuming

$$\mathbf{R} = \begin{pmatrix} r_1 & 0 & 0 \\ 0 & \ddots & 0 \\ 0 & 0 & r_n \end{pmatrix}, \tag{6.1}$$

$$\mathbf{P}^f = \begin{pmatrix} p_1 & 0 & 0 \\ 0 & \ddots & 0 \\ 0 & 0 & p_n \end{pmatrix}, \tag{6.2}$$

from (2.16) we get

$$\mathbf{K} = \begin{pmatrix} \frac{p_1}{p_1+r_1} & 0 & 0 \\ 0 & \ddots & 0 \\ 0 & 0 & \frac{p_n}{p_n+r_n} \end{pmatrix}, \tag{6.3}$$

Thus (2.15) yields

$$w_i^a = w_i^f + \frac{p_i}{p_i + r_i}\left(w_i^o - w_i^f\right) \tag{6.4}$$

$$= w_i^f \left(1 - \underbrace{\frac{1}{1+\frac{r_i}{p_i}}}_{<1} \right) + \underbrace{\frac{1}{1+\frac{r_i}{p_i}}}_{>0} w_i^o \tag{6.5}$$

$$\geq 0, \tag{6.6}$$

for all $i \in \{1, \cdots, n\}$.

□

An analogue statement holds for positivity:

Proposition 6.1.2. *If in the situation of proposition 6.1.1 we have $w_i^f > 0$, for all $i \in \{1, \cdots, n\}$, then $w_i^a > 0$, for all $i \in \{1, \cdots, n\}$.*

Proof. Analogue to proposition 6.1.1.

□

As in practical applications non-diagonal elements of $\mathbf{P}^f$ and with increasing popularity also of $\mathbf{R}$ commonly occur, an important question is when this incurs the risk of obtaining negative analysis and if the conditions in proposition 6.1.1 can be relaxed.

Another well known statement (see Cohn (1997) for the case $n = 2$)) holds for observing at a single grid point only:

Proposition 6.1.3. *Let* $\mathbf{H} = \mathbf{e}_i = (0, \cdots, 1, \cdots, 0)^T$, $\mathbf{R} = r \in \mathbb{R}_+$, $\mathbf{P}^f \in M_n$ *positive definite and let* $\mathbf{w}^o = w^o \in \mathbb{R}_+$ *and* $w_i^f \geq 0$, *then* $w_i^a \geq 0$.

Proof. From (2.16), we obtain

$$\mathbf{K} = \frac{1}{\mathbf{P}_{ii}^f + r} \begin{pmatrix} \mathbf{P}_{1i}^f \\ \vdots \\ \mathbf{P}_{ni}^f \end{pmatrix} \tag{6.7}$$

and thus (2.15) becomes

$$\mathbf{w}^a = \mathbf{w}^f + \frac{1}{\mathbf{P}_{ii}^f + r} \begin{pmatrix} \mathbf{P}_{1i}^f \\ \vdots \\ \mathbf{P}_{ni}^f \end{pmatrix} \cdot \left(w^o - w_i^f \right). \tag{6.8}$$

So we get for the i-th component

$$\begin{aligned} w_i^a &= w_i^f + \frac{\mathbf{P}_{ii}^f}{\mathbf{P}_{ii}^f + r} \left(w^o - w_i^f \right) && (6.9) \\ &= w_i^f + \frac{1}{1 + \frac{r}{\mathbf{P}_{ii}^f}} \left(w^o - w_i^f \right) && (6.10) \\ &= \underbrace{\left(1 - \frac{1}{1 + \frac{r}{\mathbf{P}_{ii}^f}} \right)}_{\geq 0} w_i^f + \underbrace{\frac{1}{1 + \frac{r}{\mathbf{P}_{ii}^f}}}_{\geq 0} w^o && (6.11) \\ &\geq 0 && (6.12) \end{aligned}$$

□

However (as shown by Cohn (1997) using a counterexample with $n = 2$), Proposition 6.1.3 does not guarantee the non-negativity of the analysis for $i \neq j$, which we will illustrate in the following remark.

Remark 6.1.1. In the situation of Proposition 6.1.3 let $w_j^f \geq 0$, for all $j \in \{1, \cdots, n\}$, then for $i \neq j$ we have

$$w_j^a = w_j^f + \frac{\mathbf{P}_{ij}^f}{\mathbf{P}_{ii}^f + r} \left(w^o - w_i^f \right). \tag{6.13}$$

If $\mathbf{P}_{ij}^f \geq 0$, this becomes

$$w_j^a = w_j^f + \frac{\mathbf{P}_{ij}^f}{\mathbf{P}_{ii}^f + r} \underbrace{\left(w^o - w_i^f\right)}_{\geq -w_i^f} \tag{6.14}$$

$$\geq w_j^f - \frac{\mathbf{P}_{ij}^f}{\mathbf{P}_{ii}^f + r} w_i^f, \tag{6.15}$$

where equality holds if $w^o = 0$. Thus, non-negativity of the right hand side of (6.15) guarantees non-negativity of the analysis, whereas otherwise negative analysis at grid point j is always possible, if w^o is small enough. Thus, the danger of negative analysis is particularly high at grid points with low values of w_j^f that are strongly (positively) correlated to grid points where observation is located that has high values of w_i^f.

The conditions mentioned in Remark 6.1.1 are especially likely to be fulfilled by points in the neighborhood of peaks, as $\mathbf{P}_{ij}^f$ typically decreases with increasing (physical) distance between the grid points i and j. Thus in the vicinity of large peaks, we expect grid points with negative analysis possibly occurring. We will further investigate this situation in Section 6.2.

6.2 Illustration of the effect of non-diagonal observation error covariances on non-negativity

We now examine the possibility of obtaining negative analysis in a simple DA experiment and identify concrete situations that can lead to negative analysis: We consider a quantity defined on a grid with 10 points. As observations and for the creation of the background we will use triangular profiles consisting of one point assuming the according maximum value and the two adjacent points assuming half of the maximum value. Background mean $\mathbf{w}_f$ and covariance $\mathbf{P}_f$ will be given by an ensemble consisting of 3 triangular profiles of height 2, centred at grid points 4 to 6 (see Figure 6.1).

Observations will be given by a triangular profile of height h_{obs} centred at x_{obs} and the observation error covariance $\mathbf{R}$ will be given by a matrix of the form

$$\mathbf{R} = \begin{pmatrix} R_0 & R_1 & \cdots & R_8 & R_9 \\ R_1 & R_0 & \cdots & R_7 & R_8 \\ \vdots & \ddots & \ddots & \ddots & \vdots \\ R_8 & R_7 & \cdots & R_0 & R_1 \\ R_9 & R_8 & \cdots & R_1 & R_0 \end{pmatrix}. \tag{6.16}$$

Furthermore, a diagonal observation error covariance matrix $\mathbf{R}_{dg}$, created by setting the non-diagonal elements of $\mathbf{R}$ to zero, will be used for comparison.

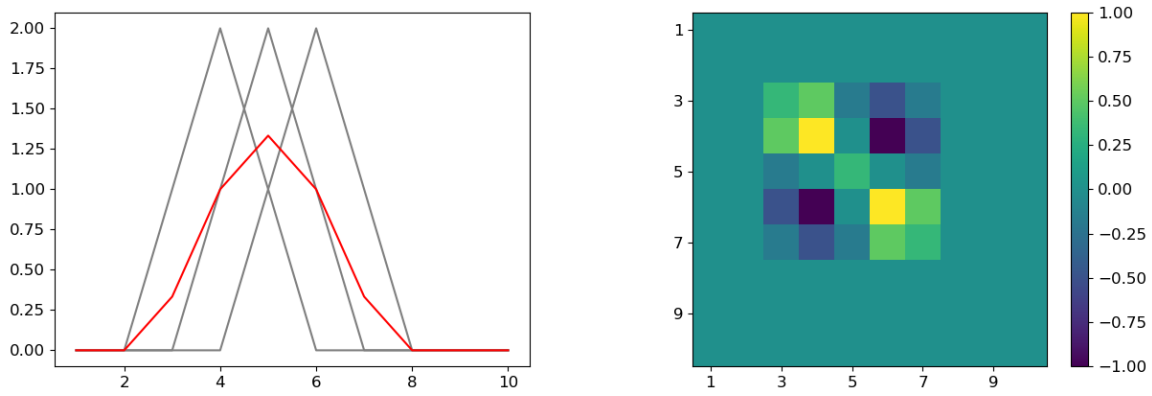

Figure 6.1: Background ensemble used in section 6.2, with the left panel showing ensemble members (grey) and ensemble mean (red) and the right panel the according background covariance matrix.

First we consider an example in which using a non-diagonal observation error covariance leads to the appearance of negative analysis in presence of pure positional error resulting from the observations being set equal to the last ensemble member.

Example 6.2.1. Consider the case $h_{obs} = 2$, $x_{obs} = 6$ and the only non-zero entries of $\mathbf{R}$ being $R_0 = \frac{2}{3}$ and $R_3 = 0.33$. In contrast to using the diagonal observation error covariance matrix $\mathbf{R}_{dg}$, this yields a negative analysis at grid point 3 (see Figure 6.2).

In the next example, we see the analogue effect for pure amplitude error:

Example 6.2.2. Consider the case $h_{obs} = 3$, $x_{obs} = 5$ again with the only non-zero entries of $\mathbf{R}$ being $R_0 = \frac{2}{3}$ and $R_3 = 0.33$. In contrast to using $\mathbf{R}_{dg}$, this yields a negative analysis at grid points 3 and 7 (see Figure 6.2).

In the next example negative analysis is also obtained for a diagonal observation error covariance due to positional and amplitude error:

Example 6.2.3. Consider the case $h_{obs} = 3$, $x_{obs} = 6$ and $\mathbf{R}$ being diagonal with $R_0 = \frac{2}{3}$. This yields a negative analysis at grid points 3 and 4 (see Figure 6.3).

As previously predicted (see Remark 6.1.1), in all examples the negative values are located at the foothills of the peak. In Example 6.2.2, they occur at both sides, while in Example 6.2.1 and Example 6.2.3 they are found only on the left side.

The analysis covariance matrices for the DA experiments in examples 6.2.1 to 6.2.3 are depicted in Figure 6.4. The non-diagonal observation error covariance yields lower values

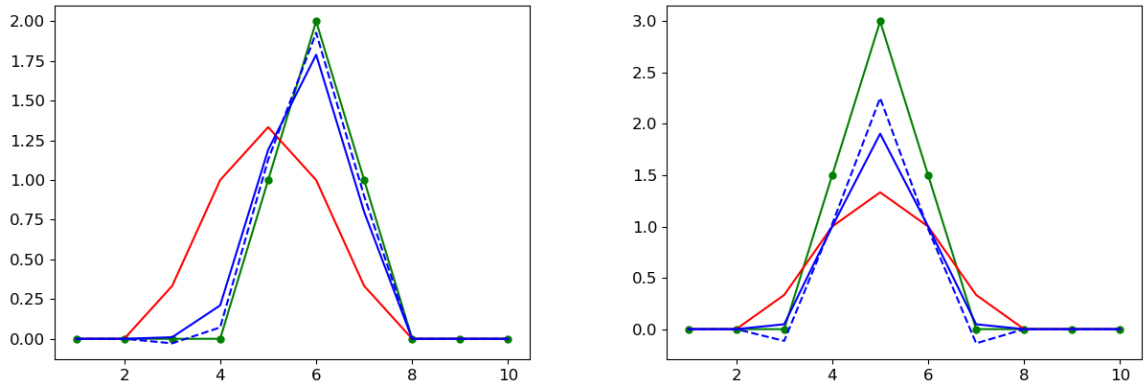

Figure 6.2: Forecast (red), observations (green circles) and analysis (blue dashed) for the DA experiment of example 6.2.1 (left panel) and example 6.2.2 (right panel) and analogue experiments with $\mathbf{R}_{dg}$ (blue continuous).

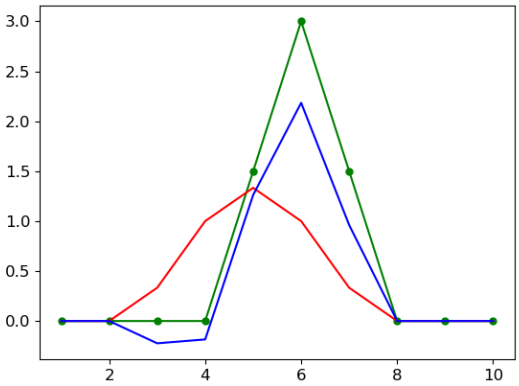

Figure 6.3: Forecast (red), observations (green) and analysis (blue) for the DA experiment of example 6.2.3.

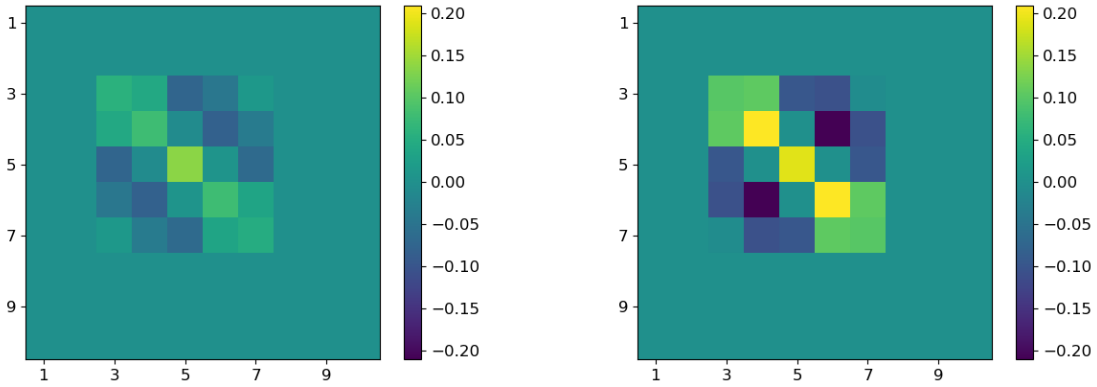

Figure 6.4: Analysis covariance matrix for the DA experiments of examples 6.2.1 to 6.2.3 (left panel) and analogue experiments using $\mathbf{R}_{dg}$ (right panel).

of analysis covariances than the diagonal version.

Thus using a non-diagonal observation error covariance might, if negative analysis occurs and is artificially set to physically plausible values, impede correction at later DA steps by decreasing the corresponding variances, even if the according errors are not amplified e.g. by application of a time evolution operator.

6.3 Numerical experiments and distribution of analysis

We now conduct a series of numerical two-component experiments to examine how frequent and under which conditions (especially with regard to the properties of $\mathbf{P}^f$) negative analysis occurs for diagonal and non-diagonal observation error covariances. Furthermore, we plot histograms of the according analysis for different scenarios. These are especially of interest, as they allow to easily see to what extent positivizing would distort the distribution of the analysis under different conditions.

Notation 6.3.1. We write

$$\mathbf{w}^a = \begin{pmatrix} w_1^a \\ w_2^a \end{pmatrix}, \mathbf{w}^f = \begin{pmatrix} w_1^f \\ w_2^f \end{pmatrix}, \mathbf{w}^o = \begin{pmatrix} w_1^o \\ w_2^o \end{pmatrix}, \Delta\mathbf{w} = \begin{pmatrix} \Delta w_1 \\ \Delta w_2 \end{pmatrix} = \begin{pmatrix} w_1^o - w_1^f \\ w_2^o - w_2^f \end{pmatrix}, \tag{6.17}$$

$$\mathbf{P}^f = \begin{pmatrix} a & c \\ c & b \end{pmatrix} = \begin{pmatrix} a & \varrho\sqrt{ab} \\ \varrho\sqrt{ab} & b \end{pmatrix}, \tag{6.18}$$

$$\mathbf{R} = \begin{pmatrix} r_1 & k \\ k & r_2 \end{pmatrix}, \tag{6.19}$$

with $-\sqrt{ab} < c < \sqrt{ab}$ and $-\sqrt{r_1 r_2} < k < \sqrt{r_1 r_2}$, $-1 < \varrho < 1$.

We draw n random samples for the components of $\mathbf{w}^o$, $\mathbf{w}^f$ and $\mathbf{R}$. $\mathbf{R}$ is subsequently symmetrized and if necessary redrawn until a positive semidefinite matrix is achieved and a diagonal version $\mathbf{R}_{dg}$ is created by setting its non-diagonal elements to zero. The components of $\mathbf{P}^f$ are set to pre specified values. For each sample, a Kalman filter is applied to obtain a analysis with both $\mathbf{R}$ and $\mathbf{R}_{dg}$ and the fraction of the samples yielding analysis with at least one negative component of the total number of involved grid points for each option is calculated.

Here we draw all random components from a uniform distribution on $[0, 1]$ and allow for multiplication of $\mathbf{w}^o$ and $\mathbf{w}^f$ by a constant factor c_o and c_f, effectively sampling those quantities from $[0, c_o]$ and $[0, c_f]$. c_o and c_f can be seen as a measure for the magnitude of the observations and background. Despite these quantities also influencing the according variance, this is probably the most simple setup. A further advantage of this setup is that only the ratio $\frac{c_o}{c_f}$ seems to be of importance, reducing the degrees of freedom and allowing for easier interpretation of the results.

As a reference for the magnitude of the effects studied in this chapter, we use an example employed by Cohn (1997) to show the possibility of negative analysis when observing only a subset of the grid points:

Example 6.3.1. According to Cohn (1997), in the situation of notation 6.3.1 with $\mathbf{H} = (1, 0)$ and $\mathbf{R} = r > 0$ the analysis is given by $w_1^a = \frac{1}{a+r}\left(rw_1^f + aw_1^o\right), w_2^a = w_2^f + \frac{c}{a+r}\left(w_1^o - w_1^f\right)$.

For all experiments in this section, we run example 6.3.1 with the parameters used in the according experiment, where r is selected to be the first entry of the according $\mathbf{R}$, and compare the obtained frequency of negative analysis. Note also that only example 6.3.1 does not observe every grid point, while all other experiments in this section employ $\mathbf{H} = \mathrm{Id}$.

Once $\frac{c_o}{c_f}$ is fixed, there seems to be no explicit dependence on c_f in all experiments shown in this section as long as $c_f \neq 0$. Therefore for all experiments we only vary $\frac{c_o}{c_f}$. We usually consider the cases $\frac{c_o}{c_f} = 0.2$, $\frac{c_o}{c_f} = 1.0$ and $\frac{c_o}{c_f} = 5.0$, corresponding to the background overestimating, correctly estimating and underestimating the truth. Note that such large differences in the magnitude of background and observations can easily occur in practice, e.g. due to positional error of a convective cell that is misplaced compared to observations due to model imperfections or simply missing a convective cell in model forecast.

6.3.1 Effect of background correlations

To investigate, how the effect of using non-diagonal $\mathbf{R}$ on non-negativity depends on background correlations, we start with a $\mathbf{P}^f$ with positive correlations:

Example 6.3.2. Let

$$\mathbf{P^f} = \begin{pmatrix} 0.33 & 0.25 \\ 0.25 & 0.33 \end{pmatrix},$$

then the fraction of experiments that yield at least one negative component of $\mathbf{w}^a$ as a function of $\frac{c_o}{c_f}$ are shown in Figure 6.5. The histograms for the distribution of $\mathbf{w}^a$ are shown in Figure 6.6.

In the non-diagonal case, the probability of negative analysis has a minimum at $\frac{c_o}{c_f} \approx 1$ and increases strongly with decreasing $\frac{c_o}{c_f}$ and moderately with increasing $\frac{c_o}{c_f}$, while in the diagonal case it decreases with $\frac{c_o}{c_f}$. Here in general, for $\frac{c_o}{c_f} > 1$, the use of non-diagonal $\mathbf{R}$ increases the probability of negative analysis, while for $\frac{c_o}{c_f} < 1$ it decreases it.

In the diagonal case, we find the distribution of $\mathbf{w}^a$ noticeably extending to negative values for $\frac{c_o}{c_f} = 0.2$ and $\frac{c_o}{c_f} = 1$. Using non-diagonal observation error covariances shifts the distribution to higher values for $\frac{c_o}{c_f} = 0.2$ and to lower ones for $\frac{c_o}{c_f} = 5.0$, whereas in the case $\frac{c_o}{c_f} = 1$ it remains unaltered. For $\frac{c_o}{c_f} = 5.0$, this shift results in the distribution noticeably extending to negative $\mathbf{w}^a$.

In the reference experiment, we see higher variances of the distribution of w_2^a for $\frac{c_o}{c_f} = 0.2$ and $\frac{c_o}{c_f} = 1$ leading to a higher fraction of experiments with negative analysis, whereas we see no large difference to example 6.3.2 for $\frac{c_o}{c_f} = 5.0$. As expected, w_1^a is always non-negative.

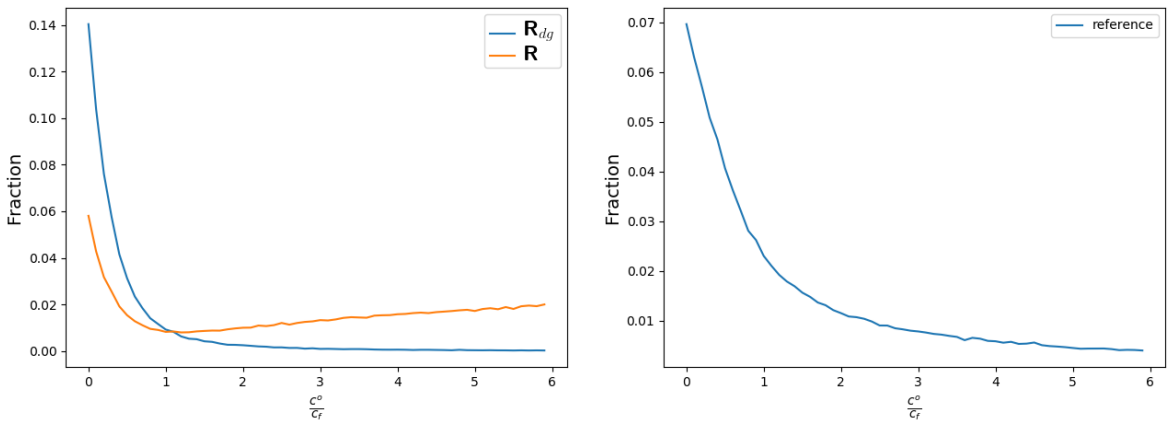

Figure 6.5: Fraction of experiments with at least one negative component of $\mathbf{w}^a$ plotted against $\frac{c_o}{c_f}$, when using $\mathbf{R}$ (orange) and $\mathbf{R}_{dg}$ (blue), in the situation of example 6.3.2 (left panel) and the corresponding version of the reference experiment example 6.3.1 (right panel). Note the difference in y-scale between the left and right panel.

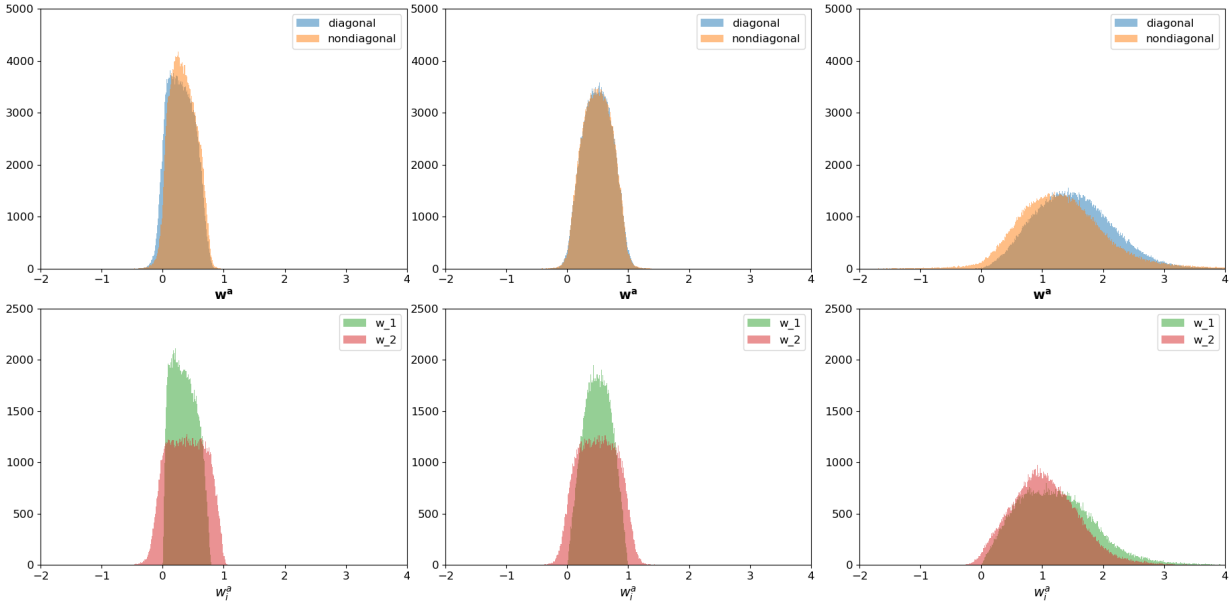

Figure 6.6: Histograms for the distribution of $\mathbf{w}^a$ when using $\mathbf{R}$ (orange) and $\mathbf{R}_{dg}$ (blue), for $\frac{c_o}{c_f} = 0.2$ (left panel), $\frac{c_o}{c_f} = 1.0$ (center panel) and $\frac{c_o}{c_f} = 5.0$ (right panel) in the situation of example 6.3.2 (top row) and of w_1^a (green) and w_2^a (red) in the corresponding version of the reference experiment given in example 6.3.1 (bottom row).

Now, we consider a diagonal $\mathbf{P}^f$:

Example 6.3.3. Let

$$\mathbf{P^f} = \begin{pmatrix} 0.33 & 0 \\ 0 & 0.33 \end{pmatrix},$$

then the fraction of experiments that yield at least one negative component of $\mathbf{w}^a$ as a function of $\frac{c_o}{c_f}$ are shown in Figure 6.7. The histograms for the distribution of $\mathbf{w}^a$ are shown in Figure 6.8.

For the non-diagonal $\mathbf{R}$ case, we see the probability of negative analysis increasing with $\frac{c_o}{c_f}$, while in the diagonal case it always remains zero. This is expected due to proposition 6.1.1. Consequently, here the use of non-diagonal $\mathbf{R}$ increases the probability of negative analysis. Furthermore, in the non-diagonal case the probability of negative analysis increases faster than in example 6.3.2. In the non-diagonal case none of the distribution extends to negative values as predicted by proposition 6.1.1. Using non-diagonal observation error covariances results in increasing spread of the distribution, creating more Gaussian like profiles, and its mean increasing for $\frac{c_o}{c_f} = 0.2$ and decreasing for $\frac{c_o}{c_f} = 5.0$. Consequently, the extension to negative $\mathbf{w}^a$ is negligible for $\frac{c_o}{c_f} = 0.2$, medium for $\frac{c_o}{c_f} = 1.0$ and significant for $\frac{c_o}{c_f} = 5.0$. As expected, in the reference experiment, w_1^a and w_2^a are always non-negative.

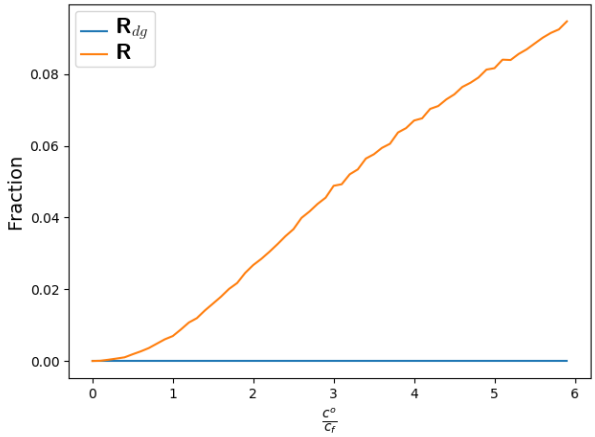

Figure 6.7: Fraction of experiments with at least one negative component of $\mathbf{w}^a$ plotted against $\frac{c_o}{c_f}$, when using $\mathbf{R}$ (orange) and $\mathbf{R}_{dg}$ (blue), in the situation of example 6.3.3. The corresponding version of the reference experiment example 6.3.1 is not shown, as it is constantly zero.

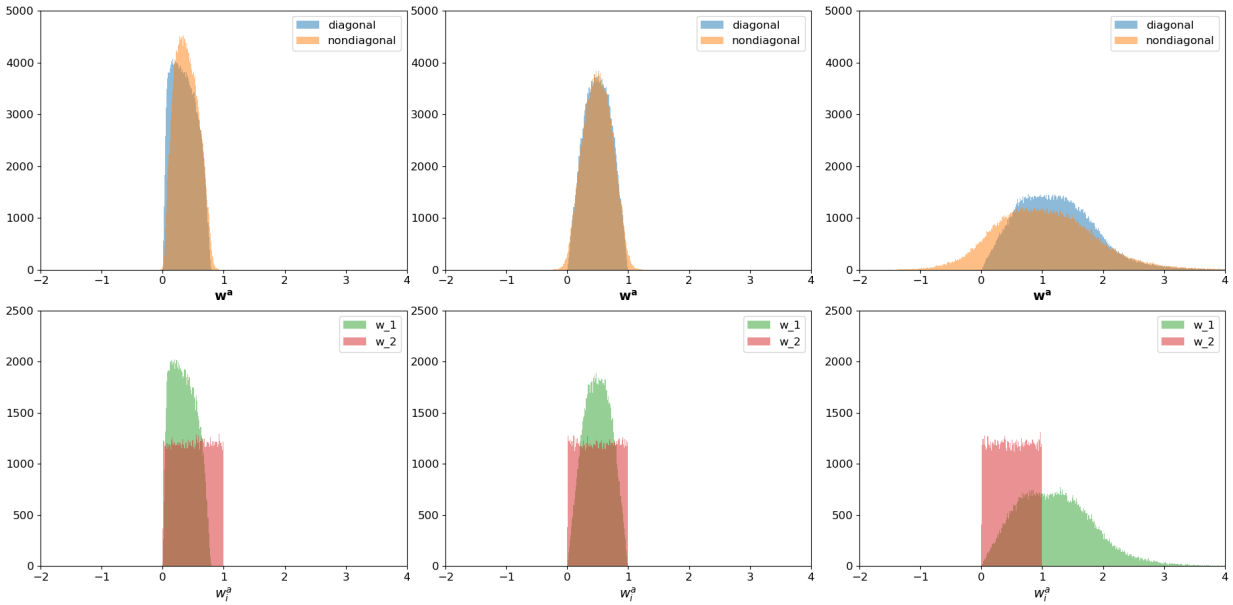

Figure 6.8: Histograms for the distribution of $\mathbf{w}^a$ when using $\mathbf{R}$ (orange) and $\mathbf{R}_{dg}$ (blue), and $\frac{c_o}{c_f} = 0.2$ (left panel), $\frac{c_o}{c_f} = 1.0$ (center panel) and $\frac{c_o}{c_f} = 5.0$ (right panel) in the situation of example 6.3.3 (top row) and of w_1^a (green) and w_2^a (red) in the corresponding version of the reference experiment example 6.3.1 (bottom row).

Finally we consider a $\mathbf{P}^f$ with negative correlations:

Example 6.3.4. Let

$$\mathbf{P^f} = \begin{pmatrix} 0.33 & -0.25 \\ -0.25 & 0.33 \end{pmatrix},$$

then the fraction of experiments that yield at least one negative component of $\mathbf{w}^a$ as a function of $\frac{c_o}{c_f}$ are shown in Figure 6.9. The histograms for the distribution of $\mathbf{w}^a$ are shown in Figure 6.10.

Here, we see the probability of negative analysis increasing with $\frac{c_o}{c_f}$ in the non-diagonal and the diagonal case, where the increase is stronger for the non-diagonal case. Thus, here the use of non-diagonal $\mathbf{R}$ increases the probability of negative analysis. Furthermore, the frequency of negative analysis is generally higher than in example 6.3.3. In the diagonal case, the distribution of $\mathbf{w}^a$ extends to negative values for all $\frac{c_o}{c_f}$, negligibly for $\frac{c_o}{c_f} = 0.2$, slightly for $\frac{c_o}{c_f} = 1.0$ and significantly for $\frac{c_o}{c_f} = 5.0$. Using non-diagonal observation error covariances increases the variance of the distribution and thus the probability of negative analysis for all $\frac{c_o}{c_f}$.

In the reference experiment, we see higher variances of the distribution of w_2^a for $\frac{c_o}{c_f} = 0.2$ and $\frac{c_o}{c_f} = 1$ and similar variances to example 6.3.2 for $\frac{c_o}{c_f} = 5.0$. Compared to example 6.3.2, the mean of the distribution of w_2^a obtained for $\frac{c_o}{c_f} = 0.2$ is higher and that obtained for $\frac{c_o}{c_f} = 5.0$ is lower. As expected, w_1^a is always non-negative.

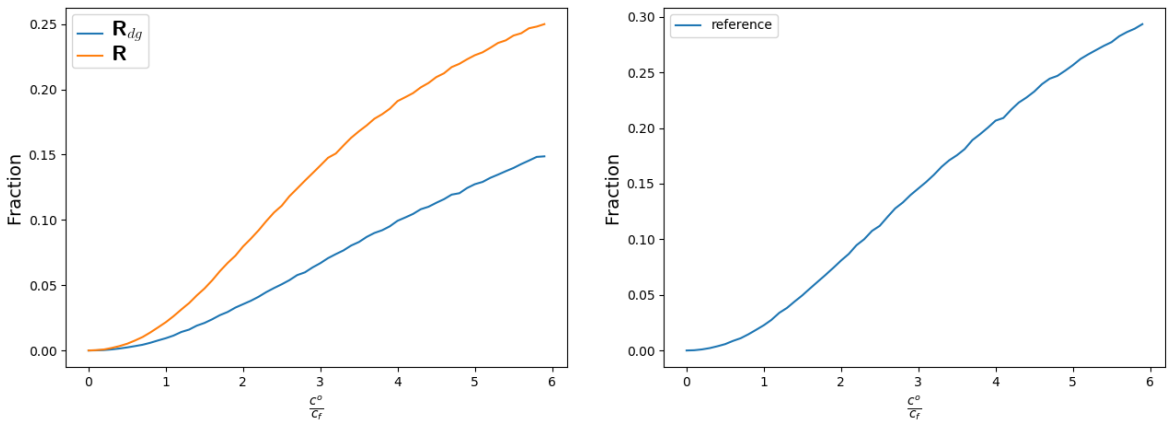

Figure 6.9: Fraction of experiments with at least one negative component of $\mathbf{w}^a$ plotted against $\frac{c_o}{c_f}$, when using $\mathbf{R}$ (orange) and $\mathbf{R}_{dg}$ (blue), in the situation of example 6.3.4 (left panel) and the corresponding version of the reference experiment example 6.3.1 (right panel).

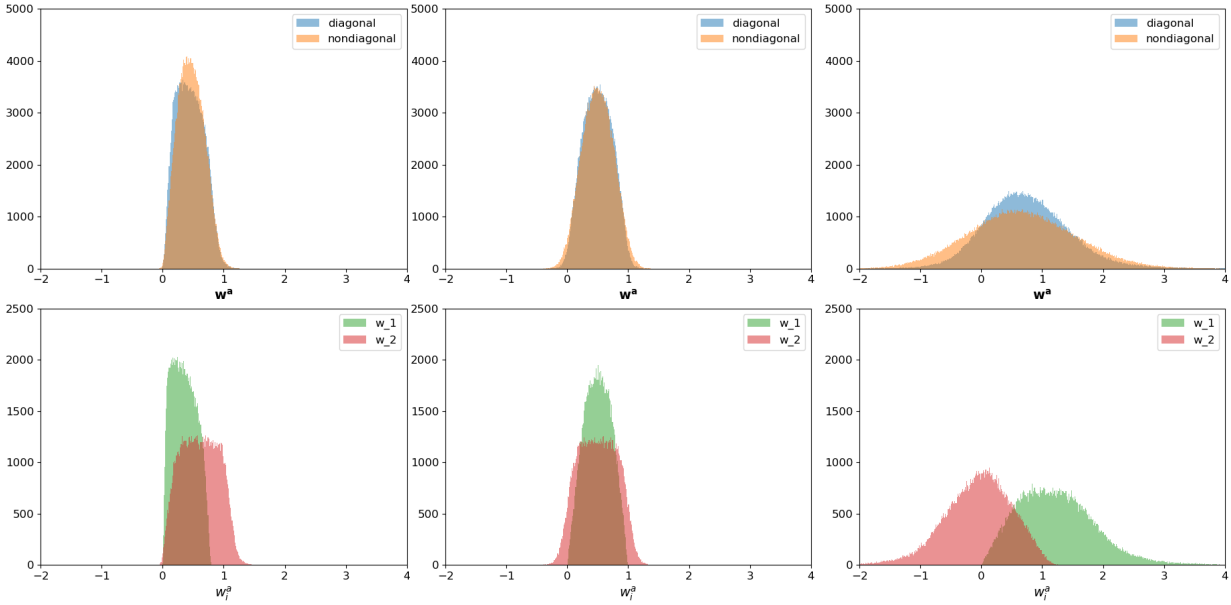

Figure 6.10: Histograms for the distribution of $\mathbf{w}^a$ when using $\mathbf{R}$ (orange) and $\mathbf{R}_{dg}$ (blue), for $\frac{c_o}{c_f} = 0.2$ (left panel), $\frac{c_o}{c_f} = 1.0$ (center panel) and $\frac{c_o}{c_f} = 5.0$ (right panel) in the situation of example 6.3.4 (top row) and of w_1^a (green) and w_2^a (red) in the corresponding version of the reference experiment example 6.3.1 (bottom row).

Generally, in the histograms we see that the use of non-diagonal $\mathbf{R}$, as well as correlations in $\mathbf{P}^f$ lead to increased Gaussianity in the distribution of $\mathbf{w}^a$. Furthermore, for $\frac{c_o}{c_f} > 1$ the mean of the distribution is increased by positive correlations in $\mathbf{P}^f$ and decreased by negative correlations in $\mathbf{P}^f$, while for $\frac{c_o}{c_f} < 1$ positive correlations decrease the mean and negative correlations increase it. Furthermore, increasing $\frac{c_o}{c_f}$ increases the width of the distribution.

In all examples in the case using a diagonal $\mathbf{R}$ the fraction of experiments yielding negative analysis depends in a similar way on $\frac{c_o}{c_f}$, as in the corresponding version of example 6.3.1, i.e. with increasing $\frac{c_o}{c_f}$ it decreases in Figure 6.5, is constant in Figure 6.7 and increases in Figure 6.9. The effect of using non-diagonal $\mathbf{R}$ on the probability of obtaining negative analysis is summarized in Table 6.1.

We conclude our analysis of background correlations by directly varying the strength of correlation, while keeping $\frac{c_o}{c_f}$ fixed:

Example 6.3.5. Let $\mathbf{P}^f$ be in the form of (6.18) and $a = b = 0.33$, then the fraction of experiments that yield at least one negative component of $\mathbf{w}^a$ as a function of ϱ are shown in Figure 6.11 for various values of $\frac{c_o}{c_f}$. Furthermore the moments of the distribution of w_2^a are shown in Figure G.1 for $\frac{c_o}{c_f} < 1$ and in Figure G.2 for $\frac{c_o}{c_f} > 1$.

	$c > 0$	$c = 0$	$c < 0$
$\frac{c_o}{c_f} > 1$	increases	enables	increases
$\frac{c_o}{c_f} = 1$	none	enables	increases
$\frac{c_o}{c_f} < 1$	decreases	enables	increases

Table 6.1: Effect of using non-diagonal $\mathbf{R}$ on the probability of obtaining negative analysis. Here "enables" indicates that negative analysis is not possible, when a diagonal $\mathbf{R}$ is used, but occurs when employing a non-diagonal $\mathbf{R}$.

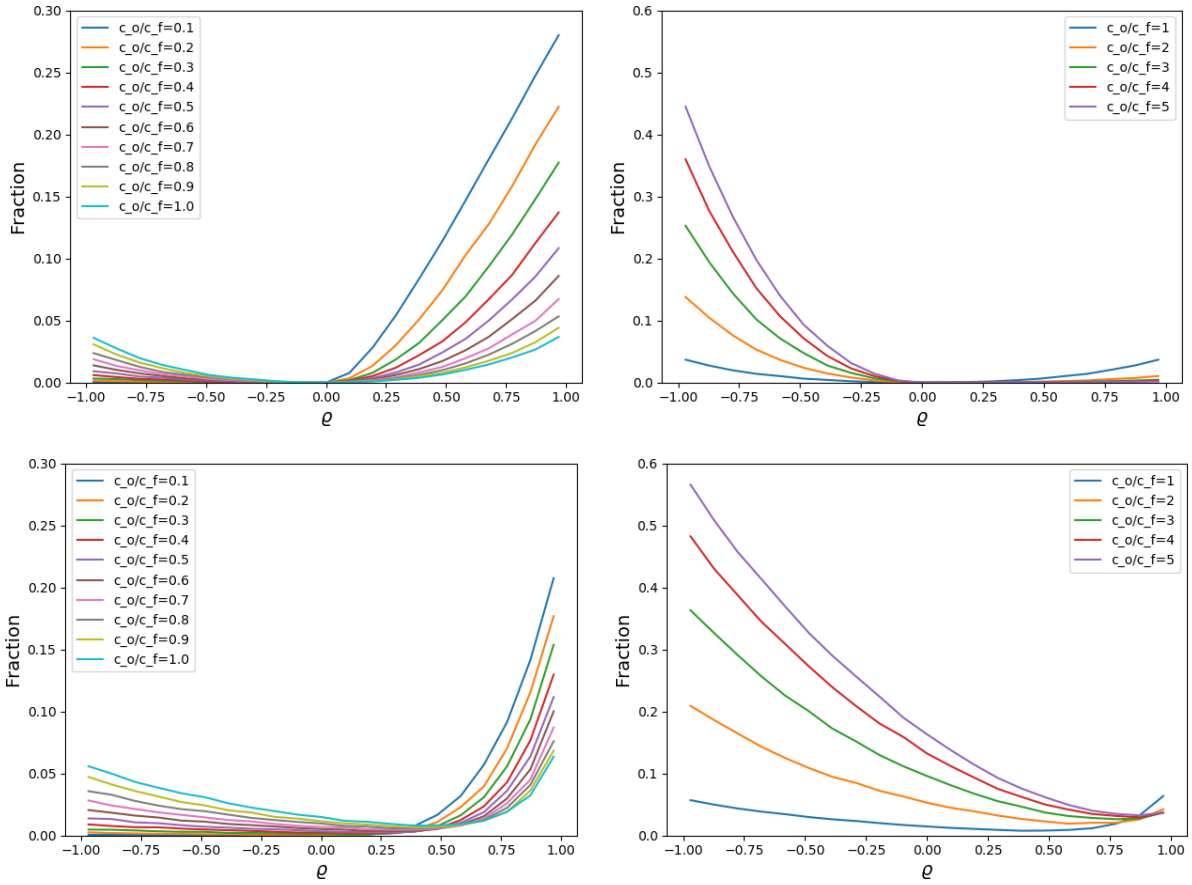

Figure 6.11: Fraction of experiments that yield at least one negative component of $\mathbf{w}^a$ as a function of ϱ for various values of $\frac{c_o}{c_f}$, when using $\mathbf{R}$ (upper panel) and $\mathbf{R}_{dg}$ (lower panel), in the situation of example 6.3.5, with the left panels showing examples for $\frac{c_o}{c_f} < 1$ and the right panels for $\frac{c_o}{c_f} > 1$.

We see that the fraction of experiments returning negative analysis has a minimum whose position strongly depends on $\frac{c_o}{c_f}$ and if diagonal or non-diagonal observation error covariances are used. In the diagonal case, it is always located roughly at $\varrho \approx 0$, while in the

non-diagonal case its position varies strongly with $\frac{c_o}{c_f}$, where larger $\frac{c_o}{c_f}$ move it closer to $\varrho \approx 1$. In both the diagonal and the non-diagonal case, when moving away from the minimum, the fraction of experiments returning negative analysis increases stronger when ϱ is increased for $\frac{c_o}{c_f} < 1$, while for $\frac{c_o}{c_f} > 1$ it increases stronger when ϱ is decreased. Overall, in the non-diagonal case the fraction is reduced for high ϱ and increased for low ϱ. In summary the effect of using non-diagonal observation error covariances on non-negativity preservation is highly dependent on what ranges of observations, forecast and background covariances are encountered.

We note that these examples are to some extent representative for convective scale data assimilation: Due to the short localization lengths used, only a few neighboring grid points influence the analysis at a given grid point (Tong and Xue (2005), Lange and Craig (2014)), a situation similar to the two grid point examples considered here. Furthermore, imperfect models can cause a large positional error for convective cells (see e.g. Roberts and Lean (2008) and Keil and Craig (2009)), allowing for huge differences in the ranges of observations and forecast (especially for variables describing rain, graupel and other hydrometeors, which are close to zero in most grid cells), as represented here by the relatively large range of $\frac{c_o}{c_f}$. A possible explanation for our experiments underestimating the fraction of grid points yielding negative analysis in convective scale data assimilation is the possibility of multiple grid points being collectively responsible for negative analysis. Nevertheless, the significant reduction of the probability for negative analysis by setting observations below a certain threshold to a that threshold (Janjić and Zeng, 2021) could be explained by only the tails of the distributions of analysis values protruding below zero, in most setups. Note however that this is the best case scenario for radar data, as discarding the measurements below the threshold is expected to result in more non-negativity violations (see e.g. Janjić and Zeng (2021)).

The moments of distribution of w_2^a plotted as a function of background correlation can be found in Figure G.1 and Figure G.2 in Appendix G.

6.3.2 Effect of background variances

We now investigate, how the diagonal elements of $\mathbf{P}^f$ and their ratio affect the probability for negative analysis. To this end, we write $\mathbf{P}^f$ in the form (6.18) and fix ϱ. In this section, we mostly consider modified versions of Example 6.3.2, for which we have $a = b = 0.33$ and $\varrho = \frac{0.25}{0.33}$. First we examine the effect of the magnitude of the variances by examining the case of a and b being reduced by a factor of 10, while their ratio remains at 1:

Example 6.3.6. Let $\mathbf{P}^f$ be given by (6.18) with $a = b = 0.033$ and $\varrho = \frac{0.25}{0.33}$, then the fraction of experiments that yield at least one negative component of $\mathbf{w}^a$ as a function of $\frac{c_o}{c_f}$ are shown in Figure 6.12.

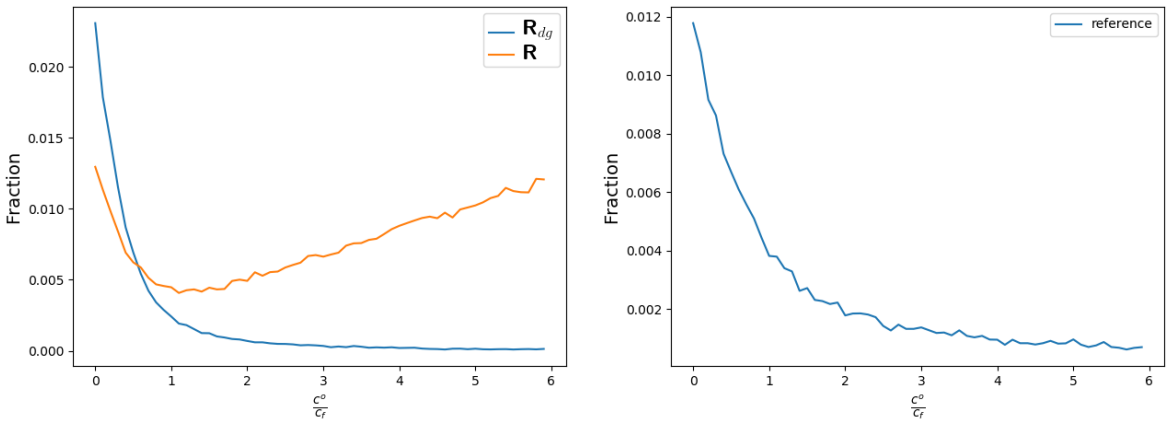

Figure 6.12: Fraction of experiments that yield at least one negative component of $\mathbf{w}^a$ plotted against $\frac{c_o}{c_f}$, when using $\mathbf{R}$ (orange) and $\mathbf{R}_{dg}$ (blue), in the situation of example 6.3.6 (left panel) and the corresponding version of the reference experiment example 6.3.1 (right panel).

The results are relatively similar to example 6.3.2, however the probabilities for negative analysis are significantly lower. Thus higher background variances seem to result in higher probability of obtaining negative analysis. Furthermore the $\frac{c_o}{c_f}$ up to which diagonal $\mathbf{R}$ are more likely to cause negative analysis than non-diagonal ones reduces to approximately 0.5, while the minimum of the probability for negative analysis using non-diagonal $\mathbf{R}$ remains at $\frac{c_o}{c_f} \approx 1$.

Now, we examine the effect of the ratio between the variances by reducing a by a factor of 10, while keeping b at 0.33:

Example 6.3.7. Let $\mathbf{P}^f$ be given by (6.18) with $a = 0.033$, $b = 0.33$ and $\varrho = \frac{0.25}{0.33}$ then the fraction of experiments that yield at least one negative component of $\mathbf{w}^a$ as a function of $\frac{c_o}{c_f}$ are shown in Figure 6.13 (left panel) and the corresponding version of the reference experiment example 6.3.1 (right panel). Note that also plots depicting single components are normalized to the total number of grid points in this section, to facilitate comparison.

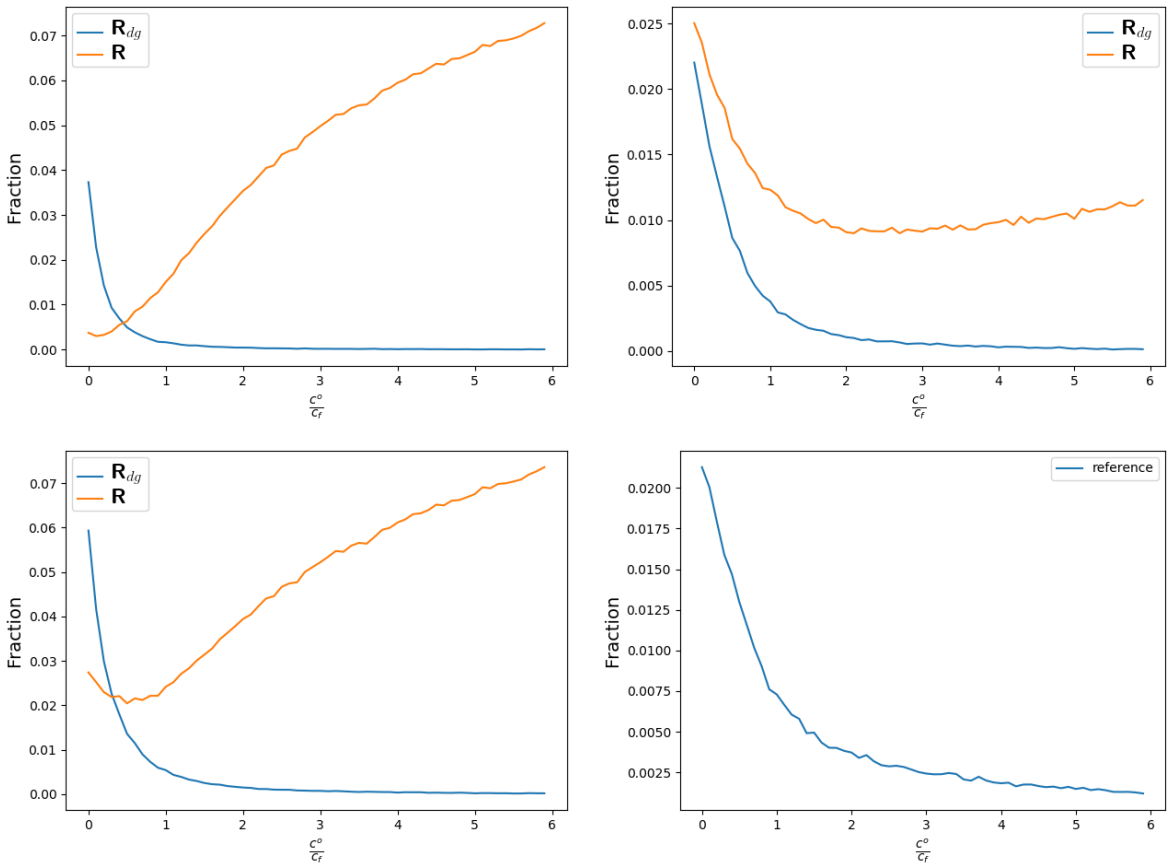

Figure 6.13: Fraction of experiments returning negative w_1^a (upper left panel) and w_2^a (upper right panel), as well as the fraction of experiments that yield at least one negative component of $\mathbf{w}^a$ (lower left panel) plotted against $\frac{c_o}{c_f}$, when using $\mathbf{R}$ (orange) and $\mathbf{R}_{dg}$ (blue), in the situation of example 6.3.7 and the corresponding version of the reference experiment example 6.3.1 (lower right panel).

Here we also obtain for diagonal $\mathbf{R}$ an increase of the probability for negative analysis with decreasing $\frac{c_o}{c_f}$, that is faster than in example 6.3.6 but slower than in example 6.3.2. Furthermore the minimum of the probability for negative analysis using non-diagonal $\mathbf{R}$ is significantly higher than in example 6.3.6 and example 6.3.2 and shifts to $\frac{c_o}{c_f} \approx 0.5$. The $\frac{c_o}{c_f}$ up to which diagonal $\mathbf{R}$ are more likely to cause negative analysis than non-diagonal is even lower than in example 6.3.6.

However due to $a \neq b$, we obtain different behaviour of w_1^a and w_2^a as shown in the upper panels. The fraction of experiments yielding negative w_2^a always increases when non-diagonal observation error correlations are used, whereas that of w_1^a follows a relative similar pattern as the overall fraction.

The absolute number of experiments returning negative analysis is found to lie between

example 6.3.2 and example 6.3.6.

Note that situations similar to example 6.3.7 can result e.g. from physical circumstances or when assimilating quantities with strongly different orders of magnitude from numerical errors.

Finally, Figure 6.14 shows the histograms of the examples presented in this section, Figure 6.15 that for the according control experiments and Figure 6.16 the histograms for the components of example 6.3.7.

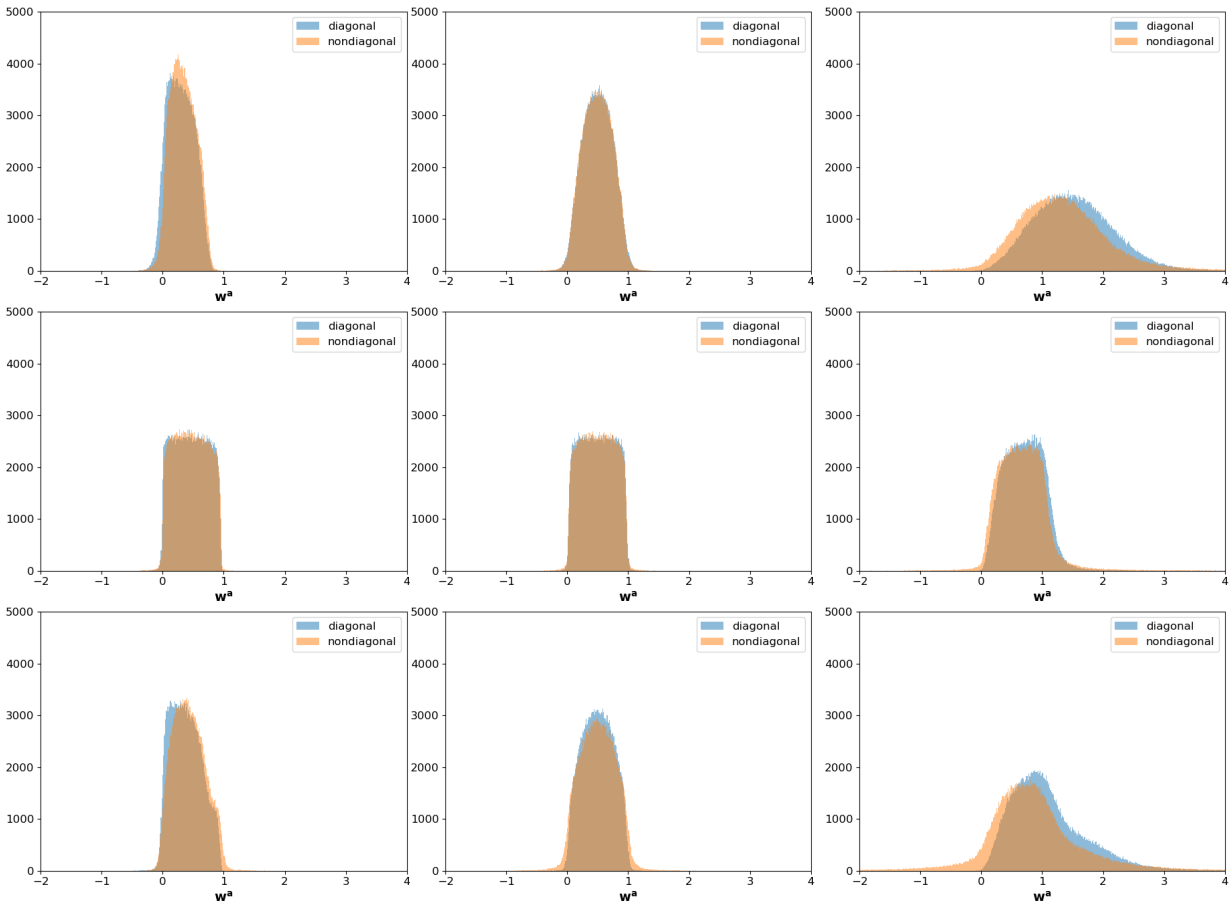

Figure 6.14: Histograms for the distribution of $\mathbf{w}^a$ when using $\mathbf{R}$ (orange) and $\mathbf{R}_{dg}$ (blue) in the situation of example 6.3.2 (upper panel), example 6.3.6 (middle panel) and example 6.3.7 (lower panel), for $\frac{c_o}{c_f} = 0.2$ (left panel), $\frac{c_o}{c_f} = 1.0$ (center panel) and $\frac{c_o}{c_f} = 5.0$ (right panel).

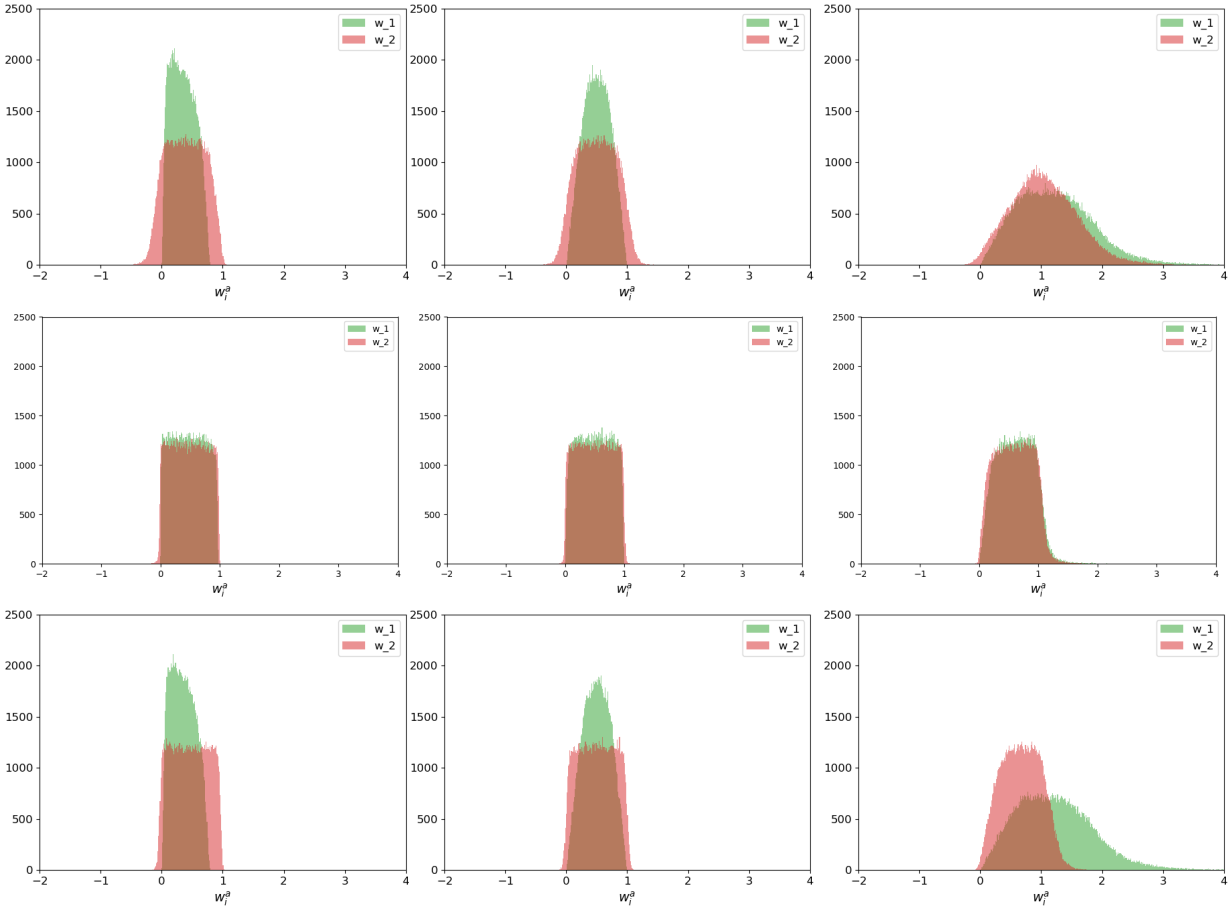

Figure 6.15: Distribution of w_1^a (green) and w_2^a (red) in the reference experiments corresponding to the experiments shown in Figure 6.14.

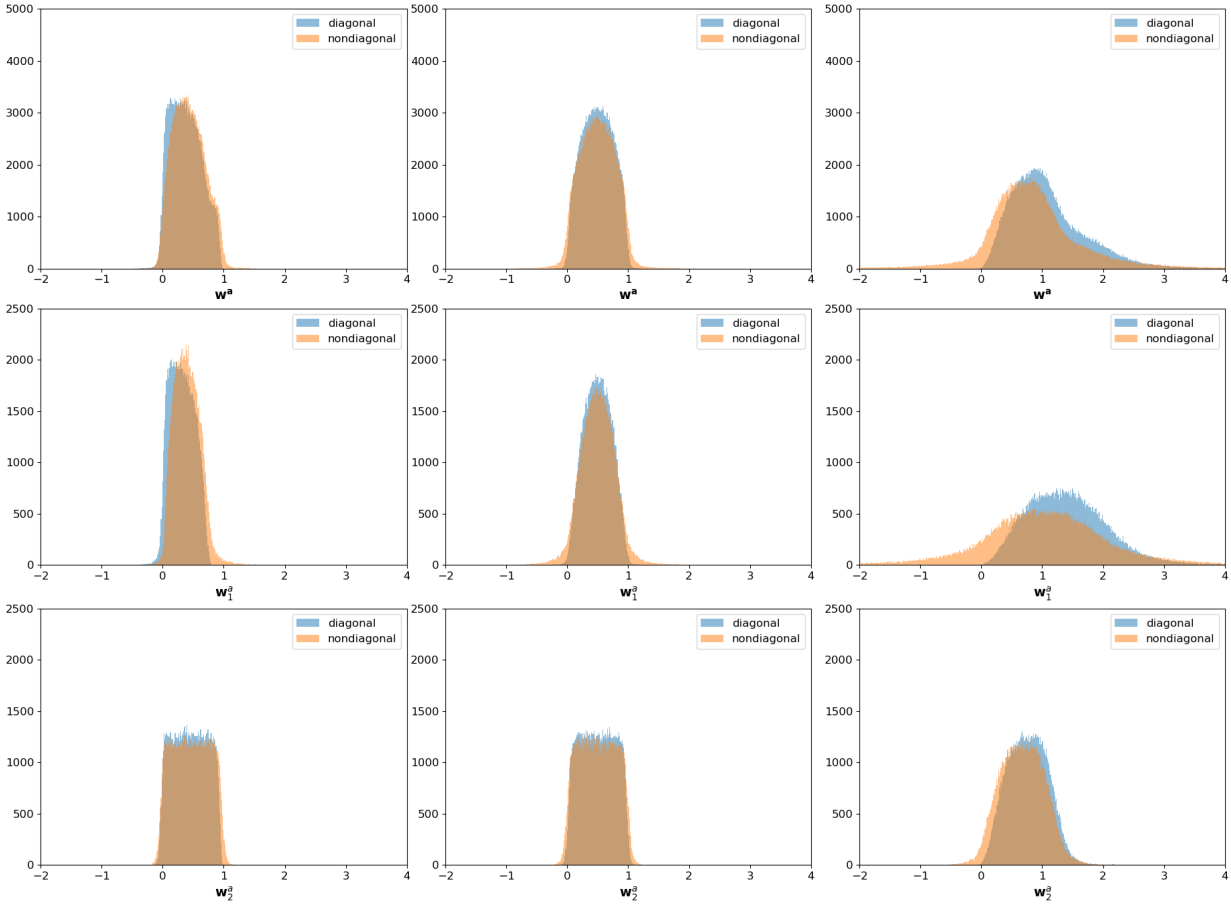

Figure 6.16: Histograms for the distribution of $\mathbf{w}^a$ when using $\mathbf{R}$ (orange) and $\mathbf{R}_{dg}$ (blue) in the situation of example 6.3.7 (upper panel) as well as for the distribution of w_1^a (center panel) and w_2^a (lower panel), for $\frac{c_o}{c_f} = 0.2$ (left panel), $\frac{c_o}{c_f} = 1.0$ (center panel) and $\frac{c_o}{c_f} = 5.0$ (right panel).

We see for the case of example 6.3.6 that especially for low $\frac{c_o}{c_f}$ we obtain a relatively uniform distribution between 0 and 1, and only a small amount of results lying outside that interval. However for $\frac{c_o}{c_f} = 5.0$, the support of the distribution widens considerably and also extends noticeably to negative values if a non-diagonal $\mathbf{R}$ is used. In the case of example 6.3.7 we see a widening of the distribution for $\frac{c_o}{c_f} = 1$, while for $\frac{c_o}{c_f} \neq 1$ we get a more complex distribution, likely resulting from the differences in the probability of negative analysis for both grid points. Note also that the use of non-diagonal $\mathbf{R}$ significantly smooths the distribution and for $\frac{c_o}{c_f} \geq 1$ significantly increases the amount of negative analysis results. For example 6.3.6, the distribution of $\mathbf{w}^a$ is relatively similar to the reference example and no large differences are seen between components or diagonal and non-diagonal case, though in the reference example w_1^a is non-negative as always.

The distribution of w_1^a and w_2^a in the according reference experiment is similar to that in

the diagonal case of example 6.3.7, except for the latter having a higher fraction of negative analysis for $\frac{c_o}{c_f} = 0.2$.

In summary, higher background variances seem to result in higher probability of obtaining negative analysis. Furthermore, they yield a smaller range of $\frac{c_o}{c_f}$ values, for which using non-diagonal $\mathbf{R}$ reduces the chances for negative analysis. Also, when using a $\mathbf{P}^f$ with $a \neq b$ the distributions of w_1^a and w_2^a can differ strongly, which renders assessing the probabilities for obtaining negative analysis more complicated.

6.3.3 Effect of unobserved grid points

Finaly, we examine the effect of not observing every grid point on non-negativity preservation. To this end, we consider an example with three grid points, in which only the first two are observed, using a notation analogue to Notation 6.3.1, with

$$\mathbf{w}^a = \begin{pmatrix} w_1^a \\ w_2^a \\ w_3^a \end{pmatrix}, \mathbf{w}^f = \begin{pmatrix} w_1^f \\ w_2^f \\ w_3^f \end{pmatrix}, \mathbf{P}^f = \begin{pmatrix} a & c & d \\ c & b & e \\ d & e & f \end{pmatrix}. \tag{6.20}$$

In this case, the analysis for the first two components equals that obtained in the two grid point example discussed in the previous sections, while the analysis at the unobserved grid point is obtained by

$$\begin{aligned} w_3^a = w_3^f + \frac{1}{(a+r_1)(b+r_2) - (c+k)^2} \left[\left(d(b+r_2) - e(c+k) \right) \Delta w_1 + \right. \\ \left. \left(e(a+r_1) - d(c+k) \right) \Delta w_2 \right] \end{aligned} \tag{6.21}$$

Example 6.3.8. Let $\mathbf{P}^f$ be given by $a = b = f = 0.33$ and $c = d = e = 0.12$ and let

$$\mathbf{H} = \begin{pmatrix} 1 & 0 & 0 \\ 0 & 1 & 0 \end{pmatrix}, \tag{6.22}$$

then the fraction of experiments that yield at least one negative component of $\mathbf{w}^a$ as a function of $\frac{c_o}{c_f}$ are shown in Figure 6.17.

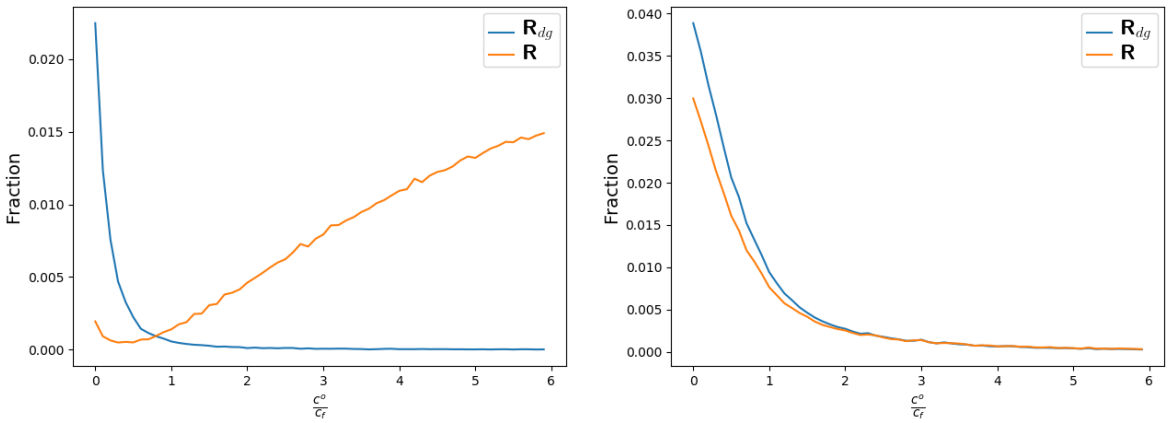

Figure 6.17: Fraction of experiments yielding negative w_2^a (left panel) and w_3^a (right panel) plotted against $\frac{c_o}{c_f}$, when using $\mathbf{R}$ (orange) and $\mathbf{R}_{dg}$ (blue), in the situation of example 6.3.8. w_1^a is not shown here, as it behaves exactly as w_2^a.

Example 6.3.9. Let $\mathbf{P}^f$ given by $a = b = f = 0.33$ and $c = d = e = 0$ and let $\mathbf{H}$ be given by (6.22), then the fraction of experiments that yield at least one negative component of $\mathbf{w}^a$ as a function of $\frac{c_o}{c_f}$ are shown in Figure 6.18.

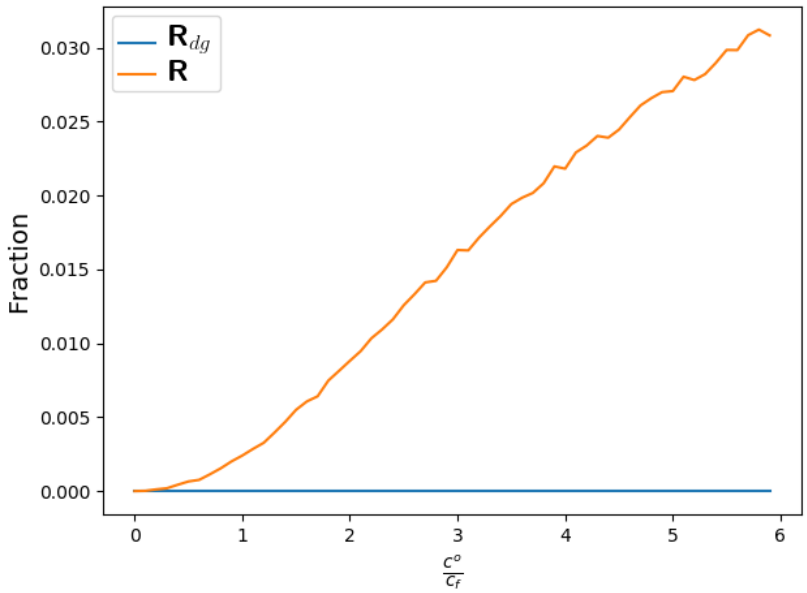

Figure 6.18: Fraction of experiments yielding negative w_2^a plotted against $\frac{c_o}{c_f}$, when using $\mathbf{R}$ (orange) and $\mathbf{R}_{dg}$ (blue), in the situation of example 6.3.9. w_1^a is not shown here, as it behaves exactly as w_2^a and w_3^a is not shown as it is constantly zero.

Example 6.3.10. Let $\mathbf{P}^f$ given by $a = b = f = 0.33$ and $c = d = e = -0.12$ and let

H be given by (6.22), then the fraction of experiments that yield at least one negative component of $\mathbf{w}^a$ as a function of $\frac{c_o}{c_f}$ are shown in Figure 6.19.

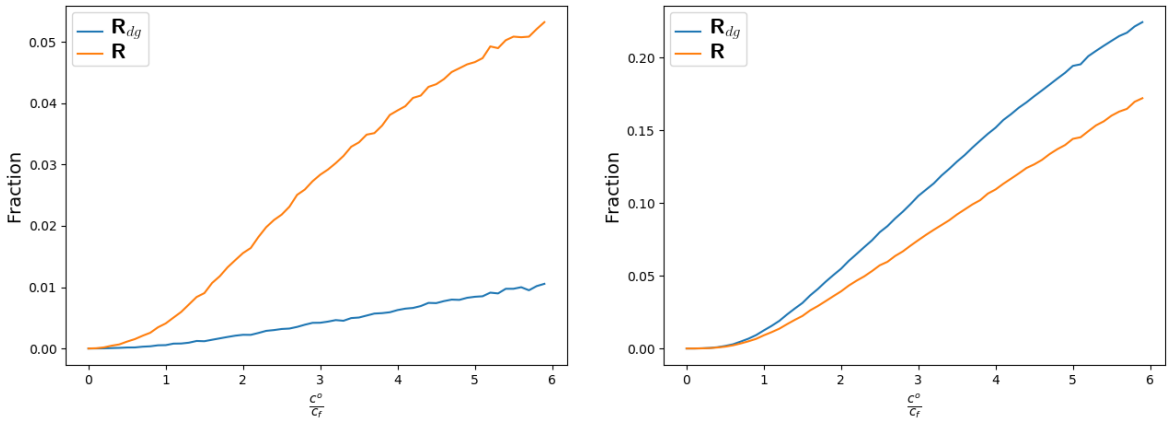

Figure 6.19: Fraction of experiments yielding negative w_2^a (left panel) and w_3^a (right panel) plotted against $\frac{c_o}{c_f}$, when using $\mathbf{R}$ (orange) and $\mathbf{R}_{dg}$ (blue), in the situation of example 6.3.10. w_1^a is not shown here, as it behaves exactly as w_2^a.

As expected, for the observed grid points w_1^a and w_2^a we obtain similar results in examples 6.3.8 to 6.3.10 as in the analogue experiments in the previous section. For the unobserved grid point w_3^a we see no non-negativity violation in example 6.3.9, i.e. when $\mathbf{P}^f$ is diagonal, regardless of observation error correlations, as in absence of background correlations $w_3^a = w_3^f \geq 0$ follows directly from (6.21). In example 6.3.8 the fraction of experiments yielding negative w_3^a decreases with $\frac{c_o}{c_f}$, while it increases with $\frac{c_o}{c_f}$ in example 6.3.10. In both experiments, for the unobserved grid point non-negativity violations are less frequent in the presence of observation error correlations. This can be explained by calculating the ratio of the analysis increment at the unobserved grid point obtained with diagonal $\mathbf{R}$ to that obtained with non-diagonal $\mathbf{R}$, which employing (6.21) yields

$$\frac{w_3^{a,k=0} - w_3^f}{w_3^a - w_3^f} = \tag{6.23}$$
$$= \underbrace{\left(1 - \frac{(c+k)^2}{(a+r_1)(b+r_2)}\right)}_{\text{always} < 1} \underbrace{\left[1 + \frac{ek\Delta w_1 + dk\Delta w_2}{(d(b+r_2) - e(c+k))\Delta w_1 + (e(a+r_1) - d(c+k))\Delta w_2}\right]}_{\text{depends on } \Delta w_1 \text{ and } \Delta w_2}.$$

While the magnitude of the second term in (6.23) depends on the observations (and is probably roughly equally likely to be smaller or larger than 1), the first term is always smaller than 1. Thus, when employing non-diagonal $\mathbf{R}$ we can expect on average higher analysis values (and thus less non-negativity violations) at the unobserved grid point.

In example 6.3.10 non-negativity violations are more common in w_3^a than in w_1^a and w_2^a regardless of observation error correlations, while in example 6.3.8 in the diagonal case, we obtain generally higher rates for w_3^a, whereas in the non-diagonal case the rates of non-negativity violations are higher for w_3^a only for low $\frac{c_o}{c_f}$, while for high $\frac{c_o}{c_f}$ we obtain higher rates for w_1^a and w_2^a. Generally, the behaviour of w_3^a is relatively similar to that seen for w_2^a in example 6.3.1 in the previous section.

6.4 Analytical examples and use as counterexamples

In order to better understand the processes that can lead to negative analysis, as observed in the previous sections, we consider a series of simple examples employing $\mathbf{w}^f$, $\mathbf{w}^o$ and $\mathbf{w}^a$ consisting of only two components. Furthermore, the examples presented in this section can help the efforts to generalize proposition 6.1.1 by serving as counterexamples to quickly disprove conjectures.

6.4.1 Examples illustrating the effect of observation error covariances on non-negativity preservation

For the reminder of the section, we assume $\mathbf{H} = \mathrm{Id}$ and that notation 6.3.1 holds. Using (6.17) and (6.19), (2.16) becomes

$$\mathbf{K} = \begin{pmatrix} a & c \\ c & b \end{pmatrix} \begin{pmatrix} a+r_1 & k+c \\ k+c & b+r_2 \end{pmatrix}^{-1} \tag{6.24}$$

$$= \frac{1}{(a+r_1)(b+r_2)-(k+c)^2} \begin{pmatrix} a(b+r_2)-c(k+c) & -ak+cr_1 \\ cr_2-bk & -c(k+c)+b(a+r_1) \end{pmatrix}. \tag{6.25}$$

Together with (2.15), we obtain for the second component of $\mathbf{w}^a$

$$w_2^a = w_2^f + \frac{1}{(a+r_1)(b+r_2)-(k+c)^2} \left[(cr_2-bk)\Delta w_1 + (b(a+r_1)-c(k+c))\Delta w_2 \right]. \tag{6.26}$$

We first look at the special case of $\mathbf{R}$ being diagonal:

Example 6.4.1. Let $k = 0$, then as shown in appendix H.1, we have $w_2^a \geq 0$, if

$$(a+r_1)w_2^f + \frac{br_1}{r_2} w_2^o + c\Delta w_1 \geq 0. \tag{6.27}$$

As we have seen in Example 6.4.1, e.g. $c\Delta w_1 \geq 0$ would be sufficient when employing diagonal $\mathbf{R}$. However this bound can become too weak to reliable exclude negative w_2^a in

presence of observation error correlations.

We want now to see, if we can still obtain a lower bound for w_2^a for positive w_2^f and positive w_1^o and w_2^o. To this end, despite being very specific, we consider the example $\Delta w_2 \approx 0$, i.e. $\Delta w_2 \in (-\epsilon, \epsilon)$, due to its advantages in illustrating the effects of interactions between grid points and its versatility as counterexample resulting from excluding this case analytically being virtually impossible.

Example 6.4.2. Assume $\Delta w_2 \in (-\epsilon, \epsilon)$, then $w_2^a < 0$ holds, if

$$0 > w_2^f + \underbrace{\frac{cr_2 - bk}{(a+r_1)(b+r_2) - (k+c)^2}}_{=:-g_1} \Delta w_1 + \underbrace{\frac{b(a+r_1) - c(k+c)}{(a+r_1)(b+r_2) - (k+c)^2}}_{=:-g_2} \Delta w_2 \tag{6.28}$$

$$\Leftrightarrow g_1 \Delta w_1 > w_2^f - g_2 \Delta w_2. \tag{6.29}$$

Due to $\Delta w_2 \in (-\epsilon, \epsilon)$ it is sufficient, if

$$g_1 \Delta w_1 > w_2^f + |g_2 \epsilon| \tag{6.30}$$

Now, we distinguish the cases

- $\Delta w_1 > 0$: Here (6.30) becomes

$$g_1 > \frac{w_2^f + |g_2 \epsilon|}{\Delta w_1} \tag{6.31}$$

  This is fulfilled for $|\Delta w_1|$ large enough (this can be achieved, as observations can take values way larger than the forecast, e.g. in case of a misplaced convective cell), if g_1 is positive.

- $\Delta w_1 < 0$: Here (6.30) becomes

$$g_1 < \frac{w_2^f + |g_2 \epsilon|}{\Delta w_1} \tag{6.32}$$

  This can be fulfilled, if g_1 is negative for $|\Delta w_1|$ large enough (however the requirement $w_1^o > 0$ can render this impossible for small values of w_1^f).

Note that $\Delta w_2 = 0$ is a special case of this example, in which the ϵ in (6.31) and (6.32) can be set to zero. Furthermore, $\Delta w_2 \geq -w_2^f$ always holds due to the definition of Δw_2.

In Example 6.4.2, we have seen that negative w_2^a can be achieved in similar conditions as present in convective scale data assimilation for positional errors of convective cells.
We now construct an example illustrating the possible influence of observation error variances on non-negativity preservation:

Example 6.4.3. Assume $k = -c > 0$, then

$$w_2^a = w_2^f + \frac{1}{(a+r_1)(b+r_2)}\left[-(kr_2+bk)\Delta w_1 + b(a+r_1)\Delta w_2\right] \tag{6.33}$$

$$= w_2^f - \frac{k}{(a+r_1)}\Delta w_1 + \frac{b}{(b+r_2)}\Delta w_2 \tag{6.34}$$

$$= w_2^f - \frac{k}{(a+r_1)}\Delta w_1 + \frac{1}{\left(1+\frac{r_2}{b}\right)}\Delta w_2. \tag{6.35}$$

Here, negative w_2^a can be achieved analogue to Example 6.4.2. Note however that in situations with very small w_2^f, Δw_2 can be expected to have a high probability of being positive and thus, due to its positive prefactor in (6.35), is expected to increase w_2^a. Thus overestimating r_2 can increase the probability for negative analysis, if it reduces the effect of Δw_2. This can be caused e.g. by numerical error in situations where the components of $\mathbf{w}$ represent different quantities with strongly differing scales, rather than different grid points.

Furthermore, as increasing the observation error variances is a common practice of accounting for the representation error (Courtier et al., 1998), Example 6.4.3 might also play a role in this context. However, such a procedure would affect both r_1 and r_2, which occur in terms with different signs. Thus estimating the effects on non-negativity preservation is complicated and the result might depend on the exact circumstances.

Finally, we consider an example demonstrating that negative w_2^a can be obtained even without any direct contribution from Δw_1. This will be shown in Appendix H.2. Note that this problem can only occur if non-diagonal $\mathbf{R}$ is used and further conditions on the ratios of background and observation error variances are met.

Despite their lack of relevance for practical applications, these examples are still valuable as counterexamples for analytical conjectures regarding non-negativity preservation, as seen in the following section.

6.4.2 Consequences for generalisation of proposition 6.1.1

In this section, we show how the examples presented in the previous section can be used to determine constraints to a possible generalisation of proposition 6.1.1. We first use example 6.4.2 to show that requiring $\mathbf{P}_f$ and $\mathbf{R}$ to be diagonal in proposition 6.1.1 can not be dropped:

Proposition 6.4.1. *We can not drop the condition of diagonality of* $\mathbf{P}_f$ *in proposition 6.1.1.*

Proof. Assuming proposition 6.1.1 would hold without demanding diagonality of $\mathbf{P}_f$, in the case of example 6.4.2, positivity of analysis would be guaranteed. However, due to $c \neq 0$ we have $f \neq 0$ and (6.30) can still be fulfilled. Thus both cases outlined in example 6.4.2 yield $w_2^a \leq 0$. □

Proposition 6.4.2. *We can not drop the condition of diagonality of* $\mathbf{R}$ *in proposition 6.1.1.*

Proof. Analogue to proposition 6.4.1. □

Furthermore, as example 6.4.2 provides examples for obtaining negative analysis for both positive and negative g_1, relaxing the condition of diagonality for $\mathbf{P}_f$ or $\mathbf{R}$ to constraining the sign of the correlations does not seem promising. However, as the proofs of proposition 6.4.1 and proposition 6.4.2 depend on (6.30), a possible strategy for generalizing proposition 6.1.1 could be trying to replace diagonality of $\mathbf{P}_f$ and $\mathbf{R}$ by further constraints on $\mathbf{w}^o$, linking positivity preservation and quality control. E.g. if we observe at every grid point, we can show for bounded $\|\Delta\mathbf{w}\|_\infty$ and strictly positive w_i^f, that also for $\mathbf{P}_f$ and $\mathbf{R}$ with sufficiently small non-diagonal elements, non-negativity of analysis is guaranteed:

Proposition 6.4.3. *Let* $\mathbf{H} = \mathrm{Id}$*, and let* $w_i^o \geq 0$ *and* $w_i^f > 0$*, for all* $i \in \{1, \cdots, n\}$*. Furthermore let* $\|\Delta\mathbf{w}\|_\infty \leq c_w$ *, for some* $c_w \in \mathbb{R}_+$ *and* $\hat{\mathbf{P}}^f, \hat{\mathbf{R}} \in M_n$ *diagonal and positive definite. Then exists a* ϵ*, such that for all* $\mathbf{P}^f \in M_n$ *and* $\mathbf{R} \in M_n$ *with* $\left\|\mathbf{P}^f - \hat{\mathbf{P}}^f\right\|_\infty < \epsilon$ *and* $\left\|\mathbf{R} - \hat{\mathbf{R}}\right\|_\infty < \epsilon$ *we have* $w_i^a \geq 0$*, for all* $i \in \{1, \cdots, n\}$*.*

Proof. Follows from proposition 6.1.2, using continuity of sum, matrix multiplication and inversion. For details see appendix H.4. □

Note that for special cases much stricter versions of proposition 6.4.3 should exist, as the above proof uses relatively coarse approximations. However, we cannot relinquish the strict positivity of w_i^f:

Proposition 6.4.4. *We can not relax* $w_i^f > 0$ *to* $w_i^f \geq 0$ *in proposition 6.4.3.*

Proof. Example 6.4.2 with $w_2^f = 0$ and $\Delta w_2 = 0$ provides a counterexample to a generalization of proposition 6.4.3 with $w_i^f > 0$ replaced by $w_i^f \geq 0$, as (6.30) becomes

$$f\Delta w_1 > 0, \tag{6.36}$$

which can be fulfilled if $\mathbf{P}^f$ or $\mathbf{R}$ are non-diagonal, as then $c \neq 0$ or $k \neq 0$ and thus $f \neq 0$. Then $\operatorname{sgn}(f) = -\operatorname{sgn}(\Delta w_1)$ is sufficient.

□

Finally we note that (also considering the results of section 6.3) finding a statistical bound limiting $\mathbb{P}(\{\mathbf{w}^a < 0\})$ might be practically more relevant, especially for high dimensional problems, as an analytical condition would be determined by the (increasingly unlikely)

worst case scenarios. Just the probability of the signs of all Δw_i aligning in the worst possible way is 2^{-n} for a system with n measurements, making the according worst case scenario extremely unlikely (and thus practically irrelevant for a stochastic approach) for large n. However, there are already several other promising approaches to tackling non-negativity preservation, such as the QPEns filter of Janjić et al. (2014) and approaches involving truncated Gaussians (Lauvernet et al., 2009).

6.5 Summary

In summary, we have seen that there exists a wide range of scenarios yielding negative analysis, ranging from (the already known effects of) positional and amplitude error of peaks to more abstract cases. Despite their limited practical relevance, the latter ones can be used as counterexamples to show that relaxing the requirement of $\mathbf{P}_f$ and $\mathbf{R}$ being diagonal for Proposition 6.1.1 is not possible. Furthermore, we have seen that the effects of employing non-diagonal $\mathbf{R}$ in DA on non-negativity-preservation are highly situation dependent. Thus we summarized the according results in Table 6.1.

Chapter 7

Future work

In this chapter, we outline promising directions of future work. We start by discussing different options to extend to the SPM in Section 7.1, such as including a more realistic observation operator in Section 7.1.1, a generalization to variable particle numbers in Section 7.1.2, as well as possible interaction models in Section 7.1.3. Thereafter we consider possible applications of the SPM in Section 7.2. In Section 7.3, we give a short outlook on the possible use of neural networks trained with output from the SPM.

7.1 Extensions to the SPM

We are now going to discuss possible extensions of the SPM, from more complicated observation operators in Section 7.1.1 over a generalization to a variable particle number in Section 7.1.2 to possible interaction models in Section 7.1.3.

7.1.1 Observation operators

As directly observing number density and liquid water content at every grid point is unrealistic for practical applications, employing a more realistic observation operator to the SPM would be of interest for future work.

7.1.1.1 General setup and constraints

We now discuss possible options for defining observation operators on the continuum and particle based state spaces and the according challenges. Possible setups for defining simple observation operators are shown in Figure 7.1: An absorption based observation operator can be defined on the continuum model as well as on the particle based one, as it (if sufficiently simplified) will only depend on the liquid water content. Thus, despite loosing some information about the variation of the resulting intensity in the x- and y-direction, both models will yield comparable observations.

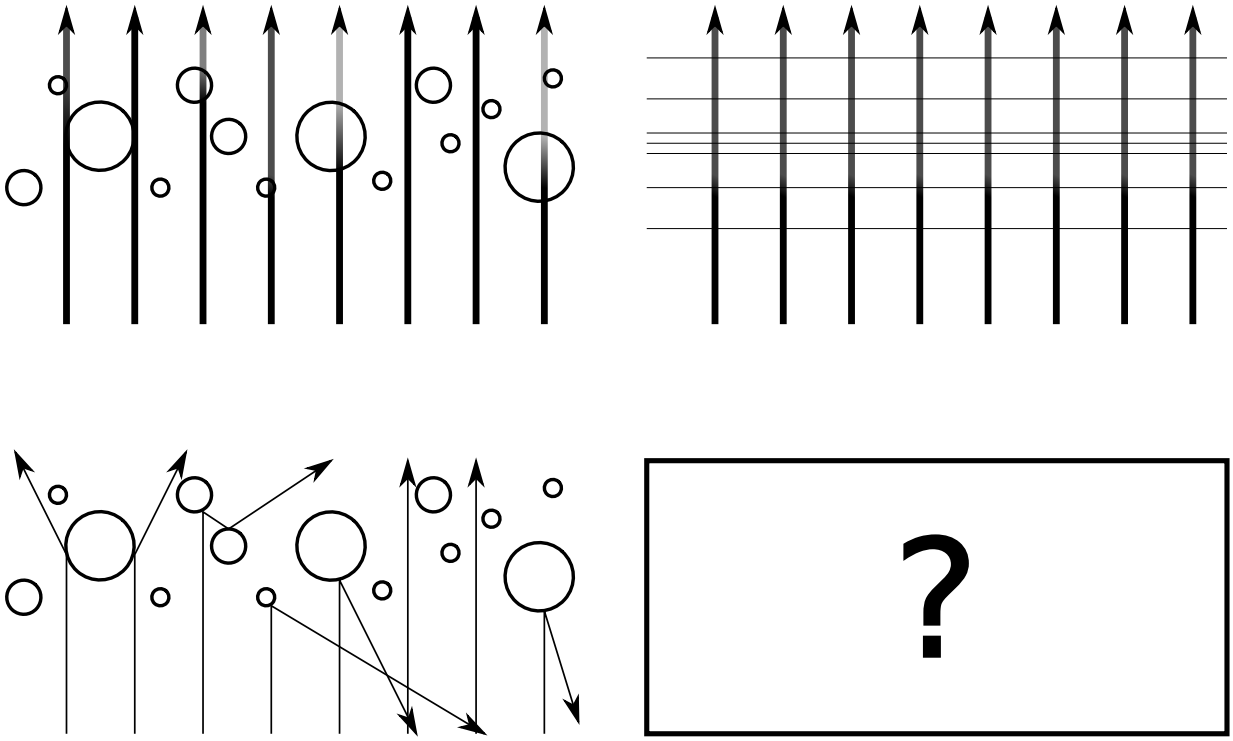

Figure 7.1: Possible setups for definitions of strongly simplified observation operators for particle based (left side) and analogue continuum models (right side). An absorption based observation operator is depicted in the upper panels, with the colour of the arrows indicating the according intensity and horizontal lines constant levels of the liquid water content. The lower panels show a reflection based observation operator, whereas the missing panel on the right side illustrates that a definition for the continuum model is not easily possible due to the loss of relevant information.

On the other hand a very simple reflection based observation operator can (assuming geometrical optics and the hydrometeors to be perfectly reflecting spheres) still be easily defined for the particle based model, whereas finding an analogue definition for the continuum model is problematic, as here information about the exact hydrometeor positions and diameters is not available (however some information might be inferred e.g. from the derivatives of the liquid water content and number density profiles).

In general, an observation operator defined for the continuum model can be easily extended to the particle based one, as it only needs to be concatenated with the according map (see (3.2) and (3.3)), whereas extending observation operators from the particle based model to the continuum model can be (as these maps usually are not invertible) difficult or even impossible.

7.1.1.2 Kernel based observation operators

It is common (see e.g. Janjić et al. (2018)) for observation operators on continuum models to be defined as a convolution of the state with a kernel κ, i.e.

$$H\left(Z_{z,t}\right) = \int \kappa\left(z' - z\right) Z_{z',t} dz', \tag{7.1}$$

which can using (3.14) be extended to the according particle based model.

One can also (at least numerically) calculate the expectation values and covariances for this observation operator: The expectation value is given by

$$\begin{aligned}
\mathbb{E}\left[H\left(Z_{z,t}\right)\right] &= \mathbb{E}\left[\int \kappa\left(z' - z\right) Z_{z',t} dz'\right] \\
&= \mathbb{E}\left[\int \kappa\left(z' - z\right) \sum_{j=1}^{n} \mathbf{1}_{\left[z' - \frac{D_j}{2}, z' + \frac{D_j}{2}\right]}\left(z_j\left(t\right)\right) g_Z\left(D_j\right) f\left(D_j, z_j, t, z'\right) dz'\right] \\
&= \mathbb{E}\left[\sum_{j=1}^{n} g_Z\left(D_j\right) \int \kappa\left(z' - z\right) \mathbf{1}_{\left[z_j(t) - \frac{D_j}{2}, z_j(t) + \frac{D_j}{2}\right]}\left(z'\right) f\left(D_j, z_j, t, z'\right) dz'\right] \\
&= \mathbb{E}\left[\sum_{j=1}^{n} g_Z\left(D_j\right) \int_{z_j(t) - \frac{D_j}{2}}^{z_j(t) + \frac{D_j}{2}} \kappa\left(z' - z\right) f\left(D_j, z_j, t, z'\right) dz'\right].
\end{aligned} \tag{7.2}$$

Now, by considerations analogue to Assumption 3.2.1 we obtain

$$\begin{aligned}
\mathbb{E}\left[H\left(Z_{z,t}\right)\right] &= \int \sum_{j=1}^{n} g_Z\left(D_j\right) \int_{z_j(t) - \frac{D_j}{2}}^{z_j(t) + \frac{D_j}{2}} \kappa\left(z' - z\right) f\left(D_j, z_j, t, z'\right) dz' d\mathbb{P}\left(\mathbf{z}, \mathbf{D}\right) \\
&= \sum_{j=1}^{n} \int g_Z\left(D_j\right) \int_{z_j(t) - \frac{D_j}{2}}^{z_j(t) + \frac{D_j}{2}} \kappa\left(z' - z\right) f\left(D_j, z_j, t, z'\right) dz' d\mathbb{P}\left(z_j, D_j\right) \\
&= \sum_{j=1}^{n} \int_0^\infty \int_{-\infty}^{\infty} g_Z\left(D_j\right) \int_{z_j(t) - \frac{D_j}{2}}^{z_j(t) + \frac{D_j}{2}} \kappa\left(z' - z\right) f\left(D_j, z_j, t, z'\right) dz' \rho_D\left(D_j\right) \rho_z\left(z_j\right) dz_j dD_j \\
&= \sum_{j=1}^{n} \int_0^\infty g_Z\left(D_j\right) \rho_D\left(D_j\right) \int_{-\infty}^{\infty} \int_{z_j(t) - \frac{D_j}{2}}^{z_j(t) + \frac{D_j}{2}} \kappa\left(z' - z\right) f\left(D_j, z_j, t, z'\right) dz' \rho_z\left(z_j\right) dz_j dD_j \\
&= n \cdot \int_0^\infty g_Z\left(D_j\right) \rho_D\left(D_j\right) \int_{-\infty}^{\infty} \int_{z_j(t) - \frac{D_j}{2}}^{z_j(t) + \frac{D_j}{2}} \kappa\left(z' - z\right) f\left(D_j, z_j, t, z'\right) dz' \rho_z\left(z_j\right) dz_j dD_j.
\end{aligned} \tag{7.3}$$

Some further simplification of (7.3) might still be possible by interchanging the integrals. However from this point likely a numerical approach is necessary.
We now turn to the the covariances, which can be obtained in an analogue way. We have

$$\mathrm{Cov}\left(H\left(X_{x,t}\right), H\left(Y_{y,s}\right)\right) = \mathbb{E}\left[H\left(X_{x,t}\right) H\left(Y_{y,s}\right)\right] - \mathbb{E}\left[H\left(X_{x,t}\right)\right] \mathbb{E}\left[H\left(Y_{y,s}\right)\right], \tag{7.4}$$

which we can further simplify by calculating (similar to Section 3.2)

$$\begin{aligned}
\mathbb{E}\left[H\left(X_{x,t}\right) H\left(Y_{y,s}\right)\right] &= \mathbb{E}\left[\int \kappa\left(x'-x\right) X_{x',t} dx' \int \kappa\left(y'-y\right) Y_{y',s} dy'\right] \\
&= \mathbb{E}\left[\sum_{j=1}^{n} g_X\left(D_j\right) \int_{z_j(t)-\frac{D_j}{2}}^{z_j(t)+\frac{D_j}{2}} \kappa\left(x'-x\right) f\left(D_j, z_j, t, x'\right) dx' \cdot \right. \\
&\quad \left. \cdot \sum_{k=1}^{n} g_Y\left(D_k\right) \int_{z_k(s)-\frac{D_k}{2}}^{z_k(s)+\frac{D_k}{2}} \kappa\left(y'-y\right) f\left(D_k, z_k, s, y'\right) dy'\right] \\
&= \sum_{j=1}^{n}\sum_{k=1}^{n} \int g_X\left(D_j\right) \int_{z_j(t)-\frac{D_j}{2}}^{z_j(t)+\frac{D_j}{2}} \kappa\left(x'-x\right) f\left(D_j, z_j, t, x'\right) dx' \cdot \\
&\quad \cdot g_Y\left(D_k\right) \int_{z_k(s)-\frac{D_k}{2}}^{z_k(s)+\frac{D_k}{2}} \kappa\left(y'-y\right) f\left(D_k, z_k, s, y'\right) dy' d\mathbb{P}\left(z_j, D_j, z_k, D_k\right)
\end{aligned} \tag{7.5}$$

and splitting the sum into

$$\begin{aligned}
\mathbb{E}\left[H\left(X_{x,t}\right) H\left(Y_{y,s}\right)\right] &= \sum_{j=1}^{n}\sum_{\substack{k=1 \\ k\neq j}}^{n} \int g_X\left(D_j\right) \int_{z_j(t)-\frac{D_j}{2}}^{z_j(t)+\frac{D_j}{2}} \kappa\left(x'-x\right) f\left(D_j, z_j, t, x'\right) dx' \cdot \\
&\quad \cdot g_Y\left(D_k\right) \int_{z_k(s)-\frac{D_k}{2}}^{z_k(s)+\frac{D_k}{2}} \kappa\left(y'-y\right) f\left(D_k, z_k, s, y'\right) dy' d\mathbb{P}\left(z_j, D_j, z_k, D_k\right) + \\
&\quad + \sum_{j=1}^{n} \int g_X\left(D_j\right) \int_{z_j(t)-\frac{D_j}{2}}^{z_j(t)+\frac{D_j}{2}} \kappa\left(x'-x\right) f\left(D_j, z_j, t, x'\right) dx' \cdot \\
&\quad \cdot g_Y\left(D_j\right) \int_{z_j(s)-\frac{D_j}{2}}^{z_j(s)+\frac{D_j}{2}} \kappa\left(y'-y\right) f\left(D_j, z_j, s, y'\right) dy' d\mathbb{P}\left(z_j, D_j\right) \\
&= \sum_{j=1}^{n}\sum_{\substack{k=1 \\ k\neq j}}^{n} \int g_X\left(D_j\right) \int_{z_j(t)-\frac{D_j}{2}}^{z_j(t)+\frac{D_j}{2}} \kappa\left(x'-x\right) f\left(D_j, z_j, t, x'\right) dx' d\mathbb{P}\left(z_j, D_j\right) \cdot \\
&\quad \cdot \int g_Y\left(D_k\right) \int_{z_k(s)-\frac{D_k}{2}}^{z_k(s)+\frac{D_k}{2}} \kappa\left(y'-y\right) f\left(D_k, z_k, s, y'\right) dy' \mathbb{P}\left(z_k, D_k\right) + \\
&\quad + \sum_{j=1}^{n} \int g_X\left(D_j\right) \int_{z_j(t)-\frac{D_j}{2}}^{z_j(t)+\frac{D_j}{2}} \kappa\left(x'-x\right) f\left(D_j, z_j, t, x'\right) dx' \cdot \\
&\quad \cdot g_Y\left(D_j\right) \int_{z_j(s)-\frac{D_j}{2}}^{z_j(s)+\frac{D_j}{2}} \kappa\left(y'-y\right) f\left(D_j, z_j, s, y'\right) dy' d\mathbb{P}\left(z_j, D_j\right),
\end{aligned} \tag{7.6}$$

where we used the independence of the properties of the individual hydrometeors. Now, we obtain

$$\begin{aligned}\mathbb{E}\left[H\left(X_{x,t}\right)H\left(Y_{y,s}\right)\right] = &\sum_{j=1}^{n}\int g_X\left(D_j\right)\int_{z_j(t)-\frac{D_j}{2}}^{z_j(t)+\frac{D_j}{2}}\kappa\left(x'-x\right)f\left(D_j,z_j,t,x'\right)dx'd\mathbb{P}\left(z_j,D_j\right)\cdot\\ &\cdot\sum_{k=1}^{n}\int g_Y\left(D_k\right)\int_{z_k(s)-\frac{D_k}{2}}^{z_k(s)+\frac{D_k}{2}}\kappa\left(y'-y\right)f\left(D_k,z_k,s,y'\right)dy'\mathbb{P}\left(z_k,D_k\right)-\\ &-\sum_{j=1}^{n}\int g_X\left(D_j\right)\int_{z_j(t)-\frac{D_j}{2}}^{z_j(t)+\frac{D_j}{2}}\kappa\left(x'-x\right)f\left(D_j,z_j,t,x'\right)dx'd\mathbb{P}\left(z_j,D_j\right)\cdot\\ &\cdot\int g_Y\left(D_j\right)\int_{z_j(s)-\frac{D_j}{2}}^{z_j(s)+\frac{D_j}{2}}\kappa\left(y'-y\right)f\left(D_j,z_j,s,y'\right)dy'\mathbb{P}\left(z_j,D_j\right)+\\ &+\sum_{j=1}^{n}\int g_X\left(D_j\right)\int_{z_j(t)-\frac{D_j}{2}}^{z_j(t)+\frac{D_j}{2}}\kappa\left(x'-x\right)f\left(D_j,z_j,t,x'\right)dx'\cdot\\ &\cdot g_Y\left(D_j\right)\int_{z_j(s)-\frac{D_j}{2}}^{z_j(s)+\frac{D_j}{2}}\kappa\left(y'-y\right)f\left(D_j,z_j,s,y'\right)dy'd\mathbb{P}\left(z_j,D_j\right),\end{aligned}\tag{7.7}$$

which becomes

$$\begin{aligned}\mathbb{E}\left[H\left(X_{x,t}\right)H\left(Y_{y,s}\right)\right] = &\,\mathbb{E}\left[H\left(X_{x,t}\right)\right]\mathbb{E}\left[H\left(Y_{y,s}\right)\right]-\\ &-\sum_{j=1}^{n}\int g_X\left(D_j\right)\int_{z_j(t)-\frac{D_j}{2}}^{z_j(t)+\frac{D_j}{2}}\kappa\left(x'-x\right)f\left(D_j,z_j,t,x'\right)dx'd\mathbb{P}\left(z_j,D_j\right)\cdot\\ &\cdot\int g_Y\left(D_j\right)\int_{z_j(s)-\frac{D_j}{2}}^{z_j(s)+\frac{D_j}{2}}\kappa\left(y'-y\right)f\left(D_j,z_j,s,y'\right)dy'\mathbb{P}\left(z_j,D_j\right)+\\ &+\sum_{j=1}^{n}\int g_X\left(D_j\right)\int_{z_j(t)-\frac{D_j}{2}}^{z_j(t)+\frac{D_j}{2}}\kappa\left(x'-x\right)f\left(D_j,z_j,t,x'\right)dx'\cdot\\ &\cdot g_Y\left(D_j\right)\int_{z_j(s)-\frac{D_j}{2}}^{z_j(s)+\frac{D_j}{2}}\kappa\left(y'-y\right)f\left(D_j,z_j,s,y'\right)dy'd\mathbb{P}\left(z_j,D_j\right),\end{aligned}\tag{7.8}$$

together with (7.4), yielding

$$\begin{aligned}\operatorname{Cov}\left(H\left(X_{x,t}\right), H\left(Y_{y,s}\right)\right) = \sum_{j=1}^{n} \int g_X\left(D_j\right) \int_{z_j(t)-\frac{D_j}{2}}^{z_j(t)+\frac{D_j}{2}} \kappa\left(x'-x\right) f\left(D_j, z_j, t, x'\right) dx' \cdot \\ \cdot\, g_Y\left(D_j\right) \int_{z_j(s)-\frac{D_j}{2}}^{z_j(s)+\frac{D_j}{2}} \kappa\left(y'-y\right) f\left(D_j, z_j, s, y'\right) dy' d\mathbb{P}\left(z_j, D_j\right) - \\ - \sum_{j=1}^{n} \int g_X\left(D_j\right) \int_{z_j(t)-\frac{D_j}{2}}^{z_j(t)+\frac{D_j}{2}} \kappa\left(x'-x\right) f\left(D_j, z_j, t, x'\right) dx' d\mathbb{P}\left(z_j, D_j\right) \cdot \\ \cdot \int g_Y\left(D_j\right) \int_{z_j(s)-\frac{D_j}{2}}^{z_j(s)+\frac{D_j}{2}} \kappa\left(y'-y\right) f\left(D_j, z_j, s, y'\right) dy' \mathbb{P}\left(z_j, D_j\right).\end{aligned} \tag{7.9}$$

Again, employing considerations analogue to Assumption 3.2.1 allows some further simplifications (not shown here) after which the according integrals can be computed numerically. However, it is yet to be determined, which formulation is the numerically most efficient.

We assumed $H = \mathrm{Id}$ in all our DA experiments. However when using a different observation operator, $\operatorname{Cov}\left(H\left(X_{x,t}\right), H\left(Y_{y,s}\right)\right)$ can again be used as proxy for the observation error covariance matrix potentially now also incorporating an observation operator error besides the error due to unresolved scales and processes.

7.1.2 Generalization to variable particle number

A major restriction of the SPM is the assumption of a fixed particle number. Thus we will now employ standard techniques from stochastic geometry, to take the first steps towards constructing measures $\hat{L}$ and $\hat{N}$ from n_η and l_η that represent liquid water content and number density, while allowing for a variable particle number. Furthermore, in the end of this section we discuss the relation of $\hat{L}$ and $\hat{N}$ to the standard definitions of L and N, as this is easier than relating n_η and l_η to L and N directly.

Definition 7.1.1. Given the assumptions of Definition 3.2.2, let[1] $\mu_N\left(\eta, \cdot\right) : \mathcal{B}\left(\mathbb{R}\right) \to \mathbb{R}_+$, $A \mapsto \mu_N\left(\eta, A\right)$ and $\mu_L\left(\eta, \cdot\right) : \mathcal{B}\left(\mathbb{R}\right) \to \mathbb{R}_+$, $A \mapsto \mu_L\left(\eta, A\right)$, with

$$\mu_N\left(\eta, A\right) = \int_A n_\eta\left(z\right) dz \tag{7.10}$$

$$\mu_L\left(\eta, A\right) = \int_A l_\eta\left(z\right) dz, \tag{7.11}$$

for all $A \in \mathcal{B}\left(\mathbb{R}\right)$.

Proposition 7.1.1. *$\mu_N\left(\eta, \cdot\right)$ and $\mu_L\left(\eta, \cdot\right)$ defined in Definition 7.1.1 are measures on $\mathcal{B}\left(\mathbb{R}\right)$.*

[1] $\mathcal{B}\left(\mathbb{R}\right)$ denotes the Borel σ-algebra on $\mathbb{R}$.

Proof. Follows directly from the definition.

□

To take care of the stochastic initial conditions, we assume the distribution of η being given by a probability measure $\mathbb{P}$.

Definition 7.1.2. Given the assumptions of Definition 7.1.1, let $\mathbb{P}$ be a probability measure on $\mathcal{N}$ (equipped with a suitable σ-algebra). Furthermore, let $\hat{N} : \mathcal{B}(\mathbb{R}) \to \mathbb{R}_+$, $A \mapsto \hat{N}(A)$ and $\hat{L} : \mathcal{B}(\mathbb{R}) \to \mathbb{R}_+$, $A \mapsto \hat{L}(A)$, with

$$\hat{N}(A) = \mathbb{E}\left[\mu_N(\cdot, A)\right] \tag{7.12}$$

$$\hat{L}(A) = \mathbb{E}\left[\mu_L(\cdot, A)\right], \tag{7.13}$$

for all $A \in \mathcal{B}(\mathbb{R})$.

Existence and uniqueness of $\hat{L}$ and $\hat{N}$ can likely be shown using known results on *intensity measures* (see e.g. Jansen (2018)). We however leave this proof (as well as showing that $\hat{L}$ and $\hat{N}$ actually are measures on $\mathcal{B}(\mathbb{R})$) for further work and assume the according statements to hold. Note, that Definition 7.1.2 does not necessarily require the particle number to be constant and thus is a first step to generalizing the SPM. Furthermore, quantities in the form of (7.12) and (7.13) are relatively common in stochastic geometry and extensive theory for them exists.

We now (up to boundary issues) can relate $\hat{L}$ and $\hat{N}$ to L and N.

Remark 7.1.1. Given the assumptions of Definition 7.1.2, let ϵ be the free parameter of the Wacker and Seifert (2001) reference model and $z \in \mathbb{R}^+$. Furthermore, assume that non-zero probability is only assigned to states containing exactly n particles and that n is large. Then (neglecting hydrometeors at the boundary), we can approximate

$$\begin{aligned} N(z) &\approx \frac{1}{2\epsilon}\hat{N}([z-\epsilon, z+\epsilon]) \\ &\approx \frac{1}{2\epsilon}\mu_N(\eta, [z-\epsilon, z+\epsilon]) \end{aligned} \tag{7.14}$$

and

$$\begin{aligned} L(z) &\approx \frac{1}{2\epsilon}\hat{L}([z-\epsilon, z+\epsilon]) \\ &\approx \frac{1}{2\epsilon}\mu_L(\eta, [z-\epsilon, z+\epsilon]), \end{aligned} \tag{7.15}$$

using an η drawn from $\mathbb{P}$.

Note, that a discussion of the direct relation between n_η and l_η to L and N (including the treatment of hydrometeors at the boundary) is shown in Appendix A.

7.1.3 Interaction models

An further interesting addition to the SPM would be interactions between particles, like collisions or processes that create or destroy hydrometeors. With respect to the overall goal of studying the structure of the covariance matrices derived from the SPM, the following classes of processes would especially be of interest:

- Deterministic collisions
- Stochastic collisions
- Deterministic creation and/or destruction of hydrometeors
- Stochastic creation and/or destruction of hydrometeors

Here stochastic interactions would induce a new source of randomness and combining them with stochastic or deterministic initial conditions would also be of interest. Another interesting direction would be comparing relatively similar interaction models with deterministic and stochastic dynamics. A very simple example would be deterministically joining hydrometeors that overlap sufficiently or assign them a probability of merging proportional to the volume of intersection (see Figure 7.2).

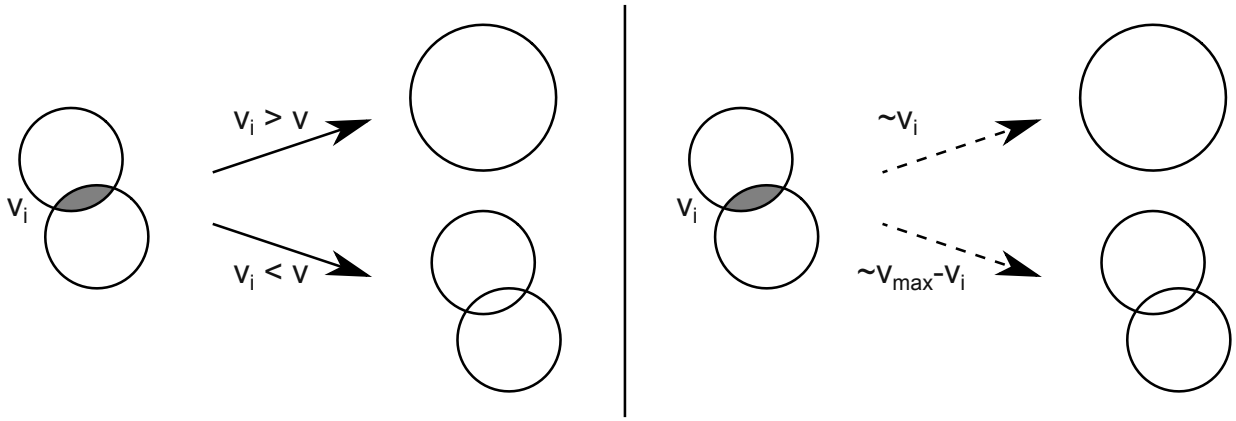

Figure 7.2: Simple deterministic (left panel) and stochastic (right panel) interaction models. Hydrometeors are either merged, when their intersection volume v_i exceeds a threshold v, or with a probability proportional to v_i.

However, when interactions are added to the SPM, the according equations become far more complicated. Thus, to obtain the according covariance matrices probably a more numerics based approach would be necessary and computational cost would significantly increase. Furthermore, the results can depend on the time step of the model and the order in which particles are merged. Thus ensuring a sufficiently small time step and consistent merging procedure are required before implementing an according extension to the SPM.

More realistic interactions can be introduced by a kernel based approach (see e.g. Murrell et al. (2004) for an example from theoretical ecology). Rewriting the according equations in the language of stochastic geometry (see e.g. Semrau (2020) for an according rewriting of the equations of Murrell et al. (2004)), would then allow to calculate the according error covariance matrices, or even employ more advanced concepts from stochastic geometry like factorial moment measures.

7.2 Possible applications of the SPM

As the stochasticity in the SPM originates purely from the stochastic initial conditions, it is particularly suitable to study that aspect. This is e.g. of interest, as according to Morrison et al. (2020) uncertain initial conditions are one of the major challenges in their suggested *Bayesian approach to scheme development*. However, to be useful in this context, extending the SPM with more complex dynamics (see Section 7.1.3) might be necessary, as Morrison et al. (2020) consider this problem in the context of chaotic systems. Implementing more complex dynamics would also be of interest on its own, as it would allow to identify the features of observation error covariance matrices caused by these dynamics. In this setup, the covariances obtained from the current form of the SPM can function as a baseline showing only the effects of particle geometry and gravitational sorting.

When extending the SPM with an interaction scheme that allows for particles to change their diameter, it also might be of use for studying *eddy hopping*, i.e. "the role of mixing of different droplet populations that have undergone different growth histories on [size distribution] broadening" (Morrison et al., 2020). Here again, the current implementation can function as baseline.

As the SPM allows to perturb the initial fall velocities and to relatively easily implement different dynamics, it can also be used to study the effect of different assumptions on the hydrometeor velocities. This is of interest, as according to Zeng et al. (2021), wrongly specified terminal hydrometeor fall speeds are a potential source of error when predicting *radial wind*.

Furthermore, repeating the DA experiments from Chapter 5 for cylindrical hydrometeors (or a mixture of spherical and cylindrical hydrometeors) is easily possible with only minor modifications to the existing code.

7.3 Neural network

Two modern approaches to modelling hydrometeors are neural networks and Lagrangian particle models. In this section, we sketch a possible option for combining these concepts to calculate the time evolution of the L and N profiles. A commonly used Lagrangian par-

ticle model is the superdroplet approach of Shima et al. (2009), describing the system by n superdroplets with the i-th superdroplet representing n_i identical copies of hydrometeors with position z_i and diameter D_i. We suggest an architecture for a NN, that only contains the connections necessary for evolving the L and N profiles by approximating them using the superdroplet approach.

Before we discuss the architecture, we give the necessary background information on neural networks following the description and (a slightly modified) notation of Bishop (2006) (equation (5.2) and (5.3)): The output $\mathbf{x}'$ of a layer of a neural network with input $\mathbf{x}$ is given by

$$x'_j = h\left(\sum_{i=1}^{D} w_{ji}x_i + w_{j0}\right), \tag{7.16}$$

for all $j \in \{1, \cdots, M\}$, with D and M being the dimension of $\mathbf{x}$ and $\mathbf{x}'$, h the *activation function*, w_{ji} the *weights* and w_{j0} the *biases*.

Now, we turn to the construction of the architecture (see Figure 7.3) mimicking the superdroplet approach: The input layer consists of the initial liquid water content and number density values for each gridpoint. These are decomposed in n superdroplets in the first (fully connected) hidden layer. Subsequently, we evolve the superdroplets by a part of the neural network containing only the connections necessary for the superdroplet approximation. As in absence of processes, which destroy or create hydrometeors or change their diameter, n_i and D_i stay constant over time, they can be directly be passed to the penultimate layer. Furthermore, as D_i can have an influence on the dynamics of z_i, it needs to be passed (together with z_i) to NN_{vel}, the part of the network which calculates the time evolution of z_i. The architecture of NN_{vel} is depicted in Figure 7.4 and will be discussed in more detail in the next paragraph. Finally, the time evolved super droplets are again combined to discretized liquid water content and number density profiles in the output layer. Also note, that only the first and last layer of the network are fully connected, while information about the structure of the problem is directly encoded in the remaining part of the architecture.

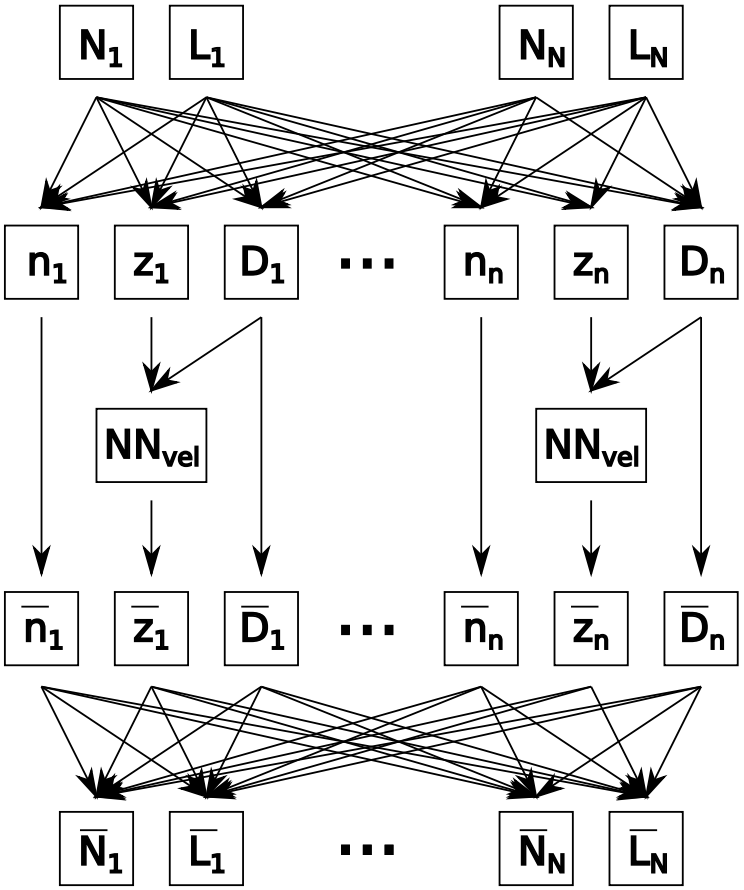

Figure 7.3: Archirecture for a neural network encompassing the structure of the superdroplet approach of Shima et al. (2009). The architecture of the part of the network evolving the position of the superdroplet (NN_{vel}) is depicted in Figure 7.4.

To construct the architecture of NN_{vel}, we note that the dynamics of the superdroplets are (under the assumptions of the SPM and the Wacker and Seifert (2001) reference model) equal to those of normal hydrometeors and thus given by (3.5) and (3.6). So, for NN_{vel} we chose an architecture composed of a (possibly pre trained) network NN_{sqrt} that only processes D_i and calculates its square root (see Eisman (1990) for a suitable architecture) and another layer that processes the output of NN_{sqrt} together with z_i to calculate the time evolved position of the super droplet. Choosing the ReLU, which has also been used e.g. by Ruckstuhl et al. (2021) for the rain variable, as activation function should lead to it having no effect, as long as $z_i > 0$ holds. Assuming the output of NN_{sqrt} actually being the square root of D_i, this yields

$$z_i' = \mathrm{ReLU}\left(w_z z_i + w_D \sqrt{D_i} + w_0\right). \tag{7.17}$$

Comparing (7.17) with (3.5) and (3.6) allows to identify conditions for the trained network

having learned the superdroplet approach correctly: The weights and biases for all copies of NN_{vel} should be equal and fulfil

$$w_z = 1 \tag{7.18}$$
$$w_D = \alpha t \tag{7.19}$$
$$w_0 = 0. \tag{7.20}$$

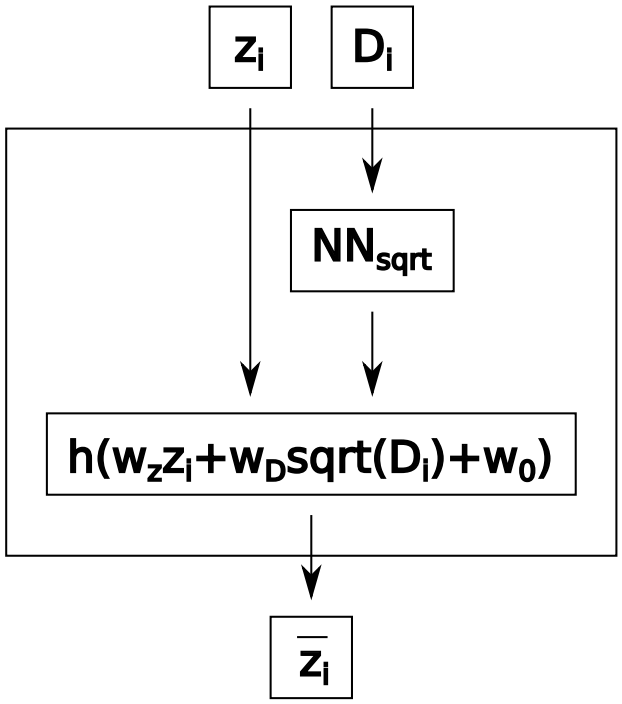

Figure 7.4: Archirecture of the part of the network evolving the position of the superdroplet.

This setup can also be extended to account for the interactions between hydrometeors, by iteratively applying NN_{vel} interlaced with layers describing the interactions of hydrometeors (see also Seifert, 2022).

Due to its relatively low computational cost and stochastic initial conditions, the SPM could also be used to generate training data for this network. This would allow to evaluate, if the suggested architecture is capable of learning the superdroplet approximation and how its performance would compare to a fully connected NN.

Chapter 8

Conclusion

In many operational applications a large percentage of the available observations is lost due to thinning, i.e. discarding of values to obtain an uncorrelated data set, which is necessary because of the inability to successfully assimilate correlated observations (Janjić et al., 2018). Thus, better understanding the spatial and temporal structure of observation error covariance matrices and its impact on DA is highly desirable. A good starting point for constructing a test case for studying observation errors arising from microphysics is provided by the Wacker and Seifert (2001) reference model, which describes the evolution of liquid water content L and number density N over time. The Wacker and Seifert (2001) reference model features stochastic initial conditions, that can (by interpreting them as a way to account for the lack of knowledge about the exact initial positions and sizes of hydrometeors) be regarded as a form of representation error. Thus, assuming no other sources of observation error being present, the Wacker and Seifert (2001) reference model would provide a suitable setup for DA experiments, if the according covariance matrices could be obtained.

However, as seen in Section 4.2, the covariance matrices of the Wacker and Seifert (2001) reference model explicitly depend on a free parameter without physical analogue, that cannot be easily disposed of. Thus, in Section 3.2 we construct a model (referred to as SPM) with well defined error covariances by modifying the definitions of L and N. By this, we effectively extract the particle model underlying the Wacker and Seifert (2001) reference model, that allows us to calculate the according covariances in Section 4.1. The profiles obtained from the SPM agree relatively well with those provided by the Wacker and Seifert (2001) reference model, though the modified definitions cause a relatively strong difference in the amplitude of the L-profile.

As the SPM (like the Wacker and Seifert (2001) reference model) only considers the case of pure sedimentation, a (positive) correlation between the measurements at two points can practically only be caused by hydrometeors simultaneously intersecting both grid points. Thus gravitational sorting has a large influence on the covariance matrix (as it has on the L and N profiles), leading to larger correlation lengths at lower z-levels (Figure 4.3).

Furthermore, the geometry of the hydrometeors plays a large role in the shape of the covariances: Cylindrical hydrometeors with constant orientation result in a triangular covariance profile with finite support, while spherical hydrometeors and randomly oriented cylindrical hydrometeors result in a more bell shaped covariance profile (see Figure 4.4). The width of the support in the former case might again be determined by gravitational sorting.

When looking at their time evolution, one finds that the variances of L evolve similarly to the according profiles, while the variances of N only minimally vary over time and always exhibit extremely large values at the top of the domain. This can again be explained by gravitational sorting and the different dependence of the definitions of L and N on the hydrometeor diameter. While L and its variance are more strongly influenced by larger hydrometeors, which move faster, N and its variance are dominated by very small hydrometeors, which stay at the top of the domain for the entire duration of the experiment.

We also tested the impact of different velocity models by comparing a simplified velocity model and McSnow of Brdar and Seifert (2018). However, we found (despite some impact on the L and N profiles) no effect on the shape of the covariance profile.

As the SPM yields error covariances that have an interesting (but not too complicated) spatial structure and change over time, we can employ it to asses the importance of accurately quantifying these aspects during DA. To this end, we conduct a series of DA experiments with an EnKF in Chapter 5. In these, we assimilate pseudo observations generated by the SPM or the Wacker and Seifert (2001) reference model with additional Gaussian noise (denoted as WSRM) employing the same 100 member ensemble, initially shifted with respect to the truth to introduce a positional error in the forecast. The ensemble is always evolved by the Wacker and Seifert (2001) two moment scheme.

Furthermore, despite the filter converging in all cases, practically throughout all experiments (except those not observing every grid point) we see higher root mean square error values when using the full $\mathbf{R}$ matrix compared to a block-diagonal (ignoring the correlations between L and N) or diagonal one. However, the dynamic $\mathbf{R}$ matrices perform better than time averaged $\mathbf{R}$ matrices or those from the initial or final time step. This indicates that accurately specifying the temporal development of $\mathbf{R}$ is more important, than precisely representing its spatial structure by introducing non zero off-diagonal elements. The full $\mathbf{R}$ matrices performing worse than diagonal and block-diagonal ones in our experiments is in disagreement with the findings of Rainwater et al. (2015). However, as in the analogue experiments of Weston et al. (2014) this is likely due to the high condition numbers of the full $\mathbf{R}$ matrices. Thus repeating our experiments with appropriate reconditioning is of interest for future work.

The ensemble spread is usually found to initially assume very low values (which is undesirable) and to slowly increase over time before becoming more or less constant. A series of exemplaric snapshots reveals that the initially low spread is likely caused by a large

amount of grid points producing negative analysis values, which are all set to a small positive threshold. This is in agreement with the results of Gleiter et al. (2022).

We also note that repeating our experiments with an absolute value applied to the observations in the WSRM scenario yields (except for the poorly converging full $\mathbf{R}$ case) the same results as the unmodified experiment. This hints that non-negative analysis originating from the DA algorithm and the need to positivize the analysis before time evolution are more critical than the non-Gaussianity of observation errors for the EnKF. To better understand the processes that lead to negative analysis, we consider several strongly simplified examples in Chapter 6, employing the Kalman filter. First, we use simple triangular profiles to demonstrate that negative analysis in the vicinity of large peaks can be caused by pure positional or amplitude error, when using a non-diagonal $\mathbf{R}$ matrix.

Subsequently we conduct a series of two-dimensional experiments using random[1] forecasts, observations and observation error covariance matrices to obtain the distribution of the analysis for diagonal and non-diagonal $\mathbf{R}$ for several different choices of the background error covariance matrix. We find that the results only depend on the ratio $\frac{c_o}{c_f}$ of the upper bounds c_o and c_f for the observation and forecast values, eliminating a degree of freedom. Besides on $\frac{c_o}{c_f}$, the effect of using non-diagonal $\mathbf{R}$ on non-negativity preservation in our experiments also depends on the sign of the background correlations, as shown in Table 6.1. When varying the magnitude of the background variances, we found higher background variances as expected resulting (at least for positive background correlations) in higher probability of obtaining negative analysis. Furthermore, employing different background variances for both grid points (as expected) resulted in the distributions of both components of the analysis differing. This yielded strongly non-Gaussian (joint) distributions of the analysis.

In an analogue three dimensional example with one unobserved grid point, we found the use of a a non-diagonal $\mathbf{R}$ matrix reducing the probability of obtaining negative analysis at the unobserved grid point, which might be explained by a reduced impact of the observations. Furthermore, in Appendix H.2 we show that when using a non-diagonal $\mathbf{R}$, non-negativity violation at a grid point is possible even if the measurements at all other grid points exactly match the forecast.

Finally, we consider a series of special cases and use them as counterexamples to show that we can neither drop the condition of diagonality of $\mathbf{P}_f$, nor that of diagonality of $\mathbf{R}$ in Proposition 6.1.1, which guarantees non-negative analysis for diagonal $\mathbf{P}_f$ and $\mathbf{R}$. Furthermore, we use them to show that we can not relax the strict positivity of the background in Proposition 6.4.3, which guarantees non-negative analysis for strictly positive background when $\mathbf{P}_f$ and $\mathbf{R}$ are sufficiently close to diagonal matrices and the observations are sufficiently close to the background. However we find that limiting the possible deviation

[1] All values drawn from independent uniform distributions on the intervals $[0, c_f]$, $[0, c_o]$ and $[0, 1]$.

of the observations from the background would allow to guarantee non-negativity of the analysis, when using non-diagonal $\mathbf{P}_f$ and $\mathbf{R}$ with sufficiently small off-diagonal elements. This indicates that quality control, which eliminates observations that deviate too much from the background, can help to ensure non-negativity preservation.

For future work, extending the SPM by including a more realistic observation operator, generalizing it to a variable particle number or allowing for interactions between or creation and destruction of hydrometeors are of special interest, as these modifications would greatly increase the number of possible applications for the SPM.

Appendix A

Relation between the definitions of SPM and WSRM

Now, we will examine how Definition 3.2.2 relates to the standard definitions of N and L given in Wacker and Seifert (2001). To that end, we consider:

Definition A.0.1. Let η be a state of a system consisting of n spherical hydrometeors as in Definition 3.2.2 and consider a domain $\Lambda = [x_{min}, x_{max}] \times [y_{min}, y_{max}] \times [z_{min}, z_{max}]$, with $(x_j, y_j, z_j) \in \Lambda$ and[1] $d\left((x_j, y_j, z_j), \partial\Lambda\right) > \frac{D_j}{2}$, for all $j \in \{1, \cdots, n\}$. We define

$$N_\Lambda = \frac{n}{(x_{max} - x_{min}) \cdot (y_{max} - y_{min}) \cdot (z_{max} - z_{min})} \tag{A.1}$$

$$L_\Lambda = \frac{l}{(x_{max} - x_{min}) \cdot (y_{max} - y_{min}) \cdot (z_{max} - z_{min})}, \tag{A.2}$$

with l being the total water mass contained in Λ, given by[2]

$$l = \rho_H \sum_{j=1}^{n} \left| B_{\frac{D_j}{2}}(x_j, y_j, z_j) \right|_V . \tag{A.3}$$

Now, we note that given the assumptions of Definition A.0.1 integrating (3.2) and (3.3) over $[z_{min}, z_{max}]$ yields

$$n = \int_{z_{min}}^{z_{max}} n_\eta(z)\, dz \tag{A.4}$$

$$l = \int_{z_{min}}^{z_{max}} l_\eta(z)\, dz. \tag{A.5}$$

[1] $\partial\Lambda$ denotes the boundary of Λ.

[2] $|S|_V$ denotes the volume of set S.

On the other hand, the particle number n and the total water mass l can be obtained from the standard definitions of N and L by integrating them over Λ, yielding

$$\begin{aligned} n &= \int_{\Lambda} N(z)\, dxdydz \\ &= (x_{max} - x_{min})(y_{max} - y_{min}) \int_{z_{min}}^{z_{max}} N(z)\, dz \end{aligned} \tag{A.6}$$

$$\begin{aligned} l &= \int_{\Lambda} L(z)\, dxdydz \\ &= (x_{max} - x_{min})(y_{max} - y_{min}) \int_{z_{min}}^{z_{max}} L(z)\, dz. \end{aligned} \tag{A.7}$$

Now combining (A.4) and (A.6), we obtain

$$\int_{z_{min}}^{z_{max}} n_\eta(z)\, dz = (x_{max} - x_{min})(y_{max} - y_{min}) \int_{z_{min}}^{z_{max}} N(z)\, dz \tag{A.8}$$

$$\Leftrightarrow \int_{z_{min}}^{z_{max}} \frac{n_\eta(z)}{(x_{max} - x_{min})(y_{max} - y_{min})} - N(z)\, dz = 0 \tag{A.9}$$

$$\Leftrightarrow \int_{\bar{z}-\frac{\Delta z}{2}}^{\bar{z}+\frac{\Delta z}{2}} \frac{n_\eta(z)}{(x_{max} - x_{min})(y_{max} - y_{min})} - N(z)\, dz = 0, \tag{A.10}$$

with $z_{min} = \bar{z} - \frac{\Delta z}{2}$ and $z_{max} = \bar{z} + \frac{\Delta z}{2}$. This motivates assuming

$$N(z) = \frac{n_\eta(z)}{(x_{max} - x_{min})(y_{max} - y_{min})}, \tag{A.11}$$

though an exact proof is not possible this way due to the assumption of the hydrometeors not protruding outside the domain and $N(z)$ not being defined on small length scales. A more rigorous approach is relating Definition 3.2.2 to the standard definitions of N and L by constructing suitable measures, as outlined in Definition 7.1.1.

An analogue consideration is possible for the liquid water content using (A.5) and (A.7).

Appendix B

Geometric considerations for cylindrical hydrometeors

Despite this problem likely been already solved, we here derive the area of intersection of a cylindric hydrometeor with the (x, y)-plane, as well as the area of its projection onto the (x, y)-plane.

B.1 General description and case distinction

Making use of the according symmetries, a cylindric hydrometeor can be described by its radius r, height h, the position of its centre z_j and its angle φ relative to the x, y-plane. Its rotation around its symmetry axis has no effect and a rotation around the z-axis does not affect its area of intersection with the (x, y)-plane.

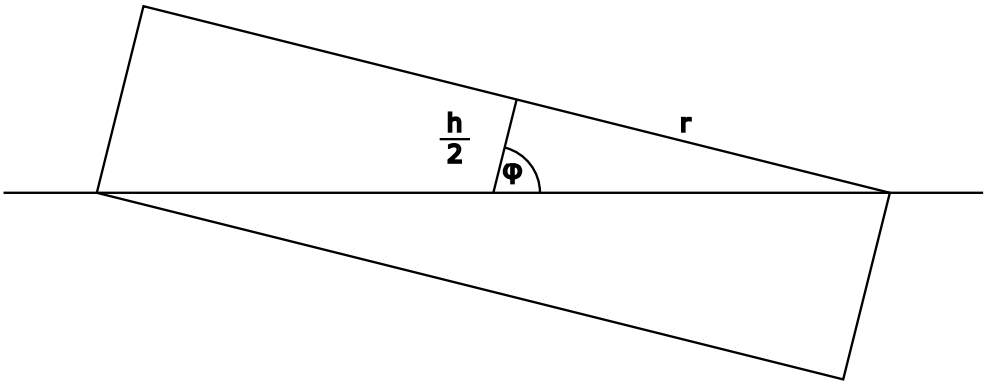

Figure B.1: Basic case distinction

We have to distinguish two cases: That where φ is so large that the area of intersection of the hydrometeor at $z_j = z$ with the (x, y)-plane is a full ellipse and that where φ is so small, that it is a sector of an ellipse, missing both ends (see Figure B.1 for borderline case). The transition between both cases occurs at

$$\varphi_0 = \arctan\left(\frac{2r}{h}\right), \tag{B.1}$$

so we get (excluding the case $\varphi = 0$, which has probability zero in all our experiments) for the area of intersection at $z_j = z$:

1. Ellipse, for $\varphi > \arctan\left(\frac{2r}{h}\right)$
2. Sector of ellipse $\varphi < \arctan\left(\frac{2r}{h}\right)$.

Now we can calculate the maximum distance d_{max}, a hydrometeor can have to the (x, y)-plane while still intersecting it in at least one point, which is independent of the above case distinction:

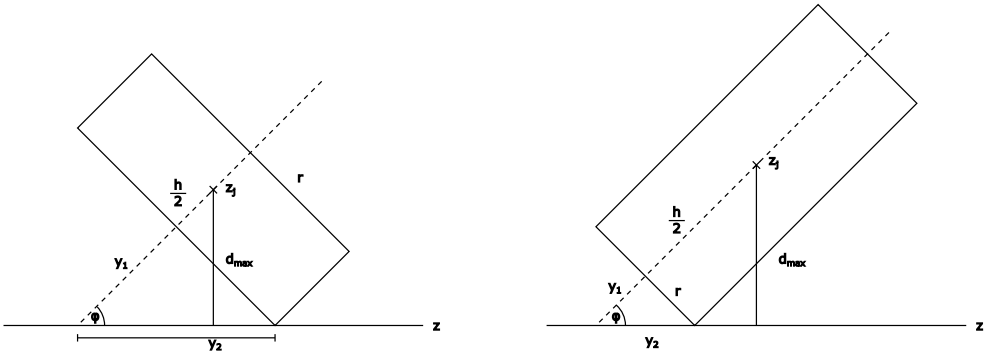

Figure B.2: Illustration of calculation of d_{max} for both cases

As illustrated in Figure B.2,

$$d_{max} = \left(\frac{h}{2} + y_1\right)\sin(\varphi) \tag{B.2}$$

and

$$\begin{aligned} \frac{r}{y_1} &= \tan(\varphi) \\ \Rightarrow y_1 &= \frac{r\cos(\varphi)}{\sin(\varphi)} \end{aligned} \tag{B.3}$$

.

We obtain from (B.2) and (B.3)

$$
\begin{aligned}
d_{max} &= \left(\frac{h}{2} + \frac{r\cos(\varphi)}{\sin(\varphi)}\right)\sin(\varphi) \\
&= \frac{h}{2}\sin(\varphi) + r\cos(\varphi)
\end{aligned}
\tag{B.4}
$$

Next we can calculate the distance d_{inner}, below which the area of intersection becomes (depending on the case) a full ellipse or ellipse sector with both ends cut off:

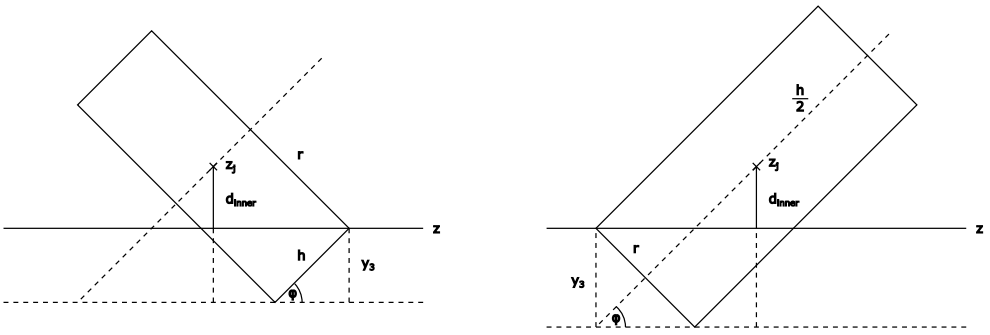

Figure B.3: Illustration of calculation of d_{inner} for both cases

As seen in Figure B.3, in both cases we have

$$
d_{inner} = d_{max} - y_3, \tag{B.5}
$$

which yields together with

$$
y_3 = \begin{cases} 2r\cos(\varphi) & \text{,if } \varphi > \arctan\left(\frac{2r}{h}\right) \\ h\sin(\varphi) & \text{,if } \varphi < \arctan\left(\frac{2r}{h}\right) \end{cases} \tag{B.6}
$$

and (B.4) following formula for d_{inner}

$$
\begin{aligned}
d_{inner} &= \begin{cases} d_{max} - 2r\cos(\varphi) & \text{,if } \varphi > \arctan\left(\frac{2r}{h}\right) \\ d_{max} - h\sin(\varphi) & \text{,if } \varphi < \arctan\left(\frac{2r}{h}\right) \end{cases} \\
&= \begin{cases} \frac{h}{2}\sin(\varphi) + r\cos(\varphi) - 2r\cos(\varphi) & \text{,if } \varphi > \arctan\left(\frac{2r}{h}\right) \\ \frac{h}{2}\sin(\varphi) + r\cos(\varphi) - h\sin(\varphi) & \text{,if } \varphi < \arctan\left(\frac{2r}{h}\right) \end{cases} \\
&= \begin{cases} \frac{h}{2}\sin(\varphi) - r\cos(\varphi) & \text{,if } \varphi > \arctan\left(\frac{2r}{h}\right) \\ r\cos(\varphi) - \frac{h}{2}\sin(\varphi) & \text{,if } \varphi < \arctan\left(\frac{2r}{h}\right) \end{cases}.
\end{aligned}
\tag{B.7}
$$

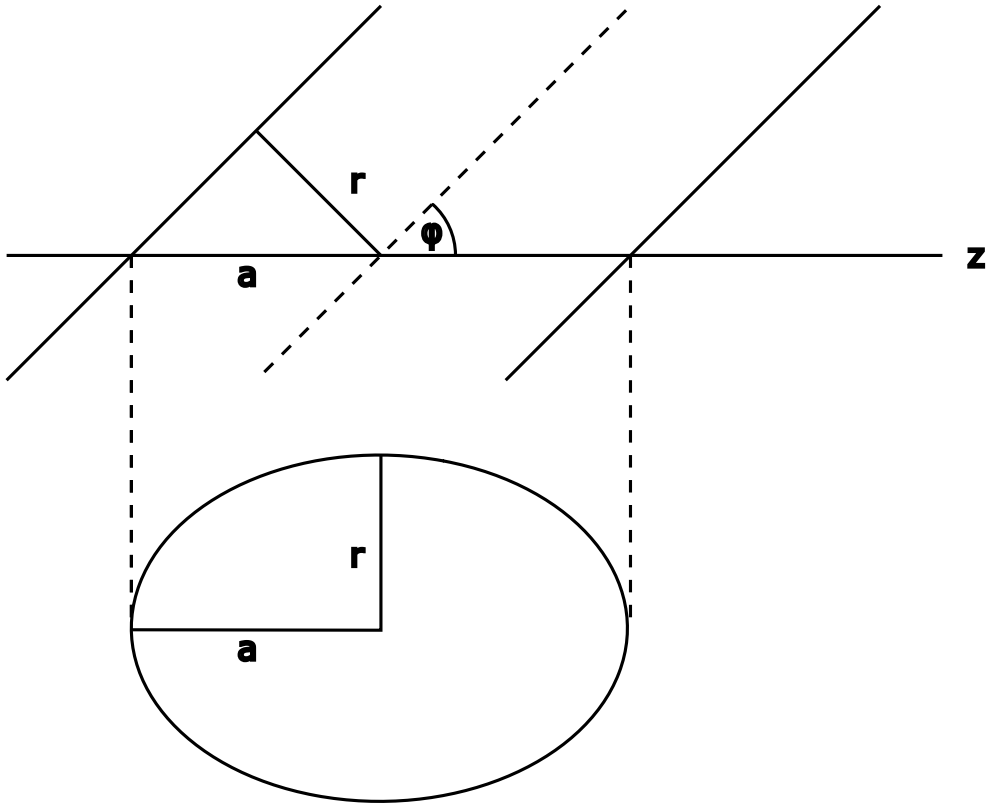

Figure B.4: Intersection between cylinder of infinite length and (x, y)-plane

B.2 Intersection areas

Excluding the case $\varphi = 0$, we start with looking at the intersection area A_{inf} of a cylinder of infinite length with the (x, y)-plane, which is an ellipse:
From Figure B.4 we can read off

$$a = \frac{r}{\sin(\varphi)},$$

which yields

$$\begin{aligned} A_{inf} &= \pi a r \\ &= \frac{\pi r^2}{\sin(\varphi)}. \end{aligned} \tag{B.8}$$

If the length of the cylinder is finite, in some cases one or both ends of this ellipse are cut of.

B.2.1 The large angle case (full ellipse)

Making use of the area of the section of an ellipse (as in Figure B.5) being given (see e.g. Bronstein Semendjajew (2008)) by

$$A_{section} = ar \arccos\left(\frac{x}{a}\right) - xy \tag{B.9}$$

and using the ellipse equation (see e.g. Bronstein Semendjajew (2008))

$$1 = \frac{x^2}{a^2} + \frac{y^2}{r^2} \tag{B.10}$$

to reexpress y as

$$y = r\sqrt{1 - \frac{x^2}{a^2}}, \tag{B.11}$$

we obtain

$$A_{section}^{short} = ar \arccos\left(\frac{x}{a}\right) - xr\sqrt{1 - \frac{x^2}{a^2}}. \tag{B.12}$$

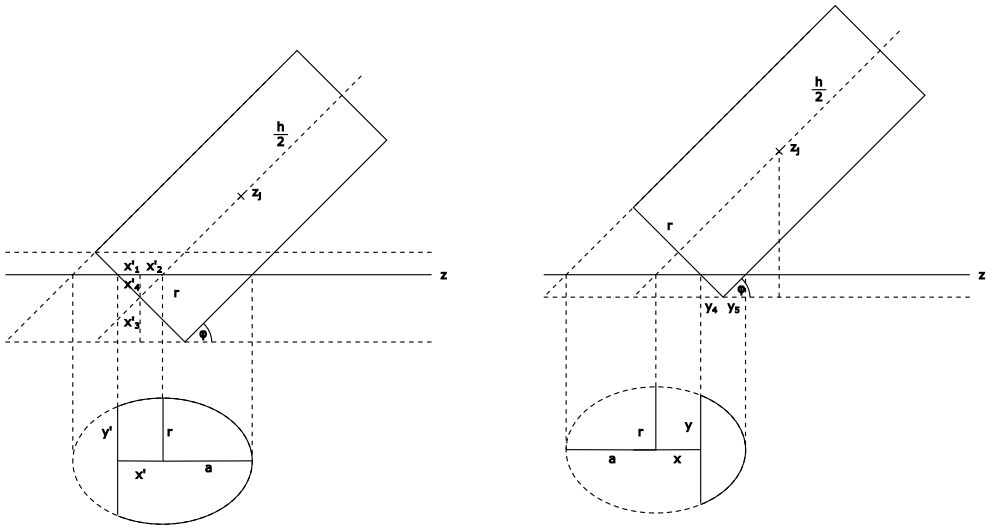

Figure B.5: Intersection between cylinder of length h and (x, y)-plane in the large angle case

Finally reading off the expressions for y_4 and y_5 from Figure B.5, we obtain

$$x = a - y_4 - y_5 \tag{B.13}$$

$$= a - \frac{d_{max} - |z - z_j|}{\tan(90° - \varphi)} - \frac{d_{max} - |z - z_j|}{\tan(\varphi)} \tag{B.14}$$

which yields from (B.12)

$$\begin{aligned} A_{section}^{short} &= ar\arccos\left(\frac{a - \frac{d_{max}-|z-z_j|}{\tan(90°-\varphi)} - \frac{d_{max}-|z-z_j|}{\tan(\varphi)}}{a}\right) - \left(a - \frac{d_{max} - |z - z_j|}{\tan(90° - \varphi)} - \frac{d_{max} - |z - z_j|}{\tan(\varphi)}\right) \cdot \\ &\quad \cdot r\sqrt{1 - \frac{\left(a - \frac{d_{max}-|z-z_j|}{\tan(90°-\varphi)} - \frac{d_{max}-|z-z_j|}{\tan(\varphi)}\right)^2}{a^2}} \qquad \text{(B.15)} \\ &= ar\arccos\left(1 - \frac{d_{max} - |z - z_j|}{a\tan(90° - \varphi)} - \frac{d_{max} - |z - z_j|}{a\tan(\varphi)}\right) - \\ &\quad - \left(a - \frac{d_{max} - |z - z_j|}{\tan(90° - \varphi)} - \frac{d_{max} - |z - z_j|}{\tan(\varphi)}\right) \cdot \\ &\quad \cdot r\sqrt{1 - \left(1 - \frac{d_{max} - |z - z_j|}{a\tan(90° - \varphi)} - \frac{d_{max} - |z - z_j|}{a\tan(\varphi)}\right)^2} \\ &= ar\arccos\left(1 - \frac{d_{max} - |z - z_j|}{a}\left(\tan(\varphi) + \frac{1}{\tan(\varphi)}\right)\right) - \\ &\quad - \left(a - (d_{max} - |z - z_j|)\left(\tan(\varphi) + \frac{1}{\tan(\varphi)}\right)\right) \cdot \\ &\quad \cdot r\sqrt{1 - \left(1 - \frac{d_{max} - |z - z_j|}{a}\left(\tan(\varphi) + \frac{1}{\tan(\varphi)}\right)\right)^2}, \end{aligned}$$

for the case $d_{max} - |z_j - z| < r\cos(\varphi)$, i.e. the area of intersection being less than a half ellipse.

In the case $(d_{max} - |z_j - z| > r\cos(\varphi))$, we have

$$A_{section}^{long} = A_{inf} - ar\arccos\left(\frac{x'}{a}\right) + x'y' \tag{B.16}$$

$$= \pi ar - ar\arccos\left(\frac{x'}{a}\right) + x'y', \tag{B.17}$$

with (reading off the expressions for x'_1, x'_2, x'_3 and x'_4 from Figure B.5)

$$
\begin{aligned}
x' &= x'_1 + x'_2 \\
&= x'_4 \tan(\varphi) + \frac{x'_4}{\tan(\varphi)} \\
&= x'_4 \left(\tan(\varphi) + \frac{1}{\tan(\varphi)} \right) \\
&= (d_{max} - |z_j - z| - x_3) \left(\tan(\varphi) + \frac{1}{\tan(\varphi)} \right) \\
&= (d_{max} - |z_j - z| - r\cos(\varphi)) \left(\tan(\varphi) + \frac{1}{\tan(\varphi)} \right).
\end{aligned}
\tag{B.18}
$$

Using

$$
y' = r\sqrt{1 - \frac{x'^2}{a^2}},
\tag{B.19}
$$

we get

$$
\begin{aligned}
A^{long}_{section} &= \pi a r - a r \arccos\left(\frac{x'}{a}\right) + x' r \sqrt{1 - \frac{x'^2}{a^2}} \\
&= \pi a r - a r \arccos\left(\frac{(d_{max} - |z_j - z| - r\cos(\varphi)) \left(\tan(\varphi) + \frac{1}{\tan(\varphi)} \right)}{a} \right) + \\
&\quad + \left((d_{max} - |z_j - z| - r\cos(\varphi)) \left(\tan(\varphi) + \frac{1}{\tan(\varphi)} \right) \right) \cdot \\
&\quad \cdot r \sqrt{1 - \frac{\left((d_{max} - |z_j - z| - r\cos(\varphi)) \left(\tan(\varphi) + \frac{1}{\tan(\varphi)} \right) \right)^2}{a^2}},
\end{aligned}
\tag{B.20}
$$

for the case $d_{max} - |z_j - z| > r\cos(\varphi)$.

So, we have

$$
\begin{aligned}
A_{largeangle} &= \begin{cases} 0 & \text{,if } |z_j - z| > d_{max} \\ A_{section}^{short} & \text{,if } d_{max} - |z_j - z| < r\cos(\varphi) \text{ and } d_{inner}^{largeangle} < |z_j - z| < d_{max} \\ A_{section}^{long} & \text{,if } d_{max} - |z_j - z| > r\cos(\varphi) \text{ and } d_{inner}^{largeangle} < |z_j - z| < d_{max} \\ A_{inf} & \text{,if } |z_j - z| < d_{inner}^{largeangle} \end{cases} \\
&= \mathbf{1}_{\left(d_{inner}^{largeangle}, d_{max}\right]}\left(|z_j - z|\right)\Big[\mathbf{1}_{[0, d_{max} - r\cos(\varphi))}\left(|z_j - z|\right) A_{section}^{long} + \\
&\quad + \mathbf{1}_{[d_{max} - r\cos(\varphi), \infty)}\left(|z_j - z|\right) A_{section}^{short}\Big] + \mathbf{1}_{\left[0, d_{inner}^{largeangle}\right]}\left(|z_j - z|\right) A_{inf} \\
&= \mathbf{1}_{[0, d_{max} - r\cos(\varphi)) \cap \left(d_{inner}^{largeangle}, d_{max}\right]}\left(|z_j - z|\right) A_{section}^{long} + \\
&\quad + \mathbf{1}_{[d_{max} - r\cos(\varphi), \infty) \cap \left(d_{inner}^{largeangle}, d_{max}\right]}\left(|z_j - z|\right) A_{section}^{short} + \mathbf{1}_{\left[0, d_{inner}^{largeangle}\right]}\left(|z_j - z|\right) A_{inf}
\end{aligned} \tag{B.21}
$$

for $\varphi > \arctan\left(\frac{2r}{h}\right)$.

B.2.2 The small angle case (ellipse section)

Now, we look at the case of $\varphi < \arctan\left(\frac{2r}{h}\right)$: We basically obtain the analogue equations with the only difference being that instead obtaining the full ellipse at $|z_j - z| < d_{inner}^{largeangle}$, we have to also remove a part of the ellipse on the other side at $|z_j - z| < d_{inner}^{smallangle}$. To calculate A_{cut}, which has to be removed for $|z_j - z| < d_{inner}^{smallangle}$, we use

$$A_{cut} = ar\arccos\left(\frac{x''}{a}\right) - x''y'' \tag{B.22}$$

and

$$y'' = r\sqrt{1 - \frac{x''^2}{a^2}} \tag{B.23}$$

to obtain

$$A_{cut} = ar\arccos\left(\frac{x''}{a}\right) - x''r\sqrt{1 - \frac{x''^2}{a^2}}. \tag{B.24}$$

Now (reading off the expressions for x_1'', x_2'', x_3'' and x_4'' from Figure B.6),

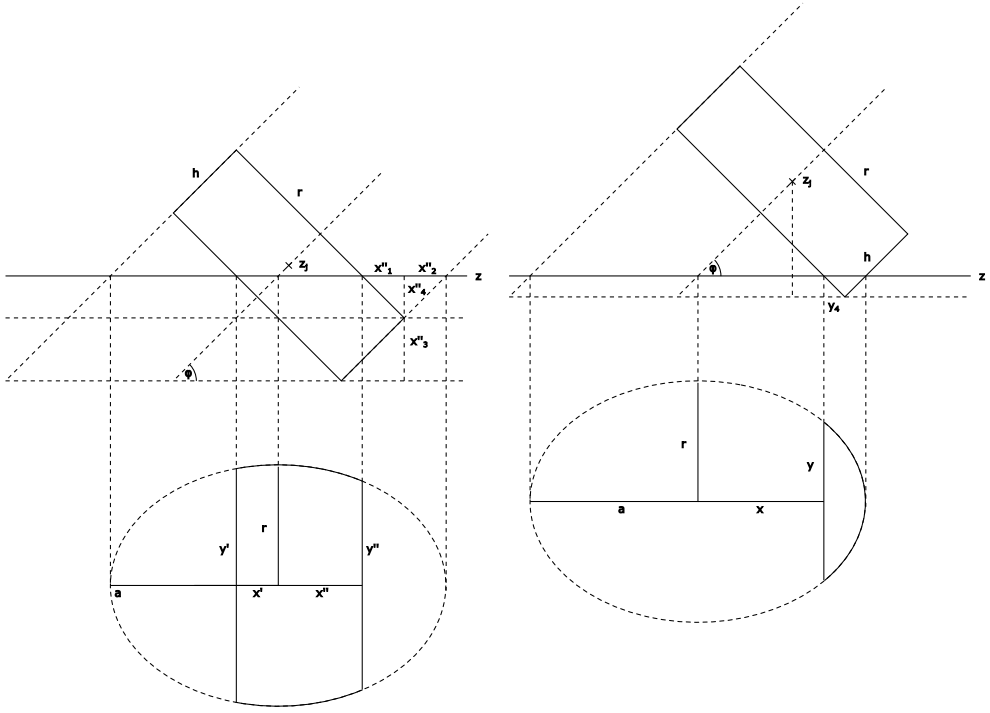

Figure B.6: Intersection between cylinder of length h and (x, y)-plane in the small angle case

$$
\begin{aligned}
x'' &= a - x_1'' - x_2'' \\
&= a - x_4'' \left(\tan(\varphi) + \frac{1}{\tan(\varphi)} \right) \\
&= a - (d_{max} - |z_j - z| - x_3'') \left(\tan(\varphi) + \frac{1}{\tan(\varphi)} \right) \\
&= a - (d_{max} - |z_j - z| - h \sin(\varphi)) \left(\tan(\varphi) + \frac{1}{\tan(\varphi)} \right)
\end{aligned}
\tag{B.25}
$$

yields

$$
\begin{aligned}
A_{cut} &= ar\arccos\left(\frac{a-\left(d_{max}-|z_j-z|-h\sin(\varphi)\right)\left(\tan(\varphi)+\frac{1}{\tan(\varphi)}\right)}{a}\right)- \\
&\quad-\left(a-\left(d_{max}-|z_j-z|-h\sin(\varphi)\right)\left(\tan(\varphi)+\frac{1}{\tan(\varphi)}\right)\right)\cdot \\
&\quad\cdot r\sqrt{1-\frac{\left(a-\left(d_{max}-|z_j-z|-h\sin(\varphi)\right)\left(\tan(\varphi)+\frac{1}{\tan(\varphi)}\right)\right)^2}{a^2}} \\
&= ar\arccos\left(1-\frac{\left(d_{max}-|z_j-z|-h\sin(\varphi)\right)}{a}\left(\tan(\varphi)+\frac{1}{\tan(\varphi)}\right)\right)- \\
&\quad-\left(a-\left(d_{max}-|z_j-z|-h\sin(\varphi)\right)\left(\tan(\varphi)+\frac{1}{\tan(\varphi)}\right)\right)\cdot \\
&\quad\cdot r\sqrt{1-\left(1-\frac{\left(d_{max}-|z_j-z|-h\sin(\varphi)\right)}{a}\left(\tan(\varphi)+\frac{1}{\tan(\varphi)}\right)\right)^2},
\end{aligned}
\tag{B.26}
$$

for $|z_j - z| < d_{inner}^{smallangle}$. So finally, we obtain

$$
\begin{aligned}
A_{smallangle} &= \mathbf{1}_{(0,d_{max}]}\left(|z_j-z|\right)\left[\mathbf{1}_{[0,d_{max}-r\cos(\varphi))}\left(|z_j-z|\right)A_{section}^{long}+\right. \\
&\quad\left.+\,\mathbf{1}_{[d_{max}-r\cos(\varphi),\infty)}\left(|z_j-z|\right)A_{section}^{short}\right]-A_{cut}\mathbf{1}_{\left[0,d_{inner}^{smallangle}\right]}\left(|z_j-z|\right) \\
&= \mathbf{1}_{[0,d_{max}-r\cos(\varphi))\cap(0,d_{max}]}\left(|z_j-z|\right)A_{section}^{long}+ \\
&\quad+\,\mathbf{1}_{[d_{max}-r\cos(\varphi),\infty)\cap(0,d_{max}]}\left(|z_j-z|\right)A_{section}^{short}-A_{cut}\mathbf{1}_{\left[0,d_{inner}^{smallangle}\right]}\left(|z_j-z|\right),
\end{aligned}
\tag{B.27}
$$

for $\varphi < \arctan\left(\frac{2r}{h}\right)$.

B.2.3 Complete formula

Combining the results of the previous sections yields for $\varphi \in (0, 90°)$

$$
A\left(z_j,\varphi,r,h,z\right) = A_{largeangle}\mathbf{1}_{\left[\arctan\left(\frac{2r}{h}\right),\frac{\pi}{2}\right)}\left(\varphi\right)+A_{smallangle}\mathbf{1}_{\left[0,\arctan\left(\frac{2r}{h}\right)\right)}\left(\varphi\right), \tag{B.28}
$$

so given a state η of n hydrometeors in the form of (3.17), we have

$$
l_\eta\left(z\right) = \varrho_H\sum_{j=1}^{n}A\left(z_j,\varphi_j,r_j,h_j,z\right), \tag{B.29}
$$

and

$$n_\eta(z) = \sum_{j=1}^{n} \frac{1}{\pi r_j^2 h_j} A(z_j, \varphi_j, r_j, h_j, z). \tag{B.30}$$

Now, our goal is to simplify the according expressions: Using the fact, that always $\varphi_j \leq \frac{\pi}{2}$ and thus $\cos(\varphi_j) \geq 0$, we obtain

$$\begin{aligned} A_{smallangle}(z_j, \varphi_j, r_j, h_j, z) = {} & \mathbf{1}_{[0, d_{max} - r_j \cos(\varphi_j))}(|z_j - z|) A_{section}^{long}(z_j, \varphi_j, r_j, h_j, z) + \\ & + \mathbf{1}_{[d_{max} - r_j \cos(\varphi_j) d_{max})}(|z_j - z|) A_{section}^{short}(z_j, \varphi_j, r_j, h_j, z) \\ & - A_{cut}(z_j, \varphi_j, r_j, h_j, z) \mathbf{1}_{\left[0, d_{inner}^{smallangle}\right]}(|z_j - z|). \end{aligned} \tag{B.31}$$

As $\cos(\varphi_j) \leq 1$, we obtain

$$\begin{aligned} d_{inner}^{largeangle} &= d_{max} - \underbrace{2 r_j \cos(\varphi_j)}_{\geq 0} && \text{(B.32)} \\ &\leq d_{max}. && \text{(B.33)} \end{aligned}$$

Thus

$$\begin{aligned} A_{largeangle}(z_j, \varphi_j, r_j, h_j, z) = {} & \mathbf{1}_{[0, d_{max} - r_j \cos(\varphi_j)) \cap \left(d_{inner}^{largeangle}, d_{max}\right]}(|z_j - z|) A_{section}^{long}(z_j, \varphi_j, r_j, h_j, z) + \\ & + \mathbf{1}_{[d_{max} - r_j \cos(\varphi_j), \infty) \cap \left(d_{inner}^{largeangle}, d_{max}\right]}(|z_j - z|) A_{section}^{short}(z_j, \varphi_j, r_j, h_j, z) \\ & + \mathbf{1}_{\left[0, d_{inner}^{largeangle}\right]}(|z_j - z|) A_{inf}(z_j, \varphi_j, r_j, h_j, z) && \text{(B.34)} \\ = {} & \mathbf{1}_{\left(d_{inner}^{largeangle}, d_{max} - r_j \cos(\varphi_j)\right]}(|z_j - z|) A_{section}^{long}(z_j, \varphi_j, r_j, h_j, z) + \\ & + \mathbf{1}_{[d_{max} - r_j \cos(\varphi_j), d_{max})}(|z_j - z|) A_{section}^{short}(z_j, \varphi_j, r_j, h_j, z) \\ & + \mathbf{1}_{\left[0, d_{inner}^{largeangle}\right]}(|z_j - z|) A_{inf}(z_j, \varphi_j, r_j, h_j, z) \end{aligned}$$

Appendix C

Proofs for Chapter 4

We now give the proofs for the theorems shown in Chapter 4 and Appendix D.

C.1 Proof of Proposition 4.1.1

We now prove Proposition 4.1.1:

Proof. We start by taking the expectation value of $Z_{z,t}$, as defined in (3.14), for an arbitrary time t and height z, yielding

$$\begin{aligned}
&\mathbb{E}\left[Z_{z,t}\right] = \qquad\qquad (C.1)\\
&= \mathbb{E}\left[\sum_{j=1}^{n} \mathbf{1}_{\left[z-\frac{D_j}{2}, z+\frac{D_j}{2}\right]}\left(z_j\left(t\right)\right) g_Z\left(D_j\right) f\left(D_j, z_j, t, z\right)\right]\\
&= \int \sum_{j=1}^{n} \mathbf{1}_{\left[z-\frac{D_j}{2}, z+\frac{D_j}{2}\right]}\left(z_j\left(t\right)\right) g_Z\left(D_j\right) f\left(D_j, z_j, t, z\right) d\mathbb{P}\left(\mathbf{z}, \mathbf{D}\right)\\
&= \sum_{j=1}^{n} \int \mathbf{1}_{\left[z-\frac{D_j}{2}, z+\frac{D_j}{2}\right]}\left(z_j\left(t\right)\right) g_Z\left(D_j\right) f\left(D_j, z_j, t, z\right) d\mathbb{P}\left(z_j, D_j\right)\\
&= \sum_{j=1}^{n} \int \mathbf{1}_{\left[z-\frac{D_j}{2}, z+\frac{D_j}{2}\right]}\left(z_j + v_T\left(D_j\right) t\right) g_Z\left(D_j\right) f\left(D_j, z_j, t, z\right) d\mathbb{P}\left(z_j, D_j\right)\\
&= \sum_{j=1}^{n} \int \mathbf{1}_{\left[z-v_T(D_j)t-\frac{D_j}{2}, z-v_T(D_j)t+\frac{D_j}{2}\right]}\left(z_j\right) g_Z\left(D_j\right) f\left(D_j, z_j, t, z\right) d\mathbb{P}\left(z_j, D_j\right),
\end{aligned}$$

where we used (3.5). Employing the probability densities given in Assumption 3.2.1, this can be further simplified to

$$
\begin{aligned}
&\mathbb{E}\left[Z_{z,t}\right] = \\
&= \sum_{j=1}^{n} \int_0^\infty \int_{-\infty}^\infty \mathbf{1}_{\left[z-v_T(D_j)t-\frac{D_j}{2}, z-v_T(D_j)t+\frac{D_j}{2}\right]}\left(z_j\right) g_Z\left(D_j\right) f\left(D_j, z_j, t, z\right) \varrho_{z_j}\left(z_j\right) \varrho_{D_j}\left(D_j\right) dz_j dD_j \\
&= \frac{1}{z_{max}-z_{min}} \sum_{j=1}^{n} \int_0^\infty \int_{-\infty}^\infty \underbrace{\mathbf{1}_{\left[z-v_T(D_j)t-\frac{D_j}{2}, z-v_T(D_j)t+\frac{D_j}{2}\right]}\left(z_j\right) \mathbf{1}_{[z_{min}, z_{max}]}\left(z_j\right)}_{=\mathbf{1}_{\left[z-v_T\left(D_j\right)t-\frac{D_j}{2}, z-v_T\left(D_j\right)t+\frac{D_j}{2}\right]\cap[z_{min}, z_{max}]}\left(z_j\right)=A(z,t,D_j,z_{min},z_{max})} \cdot \\
&\quad \cdot g_Z\left(D_j\right) f\left(D_j, z_j, t, z\right) \lambda e^{-\lambda D_j} dz_j dD_j
\end{aligned} \tag{C.2}
$$

and finally using (4.1), (4.2) and (4.3) to

$$
\begin{aligned}
\mathbb{E}\left[Z_{z,t}\right] &= \frac{1}{z_{max}-z_{min}} \sum_{j=1}^{n} \int_0^\infty \int_{A(z,t,D_j,z_{min},z_{max})} g_Z\left(D_j\right) f\left(D_j, z_j, t, z\right) \lambda e^{-\lambda D_j} dz_j dD_j \\
&= \frac{1}{z_{max}-z_{min}} \sum_{j=1}^{n} \int_0^\infty g_Z\left(D_j\right) \lambda e^{-\lambda D_j} \int_{A(z,t,D_j,z_{min},z_{max})} f\left(D_j, z_j, t, z\right) dz_j dD_j \\
&= \frac{1}{z_{max}-z_{min}} \sum_{j=1}^{n} \int_0^\infty g_Z\left(D_j\right) \lambda e^{-\lambda D_j} h_2\left(z, t, D_j, z_{min}, z_{max}\right) dD_j \\
&= \frac{1}{z_{max}-z_{min}} \sum_{j=1}^{n} I_Z\left(z, t, z_{min}, z_{max}\right) \\
&= \frac{n}{z_{max}-z_{min}} I_Z\left(z, t, z_{min}, z_{max}\right).
\end{aligned} \tag{C.3}
$$

□

C.2 Proof of Proposition 4.1.2

We now prove Proposition 4.1.2:

Proof. For two functions $X_{x,t}$ and $Y_{y,s}$ by definition the covariance is given by

$$
\operatorname{Cov}\left(X_{x,t}, Y_{y,s}\right) = \mathbb{E}\left[X_{x,t} Y_{y,s}\right] - \mathbb{E}\left[X_{x,t}\right] \mathbb{E}\left[Y_{y,s}\right]. \tag{C.4}
$$

Using the form (3.14) we calculate the first term in (C.4)

$$
\begin{aligned}
&\mathbb{E}\left[X_{x,t}Y_{y,s}\right] = \qquad\qquad (C.5)\\
&= \int \sum_{j=1}^{n} \mathbf{1}_{\left[x-\frac{D_j}{2},x+\frac{D_j}{2}\right]}\left(z_j\left(t\right)\right) g_X\left(D_j\right) f\left(D_j, z_j, t, x\right) \cdot \\
&\quad \cdot \sum_{k=1}^{n} \mathbf{1}_{\left[y-\frac{D_k}{2},y+\frac{D_k}{2}\right]}\left(z_k\left(s\right)\right) g_Y\left(D_k\right) f\left(D_k, z_k, s, y\right) d\mathbb{P}\left(\mathbf{z}, \mathbf{D}\right) \\
&= \int \sum_{j=1}^{n} \mathbf{1}_{\left[x-\frac{D_j}{2},x+\frac{D_j}{2}\right]}\left(z_j + v_T\left(D_j\right) t\right) g_X\left(D_j\right) f\left(D_j, z_j, t, x\right) \cdot \\
&\quad \cdot \sum_{k=1}^{n} \mathbf{1}_{\left[y-\frac{D_k}{2},y+\frac{D_k}{2}\right]}\left(z_k + v_T\left(D_k\right) s\right) g_Y\left(D_k\right) f\left(D_k, z_k, s, y\right) d\mathbb{P}\left(\mathbf{z}, \mathbf{D}\right) \\
&= \int \sum_{j=1}^{n} \mathbf{1}_{\left[x-v_T(D_j)t-\frac{D_j}{2},x-v_T(D_j)t+\frac{D_j}{2}\right]}\left(z_j\right) g_X\left(D_j\right) f\left(D_j, z_j, t, x\right) \cdot \\
&\quad \cdot \sum_{k=1}^{n} \mathbf{1}_{\left[y-v_T(D_k)s-\frac{D_k}{2},y-v_T(D_k)s+\frac{D_k}{2}\right]}\left(z_k\right) g_Y\left(D_k\right) f\left(D_k, z_k, s, y\right) d\mathbb{P}\left(\mathbf{z}, \mathbf{D}\right) \\
&= \sum_{j=1}^{n}\sum_{k=1}^{n} \int\int \mathbf{1}_{\left[x-v_T(D_j)t-\frac{D_j}{2},x-v_T(D_j)t+\frac{D_j}{2}\right]}\left(z_j\right) g_X\left(D_j\right) f\left(D_j, z_j, t, x\right) \cdot \\
&\quad \cdot \mathbf{1}_{\left[y-v_T(D_k)s-\frac{D_k}{2},y-v_T(D_k)s+\frac{D_k}{2}\right]}\left(z_k\right) g_Y\left(D_k\right) f\left(D_k, z_k, s, y\right) d\mathbb{P}\left(z_j, D_j, z_k, D_k\right).
\end{aligned}
$$

Now, we can split the sum to make use of the independence for $j \neq k$ and obtain

$$
\begin{aligned}
&\mathbb{E}\left[X_{x,t}Y_{y,s}\right] = \qquad\qquad (C.6)\\
&= \sum_{j=1}^{n}\sum_{\substack{k=1\\k\neq j}}^{n}\int\int \mathbf{1}_{\left[x-v_T(D_j)t-\frac{D_j}{2},x-v_T(D_j)t+\frac{D_j}{2}\right]}(z_j)\, g_X(D_j)\, f(D_j,z_j,t,x)\cdot\\
&\quad\cdot \mathbf{1}_{\left[y-v_T(D_k)s-\frac{D_k}{2},y-v_T(D_k)s+\frac{D_k}{2}\right]}(z_k)\, g_Y(D_k)\, f(D_k,z_k,s,y)\, d\mathbb{P}(z_j,D_j,z_k,D_k) +\\
&\quad+\sum_{j=1}^{n}\int \mathbf{1}_{\left[x-v_T(D_j)t-\frac{D_j}{2},x-v_T(D_j)t+\frac{D_j}{2}\right]}(z_j)\, g_X(D_j)\, f(D_j,z_j,t,x)\cdot\\
&\quad\cdot \mathbf{1}_{\left[y-v_T(D_j)s-\frac{D_j}{2},y-v_T(D_j)s+\frac{D_j}{2}\right]}(z_j)\, g_Y(D_j)\, f(D_j,z_j,s,y)\, d\mathbb{P}(z_j,D_j)\\
&= \sum_{j=1}^{n}\sum_{\substack{k=1\\k\neq j}}^{n}\int\int \mathbf{1}_{\left[x-v_T(D_j)t-\frac{D_j}{2},x-v_T(D_j)t+\frac{D_j}{2}\right]}(z_j)\, g_X(D_j)\, f(D_j,z_j,t,x)\cdot\\
&\quad\cdot \mathbf{1}_{\left[y-v_T(D_k)s-\frac{D_k}{2},y-v_T(D_k)s+\frac{D_k}{2}\right]}(z_k)\, g_Y(D_k)\, f(D_k,z_k,s,y)\, d\mathbb{P}(z_j,D_j)\, d\mathbb{P}(z_k,D_k) +\\
&\quad+\sum_{j=1}^{n}\int \mathbf{1}_{\left[x-v_T(D_j)t-\frac{D_j}{2},x-v_T(D_j)t+\frac{D_j}{2}\right]}(z_j)\, g_X(D_j)\, f(D_j,z_j,t,x)\cdot\\
&\quad\cdot \mathbf{1}_{\left[y-v_T(D_j)s-\frac{D_j}{2},y-v_T(D_j)s+\frac{D_j}{2}\right]}(z_j)\, g_Y(D_j)\, f(D_j,z_j,s,y)\, d\mathbb{P}(z_j,D_j),
\end{aligned}
$$

which can be rewritten as

$$
\begin{aligned}
&\mathbb{E}\left[X_{x,t}Y_{y,s}\right] = \qquad\qquad (C.7)\\
&= \sum_{j=1}^{n}\int \mathbf{1}_{\left[x-v_T(D_j)t-\frac{D_j}{2},x-v_T(D_j)t+\frac{D_j}{2}\right]}(z_j)\, g_X(D_j)\, f(D_j,z_j,t,x)\, d\mathbb{P}(z_j,D_j)\cdot\\
&\quad\cdot\sum_{k=1}^{n}\int \mathbf{1}_{\left[y-v_T(D_k)s-\frac{D_k}{2},y-v_T(D_k)s+\frac{D_k}{2}\right]}(z_k)\, g_Y(D_k)\, f(D_k,z_k,s,y)\, d\mathbb{P}(z_k,D_k) -\\
&\quad-\sum_{j=1}^{n}\int \mathbf{1}_{\left[x-v_T(D_j)t-\frac{D_j}{2},x-v_T(D_j)t+\frac{D_j}{2}\right]}(z_j)\, g_X(D_j)\, f(D_j,z_j,t,x)\, d\mathbb{P}(z_j,D_j)\cdot\\
&\quad\cdot\int \mathbf{1}_{\left[y-v_T(D_j)s-\frac{D_j}{2},y-v_T(D_j)s+\frac{D_j}{2}\right]}(z_j)\, g_Y(D_j)\, f(D_j,z_j,s,y)\, d\mathbb{P}(z_j,D_j) +\\
&\quad+\sum_{j=1}^{n}\int \mathbf{1}_{\left[x-v_T(D_j)t-\frac{D_j}{2},x-v_T(D_j)t+\frac{D_j}{2}\right]}(z_j)\, g_X(D_j)\, f(D_j,z_j,t,x)\cdot\\
&\quad\cdot \mathbf{1}_{\left[y-v_T(D_j)s-\frac{D_j}{2},y-v_T(D_j)s+\frac{D_j}{2}\right]}(z_j)\, g_Y(D_j)\, f(D_j,z_j,s,y)\, d\mathbb{P}(z_j,D_j).
\end{aligned}
$$

Finally, using (C.2) together with Assumption 3.2.1, we obtain

$$\begin{aligned}\mathbb{E}\left[X_{x,t}Y_{y,s}\right] &= \mathbb{E}\left[X_{x,t}\right]\mathbb{E}\left[Y_{y,s}\right] - \\ &- \sum_{j=1}^{n}\int \mathbf{1}_{\left[x-v_T(D_j)t-\frac{D_j}{2},x-v_T(D_j)t+\frac{D_j}{2}\right]}\left(z_j\right) g_X\left(D_j\right) f\left(D_j,z_j,t,x\right) d\mathbb{P}\left(z_j,D_j\right)\cdot \\ &\cdot \int \mathbf{1}_{\left[y-v_T(D_j)s-\frac{D_j}{2},y-v_T(D_j)s+\frac{D_j}{2}\right]}\left(z_j\right) g_Y\left(D_j\right) f\left(D_j,z_j,s,y\right) d\mathbb{P}\left(z_j,D_j\right) + \\ &+ \sum_{j=1}^{n}\int \mathbf{1}_{\left[x-v_T(D_j)t-\frac{D_j}{2},x-v_T(D_j)t+\frac{D_j}{2}\right]}\left(z_j\right) g_X\left(D_j\right) f\left(D_j,z_j,t,x\right)\cdot \\ &\cdot \mathbf{1}_{\left[y-v_T(D_j)s-\frac{D_j}{2},y-v_T(D_j)s+\frac{D_j}{2}\right]}\left(z_j\right) g_Y\left(D_j\right) f\left(D_j,z_j,s,y\right) d\mathbb{P}\left(z_j,D_j\right),\end{aligned} \tag{C.8}$$

and thus

$$\begin{aligned}&\operatorname{Cov}\left(X_{x,t},Y_{y,s}\right) = \\ &= \sum_{j=1}^{n}\int \mathbf{1}_{\left[x-v_T(D_j)t-\frac{D_j}{2},x-v_T(D_j)t+\frac{D_j}{2}\right]}\left(z_j\right) g_X\left(D_j\right) f\left(D_j,z_j,t,x\right)\cdot \\ &\cdot \mathbf{1}_{\left[y-v_T(D_j)s-\frac{D_j}{2},y-v_T(D_j)s+\frac{D_j}{2}\right]}\left(z_j\right) g_Y\left(D_j\right) f\left(D_j,z_j,s,y\right) d\mathbb{P}\left(z_j,D_j\right) - \\ &- \sum_{j=1}^{n}\int \mathbf{1}_{\left[x-v_T(D_j)t-\frac{D_j}{2},x-v_T(D_j)t+\frac{D_j}{2}\right]}\left(z_j\right) g_X\left(D_j\right) f\left(D_j,z_j,t,x\right) d\mathbb{P}\left(z_j,D_j\right)\cdot \\ &\cdot \int \mathbf{1}_{\left[y-v_T(D_j)s-\frac{D_j}{2},y-v_T(D_j)s+\frac{D_j}{2}\right]}\left(z_j\right) g_Y\left(D_j\right) f\left(D_j,z_j,s,y\right) d\mathbb{P}\left(z_j,D_j\right).\end{aligned} \tag{C.9}$$

Analogue to the calculations for the expectation value in Appendix C.1, we get

$$
\begin{aligned}
&\operatorname{Cov}\left(X_{x,t}, Y_{y,s}\right) = \qquad\qquad (C.10)\\
&= \sum_{j=1}^{n} \int \mathbf{1}_{\left[x-v_T(D_j)t-\frac{D_j}{2}, x-v_T(D_j)t+\frac{D_j}{2}\right]}\left(z_j\right) g_X\left(D_j\right) f\left(D_j, z_j, t, x\right) \cdot \\
&\quad \cdot \mathbf{1}_{\left[y-v_T(D_j)s-\frac{D_j}{2}, y-v_T(D_j)s+\frac{D_j}{2}\right]}\left(z_j\right) g_Y\left(D_j\right) f\left(D_j, z_j, s, y\right) d\mathbb{P}\left(z_j, D_j\right) - \\
&\quad - \frac{1}{\left(z_{max}-z_{min}\right)^2} \sum_{j=1}^{n} I_X\left(x, t, z_{min}, z_{max}\right) I_Y\left(y, s, z_{min}, z_{max}\right) \\
&= \sum_{j=1}^{n} \int \mathbf{1}_{\left[x-v_T(D_j)t-\frac{D_j}{2}, x-v_T(D_j)t+\frac{D_j}{2}\right]}\left(z_j\right) g_X\left(D_j\right) f\left(D_j, z_j, t, x\right) \cdot \\
&\quad \cdot \mathbf{1}_{\left[y-v_T(D_j)s-\frac{D_j}{2}, y-v_T(D_j)s+\frac{D_j}{2}\right]}\left(z_j\right) g_Y\left(D_j\right) f\left(D_j, z_j, s, y\right) d\mathbb{P}\left(z_j, D_j\right) - \\
&\quad - \frac{n}{\left(z_{max}-z_{min}\right)^2} I_X\left(x, t, z_{min}, z_{max}\right) I_Y\left(y, s, z_{min}, z_{max}\right) \\
&= \sum_{j=1}^{n} \int \mathbf{1}_{\left[x-v_T(D_j)t-\frac{D_j}{2}, x-v_T(D_j)t+\frac{D_j}{2}\right] \cap \left[y-v_T(D_j)s-\frac{D_j}{2}, y-v_T(D_j)s+\frac{D_j}{2}\right]}\left(z_j\right) \cdot \\
&\quad \cdot g_X\left(D_j\right) g_Y\left(D_j\right) f\left(D_j, z_j, t, x\right) f\left(D_j, z_j, s, y\right) d\mathbb{P}\left(z_j, D_j\right) - \\
&\quad - \frac{n}{\left(z_{max}-z_{min}\right)^2} I_X\left(x, t, z_{min}, z_{max}\right) I_Y\left(y, s, z_{min}, z_{max}\right),
\end{aligned}
$$

which can be (employing the probability densities given in Assumption 3.2.1) rewritten as

$$
\begin{aligned}
&\operatorname{Cov}\left(X_{x,t}, Y_{y,s}\right) = \qquad\qquad (C.11)\\
&= \sum_{j=1}^{n} \int_0^{\infty} \int_{-\infty}^{\infty} \mathbf{1}_{\left[x-v_T(D_j)t-\frac{D_j}{2}, x-v_T(D_j)t+\frac{D_j}{2}\right] \cap \left[y-v_T(D_j)s-\frac{D_j}{2}, y-v_T(D_j)s+\frac{D_j}{2}\right]}\left(z_j\right) \cdot \\
&\quad \cdot g_X\left(D_j\right) g_Y\left(D_j\right) f\left(D_j, z_j, t, x\right) f\left(D_j, z_j, s, y\right) \varrho_{z_j}\left(z_j\right) \varrho_{D_j}\left(D_j\right) dz_j dD_j - \\
&\quad - \frac{n}{\left(z_{max}-z_{min}\right)^2} I_X\left(x, t, z_{min}, z_{max}\right) I_Y\left(y, s, z_{min}, z_{max}\right) \\
&= \frac{1}{z_{max}-z_{min}} \sum_{j=1}^{n} \int_0^{\infty} \int_{-\infty}^{\infty} g_X\left(D_j\right) g_Y\left(D_j\right) f\left(D_j, z_j, t, x\right) f\left(D_j, z_j, s, y\right) \lambda e^{-\lambda D_j} \cdot \\
&\quad \cdot \mathbf{1}_{\left[x-v_T(D_j)t-\frac{D_j}{2}, x-v_T(D_j)t+\frac{D_j}{2}\right] \cap \left[y-v_T(D_j)s-\frac{D_j}{2}, y-v_T(D_j)s+\frac{D_j}{2}\right]}\left(z_j\right) \mathbf{1}_{[z_{min}, z_{max}]}\left(z_j\right) dz_j dD_j - \\
&\quad - \frac{n}{\left(z_{max}-z_{min}\right)^2} I_X\left(x, t, z_{min}, z_{max}\right) I_Y\left(y, s, z_{min}, z_{max}\right) \\
&= \frac{1}{z_{max}-z_{min}} \sum_{j=1}^{n} \int_0^{\infty} \int_{-\infty}^{\infty} g_X\left(D_j\right) g_Y\left(D_j\right) f\left(D_j, z_j, t, x\right) f\left(D_j, z_j, s, y\right) \lambda e^{-\lambda D_j} \cdot \\
&\quad \cdot \mathbf{1}_{\left[x-v_T(D_j)t-\frac{D_j}{2}, x-v_T(D_j)t+\frac{D_j}{2}\right] \cap \left[y-v_T(D_j)s-\frac{D_j}{2}, y-v_T(D_j)s+\frac{D_j}{2}\right] \cap [z_{min}, z_{max}]}\left(z_j\right) dz_j dD_j - \\
&\quad - \frac{n}{\left(z_{max}-z_{min}\right)^2} I_X\left(x, t, z_{min}, z_{max}\right) I_Y\left(y, s, z_{min}, z_{max}\right).
\end{aligned}
$$

Using (4.5) and (4.6), we obtain

$$
\begin{aligned}
&\operatorname{Cov}\left(X_{x,t}, Y_{y,s}\right) = \qquad\qquad (C.12)\\
&= \frac{1}{z_{max}-z_{min}} \sum_{j=1}^{n} \int_0^{\infty} \int_{B(x,y,t,s,D_j,z_{min},z_{max})} g_X\left(D_j\right) g_Y\left(D_j\right) f\left(D_j, z_j, t, x\right) \cdot \\
&\quad \cdot f\left(D_j, z_j, s, y\right) \lambda e^{-\lambda D_j} dz_j dD_j - \\
&\quad - \frac{n}{\left(z_{max}-z_{min}\right)^2} I_X\left(x, t, z_{min}, z_{max}\right) I_Y\left(y, s, z_{min}, z_{max}\right) \\
&= \frac{1}{z_{max}-z_{min}} \sum_{j=1}^{n} \int_0^{\infty} g_X\left(D_j\right) g_Y\left(D_j\right) \lambda e^{-\lambda D_j} \int_{B(x,y,t,s,D_j,z_{min},z_{max})} f\left(D_j, z_j, t, x\right) \cdot \\
&\quad \cdot f\left(D_j, z_j, s, y\right) dz_j dD_j - \frac{n}{\left(z_{max}-z_{min}\right)^2} I_X\left(x, t, z_{min}, z_{max}\right) I_Y\left(y, s, z_{min}, z_{max}\right) \\
&= \frac{1}{z_{max}-z_{min}} \sum_{j=1}^{n} \int_0^{\infty} g_X\left(D_j\right) g_Y\left(D_j\right) \lambda e^{-\lambda D_j} k_2\left(x, y, t, s, D_j, z_{min}, z_{max}\right) dD_j - \\
&\quad - \frac{n}{\left(z_{max}-z_{min}\right)^2} I_X\left(x, t, z_{min}, z_{max}\right) I_Y\left(y, s, z_{min}, z_{max}\right).
\end{aligned}
$$

Finally, using (4.7) we obtain

$$
\begin{aligned}
&\operatorname{Cov}\left(X_{x,t}, Y_{y,s}\right) = \qquad\qquad (C.13)\\
&= \frac{1}{z_{max} - z_{min}} \sum_{j=1}^{n} \underbrace{\int_0^\infty g_X\left(D_j\right) g_Y\left(D_j\right) \lambda e^{-\lambda D_j} k_2\left(x, y, t, s, D_j, z_{min}, z_{max}\right) dD_j}_{= J_{XY}(x,y,t,s,z_{min},z_{max})} - \\
&\quad - \frac{n}{\left(z_{max} - z_{min}\right)^2} I_X\left(x, t, z_{min}, z_{max}\right) I_Y\left(y, s, z_{min}, z_{max}\right).\\
&= \frac{n}{z_{max} - z_{min}} J_{XY}\left(x, y, t, s, z_{min}, z_{max}\right) - \\
&\quad - \frac{n}{\left(z_{max} - z_{min}\right)^2} I_X\left(x, t, z_{min}, z_{max}\right) I_Y\left(y, s, z_{min}, z_{max}\right).
\end{aligned}
$$

□

Appendix D

Simplification of auxiliary quantities from Chapter 4

We now give two propositions that allow to further simplify auxiliary quantities defined in for Chapter 4. These might be useful in further attempts to obtain analytical covariance matrices.

First, we notice that we can explicitly calculate the integral in (4.2):

Proposition D.0.1. *Given the assumptions of Proposition 4.1.1, let*

$$
\begin{aligned}
h_1\left(z,t,D_j,z_{min},z_{max}\right) = &\left(\frac{D_j^2}{4} - z^2 + 2z\alpha\sqrt{D_j}t - \alpha^2 D_j t^2\right)\cdot \\
&\cdot\left(\min\left(z-\alpha\sqrt{D_j}t+\frac{D_j}{2},z_{max}\right) - \max\left(z-\alpha\sqrt{D_j}t-\frac{D_j}{2},z_{min}\right)\right)+ \\
&+\left(\min\left(z-\alpha\sqrt{D_j}t+\frac{D_j}{2},z_{max}\right)^2 - \max\left(z-\alpha\sqrt{D_j}t-\frac{D_j}{2},z_{min}\right)^2\right)\left(z-\alpha\sqrt{D_j}t\right)- \\
&-\frac{1}{3}\left(\min\left(z-\alpha\sqrt{D_j}t+\frac{D_j}{2},z_{max}\right)^3 - \max\left(z-\alpha\sqrt{D_j}t-\frac{D_j}{2},z_{min}\right)^3\right),
\end{aligned}
\tag{D.1}
$$

then

$$
h_2\left(z,t,D_j,z_{min},z_{max}\right) = \begin{cases} h_1\left(z,t,D_j,z_{min},z_{max}\right) & \text{,if } A\left(z,t,D_j,z_{min},z_{max}\right)\neq\emptyset \\ 0 & \text{, else} \end{cases}. \tag{D.2}
$$

Proof. Using (3.5) and (3.10), we have

$$
\begin{aligned}
f\left(D_j, z_j, t, z\right) &= \left[\frac{D_j^2}{4} - \left(z_j + v_T\left(D_j\right) t - z\right)^2\right] \\
&= \left[\frac{D_j^2}{4} - \left(\left(z_j - z\right) + v_T\left(D_j\right) t\right)^2\right] \\
&= \left[\frac{D_j^2}{4} - \left(z_j - z\right)^2 - 2\left(z_j - z\right) v_T\left(D_j\right) t - v_T^2\left(D_j\right) t^2\right] \\
&= \left[\frac{D_j^2}{4} - z_j^2 + 2 z_j z - z^2 - 2\left(z_j - z\right) v_T\left(D_j\right) t - v_T^2\left(D_j\right) t^2\right] \\
&= \left[\frac{D_j^2}{4} - z^2 + 2 z v_T\left(D_j\right) t - v_T^2\left(D_j\right) t^2 + 2 z_j\left(z - v_T\left(D_j\right) t\right) - z_j^2\right]
\end{aligned} \tag{D.3}
$$

and thus by employing (4.1) and (D.1)

$$
\begin{aligned}
&\int_{A(z,t,D_j,z_{min},z_{max})} f\left(D_j, z_j, t, z\right) dz_j = \int_{A(z,t,D_j,z_{min},z_{max})} \left[\frac{D_j^2}{4} - \left(z_j + v_T\left(D_j\right) t - z\right)^2\right] dz_j \\
&= \int_{A(z,t,D_j,z_{min},z_{max})} \left[\frac{D_j^2}{4} - z^2 + 2 z v_T\left(D_j\right) t - v_T^2\left(D_j\right) t^2 + 2 z_j\left(z - v_T\left(D_j\right) t\right) - z_j^2\right] dz_j \\
&= \left[\left(\frac{D_j^2}{4} - z^2 + 2 z v_T\left(D_j\right) t - v_T^2\left(D_j\right) t^2\right) z_j + \right. \\
&\quad \left. + z_j^2\left(z - v_T\left(D_j\right) t\right) - \frac{1}{3} z_j^3\right]_{z_j = \max\left(z - v_T(D_j) t - \frac{D_j}{2}, z_{min}\right)}^{z_j = \min\left(z - v_T(D_j) t + \frac{D_j}{2}, z_{max}\right)} \\
&= \left(\frac{D_j^2}{4} - z^2 + 2 z v_T\left(D_j\right) t - v_T^2\left(D_j\right) t^2\right) \cdot \\
&\quad \cdot \left[\min\left(z - v_T\left(D_j\right) t + \frac{D_j}{2}, z_{max}\right) - \max\left(z - v_T\left(D_j\right) t - \frac{D_j}{2}, z_{min}\right)\right] + \\
&\quad + \left[\min\left(z - v_T\left(D_j\right) t + \frac{D_j}{2}, z_{max}\right)^2 - \max\left(z - v_T\left(D_j\right) t - \frac{D_j}{2}, z_{min}\right)^2\right]\left(z - v_T\left(D_j\right) t\right) - \\
&\quad - \frac{1}{3}\left(\min\left(z - v_T\left(D_j\right) t + \frac{D_j}{2}, z_{max}\right)^3 - \max\left(z - v_T\left(D_j\right) t - \frac{D_j}{2}, z_{min}\right)^3\right) \\
&= h_1\left(z, t, D_j, z_{min}, z_{max}\right)
\end{aligned} \tag{D.4}
$$

in the case $A\left(z, t, D_j, z_{min}, z_{max}\right) \neq \emptyset$ and

$$
\int_{A(z,t,D_j,z_{min},z_{max})} f\left(D_j, z_j, t, z\right) dz_j = 0, \tag{D.5}
$$

otherwise.

□

Analogue, we obtain an analytic expression for (4.6).

Proposition D.0.2. *Given the assumptions of Proposition 4.1.2, let*

$$
\begin{aligned}
&k_1\left(x,y,t,s,D_j,z_{min},z_{max}\right) = \qquad\qquad (D.6)\\
&= \left[\left(\frac{D_j^2}{4}-x^2+2x\alpha\sqrt{D_j}t-\alpha^2D_jt^2\right)\left(\frac{D_j^2}{4}-y^2+2y\alpha\sqrt{D_j}s-\alpha^2D_js^2\right)z_j+\right.\\
&\quad+\left[\left(\frac{D_j^2}{4}-x^2+2x\alpha\sqrt{D_j}t-\alpha^2D_jt^2\right)\left(y-\alpha\sqrt{D_j}s\right)+\right.\\
&\quad\left.+\left(x-\alpha\sqrt{D_j}t\right)\left(\frac{D_j^2}{4}-y^2+2y\alpha\sqrt{D_j}s-\alpha^2D_js^2\right)\right]z_j^2+\\
&\quad+\frac{1}{3}\left[4\left(x-\alpha\sqrt{D_j}t\right)\left(y-\alpha\sqrt{D_j}s\right)-\left(\frac{D_j^2}{4}-x^2+2x\alpha\sqrt{D_j}t-\alpha^2D_jt^2\right)-\right.\\
&\quad\left.-\left(\frac{D_j^2}{4}-y^2+2y\alpha\sqrt{D_j}s-\alpha^2D_js^2\right)\right]z_j^3-\frac{1}{2}\left(\left(x-\alpha\sqrt{D_j}t\right)+\left(y-\alpha\sqrt{D_j}s\right)\right)z_j^4+\\
&\quad+\frac{1}{5}z_j^5,\Big]_{z_j=\max\left(\left\{x-\alpha\sqrt{D_j}t-\frac{D_j}{2},y-\alpha\sqrt{D_j}s-\frac{D_j}{2},z_{min}\right\}\right)}^{z_j=\min\left(\left\{x-\alpha\sqrt{D_j}t+\frac{D_j}{2},y-\alpha\sqrt{D_j}s+\frac{D_j}{2},z_{max}\right\}\right)}
\end{aligned}
$$

then

$$
\begin{aligned}
&k_2\left(x,y,t,s,D_j,z_{min},z_{max}\right) \coloneqq \qquad\qquad (D.7)\\
&\coloneqq\begin{cases}k_1\left(x,y,t,s,D_j,z_{min},z_{max}\right) & ,\ \textit{if } B\left(x,y,t,s,D_j,z_{min},z_{max}\right)\neq\emptyset\\ 0 & ,\ \textit{else}\end{cases}.
\end{aligned}
$$

Proof. Using (3.5), (3.10) and (D.3), we obtain

$$
\begin{aligned}
&f\left(D_j, z_j, t, x\right) f\left(D_j, z_j, s, y\right) = \qquad \text{(D.8)}\\
&= \left[\frac{D_j^2}{4} - \left(z_j + v_T\left(D_j\right) t - x\right)^2\right]\left[\frac{D_j^2}{4} - \left(z_j + v_T\left(D_j\right) s - y\right)^2\right]\\
&= \left[\frac{D_j^2}{4} - x^2 + 2x v_T\left(D_j\right) t - v_T^2\left(D_j\right) t^2 + 2 z_j\left(x - v_T\left(D_j\right) t\right) - z_j^2\right] \cdot\\
&\quad \cdot \left[\frac{D_j^2}{4} - y^2 + 2y v_T\left(D_j\right) s - v_T^2\left(D_j\right) s^2 + 2 z_j\left(y - v_T\left(D_j\right) s\right) - z_j^2\right]\\
&= \left(\frac{D_j^2}{4} - x^2 + 2x v_T\left(D_j\right) t - v_T^2\left(D_j\right) t^2\right)\left(\frac{D_j^2}{4} - y^2 + 2y v_T\left(D_j\right) s - v_T^2\left(D_j\right) s^2\right) +\\
&\quad + 2\left[\left(\frac{D_j^2}{4} - x^2 + 2x v_T\left(D_j\right) t - v_T^2\left(D_j\right) t^2\right)\left(y - v_T\left(D_j\right) s\right) +\right.\\
&\quad \left. + \left(x - v_T\left(D_j\right) t\right)\left(\frac{D_j^2}{4} - y^2 + 2y v_T\left(D_j\right) s - v_T^2\left(D_j\right) s^2\right)\right] z_j +\\
&\quad + \left[4\left(x - v_T\left(D_j\right) t\right)\left(y - v_T\left(D_j\right) s\right) - \left(\frac{D_j^2}{4} - x^2 + 2x v_T\left(D_j\right) t - v_T^2\left(D_j\right) t^2\right) -\right.\\
&\quad \left. - \left(\frac{D_j^2}{4} - y^2 + 2y v_T\left(D_j\right) s - v_T^2\left(D_j\right) s^2\right)\right] z_j^2 - 2\left[\left(x - v_T\left(D_j\right) t\right) + \left(y - v_T\left(D_j\right) s\right)\right] z_j^3 + z_j^4
\end{aligned}
$$

which yields by employing (4.5) and (D.6)

$$
\begin{aligned}
&\int_{B(x,y,t,s,D_j,z_{min},z_{max})} f\left(D_j, z_j, t, x\right) f\left(D_j, z_j, s, y\right)\left(z_j\right) dz_j = \qquad \text{(D.9)}\\
&= \left\{\left(\frac{D_j^2}{4} - x^2 + 2x v_T\left(D_j\right) t - v_T^2\left(D_j\right) t^2\right)\left(\frac{D_j^2}{4} - y^2 + 2y v_T\left(D_j\right) s - v_T^2\left(D_j\right) s^2\right) z_j +\right.\\
&\quad + \left[\left(\frac{D_j^2}{4} - x^2 + 2x v_T\left(D_j\right) t - v_T^2\left(D_j\right) t^2\right)\left(y - v_T\left(D_j\right) s\right) +\right.\\
&\quad \left. + \left(x - v_T\left(D_j\right) t\right)\left(\frac{D_j^2}{4} - y^2 + 2y v_T\left(D_j\right) s - v_T^2\left(D_j\right) s^2\right)\right] z_j^2 +\\
&\quad + \frac{1}{3}\left[4\left(x - v_T\left(D_j\right) t\right)\left(y - v_T\left(D_j\right) s\right) - \left(\frac{D_j^2}{4} - x^2 + 2x v_T\left(D_j\right) t - v_T^2\left(D_j\right) t^2\right) -\right.\\
&\quad \left. - \left(\frac{D_j^2}{4} - y^2 + 2y v_T\left(D_j\right) s - v_T^2\left(D_j\right) s^2\right)\right] z_j^3 - \frac{1}{2}\left(\left(x - v_T\left(D_j\right) t\right) + \left(y - v_T\left(D_j\right) s\right)\right) z_j^4 +\\
&\quad \left. + \frac{1}{5} z_j^5,\right\}_{z_j = \max\left(\left\{x - v_T(D_j)t - \frac{D_j}{2}, y - v_T(D_j)s - \frac{D_j}{2}, z_{min}\right\}\right)}^{z_j = \min\left(\left\{x - v_T(D_j)t + \frac{D_j}{2}, y - v_T(D_j)s + \frac{D_j}{2}, z_{max}\right\}\right)}\\
&\quad = k_1\left(x, y, t, s, D_j, z_{min}, z_{max}\right),
\end{aligned}
$$

for $B\left(x,y,t,s,D_j,z_{min},z_{max}\right) \neq \emptyset$ and

$$\int_{B(x,y,t,s,D_j,z_{min},z_{max})} f\left(D_j,z_j,t,x\right) f\left(D_j,z_j,s,y\right)\left(z_j\right) dz_j = 0, \tag{D.10}$$

for $B\left(x,y,t,s,D_j,z_{min},z_{max}\right) = \emptyset$.

□

Appendix E

Velocity models

Here, we shortly discuss (besides our strongly simplified velocity model for spherical hydrometeors) the velocity models of Brdar and Seifert (2018) in connection with the axis ratios provided by Auer and Veal (1970). Furthermore, we mention the experimental results of Heymsfield and Kajikawa (1987), for assessing potential model errors introduced by the velocity model. This discussion of the different velocity models can facilitate interpreting our results for different hydrometeor geometries (which employ these velocity models), as gravitational sorting and thus the dependence of the terminal fall velocities on hydrometeor mass and velocity have a large influence on the number density and liquid water content profiles and correlations. Note that for this thesis we adopted the nomenclature for the hydrometeor types from the sources cited in this chapter.

Figure E.1 shows the terminal fall velocities obtained from the results of Brdar and Seifert (2018), when combined with axis ratios determined by the according power laws given in Auer and Veal (1970). Note that Brdar and Seifert (2018) obtained their results from mathematical modelling, while Auer and Veal (1970) attained their results by fitting power laws to experimental data. Furthermore, Figure E.1 shows terminal fall velocities obtained by equating gravitational force and friction (refered to as simplified model), as well as reference values from the power laws obtained for the terminal fall velocity by Heymsfield and Kajikawa (1987) from experimental data. The curves can be useful to explain the effect of gravitational sorting on our profiles and covariances. The (experimental) results from Heymsfield and Kajikawa, 1987 are included to better asess the accuracy of the used velocity models and evaluate how the differences between the McSnow model (Brdar and Seifert, 2018) and the simplified velocity model compare to the model error, i.e. the difference between the model and physical reality. Terminal fall velocities in Figure E.1 are shown for different hydrometeor geometries in the mass range $[4.8 \cdot 10^{-10} kg, 3.8 \cdot 10^{-6} kg]$ (left panel) and $[4.8 \cdot 10^{-10} kg, 6.0 \cdot 10^{-2} kg]$.

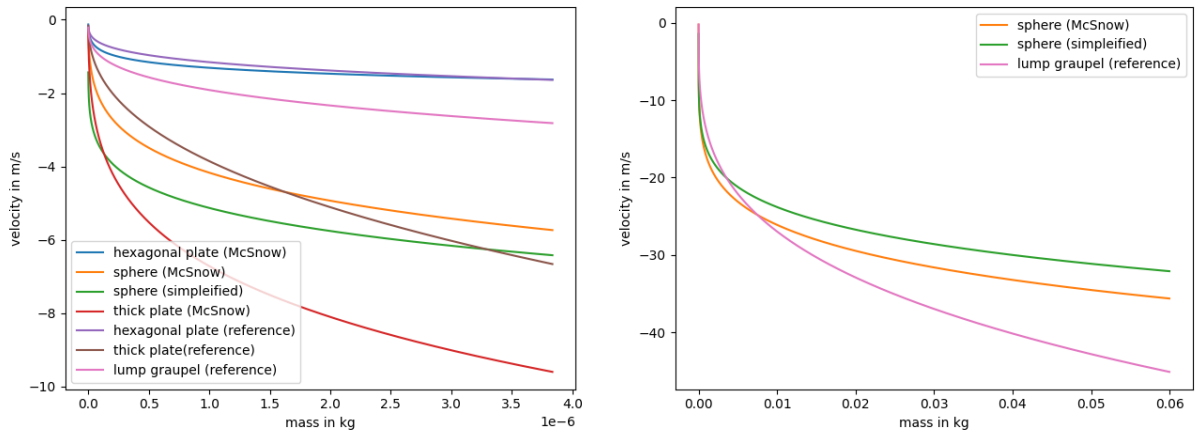

Figure E.1: Terminal fall velocities for different hydrometeor geometries in the mass range $[4.8 \cdot 10^{-10} kg, 3.8 \cdot 10^{-6} kg]$ (left panel) and $[4.8 \cdot 10^{-10} kg, 6.0 \cdot 10^{-2} kg]$ (right panel). Axis ratios are assumed to be determined by the according power laws given in Auer and Veal, 1970 and terminal fall velocities are calculated using the results of Brdar and Seifert, 2018 (McSnow), or by equating gravitational force and friction (simplified). The power laws given for the terminal fall velocity in Heymsfield and Kajikawa, 1987 are used as reference.

In the left panel of Figure E.1, we see that that for hexagonal plates the velocities predicted by the McSnow model (Brdar and Seifert, 2018) agree relatively well with the experimental predictions from Heymsfield and Kajikawa, 1987. However for thick plates there are larger differences, especially for higher hydrometeor masses. For the spherical hydrometeors, we see that both the McSnow model (Brdar and Seifert, 2018) and the simplified velocity model overestimate the terminal fall velocity for smaller hydrometeor masses, whereas they underestimate it for larger hydrometeor masses. Here the differences between the McSnow model (Brdar and Seifert, 2018) and the simplified velocity model are for most hydrometeor masses smaller than the deviation from the experimental results from Heymsfield and Kajikawa, 1987.
Differences between the predictions for the terminal fall velocity of hexagonal plates to the reference model might be explained by using only the axis ratio of a hexagonal plate, but for simplicity the cross section of a cylinder. Further reasons for differences to experimental data might include density variations due to rhiming (we assume hydrometeors here to be composed of massive ice), deviations of real hydrometeors from idealized geometries and axis ratios, the effects of particle orientations varying over time and interactions between hydrometeors.

Appendix F

Upwind scheme

F.1 Diagonalization

We can use (2.46), (2.47), (2.48) and (2.49) together with $\gamma = \frac{1}{6}$ to rewrite (2.51) in a simpler way:

$$A(\bar{x}) = \begin{pmatrix} \chi_N (1-\gamma)\bar{x}^\gamma & \chi_N \gamma \bar{x}^{\gamma-1} \rho_w^{-1} D_v^{-3} \\ -\chi_L \bar{x}^{\gamma+1} \rho_w D_v^3 & \chi_L (1+\gamma)\bar{x}^\gamma \end{pmatrix} \tag{F.1}$$

$$\overset{(2.46)}{=} \begin{pmatrix} \chi_N (1-\gamma)\bar{x}^\gamma & \chi_N \gamma \bar{x}^\gamma \frac{\rho_w D_v^3 N}{L} \rho_w^{-1} D_v^{-3} \\ -\chi_L \bar{x}^\gamma \frac{L}{\rho_w D_v^3 N} \rho_w D_v^3 & \chi_L (1+\gamma)\bar{x}^\gamma \end{pmatrix} \tag{F.2}$$

$$= \begin{pmatrix} \chi_N (1-\gamma)\bar{x}^\gamma & \chi_N \gamma \bar{x}^\gamma \frac{N}{L} \\ -\chi_L \bar{x}^\gamma \frac{L}{N} & \chi_L (1+\gamma)\bar{x}^\gamma \end{pmatrix} \tag{F.3}$$

$$= \bar{x}^\gamma \begin{pmatrix} \chi_N (1-\gamma) & \chi_N \gamma \frac{N}{L} \\ -\chi_L \frac{L}{N} & \chi_L (1+\gamma) \end{pmatrix} \tag{F.4}$$

$$\overset{(2.48)}{=} \bar{x}^\gamma \begin{pmatrix} \chi_N (1-\gamma) & \chi_N \gamma \frac{N}{L} \\ -\frac{35}{16} \chi_N \frac{L}{N} & \frac{35}{16} \chi_N (1+\gamma) \end{pmatrix} \tag{F.5}$$

$$= \chi_N \bar{x}^\gamma \begin{pmatrix} (1-\gamma) & \gamma \frac{N}{L} \\ -\frac{35}{16} \frac{L}{N} & \frac{35}{16} (1+\gamma) \end{pmatrix} \tag{F.6}$$

$$\overset{\gamma=\frac{1}{6}}{=} \chi_N \bar{x}^{\frac{1}{6}} \begin{pmatrix} \left(1-\frac{1}{6}\right) & \frac{1}{6} \frac{N}{L} \\ -\frac{35}{16} \frac{L}{N} & \frac{35}{16} \left(1+\frac{1}{6}\right) \end{pmatrix} \tag{F.7}$$

$$= \chi_N \bar{x}^{\frac{1}{6}} \begin{pmatrix} \left(\frac{6}{6}-\frac{1}{6}\right) & \frac{1}{6} \frac{N}{L} \\ -\frac{35}{16} \frac{L}{N} & \frac{35}{16} \left(\frac{6}{6}+\frac{1}{6}\right) \end{pmatrix} \tag{F.8}$$

$$= \chi_N \bar{x}^{\frac{1}{6}} \begin{pmatrix} \frac{5}{6} & \frac{1}{6} \frac{N}{L} \\ -\frac{35}{16} \frac{L}{N} & \frac{35}{16} \frac{7}{6} \end{pmatrix} \tag{F.9}$$

$$= \chi_N \bar{x}^{\frac{1}{6}} \begin{pmatrix} \frac{5}{6} & \frac{1}{6} \frac{N}{L} \\ -\frac{35}{16} \frac{L}{N} & \frac{245}{96}. \end{pmatrix} \tag{F.10}$$

Denoting e.g. $k = \frac{L}{N}$, this becomes

$$A(\bar{x}) = \chi_N \bar{x}^{\frac{1}{6}} \begin{pmatrix} \frac{5}{6} & \frac{1}{6}\frac{1}{k} \\ -\frac{35}{16}k & \frac{245}{96} \end{pmatrix} \tag{F.11}$$

and can be passed to Wolfram|Alpha, n.d. for diagonalization, yielding

$$A(\bar{x}) = \chi_N \bar{x}^{\frac{1}{6}} \cdot S \cdot J \cdot S^{-1}, \tag{F.12}$$

with

$$S = \begin{pmatrix} \frac{165+\sqrt{13785}}{420k} & -\frac{\sqrt{13785}-165}{420k} \\ 1 & 1 \end{pmatrix} \tag{F.13}$$

$$= \begin{pmatrix} \frac{165+\sqrt{13785}}{420k} & \frac{165-\sqrt{13785}}{420k} \\ 1 & 1 \end{pmatrix} \tag{F.14}$$

$$= \begin{pmatrix} \frac{165+\sqrt{13785}}{420}\frac{N}{L} & \frac{165-\sqrt{13785}}{420}\frac{N}{L} \\ 1 & 1 \end{pmatrix} \tag{F.15}$$

and

$$J = \begin{pmatrix} \frac{1}{192}\left(325-\sqrt{13785}\right) & 0 \\ 0 & \frac{1}{192}\left(325+\sqrt{13785}\right) \end{pmatrix}, \tag{F.16}$$

as well as

$$S^{-1} = \begin{pmatrix} 14\sqrt{\frac{15}{919}}k & \frac{1}{2} - \frac{11\sqrt{\frac{15}{919}}}{2} \\ -14\sqrt{\frac{15}{919}}k & \frac{1}{2} + \frac{11\sqrt{\frac{15}{919}}}{2}. \end{pmatrix} \tag{F.17}$$

$$= \begin{pmatrix} 14\sqrt{\frac{15}{919}}k & \frac{1}{2}\left(1-11\sqrt{\frac{15}{919}}\right) \\ -14\sqrt{\frac{15}{919}}k & \frac{1}{2}\left(1+11\sqrt{\frac{15}{919}}\right). \end{pmatrix} \tag{F.18}$$

$$= \begin{pmatrix} 14\sqrt{\frac{15}{919}}\frac{L}{N} & \frac{1}{2}\left(1-11\sqrt{\frac{15}{919}}\right) \\ -14\sqrt{\frac{15}{919}}\frac{L}{N} & \frac{1}{2}\left(1+11\sqrt{\frac{15}{919}}\right). \end{pmatrix} \tag{F.19}$$

F.2 System of equations

Now, we can solve the according system of equations: Adding (5.19) and (5.20), yields

$$0 = 14\sqrt{\frac{15}{919}}\frac{L_{k,l}}{N_{k,l}}\left[\frac{N_{k,l+1}-N_{k,l}}{\Delta t}+c_{+}\left(k,l\right)\frac{N_{k+1,l}-N_{k,l}}{\Delta x}\right]+ \tag{F.20}$$

$$+\frac{1}{2}\left(1-11\sqrt{\frac{15}{919}}\right)\left[\frac{L_{k,l+1}-L_{k,l}}{\Delta t}+c_{+}\left(k,l\right)\frac{L_{k+1,l}-L_{k,l}}{\Delta x}\right],-$$

$$-14\sqrt{\frac{15}{919}}\frac{L_{k,l}}{N_{k,l}}\left[\frac{N_{k,l+1}-N_{k,l}}{\Delta t}+c_{-}\left(k,l\right)\frac{N_{k+1,l}-N_{k,l}}{\Delta x}\right]+ \tag{F.21}$$

$$+\frac{1}{2}\left(1+11\sqrt{\frac{15}{919}}\right)\left[\frac{L_{k,l+1}-L_{k,l}}{\Delta t}+c_{-}\left(k,l\right)\frac{L_{k+1,l}-L_{k,l}}{\Delta x}\right],$$

$$=14\sqrt{\frac{15}{919}}\frac{L_{k,l}}{N_{k,l}}\left[c_{+}\left(k,l\right)-c_{-}\left(k,l\right)\right]\frac{N_{k+1,l}-N_{k,l}}{\Delta x}+\frac{L_{k,l+1}-L_{k,l}}{\Delta t}+ \tag{F.22}$$

$$+\left[\frac{1}{2}\left(1-11\sqrt{\frac{15}{919}}\right)c_{+}\left(k,l\right)+\frac{1}{2}\left(1+11\sqrt{\frac{15}{919}}\right)c_{-}\left(k,l\right)\right]\frac{L_{k+1,l}-L_{k,l}}{\Delta x},$$

becoming

$$L_{k,l+1}=L_{k,l}-\Delta t\left(14\sqrt{\frac{15}{919}}\frac{L_{k,l}}{N_{k,l}}\left[c_{+}\left(k,l\right)-c_{-}\left(k,l\right)\right]\frac{N_{k+1,l}-N_{k,l}}{\Delta x}+\right. \tag{F.23}$$

$$\left.+\left[\frac{1}{2}\left(1-11\sqrt{\frac{15}{919}}\right)c_{+}\left(k,l\right)+\frac{1}{2}\left(1+11\sqrt{\frac{15}{919}}\right)c_{-}\left(k,l\right)\right]\frac{L_{k+1,l}-L_{k,l}}{\Delta x}\right)$$

$$=L_{k,l}-\frac{\Delta t}{\Delta x}L_{k,l}\left\{14\sqrt{\frac{15}{919}}\left[c_{+}\left(k,l\right)-c_{-}\left(k,l\right)\right]\left(\frac{N_{k+1,l}}{N_{k,l}}-1\right)+\right. \tag{F.24}$$

$$\left.+\left[\frac{1}{2}\left(1-11\sqrt{\frac{15}{919}}\right)c_{+}\left(k,l\right)+\frac{1}{2}\left(1+11\sqrt{\frac{15}{919}}\right)c_{-}\left(k,l\right)\right]\left(\frac{L_{k+1,l}}{L_{k,l}}-1\right)\right\}$$

$$=L_{k,l}\left[1-\frac{\Delta t}{\Delta x}\left\{14\sqrt{\frac{15}{919}}\left[c_{+}\left(k,l\right)-c_{-}\left(k,l\right)\right]\left(\frac{N_{k+1,l}}{N_{k,l}}-1\right)+\right.\right. \tag{F.25}$$

$$\left.\left.+\left[\frac{1}{2}\left(1-11\sqrt{\frac{15}{919}}\right)c_{+}\left(k,l\right)+\frac{1}{2}\left(1+11\sqrt{\frac{15}{919}}\right)c_{-}\left(k,l\right)\right]\left(\frac{L_{k+1,l}}{L_{k,l}}-1\right)\right\}\right].$$

Now, using

$$c_{+}\left(k,l\right)=\frac{\chi_N}{192}\left(\frac{1}{\rho_w D_v^3}\right)^{\frac{1}{6}}\left(\frac{L_{k,l}}{N_{k,l}}\right)^{\frac{1}{6}}\cdot\left(\sqrt{13785}-325\right) \tag{F.26}$$

$$c_{-}\left(k,l\right)=-\frac{\chi_N}{192}\left(\frac{1}{\rho_w D_v^3}\right)^{\frac{1}{6}}\left(\frac{L_{k,l}}{N_{k,l}}\right)^{\frac{1}{6}}\cdot\left(\sqrt{13785}+325\right), \tag{F.27}$$

we get

$$c_+(k,l) - c_-(k,l) = \frac{\chi_N}{192}\left(\frac{1}{\rho_w D_v^3}\right)^{\frac{1}{6}}\left(\frac{L_{k,l}}{N_{k,l}}\right)^{\frac{1}{6}} \cdot \left(\sqrt{13785} - 325\right) + \tag{F.28}$$

$$+ \frac{\chi_N}{192}\left(\frac{1}{\rho_w D_v^3}\right)^{\frac{1}{6}}\left(\frac{L_{k,l}}{N_{k,l}}\right)^{\frac{1}{6}} \cdot \left(\sqrt{13785} + 325\right)$$

$$= \frac{\chi_N}{192}\left(\frac{1}{\rho_w D_v^3}\right)^{\frac{1}{6}}\left(\frac{L_{k,l}}{N_{k,l}}\right)^{\frac{1}{6}} \cdot \left(\sqrt{13785} - 325 + \sqrt{13785} + 325\right) \tag{F.29}$$

$$= \frac{\chi_N}{192}\left(\frac{1}{\rho_w D_v^3}\right)^{\frac{1}{6}}\left(\frac{L_{k,l}}{N_{k,l}}\right)^{\frac{1}{6}} \cdot 2 \cdot \sqrt{13785} \tag{F.30}$$

and

$$\frac{1}{2}\left(1 - 11\sqrt{\frac{15}{919}}\right) c_+(k,l) + \frac{1}{2}\left(1 + 11\sqrt{\frac{15}{919}}\right) c_-(k,l) = \tag{F.31}$$

$$= \frac{1}{2}\left(1 - 11\sqrt{\frac{15}{919}}\right) \frac{\chi_N}{192}\left(\frac{1}{\rho_w D_v^3}\right)^{\frac{1}{6}}\left(\frac{L_{k,l}}{N_{k,l}}\right)^{\frac{1}{6}} \cdot \left(\sqrt{13785} - 325\right) - \tag{F.32}$$

$$- \frac{1}{2}\left(1 + 11\sqrt{\frac{15}{919}}\right) \frac{\chi_N}{192}\left(\frac{1}{\rho_w D_v^3}\right)^{\frac{1}{6}}\left(\frac{L_{k,l}}{N_{k,l}}\right)^{\frac{1}{6}} \cdot \left(\sqrt{13785} + 325\right)$$

$$= \frac{1}{2}\frac{\chi_N}{192}\left(\frac{1}{\rho_w D_v^3}\right)^{\frac{1}{6}}\left(\frac{L_{k,l}}{N_{k,l}}\right)^{\frac{1}{6}} \cdot \left[\left(1 - 11\sqrt{\frac{15}{919}}\right)\left(\sqrt{13785} - 325\right) - \tag{F.33}\right.$$

$$\left. - \left(1 + 11\sqrt{\frac{15}{919}}\right)\left(\sqrt{13785} + 325\right)\right]$$

$$= \frac{\chi_N}{192}\left(\frac{1}{\rho_w D_v^3}\right)^{\frac{1}{6}}\left(\frac{L_{k,l}}{N_{k,l}}\right)^{\frac{1}{6}} \cdot s_2,$$

setting (using Wolfram|Alpha, n.d.)

$$s_1 \coloneqq 14\sqrt{\frac{15}{919}} \cdot 2 \cdot \sqrt{13785} \tag{F.34}$$

$$= 420 \tag{F.35}$$

$$s_2 \coloneqq \frac{1}{2}\left[\left(1 - 11\sqrt{\frac{15}{919}}\right)\left(\sqrt{13785} - 325\right) - \left(1 + 11\sqrt{\frac{15}{919}}\right)\left(\sqrt{13785} + 325\right)\right] \tag{F.36}$$

$$= -490 \tag{F.37}$$

After inserting $c_+(k,l)$ and $c_-(k,l)$, (F.25) becomes

$$L_{k,l+1} = L_{k,l}\left[1 - \frac{\Delta t}{\Delta x}\left(14\sqrt{\frac{15}{919}}\left[\frac{\chi_N}{192}\left(\frac{1}{\rho_w D_v^3}\right)^{\frac{1}{6}}\left(\frac{L_{k,l}}{N_{k,l}}\right)^{\frac{1}{6}}\cdot 2\cdot\sqrt{13785}\right]\left(\frac{N_{k+1,l}}{N_{k,l}}-1\right)+\right.\right. \tag{F.38}$$
$$\left.\left. + \left[\frac{\chi_N}{192}\left(\frac{1}{\rho_w D_v^3}\right)^{\frac{1}{6}}\left(\frac{L_{k,l}}{N_{k,l}}\right)^{\frac{1}{6}}\cdot s_2\right]\left(\frac{L_{k+1,l}}{L_{k,l}}-1\right)\right)\right]$$
$$= L_{k,l}\left[1 - \frac{\Delta t}{\Delta x}\frac{\chi_N}{192}\left(\frac{1}{\rho_w D_v^3}\right)^{\frac{1}{6}}\left(\frac{L_{k,l}}{N_{k,l}}\right)^{\frac{1}{6}}\left(14\sqrt{\frac{15}{919}}\cdot 2\cdot\sqrt{13785}\left(\frac{N_{k+1,l}}{N_{k,l}}-1\right)+\right.\right. \tag{F.39}$$
$$\left.\left. + s_2\left(\frac{L_{k+1,l}}{L_{k,l}}-1\right)\right)\right]$$
$$= L_{k,l}\left[1 - \frac{\Delta t}{\Delta x}\frac{\chi_N}{192}\left(\frac{1}{\rho_w D_v^3}\right)^{\frac{1}{6}}\left(\frac{L_{k,l}}{N_{k,l}}\right)^{\frac{1}{6}}\left(s_1\left(\frac{N_{k+1,l}}{N_{k,l}}-1\right)+s_2\left(\frac{L_{k+1,l}}{L_{k,l}}-1\right)\right)\right].$$

Analogue, setting

$$F := \frac{\left(1 - 11\sqrt{\frac{15}{919}}\right)}{\left(1 + 11\sqrt{\frac{15}{919}}\right)}, \tag{F.40}$$

(5.19)-F(5.20) yields

$$
\begin{aligned}
0 = {} & 14\sqrt{\frac{15}{919}}\frac{L_{k,l}}{N_{k,l}}\left[\frac{N_{k,l+1}-N_{k,l}}{\Delta t}+c_{+}\left(k,l\right)\frac{N_{k+1,l}-N_{k,l}}{\Delta x}\right]+ \qquad \text{(F.41)}\\
& +\frac{1}{2}\left(1-11\sqrt{\frac{15}{919}}\right)\left[\frac{L_{k,l+1}-L_{k,l}}{\Delta t}+c_{+}\left(k,l\right)\frac{L_{k+1,l}-L_{k,l}}{\Delta x}\right]+\\
& +14\sqrt{\frac{15}{919}}\frac{L_{k,l}}{N_{k,l}}F\left[\frac{N_{k,l+1}-N_{k,l}}{\Delta t}+c_{-}\left(k,l\right)\frac{N_{k+1,l}-N_{k,l}}{\Delta x}\right]-\\
& -F\frac{1}{2}\left(1+11\sqrt{\frac{15}{919}}\right)\left[\frac{L_{k,l+1}-L_{k,l}}{\Delta t}+c_{-}\left(k,l\right)\frac{L_{k+1,l}-L_{k,l}}{\Delta x}\right]\\
= {} & 14\sqrt{\frac{15}{919}}\frac{L_{k,l}}{N_{k,l}}\left[\frac{N_{k,l+1}-N_{k,l}}{\Delta t}+c_{+}\left(k,l\right)\frac{N_{k+1,l}-N_{k,l}}{\Delta x}\right]+ \qquad \text{(F.42)}\\
& +\frac{1}{2}\left(1-11\sqrt{\frac{15}{919}}\right)\left[\frac{L_{k,l+1}-L_{k,l}}{\Delta t}+c_{+}\left(k,l\right)\frac{L_{k+1,l}-L_{k,l}}{\Delta x}\right]+\\
& +14\sqrt{\frac{15}{919}}\frac{L_{k,l}}{N_{k,l}}F\left[\frac{N_{k,l+1}-N_{k,l}}{\Delta t}+c_{-}\left(k,l\right)\frac{N_{k+1,l}-N_{k,l}}{\Delta x}\right]-\\
& -\frac{\left(1-11\sqrt{\frac{15}{919}}\right)}{\left(1+11\sqrt{\frac{15}{919}}\right)}\frac{1}{2}\left(1+11\sqrt{\frac{15}{919}}\right)\left[\frac{L_{k,l+1}-L_{k,l}}{\Delta t}+c_{-}\left(k,l\right)\frac{L_{k+1,l}-L_{k,l}}{\Delta x}\right]\\
= {} & 14\sqrt{\frac{15}{919}}\frac{L_{k,l}}{N_{k,l}}\left[\frac{N_{k,l+1}-N_{k,l}}{\Delta t}+c_{+}\left(k,l\right)\frac{N_{k+1,l}-N_{k,l}}{\Delta x}\right]+ \qquad \text{(F.43)}\\
& +\frac{1}{2}\left(1-11\sqrt{\frac{15}{919}}\right)\left[\frac{L_{k,l+1}-L_{k,l}}{\Delta t}+c_{+}\left(k,l\right)\frac{L_{k+1,l}-L_{k,l}}{\Delta x}\right]+\\
& +14\sqrt{\frac{15}{919}}\frac{L_{k,l}}{N_{k,l}}F\left[\frac{N_{k,l+1}-N_{k,l}}{\Delta t}+c_{-}\left(k,l\right)\frac{N_{k+1,l}-N_{k,l}}{\Delta x}\right]-\\
& -\frac{1}{2}\left(1-11\sqrt{\frac{15}{919}}\right)\left[\frac{L_{k,l+1}-L_{k,l}}{\Delta t}+c_{-}\left(k,l\right)\frac{L_{k+1,l}-L_{k,l}}{\Delta x}\right],
\end{aligned}
$$

becoming

$$0 = 14\sqrt{\frac{15}{919}}\frac{L_{k,l}}{N_{k,l}}\left[\frac{N_{k,l+1}-N_{k,l}}{\Delta t}+c_{+}\left(k,l\right)\frac{N_{k+1,l}-N_{k,l}}{\Delta x}\right]+ \tag{F.44}$$
$$+\frac{1}{2}\left(1-11\sqrt{\frac{15}{919}}\right)\left[\frac{L_{k,l+1}-L_{k,l}}{\Delta t}+c_{+}\left(k,l\right)\frac{L_{k+1,l}-L_{k,l}}{\Delta x}\right]+$$
$$+14\sqrt{\frac{15}{919}}\frac{L_{k,l}}{N_{k,l}}F\left[\frac{N_{k,l+1}-N_{k,l}}{\Delta t}+c_{-}\left(k,l\right)\frac{N_{k+1,l}-N_{k,l}}{\Delta x}\right]-$$
$$-\frac{1}{2}\left(1-11\sqrt{\frac{15}{919}}\right)\left[\frac{L_{k,l+1}-L_{k,l}}{\Delta t}+c_{-}\left(k,l\right)\frac{L_{k+1,l}-L_{k,l}}{\Delta x}\right]$$
$$= 14\sqrt{\frac{15}{919}}\frac{L_{k,l}}{N_{k,l}}\left[\frac{N_{k,l+1}-N_{k,l}}{\Delta t}+c_{+}\left(k,l\right)\frac{N_{k+1,l}-N_{k,l}}{\Delta x}\right]+ \tag{F.45}$$
$$+\frac{1}{2}\left(1-11\sqrt{\frac{15}{919}}\right)\left[c_{+}\left(k,l\right)\frac{L_{k+1,l}-L_{k,l}}{\Delta x}\right]+$$
$$+14\sqrt{\frac{15}{919}}\frac{L_{k,l}}{N_{k,l}}F\left[\frac{N_{k,l+1}-N_{k,l}}{\Delta t}+c_{-}\left(k,l\right)\frac{N_{k+1,l}-N_{k,l}}{\Delta x}\right]-$$
$$-\frac{1}{2}\left(1-11\sqrt{\frac{15}{919}}\right)\left[c_{-}\left(k,l\right)\frac{L_{k+1,l}-L_{k,l}}{\Delta x}\right]$$
$$= 14\sqrt{\frac{15}{919}}\frac{L_{k,l}}{N_{k,l}}\left[\frac{N_{k,l+1}-N_{k,l}}{\Delta t}+c_{+}\left(k,l\right)\frac{N_{k+1,l}-N_{k,l}}{\Delta x}\right]+ \tag{F.46}$$
$$+\frac{1}{2}\left(1-11\sqrt{\frac{15}{919}}\right)\left[c_{+}\left(k,l\right)-c_{-}\left(k,l\right)\right]\frac{L_{k+1,l}-L_{k,l}}{\Delta x}+$$
$$+14\sqrt{\frac{15}{919}}\frac{L_{k,l}}{N_{k,l}}F\left[\frac{N_{k,l+1}-N_{k,l}}{\Delta t}+c_{-}\left(k,l\right)\frac{N_{k+1,l}-N_{k,l}}{\Delta x}\right]$$

and consequently

$$0 = 14\sqrt{\frac{15}{919}}\frac{L_{k,l}}{N_{k,l}}\left[\frac{N_{k,l+1}-N_{k,l}}{\Delta t} + c_+(k,l)\,\frac{N_{k+1,l}-N_{k,l}}{\Delta x}\right] + \tag{F.47}$$
$$+\frac{1}{2}\left(1-11\sqrt{\frac{15}{919}}\right)[c_+(k,l)-c_-(k,l)]\,\frac{L_{k+1,l}-L_{k,l}}{\Delta x}+$$
$$+14\sqrt{\frac{15}{919}}\frac{L_{k,l}}{N_{k,l}}F\left[\frac{N_{k,l+1}-N_{k,l}}{\Delta t} + c_-(k,l)\,\frac{N_{k+1,l}-N_{k,l}}{\Delta x}\right]$$
$$= 14\sqrt{\frac{15}{919}}\frac{L_{k,l}}{N_{k,l}}(1+F)\,\frac{N_{k,l+1}-N_{k,l}}{\Delta t} + 14\sqrt{\frac{15}{919}}\frac{L_{k,l}}{N_{k,l}}\left[c_+(k,l)\,\frac{N_{k+1,l}-N_{k,l}}{\Delta x}\right] + \tag{F.48}$$
$$+\frac{1}{2}\left(1-11\sqrt{\frac{15}{919}}\right)[c_+(k,l)-c_-(k,l)]\,\frac{L_{k+1,l}-L_{k,l}}{\Delta x}+$$
$$+14\sqrt{\frac{15}{919}}\frac{L_{k,l}}{N_{k,l}}F\left[c_-(k,l)\,\frac{N_{k+1,l}-N_{k,l}}{\Delta x}\right]$$
$$= 14\sqrt{\frac{15}{919}}\frac{L_{k,l}}{N_{k,l}}(1+F)\,\frac{N_{k,l+1}-N_{k,l}}{\Delta t} + 14\sqrt{\frac{15}{919}}\frac{L_{k,l}}{N_{k,l}}[c_+(k,l)+Fc_-(k,l)]\,\frac{N_{k+1,l}-N_{k,l}}{\Delta x}+$$
$$+\frac{1}{2}\left(1-11\sqrt{\frac{15}{919}}\right)[c_+(k,l)-c_-(k,l)]\,\frac{L_{k+1,l}-L_{k,l}}{\Delta x}. \tag{F.49}$$

Now, multiplying by $\frac{1}{14}\sqrt{\frac{919}{15}}\frac{N_{k,l}}{L_{k,l}}\frac{1}{(1+F)}$, this becomes

$$0 = \frac{N_{k,l+1}-N_{k,l}}{\Delta t} + \frac{1}{14}\sqrt{\frac{919}{15}}\frac{N_{k,l}}{L_{k,l}}\frac{1}{(1+F)}14\sqrt{\frac{15}{919}}\frac{L_{k,l}}{N_{k,l}}[c_+(k,l)+Fc_-(k,l)]\,\frac{N_{k+1,l}-N_{k,l}}{\Delta x}+$$
$$+\frac{1}{14}\sqrt{\frac{919}{15}}\frac{N_{k,l}}{L_{k,l}}\frac{1}{(1+F)}\frac{1}{2}\left(1-11\sqrt{\frac{15}{919}}\right)[c_+(k,l)-c_-(k,l)]\,\frac{L_{k+1,l}-L_{k,l}}{\Delta x} \tag{F.50}$$
$$= \frac{N_{k,l+1}-N_{k,l}}{\Delta t} + \frac{1}{(1+F)}[c_+(k,l)+Fc_-(k,l)]\,\frac{N_{k+1,l}-N_{k,l}}{\Delta x}+ \tag{F.51}$$
$$+\frac{1}{2\cdot 14}\sqrt{\frac{919}{15}}\frac{N_{k,l}}{L_{k,l}}\frac{1}{(1+F)}\left(1-11\sqrt{\frac{15}{919}}\right)[c_+(k,l)-c_-(k,l)]\,\frac{L_{k+1,l}-L_{k,l}}{\Delta x}$$
$$= \frac{N_{k,l+1}-N_{k,l}}{\Delta t} + \frac{1}{(1+F)}[c_+(k,l)+Fc_-(k,l)]\,\frac{N_{k+1,l}-N_{k,l}}{\Delta x}+ \tag{F.52}$$
$$+\frac{1}{2\cdot 14}\frac{N_{k,l}}{L_{k,l}}\frac{1}{(1+F)}\left(\sqrt{\frac{919}{15}}-11\right)[c_+(k,l)-c_-(k,l)]\,\frac{L_{k+1,l}-L_{k,l}}{\Delta x},$$

yielding

$$N_{k,l+1} = N_{k,l} - \Delta t \left[\frac{1}{(1+F)} \left[c_+(k,l) + F c_-(k,l) \right] \frac{N_{k+1,l} - N_{k,l}}{\Delta x} + \right. \tag{F.53}$$
$$\left. + \frac{1}{2 \cdot 14} \frac{N_{k,l}}{L_{k,l}} \frac{1}{(1+F)} \left(\sqrt{\frac{919}{15}} - 11 \right) \left[c_+(k,l) - c_-(k,l) \right] \frac{L_{k+1,l} - L_{k,l}}{\Delta x} \right]$$
$$= N_{k,l} - \frac{\Delta t}{\Delta x} \left[\frac{1}{(1+F)} \left[c_+(k,l) + F c_-(k,l) \right] (N_{k+1,l} - N_{k,l}) + \right. \tag{F.54}$$
$$\left. + \frac{1}{2 \cdot 14} \frac{N_{k,l}}{L_{k,l}} \frac{1}{(1+F)} \left(\sqrt{\frac{919}{15}} - 11 \right) \left[c_+(k,l) - c_-(k,l) \right] (L_{k+1,l} - L_{k,l}) \right]$$
$$= N_{k,l} - \frac{\Delta t}{\Delta x} \left[\frac{1}{(1+F)} \left[c_+(k,l) + F c_-(k,l) \right] N_{k,l} \left(\frac{N_{k+1,l}}{N_{k,l}} - 1 \right) + \right. \tag{F.55}$$
$$\left. + \frac{1}{2 \cdot 14} \frac{N_{k,l}}{L_{k,l}} \frac{1}{(1+F)} \left(\sqrt{\frac{919}{15}} - 11 \right) \left[c_+(k,l) - c_-(k,l) \right] L_{k,l} \left(\frac{L_{k+1,l}}{L_{k,l}} - 1 \right) \right]$$
$$= N_{k,l} - \frac{\Delta t}{\Delta x} N_{k,l} \left[\frac{1}{(1+F)} \left[c_+(k,l) + F c_-(k,l) \right] \left(\frac{N_{k+1,l}}{N_{k,l}} - 1 \right) + \right. \tag{F.56}$$
$$\left. + \frac{1}{2 \cdot 14} \frac{1}{(1+F)} \left(\sqrt{\frac{919}{15}} - 11 \right) \left[c_+(k,l) - c_-(k,l) \right] \left(\frac{L_{k+1,l}}{L_{k,l}} - 1 \right) \right]$$
$$= N_{k,l} \left(1 - \frac{\Delta t}{\Delta x} \left[\frac{1}{(1+F)} \left[c_+(k,l) + F c_-(k,l) \right] \left(\frac{N_{k+1,l}}{N_{k,l}} - 1 \right) + \right. \right. \tag{F.57}$$
$$\left. \left. + \frac{1}{2 \cdot 14} \frac{1}{(1+F)} \left(\sqrt{\frac{919}{15}} - 11 \right) \left[c_+(k,l) - c_-(k,l) \right] \left(\frac{L_{k+1,l}}{L_{k,l}} - 1 \right) \right] \right)$$

As we have

$$c_+(k,l) + F c_-(k,l) = \frac{\chi_N}{192} \left(\frac{1}{\rho_w D_v^3} \right)^{\frac{1}{6}} \left(\frac{L_{k,l}}{N_{k,l}} \right)^{\frac{1}{6}} \cdot \left(\sqrt{13785} - 325 \right) - \tag{F.58}$$
$$- F \frac{\chi_N}{192} \left(\frac{1}{\rho_w D_v^3} \right)^{\frac{1}{6}} \left(\frac{L_{k,l}}{N_{k,l}} \right)^{\frac{1}{6}} \cdot \left(\sqrt{13785} + 325 \right)$$
$$= \frac{\chi_N}{192} \left(\frac{1}{\rho_w D_v^3} \right)^{\frac{1}{6}} \left(\frac{L_{k,l}}{N_{k,l}} \right)^{\frac{1}{6}} \cdot \left(\left(\sqrt{13785} - 325 \right) - F \left(\sqrt{13785} + 325 \right) \right), \tag{F.59}$$

we get

$$\frac{1}{(1+F)}\left[c_+(k,l)+Fc_-(k,l)\right]= \tag{F.60}$$

$$=\frac{\chi_N}{192}\left(\frac{1}{\rho_w D_v^3}\right)^{\frac{1}{6}}\left(\frac{L_{k,l}}{N_{k,l}}\right)^{\frac{1}{6}}\cdot\frac{\left(\sqrt{13785}-325\right)-F\left(\sqrt{13785}+325\right)}{(1+F)} \tag{F.61}$$

$$=\frac{\chi_N}{192}\left(\frac{1}{\rho_w D_v^3}\right)^{\frac{1}{6}}\left(\frac{L_{k,l}}{N_{k,l}}\right)^{\frac{1}{6}}\cdot s_3 \tag{F.62}$$

with (using Wolfram|Alpha, n.d.)

$$s_3=\frac{\left(\sqrt{13785}-325\right)-F\left(\sqrt{13785}+325\right)}{(1+F)} \tag{F.63}$$

$$=-160. \tag{F.64}$$

Now, (F.57) becomes

$$N_{k,l+1}=N_{k,l}\left(1-\frac{\Delta t}{\Delta x}\left[\frac{\chi_N}{192}\left(\frac{1}{\rho_w D_v^3}\right)^{\frac{1}{6}}\left(\frac{L_{k,l}}{N_{k,l}}\right)^{\frac{1}{6}}\cdot s_3\left(\frac{N_{k+1,l}}{N_{k,l}}-1\right)+\right.\right. \tag{F.65}$$

$$\left.\left.+\frac{1}{2\cdot 14}\frac{1}{(1+F)}\left(\sqrt{\frac{919}{15}}-11\right)\frac{\chi_N}{192}\left(\frac{1}{\rho_w D_v^3}\right)^{\frac{1}{6}}\left(\frac{L_{k,l}}{N_{k,l}}\right)^{\frac{1}{6}}\cdot 2\cdot\sqrt{13785}\left(\frac{L_{k+1,l}}{L_{k,l}}-1\right)\right]\right)$$

$$=N_{k,l}\left(1-\frac{\Delta t}{\Delta x}\frac{\chi_N}{192}\left(\frac{1}{\rho_w D_v^3}\right)^{\frac{1}{6}}\left(\frac{L_{k,l}}{N_{k,l}}\right)^{\frac{1}{6}}\left[s_3\left(\frac{N_{k+1,l}}{N_{k,l}}-1\right)+\right.\right. \tag{F.66}$$

$$\left.\left.+\frac{1}{2\cdot 14}\frac{1}{(1+F)}\left(\sqrt{\frac{919}{15}}-11\right)\cdot 2\cdot\sqrt{13785}\left(\frac{L_{k+1,l}}{L_{k,l}}-1\right)\right]\right)$$

$$=N_{k,l}\left(1-\frac{\Delta t}{\Delta x}\frac{\chi_N}{192}\left(\frac{1}{\rho_w D_v^3}\right)^{\frac{1}{6}}\left(\frac{L_{k,l}}{N_{k,l}}\right)^{\frac{1}{6}}\left[s_3\left(\frac{N_{k+1,l}}{N_{k,l}}-1\right)+s_4\left(\frac{L_{k+1,l}}{L_{k,l}}-1\right)\right]\right),$$

with (using Wolfram|Alpha, n.d.)

$$s_4=\frac{1}{2\cdot 14}\frac{1}{(1+F)}\left(\sqrt{\frac{919}{15}}-11\right)\cdot 2\cdot\sqrt{13785} \tag{F.67}$$

$$=\frac{1}{14}\frac{1}{(1+F)}\left(\sqrt{\frac{919}{15}}-11\right)\cdot\sqrt{13785} \tag{F.68}$$

$$=-32. \tag{F.69}$$

Appendix G

Additional plots for Chapter 6

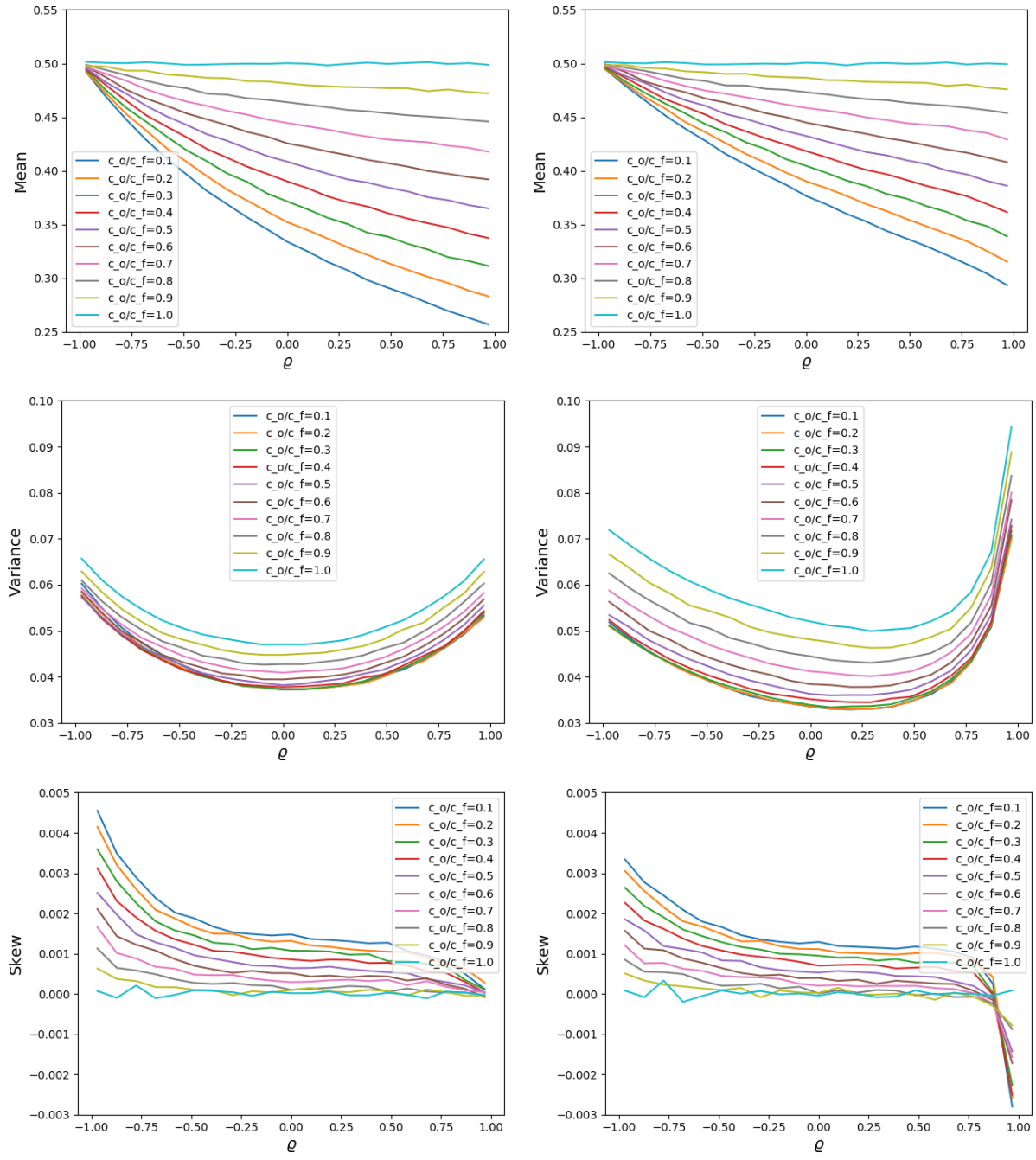

Figure G.1: Moments of the distribution of w_2^a for several examples of $\frac{c_o}{c_f} < 1$, in the situation of Example 6.3.5, when using $\mathbf{R}$ (left panel) and $\mathbf{R}_{dg}$ (right panel), with mean shown in the upper panel, variance in the central panel and skewness in the lower panel.

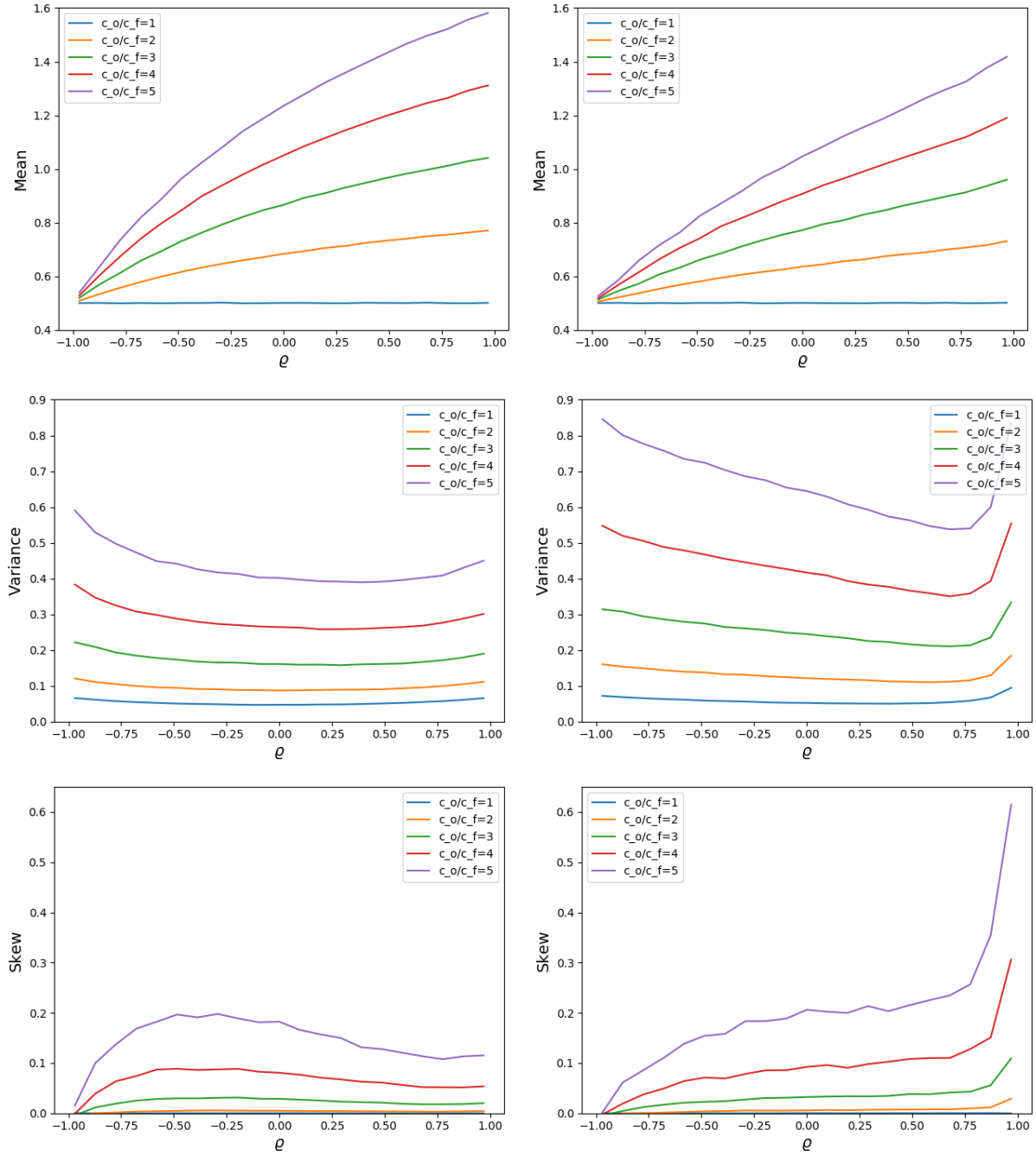

Figure G.2: Moments of the distribution of w_2^a for several examples of $\frac{c_o}{c_f} > 1$, in the situation of Example 6.3.5, when using $\mathbf{R}$ (left panel) and $\mathbf{R}_{dg}$ (right panel), with mean is shown in the upper panel, variance in the central panel and skewness in the lower panel.

We see that the mean of the distribution of w_2^a increases with ϱ for $\frac{c_o}{c_f} > 1$ and decreases with ϱ for $\frac{c_o}{c_f} < 1$, where this effect is weaker, when non-diagonal error covariances are

used. Non-diagonal observation error covariances increase the variance of the distribution, especially for large $\|\varrho\|$. Furthermore, they decrease the skewness of the distribution for $\frac{c_o}{c_f} < 1$ and increase it for $\frac{c_o}{c_f} > 1$, especially for large ϱ.

Appendix H

Additional calculations, proofs and examples for Chapter 6

H.1 Calculations for Example 6.4.1

We have $k = 0$ and thus

$$
\begin{aligned}
w_2^a &= w_2^f + \frac{1}{(a+r_1)(b+r_2)-c^2}\left[cr_2\Delta w_1 + \left(b(a+r_1)-c^2\right)\Delta w_2\right] \qquad \text{(H.1)}\\
&= w_2^f + \frac{1}{(a+r_1)(b+r_2)-c^2}\left[cr_2\left(w_1^o - w_1^f\right) + \left(b(a+r_1)-c^2\right)\left(w_2^o - w_2^f\right)\right]\\
&= w_2^f\left[1 - \frac{b(a+r_1)-c^2}{(a+r_1)(b+r_2)-c^2}\right] + \frac{1}{(a+r_1)(b+r_2)-c^2}\left[cr_2\left(w_1^o - w_1^f\right) + \left(b(a+r_1)-c^2\right)w_2^o\right]\\
&= w_2^f\left[\frac{(a+r_1)(b+r_2)-c^2-b(a+r_1)+c^2}{(a+r_1)(b+r_2)-c^2}\right] +\\
&\quad + \frac{1}{(a+r_1)(b+r_2)-c^2}\left[cr_2\left(w_1^o - w_1^f\right) + \left(b(a+r_1)-c^2\right)w_2^o\right]\\
&= w_2^f\left[\frac{(a+r_1)r_2}{(a+r_1)(b+r_2)-c^2}\right] + \frac{1}{(a+r_1)(b+r_2)-c^2}\left[cr_2\left(w_1^o - w_1^f\right) + \left(b(a+r_1)-c^2\right)w_2^o\right]\\
&= \underbrace{\frac{1}{(a+r_1)(b+r_2)-c^2}}_{\geq 0}\Big[(a+r_1)r_2w_2^f + cr_2\left(w_1^o - w_1^f\right) + \underbrace{\left(b(a+r_1)-c^2\right)w_2^o}_{\geq br_1w_2^o,\ \text{because } ab\geq c^2 \text{ and } w_2^o\geq 0}\Big]\\
&\geq \frac{1}{(a+r_1)(b+r_2)-c^2}\Big[\underbrace{(a+r_1)r_2w_2^f + br_1w_2^o}_{\geq 0} + cr_2\left(w_1^o - w_1^f\right)\Big]\\
&= \frac{r_2}{(a+r_1)(b+r_2)-c^2}\left[(a+r_1)w_2^f + \frac{br_1}{r_2}w_2^o + c\Delta w_1\right]
\end{aligned}
$$

which yields $w_2^a \geq 0$, if

$$(a + r_1)\, w_2^f + \frac{br_1}{r_2} w_2^o + c\Delta w_1 \geq 0. \tag{H.2}$$

H.2 Analytical example for non-negativity violation without influence from measurements at other grid points

Example H.2.1. Assume $\Delta w_1 = 0$ and $\Delta w_2 = -w_2^f$, then

$$w_2^a = w_2^f + \frac{1}{(a + r_1)(b + r_2) - (k + c)^2} \left[(cr_2 - bk)\, \Delta w_1 + (b\,(a + r_1) - c\,(k + c))\, \Delta w_2 \right] \tag{H.3}$$

$$= w_2^f - \frac{b\,(a + r_1) - c\,(k + c)}{(a + r_1)(b + r_2) - (k + c)^2} w_2^f \tag{H.4}$$

$$= \left[(a + r_1)(b + r_2) - (k + c)^2 - (b\,(a + r_1) - c\,(k + c)) \right] \frac{w_2^f}{(a + r_1)(b + r_2) - (k + c)^2} \tag{H.5}$$

$$= \underbrace{\left[(a + r_1)\, r_2 - k\,(k + c) \right]}_{:= \tilde{g}} \frac{w_2^f}{(a + r_1)(b + r_2) - (k + c)^2}, \tag{H.6}$$

thus $w_2^a < 0$ holds, if $\tilde{g} < 0$, i.e.

$$0 > \tilde{g} \tag{H.7}$$

$$\Leftrightarrow 0 > (a + r_1)\, r_2 - k\,(k + c) \tag{H.8}$$

$$\Leftrightarrow 0 > (a + r_1)\, r_2 - \tilde{\rho}^2 r_1 r_2 - \tilde{\rho}\rho\sqrt{r_1 r_2 ab} \tag{H.9}$$

$$\Leftrightarrow \tilde{\rho}\rho\sqrt{r_1 r_2 ab} > (a + r_1)\, r_2 - \tilde{\rho}^2 r_1 r_2 \tag{H.10}$$

$$\Leftrightarrow \sqrt{b} > \frac{1}{\tilde{\rho}\rho\sqrt{r_1 r_2 a}} \left[(a + r_1)\, r_2 - \tilde{\rho}^2 r_1 r_2 \right] \tag{H.11}$$

$$b > \left(\frac{1}{\tilde{\rho}\rho\sqrt{r_1 r_2 a}} \left[(a + r_1)\, r_2 - \tilde{\rho}^2 r_1 r_2 \right] \right)^2 \tag{H.12}$$

This allows (if one choses $0 < \tilde{\rho}, \rho < 1$ and $a, b, r_1, r_2 > 0$) finding positive semidefinite $\mathbf{P}_f$ and $\mathbf{R}$, that produce negative analysis without any effect from $\Delta w_1 = 0$. Note, that this is only possible, if $k \neq 0$, i.e. this problem can only occur if non-diagonal $\mathbf{R}$ is used. Furthermore, even assuming the worst case of $\tilde{\rho}, \rho = 1$, it only occurs if $b > a\frac{r_1}{r_2}$, e.g. if quantities of strongly differing scales are assimilated.

H.3 Analytical examples involving multiple grid points

We look at the conditions for obtaining negative analysis at grid point 2 in an example involving 3 grid points. To this end, we consider an example with three grid points, in which only the first two are observed, using a notation analogue to Notation 6.3.1, with

$$\mathbf{w}^a = \begin{pmatrix} w_1^a \\ w_2^a \\ w_3^a \end{pmatrix}, \mathbf{w}^f = \begin{pmatrix} w_1^f \\ w_2^f \\ w_3^f \end{pmatrix}, \mathbf{P}^f = \begin{pmatrix} a & c & d \\ c & b & e \\ d & e & f \end{pmatrix}, \mathbf{R} = \begin{pmatrix} r_1 & k & l \\ k & r_2 & m \\ l & m & r_3 \end{pmatrix}. \tag{H.13}$$

We start with the case of the observations only differing from the forecast at grid point 1:

Example H.3.1. Let $\Delta w_2 = \Delta w_3 = 0$, then

$$w_2^a = w_2^f - F\Delta w_1, \tag{H.14}$$

with

$$F = -\frac{c\left[(b+r_2)(f+r_3)-(e+m)^2\right]+e\left[(c+k)(e+m)-(b+r_2)(d+l)\right]+b\left[(d+l)(e+m)-(f+r_3)(c+k)\right]}{(a+r_1)(b+r_2)(f+r_3)-(a+r_1)(e+m)^2-(b+r_2)(d+l)^2-(f+r_3)(c+k)^2+2(c+k)(d+l)(e+m)}. \tag{H.15}$$

Thus, we get $w_2^a < 0$, iff

$$F\Delta w_1 > w_2^f. \tag{H.16}$$

Now, we look at the case of grid points 1 and 3 having equal increments and correlations to grid point 2:

Example H.3.2. Let $\Delta w_2 = 0$, $\Delta w_3 = \Delta w_1$, $a = f$, $r_1 = r_3$, $k = m$ and $c = e$, then

$$w_2^a = w_2^f - 2F\Delta w_1. \tag{H.17}$$

Thus, we get $w_2^a < 0$, iff

$$2F\Delta w_1 > w_2^f. \tag{H.18}$$

H.4 Proof of Proposition 6.4.3

Proof. Using $\mathbf{H} = \mathrm{Id}$, from (2.15) follows

$$\mathbf{w}^a = \mathbf{w}^f + \mathbf{K}\Delta\mathbf{w}, \tag{H.19}$$

and from (2.16) follows

$$\mathbf{K} = \mathbf{P}^f \left(\mathbf{P}^f + \mathbf{R}\right)^{-1}. \tag{H.20}$$

Now setting

$$\hat{\mathbf{K}} = \hat{\mathbf{P}}^f \left(\hat{\mathbf{P}}^f + \hat{\mathbf{R}}\right)^{-1}, \tag{H.21}$$

we can rewrite (H.19) as

$$\mathbf{w}^a = \underbrace{\mathbf{w}^f + \hat{\mathbf{K}}\Delta\mathbf{w}}_{:=\hat{\mathbf{w}}^a} + \left(\mathbf{K} - \hat{\mathbf{K}}\right)\Delta\mathbf{w} \tag{H.22}$$

Now, using the strict positivity of the forecast and the diagonality of $\hat{\mathbf{P}}^f$ and $\hat{\mathbf{R}}$, from Proposition 6.1.2 follows $\hat{w}_i^a > 0$, for all $i \in \{1, \cdots, n\}$.
Now, we note that (H.20) is concatenation of matrix multiplication, addition and inversion (which all are continuous functions) and thus continuous in $\mathbf{P}^f$ and $\mathbf{R}$. Thus, we can pick ϵ so that

$$\left\|\mathbf{K} - \hat{\mathbf{K}}\right\|_\infty \leq \min_i \frac{\hat{w}_i^a}{n c_w} \tag{H.23}$$

Now, considering the components of (H.22) we get

$$\begin{aligned}
w_i^a &= \hat{w}_i^a + \left[\left(\mathbf{K} - \hat{\mathbf{K}}\right)\Delta\mathbf{w}\right]_i && \text{(H.24)}\\
&\geq \hat{w}_i^a - \left|\left[\left(\mathbf{K} - \hat{\mathbf{K}}\right)\Delta\mathbf{w}\right]_i\right| && \text{(H.25)}\\
&\geq \hat{w}_i^a - n \underbrace{\left\|\mathbf{K} - \hat{\mathbf{K}}\right\|_\infty}_{\leq \min_i \frac{\hat{w}_i^a}{n c_w}} \underbrace{\|\Delta\mathbf{w}\|_\infty}_{\leq c_w} && \text{(H.26)}\\
&\geq \hat{w}_i^a - \min_i \frac{\hat{w}_i^a}{c_w} c_w && \text{(H.27)}\\
&= \hat{w}_i^a - \min_i \hat{w}_i^a && \text{(H.28)}\\
&\geq 0, && \text{(H.29)}
\end{aligned}$$

for all $i \in \{1, \cdots, n\}$.

□

AMS (2022). *Glossary of Meteorology*. https://glossary.ametsoc.org/wiki/Hydrometeor. Accessed: March 05. 2024.

Auer, A. H. and D. L. Veal (1970). "The Dimension of Ice Crystals in Natural Clouds". In: *Journal of Atmospheric Sciences* 27.6, pp. 919–926. DOI: 10.1175/1520-0469(1970)027<0919:TDOICI>2.0.CO;2.

Bannister, R. N., H. G. Chipilski, and O. Martinez-Alvarado (2020). "Techniques and challenges in the assimilation of atmospheric water observations for numerical weather prediction towards convective scales". In: *Quarterly Journal of the Royal Meteorological Society* 146.726, pp. 1–48. DOI: https://doi.org/10.1002/qj.3652.

Berry, E. X. and R. L. Reinhardt (1974). "An Analysis of Cloud Drop Growth by Collection: Part I. Double Distributions". In: *Journal of Atmospheric Sciences* 31.7, pp. 1814–1824. DOI: 10.1175/1520-0469(1974)031<1814:AAOCDG>2.0.CO;2.

Bishop, C. M. (2006). *Pattern Recognition and Machine Learning*. Cambridge: Springer Science+Business Media, LLC.

Bishop, C. and D. Hodyss (2009). "Ensemble covariances adaptively localized with ECO-RAP. Part 1: tests on simple error models". In: *Tellus A: Dynamic Meteorology and Oceanography* 61.1, pp. 84–96. DOI: 10.1111/j.1600-0870.2007.00371.x.

Bishop, C. H. (2016). "The GIGG-EnKF: ensemble Kalman filtering for highly skewed non-negative uncertainty distributions". In: *Quarterly Journal of the Royal Meteorological Society* 142.696, pp. 1395–1412. DOI: https://doi.org/10.1002/qj.2742.

— (2019). "Data assimilation strategies for state-dependent observation error variances". In: *Quarterly Journal of the Royal Meteorological Society* 145.718, pp. 217–227. DOI: https://doi.org/10.1002/qj.3424.

Bishop, C. H., B. J. Etherton, and S. J. Majumdar (2001). "Adaptive Sampling with the Ensemble Transform Kalman Filter. Part I: Theoretical Aspects". In: *Monthly Weather Review* 129.3, pp. 420–436. DOI: https://doi.org/10.1175/1520-0493(2001)129<0420:ASWTET>2.0.CO;2.

Brdar, S. and A. Seifert (2018). "McSnow: A Monte-Carlo Particle Model for Riming and Aggregation of Ice Particles in a Multidimensional Microphysical Phase Space". In: *Journal of Advances in Modeling Earth Systems* 10.1, pp. 187–206. DOI: https://doi.org/10.1002/2017MS001167.

Bronstein Semendjajew Musiol, M. (2008). *Taschenbuch der Mathematik*. Verlag Harri Deutsch.

Burgers, G., P. J. van Leeuwen, and G. Evensen (1998). "Analysis Scheme in the Ensemble Kalman Filter". In: *Monthly Weather Review* 126.6, pp. 1719–1724. DOI: https://doi.org/10.1175/1520-0493(1998)126<1719:ASITEK>2.0.CO;2.

Cohn, S. E. (1997). "An introduction to estimation theory". In: *J. Meteor. Soc. Japan* 75, pp. 257–288.

Courant, R., E. Isaacson, and M. Rees (1952a). "On the solution of nonlinear hyperbolic differential equations by finite differences". In: *Communications on Pure and Applied Mathematics* 5.3, pp. 243–255. DOI: https://doi.org/10.1002/cpa.3160050303.

Courant, R., E. Isaacson, and M. Rees (1952b). "On the solution of nonlinear hyperbolic differential equations by finite differences". In: *Communications on Pure and Applied Mathematics* 5.3, pp. 243–255. DOI: https://doi.org/10.1002/cpa.3160050303.

Courtier, P., E. Andersson, W. Heckley, et al. (1998). "The ECMWF implementation of three-dimensional variational assimilation (3D-Var). I: Formulation". In: *Q J R Meteorol Soc* 124, pp. 1783–1807.

Croucher, M. (2014). *GitHub*. https://github.com/mikecroucher/nearest_correlation.

Degelia, S. and X. Wang (Dec. 2022). "Impacts of Methods for Estimating the Observation Error Variance for the Frequent Assimilation of Thermodynamic Profilers on Convective-Scale Forecasts". In: *Monthly Weather Review* 151. DOI: 10.1175/MWR-D-21-0049.1.

Destouches, M., T. Montmerle, Y. Michel, et al. (2023). "Impact of hydrometeor control variables in a convective-scale 3DEnVar data assimilation scheme". In: *Quarterly Journal of the Royal Meteorological Society* 149.752, pp. 757–780. DOI: https://doi.org/10.1002/qj.4426.

Eisman, G. S. (1990). "A neural network which computes the square root". In: *Journal of Pure and Applied Algebra* 63.1, pp. 29–47. ISSN: 0022-4049. DOI: https://doi.org/10.1016/0022-4049(90)90054-L.

Evensen, G. (1994). "Sequential data assimilation with a nonlinear quasi-geostrophic model using Monte Carlo methods to forecast error statistics". In: *Journal of Geophysical Research* 99, pp. 10143–10162.

Gleiter, T., T. Janjić, and N. Chen (2022). "Ensemble Kalman filter based data assimilation for tropical waves in the MJO skeleton model". In: *Quarterly Journal of the Royal Meteorological Society* 148.743, pp. 1035–1056. DOI: https://doi.org/10.1002/qj.4245.

Gustafsson, N., T. Janjić, C. Schraff, et al. (2018). "Survey of data assimilation methods for convective-scale numerical weather prediction at operational centres". In: *Quarterly Journal of the Royal Meteorological Society* 144.713, pp. 1218–1256. DOI: https://doi.org/10.1002/qj.3179.

Harten, A., P. Lax, and B. van Leer (Jan. 1983). "On Upstream Differencing and Godunov-Type Schemes for Hyperbolic Conservation Laws". In: *SIAM Rev* 25, pp. 35–61.

Heymsfield, A. J. and M. Kajikawa (1987). "An Improved Approach to Calculating Terminal Velocities of Plate-like Crystals and Graupel". In: *Journal of Atmospheric Sciences* 44.7, pp. 1088–1099. DOI: 10.1175/1520-0469(1987)044<1088:AIATCT>2.0.CO;2.

Higham, N. J. (July 2002). "Computing the nearest correlation matrix—a problem from finance". In: *IMA Journal of Numerical Analysis* 22.3, pp. 329–343. ISSN: 0272-4979. DOI: 10.1093/imanum/22.3.329.

Hunt, B. R., E. J. Kostelich, and I. Szunyogh (2007). "Efficient data assimilation for spatiotemporal chaos: A local ensemble transform Kalman filter". In: *Physica D: Nonlinear Phenomena* 230.1. Data Assimilation, pp. 112–126. ISSN: 0167-2789. DOI: https://doi.org/10.1016/j.physd.2006.11.008.

Ide, K., P. Courtier, M. Ghil, et al. (1997). "Unified Notation for Data Assimilation : Operational, Sequential and Variational (gtSpecial IssueltData Assimilation in Meteology

and Oceanography: Theory and Practice)". In: *Journal of the Meteorological Society of Japan. Ser. II* 75.1B, pp. 181–189. DOI: 10.2151/jmsj1965.75.1B_181.

Igel, A. L., M. R. Igel, and S. C. van den Heever (2015). "Make It a Double? Sobering Results from Simulations Using Single-Moment Microphysics Schemes". In: *Journal of the Atmospheric Sciences* 72.2, pp. 910–925. DOI: 10.1175/JAS-D-14-0107.1.

Janjić, T., N. Bormann, M. Bocquet, et al. (2018). "On the representation error in data assimilation". In: *Quarterly Journal of the Royal Meteorological Society* 144.713, pp. 1257–1278. DOI: https://doi.org/10.1002/qj.3130.

Janjić, T. and S. E. Cohn (2006a). "Treatment of Observation Error due to Unresolved Scales in Atmospheric Data Assimilation." In: *Mon. Wea. Rev* 134, pp. 2900–2915.

Janjić, T., D. McLaughlin, S. E. Cohn, et al. (2014). "Conservation of mass and preservation of positivity with ensemble-type Kalman filter algorithms". In: *Mon. Wea. Rev.* 142.2, pp. 755–773. DOI: https://doi.org/10.1175/MWR-D-13-00056.1.

Janjić, T. and S. E. Cohn (2006b). "Treatment of Observation Error due to Unresolved Scales in Atmospheric Data Assimilation". In: *Monthly Weather Review* 134.10, pp. 2900–2915. DOI: 10.1175/MWR3229.1.

Janjić, T., M. Sommer, and G. C. Craig (2017). *Atmospheric Data Assimilation (lecture notes)*.

Janjić, T. and Y. Zeng (Dec. 2021). "Weakly Constrained LETKF for Estimation of Hydrometeor Variables in Convective-Scale Data Assimilation". In: *Geophysical Research Letters* 48.24. DOI: 10.1029/2021gl094962.

Jansen, S. (2018). *Gibbsian Point Processes (lecture notes)*. https://www.mathematik.uni-muenchen.de/~jansen/gibbspp.pdf.

Kalman, R. E. et al. (1960). "A new approach to linear filtering and prediction problems [J]". In: *Journal of basic Engineering* 82.1, pp. 35–45.

Keil, C. and G. C. Craig (2009). "A Displacement and Amplitude Score Employing an Optical Flow Technique". In: *Weather and Forecasting* 24.5, pp. 1297–1308. DOI: 10.1175/2009WAF2222247.1.

Lange, H. and G. C. Craig (2014). "The Impact of Data Assimilation Length Scales on Analysis and Prediction of Convective Storms". In: *Mon. Wea. Rev* 142, pp. 3781–3808. DOI: {http://dx.doi.org/10.1175/MWR-D-13-00304.1}.

Lange, H. and T. Janjić (2016). "Assimilation of Mode-S EHS Aircraft Observations in COSMO-KENDA". In: *Monthly Weather Review* 144.5, pp. 1697–1711. DOI: 10.1175/MWR-D-15-0112.1.

Lauvernet, C., J.-M. Brankart, F. Castruccio, et al. (2009). "A truncated Gaussian filter for data assimilation with inequality constraints: Application to the hydrostatic stability condition in ocean models". In: *Ocean Modelling* 27.1, pp. 1–17. ISSN: 1463-5003. DOI: https://doi.org/10.1016/j.ocemod.2008.10.007.

Morrison, H., M. van Lier-Walqui, A. M. Fridlind, et al. (2020). "Confronting the Challenge of Modeling Cloud and Precipitation Microphysics". In: *Journal of Advances in Modeling Earth Systems* 12.8. e2019MS001689 2019MS001689, e2019MS001689. DOI: https://doi.org/10.1029/2019MS001689.

Murrell, D. J., U. Dieckmann, and R. Law (2004). "On moment closures for population dynamics in continuous space". In: *Journal of Theoretical Biology* 229.3, pp. 421–432. ISSN: 0022-5193. DOI: https://doi.org/10.1016/j.jtbi.2004.04.013.

Onof, C., R. Chandler, A. Kakou, et al. (Jan. 2000). "Rainfall modelling using Poisson-cluster processes: A review of developments". In: *Stochastic Environmental Research and Risk Assessment* 14, pp. 384–411. DOI: 10.1007/s004770000043.

Rainwater, S., C. Bishop, and W. Campbell (May 2015). "The benefits of correlated observation errors for small scales: Correlated Observation Error Benefits". In: *Quarterly Journal of the Royal Meteorological Society* 141. DOI: 10.1002/qj.2582.

Roberts, N. M. and H. W. Lean (2008). "Scale-Selective Verification of Rainfall Accumulations from High-Resolution Forecasts of Convective Events". In: *Monthly Weather Review* 136.1, pp. 78–97. DOI: https://doi.org/10.1175/2007MWR2123.1.

Ruckstuhl, Y., T. Janjić, and S. Rasp (2021). "Training a convolutional neural network to conserve mass in data assimilation". In: *Nonlinear Processes in Geophysics* 28.1, pp. 111–119. DOI: 10.5194/npg-28-111-2021.

Seifert, A. (2022). private communication.

Semrau, F. (2020). "Towards moment closures in theoretical ecology". Master's Thesis. Ludwig Maximilian University Munich.

Shima, S.-i., K. Kusano, A. Kawano, et al. (June 2009). "The super-droplet method for the numerical simulation of clouds and precipitation: a particle-based and probabilistic microphysics model coupled with a non-hydrostatic model". In: *Quarterly Journal of the Royal Meteorological Society* 135, pp. 1307–1320. DOI: 10.1002/qj.441.

Simon, E. and L. Bertino (2009). "Application of the Gaussian anamorphosis to assimilation in a 3-D coupled physical-ecosystem model of the North Atlantic with the EnKF: a twin experiment". In: *Ocean Science* 5.4, pp. 495–510. DOI: 10.5194/os-5-495-2009.

Tabeart, J. M., S. L. Dance, A. S. Lawless, et al. (2020). "Improving the condition number of estimated covariance matrices". In: *Tellus A: Dynamic Meteorology and Oceanography* 72.1, pp. 1–19. DOI: 10.1080/16000870.2019.1696646.

Terasaki, K. and T. Miyoshi (Nov. 2023). "Including the horizontal observation error correlation in the ensemble Kalman filter: idealized experiments with NICAM-LETKF". In: *Monthly Weather Review*. DOI: 10.1175/MWR-D-23-0053.1.

Tong, M. and M. Xue (2005). "Ensemble Kalman Filter Assimilation of Doppler Radar Data with a Compressible Nonhydrostatic Model: OSS Experiments". In: *Monthly Weather Review* 133.7, pp. 1789–1807. DOI: 10.1175/MWR2898.1.

Wacker, U. and A. Seifert (June 2001). "Evolution of rain water profiles resulting from pure sedimentation: Spectral vs. parameterized description". In: *Atmospheric Research - ATMOS RES* 58, pp. 19–39. DOI: 10.1016/S0169-8095(01)00081-3.

Weston, P. P., W. Bell, and J. R. Eyre (2014). "Accounting for correlated error in the assimilation of high-resolution sounder data". In: *Quarterly Journal of the Royal Meteorological Society* 140.685, pp. 2420–2429. DOI: https://doi.org/10.1002/qj.2306.

Wolfram|Alpha (n.d.). https://www.wolframalpha.com. Wolfram Alpha LLC.

Zeng, Y., T. Janjic, Y. Feng, et al. (2021). "Interpreting estimated observation error statistics of weather radar measurements using the ICON-LAM-KENDA system". In: *Atmo-*

spheric Measurement Techniques 14.8, pp. 5735–5756. DOI: 10.5194/amt-14-5735-2021.

Acknowledgments

First of all I want to thank the supervisor of my thesis Professor Dr. Janjic for her help and advice. I also want to thank Dr. Axel Seifert for his advice on microphysics and numerics. Furthermore I want to thank my colleagues, especially Mathias for his advice on all general meteorological questions, Julien for his recommendations on numerical methods and discretization and Maryam and Yvonne for their tips on scientific writing.

I also want to thank my friends and my family, especially my girlfriend Azade for their emotional support and understanding. Furthermore, I would like to thank the employees of Rischart at Munich central station for making travelling to Ingolstadt a lot more fun.